PB90-186354

Evaluation of the Wake Effects on Plume Dispersion Using Video Image Analysis

North Carolina State Univ. at Raleigh

Prepared for:

Environmental Protection Agency, Research Triangle Park, NC

Mar 90

U.S. Department of Commerce
National Technical Information Service
NTIS

PB90-186354

EPA/600/3-90/027
March 1990

EVALUATION OF THE WAKE EFFECTS ON PLUME DISPERSION USING VIDEO IMAGE ANALYSIS

by

Sarah A. Rajala
David S. Trotter

North Carolina State University
Department of Electrical and Computer Engineering
Campus Box 7911
Raleigh, N.C. 27695-7911

Cooperative Research Agreement
No. CR-813368

Project Officer

Alan H. Huber
Atmospheric Sciences Modeling Division
Atmospheric Research and Exposure Assessment Laboratory
Research Triangle Park, North Carolina 27711

ATMOSPHERIC RESEARCH AND EXPOSURE ASSESSMENT LABORATORY
OFFICE OF RESEARCH AND DEVELOPMENT
U.S. ENVIRONMENTAL PROTECTION AGENCY
RESEARCH TRIANGLE PARK, NORTH CAROLINA 27711

REPRODUCED BY
U.S. DEPARTMENT OF COMMERCE
NATIONAL TECHNICAL INFORMATION SERVICE
SPRINGFIELD, VA. 22161

TECHNICAL REPORT DATA

(Please read Instructions on the reverse before completing)

1. REPORT NO. 600/3-90/027

2.

3. RECIPIENT'S ACCESSION NO. PB90 186354/AS

4. TITLE AND SUBTITLE
EVALUATION OF THE WAKE EFFECTS ON PLUME DISPERSION USING VIDEO IMAGE ANALYSIS

5. REPORT DATE

6. PERFORMING ORGANIZATION CODE

7. AUTHOR(S)
Sarah A. Rajala & David S. Trotter

8. PERFORMING ORGANIZATION REPORT NO.

9. PERFORMING ORGANIZATION NAME AND ADDRESS
Department of Electrical and Computer Eng.
North Carolina State University
Raleigh, North Carolina 27695

10. PROGRAM ELEMENT NO.
A101G/B/73/01 (FY-90)

11. CONTRACT/GRANT NO.
CR-813368

12. SPONSORING AGENCY NAME AND ADDRESS
Atmospheric Research & Exposure Assessment Lab.
Office of Research and Development
U.S. Environmental Protection Agency
Research Triangle Park, North Carolina 27711

13. TYPE OF REPORT AND PERIOD COVERED

14. SPONSORING AGENCY CODE
EPA/600/09

15. SUPPLEMENTARY NOTES

16. ABSTRACT

The report summarizes results from a cooperative research agreement entitled "Evaluation of Wake Effects on Plume Dispersion using Video Image Analysis." Video images of smoke flow in the wake of a model building which were collected in previous wind tunnel studies conducted by EPA at its Fluid Modeling Facility were further analyzed in this research. Three distinct research projects were conducted. The first project evaluated existing image analysis/processing techniques to determine the contents of the data, develop a scheme for separating the smoke from the background, and ultimately determine the potential for analyzing the motion characteristics of the smoke flow. The second project used the theory of fractals to extract information from the smoke images. Results from these two projects identified a number of difficulties in trying to characterize smoke images. In the third project, a new technique for video imaging using laser sheet lighting was developed and tested. The resulting smoke images were observed to be more distinct and the noise levels were lower.

17. KEY WORDS AND DOCUMENT ANALYSIS

a. DESCRIPTORS	b. IDENTIFIERS/OPEN ENDED TERMS	c. COSATI Field/Group

18. DISTRIBUTION STATEMENT

19. SECURITY CLASS *(This Report)* UNCLASSIFIED

20. SECURITY CLASS *(This page)* UNCLASSIFIED

21. NO. OF PAGES 303

22. PRICE A14

Notice

The information in this document has been funded by the United States Environmental Protection Agency under Cooperative Research Agreement No. CR-813368 with North Carolina State University. It has been subjected to the agency's peer and administrative review, and it has been approved for publication as an EPA document. Mention of trade names or commercial products does not constitute endorsement or recommendation for use.

Abstract

The report summarizes results from a cooperative research agreement entitled "Evaluation of Wake Effects on Plume Dispersion using Video Image Analysis". Video images of smoke flow in the wake of a model building which were collected in previous wind tunnel studies conducted by EPA at its Fluid Modeling Facility were further analyzed in this research. Three distinct research projects were conducted. The first project evaluated existing image analysis/processing techniques to determine the contents of the data, develop a scheme for separating the smoke from the background, and ultimately, determine the potential for analyzing the motion characteristics of the smoke flow. The second project used the theory of fractals to extract information from the smoke images. Results from these two projects identified a number of difficulties in trying to characterize smoke images. In the third project, a new technique for video imaging using laser sheet lighting was developed and tested. The resulting smoke images were observed to be more distinct and the noise levels were lower.

Table of Contents

Notice ii
Abstract iii

1. Introduction 1

2. Image Analysis Techniques for Analyzing Smoke Image Data 4

3. Video Image Segmentation 36

4. Motion Detection 52

5. A Fractal-Based Model for the Representation of Smoke Image Data 64

6. Visualization of Smoke Dispersion Using Laser Light Sheets 155

7. Summary and Conclusions 188

8. References 193

Appendices

A. "Applications for Video Image Analysis of Smoke Dispersion in the Near Wake of a Model Building"

B. "Dimensionally Measurements for Chaotic Dynamical Systems"

C. "User's Guide: Spectra-Physics Model 164 Laser"

D. "Preliminary Evaluation of Laser Video Flow Data"

1 INTRODUCTION

The Clean Air Act calls for regulations which specify the use of dispersion models in evaluating compliance with air quality standards. As a result, there is a special need for improved dispersion models for predicting concentrations near sources which exhibit frequent building downwash problems. In addition, regulations on the design of "good engineering practice" stack heights require a better understanding of the extent of building wake effects. Until recently researchers have obtained meteorological measurements and concentrations of air pollutants by sampling several fixed points over the spatial region and temporal period of interest. The recorded data is then combined with available mathematical models to infer the over all pattern of pollutant concentrations for risk assessment. Unfortunately, these limited measurements do not always provide all the information needed to adequately understand the atmospheric processes under complex conditions, e.g., near buildings, mountainous terrain and/or for situations with chemically reacting pollutants.

One approach to improving the dispersion models is to combine the traditionally obtained measurements with visual images of smoke to provide a visualization of the pattern of atmospheric transport. In fact, exploratory studies at the U.S. EPA Meteorology Division Fluid Modeling Facility in cooperation with North Carolina State University demonstrated the feasibility of using video sequence image analysis techniques for studying wake effects (Huber, 1985). Based on the results of this initial study, it was clear that further research was warranted to develop and evaluate techniques for recording, processing, and analyzing video image sequences of wake effects and to develop methodologies for utilizing this information to improve dispersion models. As a result, a cooperative research agreement (CR-813368, entitled Evaluation of the Wake Effects on Plume Dispersion using Video Image Analysis) was established to continue this research.

The cooperative agreement was established to examine the near-wake flow downstream of buildings to determine how this highly turbulent near-wake flow affects plume dispersion downwind of buildings. To accomplish this objective, North Carolina State University (NCSU) would provide the EPA with further guidance and support for developing and applying video sequence analysis to the evaluation of wake effects. The EPA would conduct the fluid modeling studies of wake effects on plume dispersion. NCSU would advise and assist the EPA in the collection of any new image sequence data. In addition, the education and training of the graduate students participating in this research would be enhanced.

To achieve the goals of this research, it was decided that the resources would be used to support one graduate student per year and that three research topics would be addressed. In the first two projects we evaluated different approaches to analyzing the smoke flow data. Project 1 would evaluate standard image processing techniques for analyzing the video image sequences.

Project 2 would explore the feasibility of using the recent work on fractal theory to model and analyze the video image sequences. The results of the first two projects indicated a need for cleaner more detailed imagery. As a result, it was decided that Project 3 would design and implement a laser-sheet lighting experiment for recording new video image sequence data. It should be noted that Projects 1 and 2 utilized video image sequence data collected at the U.S. EPA Meteorology Division Fluid Modeling Facility which was described in Huber (1985). In this report, we present the results from this cooperative research agreement.

One of the characteristics of the image data we were interested in quantifying, if possible, was the motion of the smoke, i.e. the time-varying changes in the image intensity values. In recent years, an important research area in image processing has been the analysis of time-varying imagery. One of the main concerns of the researchers has been the modeling and extraction of motion information contained in time-sequences of imagery. A number of different models exist that can be used to characterize objects moving through space and time (Gonzalez, 1988; Jain, 1989). From an image processing viewpoint, the smoke can be thought of as an object and as such we should be able to extract its spatial and temporal characteristics. However, the deformable nature of the smoke flow makes it difficult or impossible to use existing motion analysis techniques. Most of the existing motion estimation algorithms make assumptions about the data that are not valid in this application. The three most common assumptions are that the moving object (i.e., the smoke) is a rigid body, the motion is linear, and the motion is in the image plane. None of these were true in this application. This led us to consider the two following alternatives for analyzing the image data.

In the first project, we assessed the potential for using existing image analysis/processing techniques to determine the contents of the data, develop a scheme for separating the smoke from the background, and ultimately, determine the potential for analyzing the motion characteristics of the smoke flow. Prior to doing an extensive amount of processing, we wanted to determine the amount of noise and signal degradation that was introduced in the recording process and if necessary, suggest appropriate filtering to reduce any artifacts. Several methods were used to assess the amount of signal and noise in the data and to determine whether the spatial sampling rate was adequate. It was determined that the sampling rate was adequate, thus no aliasing was present and that there was noise in the data, albeit a small amount. Several noise cleaning techniques were investigated. After the initial evaluation of the data, the objective was to find a way to extract the motion characteristics of the smoke. The difficulty is that the smoke is not a well-defined, high-contrast, rigid body object. Thus many of the existing image analysis techniques could not be applied. The approach we decided upon was to separate the smoke from the background and then using the segmented image data attempt to extract the motion characteristics. The techniques we used for separating the smoke from the background are those used for image

2 IMAGE ANALYSIS TECHNIQUES FOR ANALYZING SMOKE IMAGE DATA

2.1 Introduction

The analysis of recorded video images of smoke has the potential for providing more spatial and temporal information than is possible to attain from traditional point-sampling techniques. Hence, a better understanding of the dispersion process is possible. In this section, we describe the image analysis tools we applied to the image data.

Over the years photographs of smoke have been used for visualizing dispersion patterns. For the most part, the photographs have been viewed qualitatively because of the complexities involved in quantifying the data. However, data recorded in video format has great potential as an easily digitized electronic medium. The digitized video data (each picture element being referred to as a pixel) can be analyzed using tools from the fields of digital image processing and analysis. As a result, digital image processing and analysis are becoming important elements in fluid dynamics research. Summaries of recent contributions can be found in Von Karman Institute (1984) and Hesselink (1988).

Frames 1, 10, 20, and 30 of one of the image sequences we utilized in this research are shown in figure 2.1. The experiments conducted to collect this sequence of data were performed in the Meteorological Wind Tunnel at the U.S. Environmental Protection Agency's Fluid Modeling Facility. It is an open-return wind tunnel with a test section 2.1 m high, 3.7 m wide, and 18.3 m long (Snyder, 1979). Flow downstream of a 0.1 m and a 0.2 m high rectangular-shaped block was studied. The along-stream building length was equal to the building height. The cross-stream building length was twice the building height and was oriented perpendicular to and at a 45 degree angle to the freestream flow.

An oil-fog smoke was generated and emitted into the wind tunnel through a pie, with the outflow pointed downstream. The stream of smoke simulated point-source emissions at ground level, midway along the leeward side of the building. The origin of the x,y,z coordinate system was set at this same point. A 600-W flood light was placed 3 m downstream from the leeward building edge. It was mounted in the center of the tunnel and elevated approximately 0.3 m. The light was aimed horizontally upstream toward the building.

Black-and-white images of the smoke were recorded at a rate of 30 frames per second with the camera connected to an NTSC-format VHS recorder. The camera was mounted outside the wind tunnel either looking down through a ceiling window (top view) or looking through a side window (side view). For more details, see Appendix A. The sequence of data shown in figure 2.1 is part of the top view sequence. At the bottom center of each frame is a portion of the building, the smoke flows over the central part of each frame from bottom to top, and a white grid can be segmentation. Because the data was basically bimodal (the smoke is light and the background is dark), the boundaries are not high contrast or well-defined, we chose a technique based on optimal thresholding (Chow, 1972). After segmentation was complete, the segmented image data was used to estimate the motion parameters. This was done by extracting the boundary of the segmented object, finding its centroid and then tracking the centroid from frame-to-frame.

In summary, we were able to estimate basic motion characteristics from the segmented image data. The processing included the following: (1) We determined the amount of signal content vs. noise content in the data. This required the use of a number of noise analysis techniques. (2) We applied several noise cleaning procedures in an attempt to increase the signal-to-noise ratio. (3) We segmented the image data to separate the smoke from the background. (4) We evaluated several schemes for extracting motion information from the data.

In the second project, we used the theory of fractals to extract information from the smoke flow data. Estimates of the fractal dimension and related measures (information and correlation dimensions) were calculated from the data. The estimates of fractal dimension were related qualitatively to the motion characteristics of the smoke flow in the image data. The estimates of information and correlation dimension were related to the concentration of the smoke flow. The results are preliminary, but promising.

Finally, in the third project we designed and implemented an alternative approach for capturing the smoke flow image data. The image data that was recorded previously was captured under flood lighting conditions. As a result, the two-dimensional image data was a projection of the three-dimensional volume of smoke flow onto a two-dimensional image plane. Thus, there is a loss in information. In addition, it was hoped that any new experiment would give clearer more detailed data for analysis. In the new system, laser lighting was used to generate a plane of illumination. As a result, we could selectively illuminate planar surfaces in the three-dimensional volume of smoke flow.

The remainder of this report describes the results of this research project. In section 2 we review many of the image analysis tools we applied to the data for noise assessment and noise cleaning. In section 3 we present the problem of image segmentation and discuss in detail an optimal thresholding segmentation scheme we implemented and show the results of this work. In section 4, we discuss approaches to do the processing necessary to extract motion information from the data. In section 5, we present an overview of the use of fractals in image processing/analysis, the proposed theory for using them in the context of analyzing smoke flow data, and then present the outcome of the processing that was performed. In section 6, the design of the laser-sheet lighting set-up, its implementation and results of a preliminary analysis of the recorded data are given. Finally, a summary and conclusions are made in section 7.

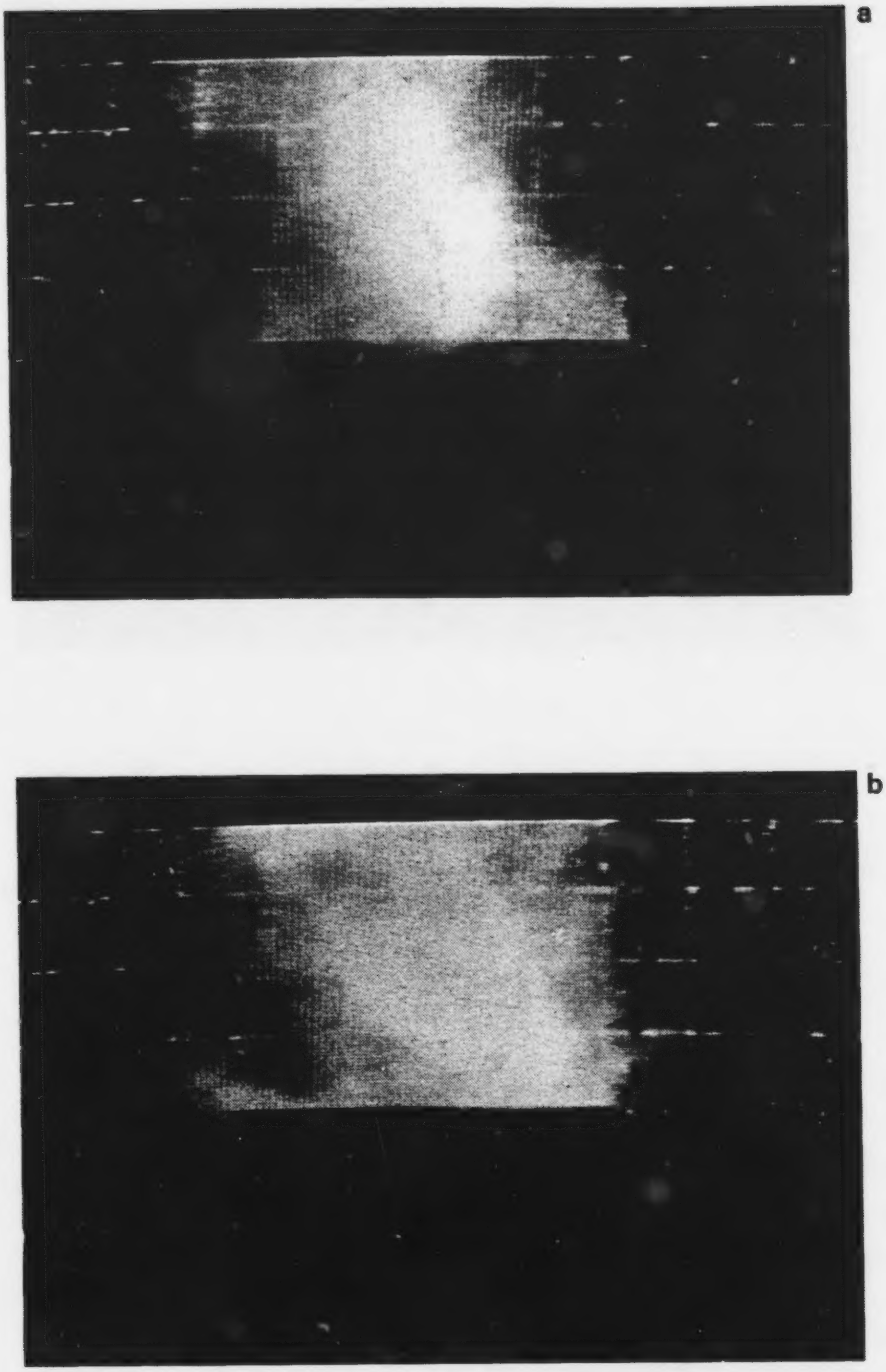

Figure 2.1: Top view of the smoke released from the downwind edge of a cubical building inside a wind tunnel. A grid painted on the floor of the tunnel shows in the background. Wind flows from the bottom to the top of th photograph. The building occupies the bottom half of the photograph. (a) Frame 1 of the image sequence; (b) Frame 10 of the image sequence;

roduced from
vailable copy.

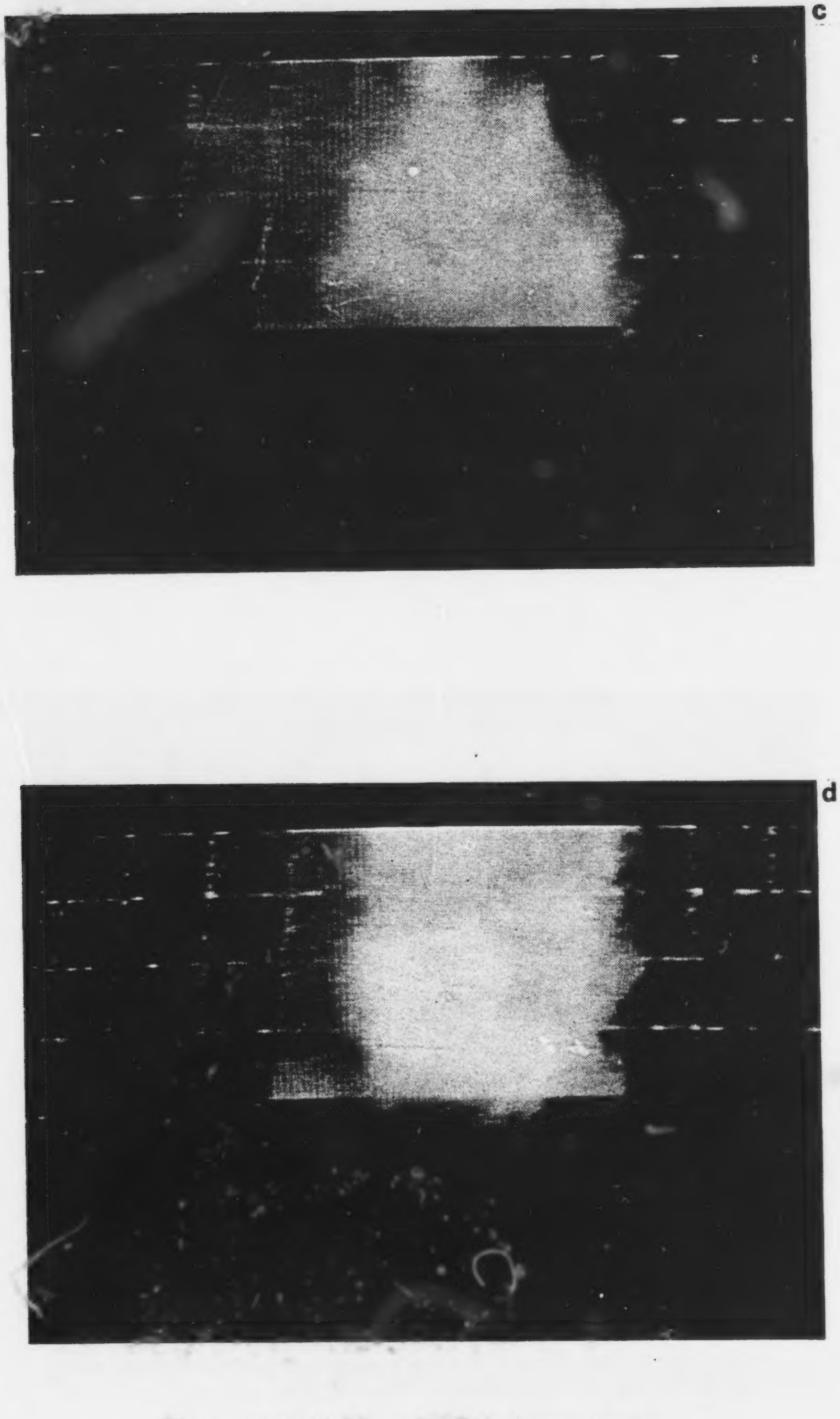

Figure 2.1: (c) Frame 20 of the image sequence;
(d) Frame 30 of the image sequence.

Reproduced from
best available copy.

seen on the floor of the wind tunnel.

2.2 Analysis of the Signal Characteristics

In order to determine the amount of useful signal information in the digitized data several operations were performed. First, we characterized the dynamic range of the digitized data by generating a histogram of each frame of the data and a histogram of an average of N frames of data. The histogram represents the relative frequency of occurrence of the gray levels (intensity) in an image. If the image pixel value (gray level) is considered to be random variable and the ordinate of the histogram is normalized by the total number of pixels in the image, then the histogram is an approximation of the probability density function for the gray level.

The average frame is calculated using:

$$\bar{g}(m,n) = \frac{1}{N}\sum_{p=1}^{N} g(m,n,p) \tag{2.1}$$

where $g(m,n,p)$ represents the intensity of the pixel at the (m,n) location in the pth frame. Figure 2.2 shows the histogram of frames 1, 10, 20 and 30. The average image for $N=50$ is shown in figure 2.3 and the histogram of this average data is shown in figure 2.4. It is clear from these histograms that the dynamic range of the digitized data typically goes from a gray level of 10 to gray level 220. It, however, does not tell us how much of the data corresponds to useful signal information and how much corresponds to noise.

To get a better handle on the signal-to-noise ratio of the recorded data, we needed to determine the accuracy of the quantization process. The intensity at each pixel in the digitized image data is represented by an 8-bit value, or one of 256 levels. However, depending on the amount of quantization noise introduced in the analog-to-digital conversion, the entire 8-bit dynamic range may not be fully utilized. A method for determining the extent to which quantization noise is introduced is to look at the information contained in the bit planes in the image data. For an 8-bit image there are eight binary bit planes. Any bit plane containing a purely random distribution of ones and zeros can be attributed to noise. Each of the bit planes, beginning with the least significant, was displayed to determine if any correlated information was present in that plane. For the visualization, a binary one was assigned to white and a binary zero was assigned to black. The three least significant bit planes for frame 10 are shown in figure 2.5. As can be seen, only the least significant bit plane appears to be a random distribution of ones and zeros, both the second and third bit plane contain some structured information. This was true for the rest of the data, as well. Thus it appears that the least significant bit plane contains little or no signal information.

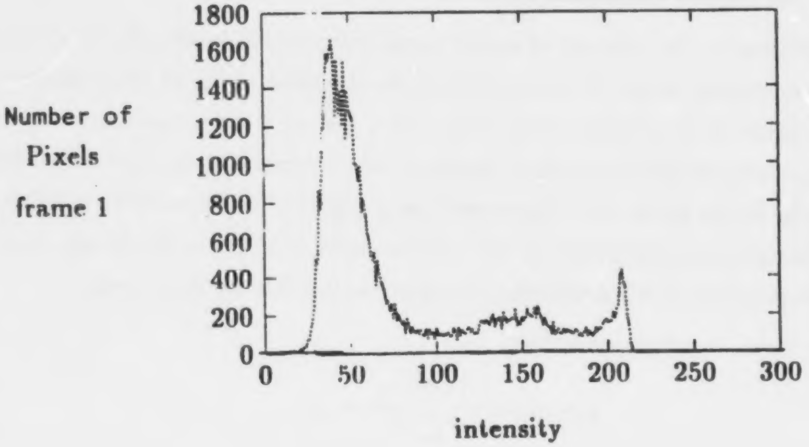

Figure 2.2(a): Histogram of frame 1 of the data shown in figure 1(a)

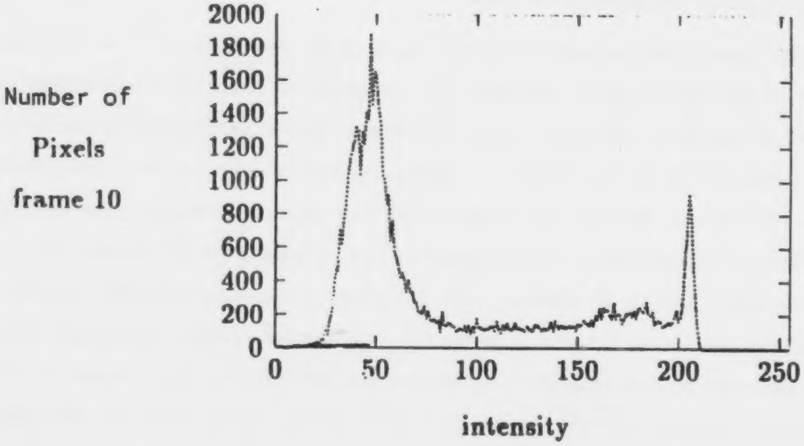

Figure 2.2(b): Histogram of frame 10 of the data shown in figure 1(b).

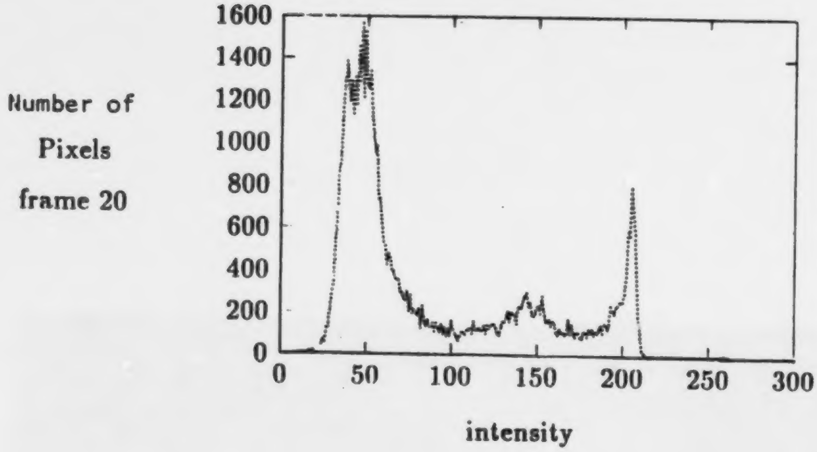

Figure 2.2(c): Histogram of frame 20 of the data shown in figure 1(c)

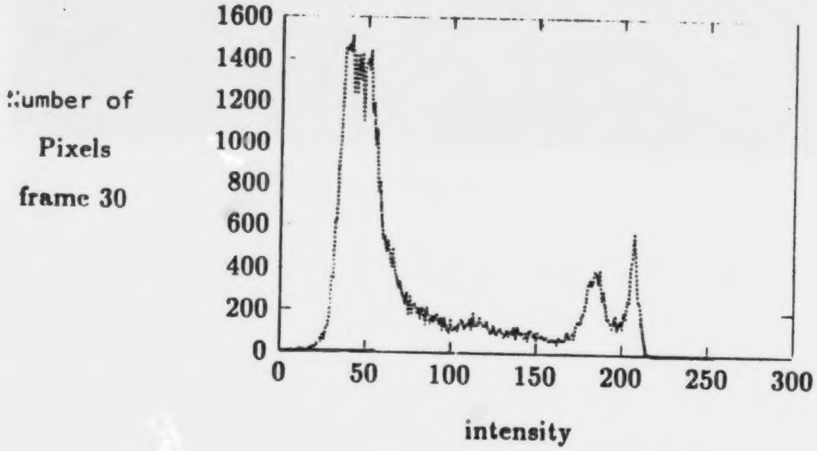

Figure 2.2(d): Histogram of frame 30 of the data shown in figure 1(d).

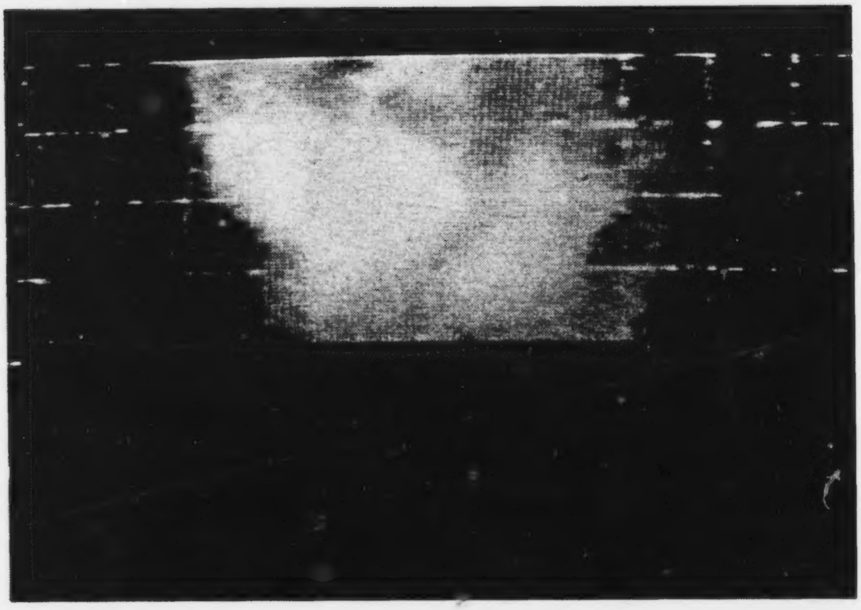

Figure 2.3: An average image. The average is computed over the first 50 frames of the image sequence.

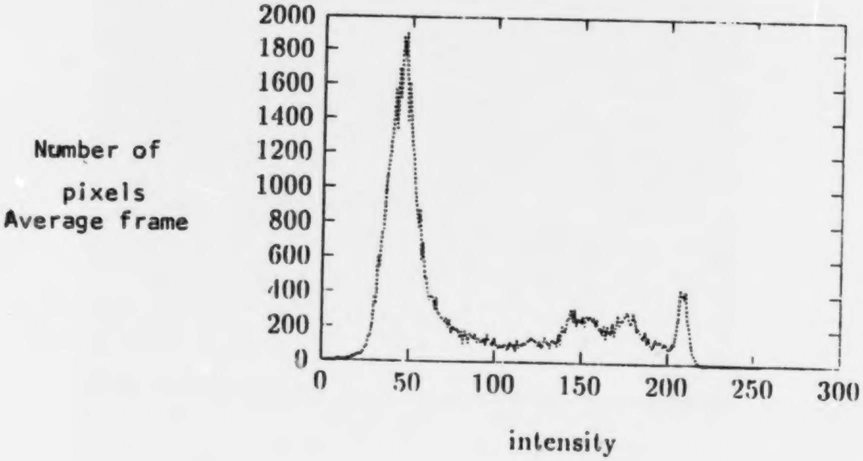

Figure 2.4: Histogram of the average data.

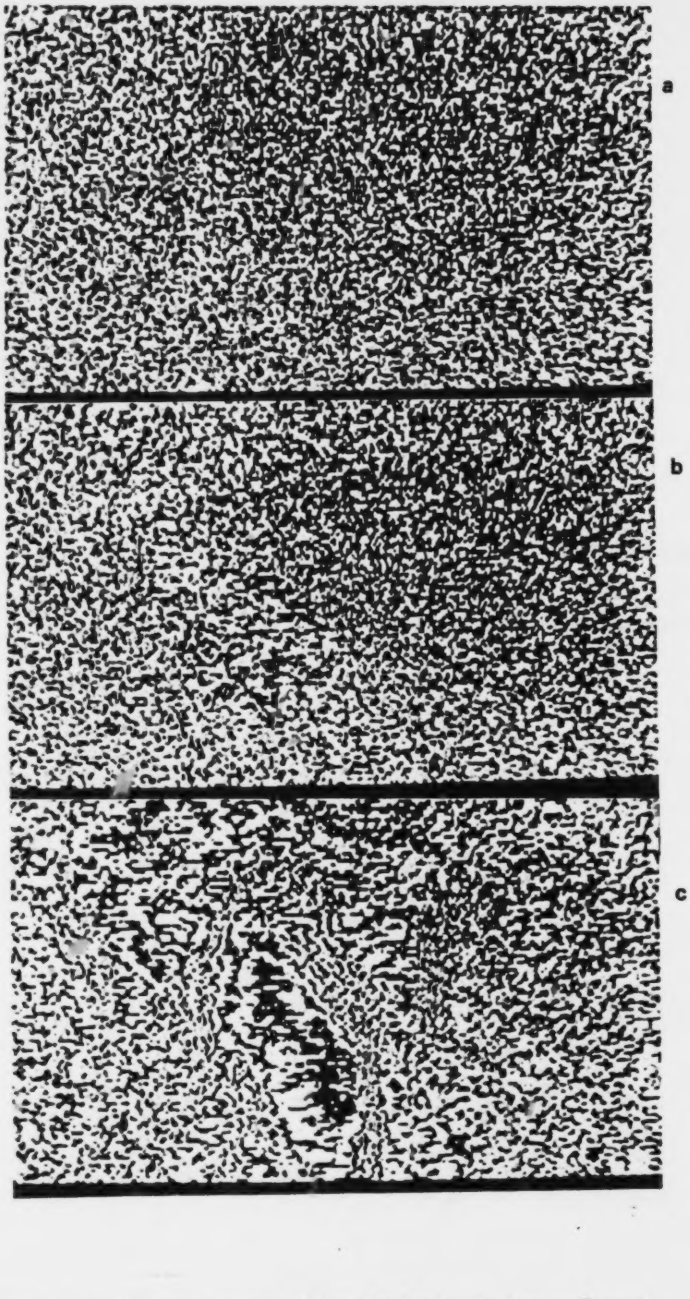

Figure 2.5: Images generated by displaying in image format a single bit of the eight-bit representation for each pixel in an image. A binary value of 1 is represented by white and a binary value of 0 is represented by black. The three least significant bit planes are shown.
(a) The least significant (first) bit plane from frame 10;
(b) The second bit plane from frame 10; and
(c) the third bit plane from frame 10.

Reproduced from
best available copy.

Another approach for attempting to verify that the bit planes are in fact uncorrelated random noise is to obtain an an estimate of the spatial autocorrelation for each bit plane. If the data are uncorrelated and wide-sense stationary (its mean is equal to a constant and its autocorrelation is shift-invariant), the autocorrelation should approximate a unit impulse function. The estimate we used for the autocorrelation function is given by

$$r(m,n) = \sum_{i=-(m-1)/2}^{(m-1)/2} \sum_{j=-(n-1)/2}^{(n-1)/2} g(i,j)g(m+i,n+j) \qquad (2.2)$$

The estimates of the autocorrelation for $r(m,n)$, $m,n = -2,\ldots,2$ for the three least significant bit planes are shown in Table 2.1. What can be seen in from Table 2.1 is that the estimate of the autocorrelation for the least significant bit plane is approximately a unit impulse function. For bit planes 1 and 2 the autocorrelations become less like a unit impulse, there is correlation between adjacent pixel values. This corroborates what we visually saw in figure 2.5. What we can conclude is that a 7 bit binary representation is adequate to represent the signal information contained in this image data. Alternatively, we can say that for each 8 bit pixel intensity there is approximately 1 bit of random error.

The final interpretation is that these data have a signal-to-noise ratio no greater than 42 dB. This is based on the rule-of-thumb that there is approximately a 6 dB increase in signal-to-noise ratio for each additional bit of information. This rule-of-thumb is based on the performance of a pulse code modulation (PCM) system with uniform quantization, (Couch, 1983).

In order to give an assessment of the spatial bandwidth of the image data, to determine whether the image data is likely to have aliasing due to spatial undersampling and to visualize the noise, a discrete Fourier transform (DFT) of the image data was obtained. The magnitude of the DFT of each image frame can be displayed as an image, with the dynamic range of the data rescaled so the largest value is assigned to 255 (white) and the smallest value to 0 (black). The DFT for frame 10 is shown in figure 2.6. It is clear from these images that the image data has a low spatial bandwidth, that is, the data has been spatially oversampled (the highest frequency of the data is much less than the Nyquist frequency), so no aliasing is present. In addition, as we should expect from the previous discussion, the intraframe noise is not a dominant factor even at the high frequencies.

2.3 Image Smoothing and Noise Removal

Although the intraframe noise levels as determined in the previous section are not overwhelming, pre-processing the data using a noise removal filter can improve the performance of subsequent operations. Hence, we needed to determine which were the most appropriate methods for reducing the amount of noise without sacrificing important signal information and

bit plane 0	.38	.01	.04	.01	.00
	-.01	.00	.00	-.04	.02
	-.01	.03	-.01	.00	-.02
	-.02	-.01	.01	-.01	.02
	-.00	.00	-.03	-.03	-.03

(a)

bit plane 1	.38	.07	.03	.01	.00
	-.04	-.04	-.02	-.01	-.01
	.04	.00	-.01	-.02	-.02
	01	-.05	.00	.00	.01
	.02	-.01	.01	.00	.00

(b)

bit plane 2	.38	.19	.08	.03	-.03
	.02	-.03	-.02	-.04	-.04
	-.01	.04	.02	-.03	-.03
	.03	-.02	-.03	.00	.02
	-.03	.00	.02	.03	.00

(c)

Table 2.1: Estimates of the autocorrelation $r(m,n), m,n = -2,\ldots,2$ for the three least significant bit planes for frame 10 of the original image data. (a) Least significant (first) bit plane; (b) Second bit plane; (c) Third bit plane.

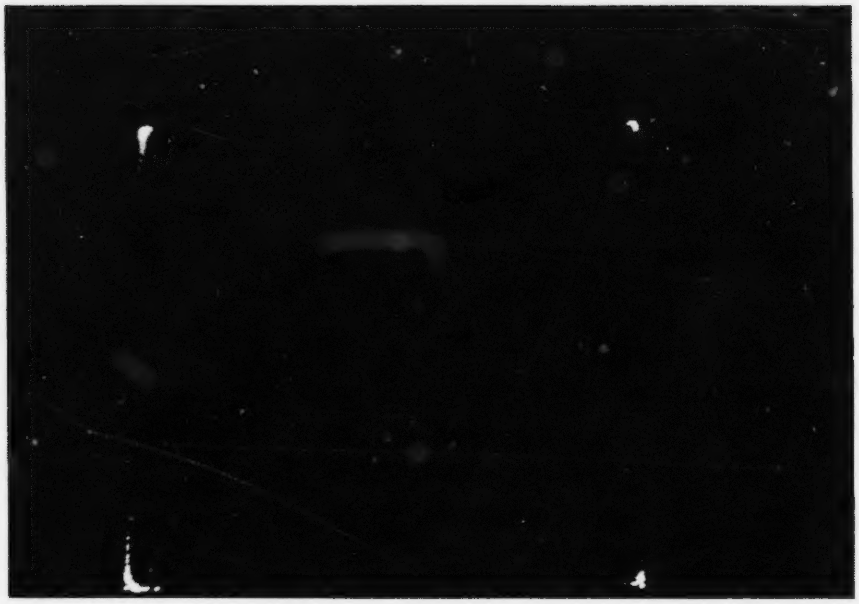

Figure 2.6: An image of the magnitude of the discrete Fourier transform of frame 10 of the original image sequence. This shows the spatial frequency distribution for frame 10. It can be seen from this figure that the image data has been highly oversampled in the spatial directions.

Reproduced from
best available copy.

how much impact this processing had on subsequent operations. Noise-removal techniques are generally referred to as smoothing techniques in the image processing literature (Pratt, 1978; Rosenfeld and Kak, 1982; Gonzalez and Wintz, 1988; Jain, 1989). These techniques can be implemented in either the image domain or the frequency domain. In this research we restricted our attention to the use of image domain techniques (techniques which operate directly on the image data), as both linear and nonlinear operations could be implemented in this domain.

In this work we assumed that the noise was additive, signal independent and white and the signal information was dominant only at the lower frequencies, see figure 2.6. The recorded image data were modeled as follows,

$$g(m,n,p) = f(m,n,p) + w(m,n,p) \tag{2.3}$$

where $g(m,n,p)$ is the recorded image data, $f(m,n,p)$ is the original image information, and $w(m,n,p)$ is the additive, white noise with zero mean and variance σ_w^2 at pixel location (m,n) in frame p.

If the noise is additive and white and the signal is low-pass, the only portion of the frequency spectrum in which the noise could dominate is the high frequency range. The simplest form of image smoothing is spatial low-pass filtering, that is maintaining the low frequency information and de-emphasizing the high frequency information. This is accomplished by passing the image data through a linear, shift-invariant filter. The output of the filter is given by

$$y(m,n,p) = \sum\sum\sum_{(j,k,l)\in W} a(j,k,l)g(m-j,n-k,p-l) \tag{2.4}$$

where $g(m,n,p)$ is the recorded image data, $y(m,n,p)$ is the output of the smoothing filter, W is the local neighborhood on which the filter is applied, and $a(j,k,l)$ is the filter impulse response. This is an example of a nonrecursive, finite-impulse response filter.

Substituting eq. (2.3) into eq. (2.4) yields,

$$y(m,n,p) = \frac{1}{N_W} \sum\sum\sum_{(j,k,l)\in W} a(j,k,l)[f(m-j,n-k,p-l) + w(m-j,n-k,p-l)] \tag{2.5}$$

where N_W is the number of pixels in neighborhood W. If

$$\mathbf{w}(m,n,p) = \frac{1}{N_W} \sum\sum\sum_{(j,k,l)\in W} a(j,k,l)w(m-j,n-k,p-l) \tag{2.6}$$

and the $a(j,k,l) = 1$, it is straightforward to show that $\mathbf{w}(\mathrm{m,n,p})$ has zero mean and variance $\sigma_{\mathbf{w}}^2 = \sigma_w^2/N_W$. Therefore, the noise power is reduced by a factor equal to the number of pixels in the neighborhood and the signal-to-noise ratio is increased by a factor of N_W.

In practice, however, N_W is limited because the filter operates on the signal as well as the noise. If $f(m,n,p)$ contains frequency information at frequencies higher than the filter cut-off frequency of the filter, a distortion will be introduced.

In this work we applied separate spatial and temporal low-pass filters. The spatial low-pass filter is given by

$$y(m,n,p) = \frac{1}{N_W} \sum\sum_{(j,k)\in W} a(j,k)g(m-j,n-k,p) \tag{2.7}$$

where $a(j,k)$ is the filter impulse response. An example of a commonly chosen filter impulse responses are shown in figure 2.7. A number of different filter impulse responses were evaluated and the results were all visually similar. The results of spatial low-pass filtering the recorded image data using the impulse response shown in figure 2.7 are shown in figure 2.8. Visually, there is not a significant difference between the original data (figure 2.1) and the filtered data. These results are not surprising, given the amount of noise degradation in the signal.

$\frac{1}{9}$	$\frac{1}{9}$	$\frac{1}{9}$
$\frac{1}{9}$	$\frac{1}{9}$	$\frac{1}{9}$
$\frac{1}{9}$	$\frac{1}{9}$	$\frac{1}{9}$

Figure 2.7: A typical spatial domain impulse response for a linear shift-invariant smoothing filter.

In a similar fashion, a temporal low-pass filter was applied to the image data. The temporal low-pass filter is given by

$$y(m,n,p) = \frac{1}{N_W} \sum_{l\in W} a(l)g(m,n,p-l) \tag{2.8}$$

Again we assume that $a(l) = 1$, if $l \in W$ and $W=3$. The results of the temporal low-pass filtering are shown in figure 2.9. There is some improvement here when the original data (figure 2.1) and the filtered data are compared. This leads us to believe that there is some interframe noise that was not indicated in the previous intraframe analysis.

Independent of the choice of the filter coefficients $a(j,k,l)$, all of the above assume a linear structure for the filter. An alternative is to choose a nonlinear filter. This is particularly appropriate if the noise is not precisely modeled as an additive, white noise source. A popular alternative is to apply a median filter (Gallagher, et al., 1986). Here the recorded image pixel is

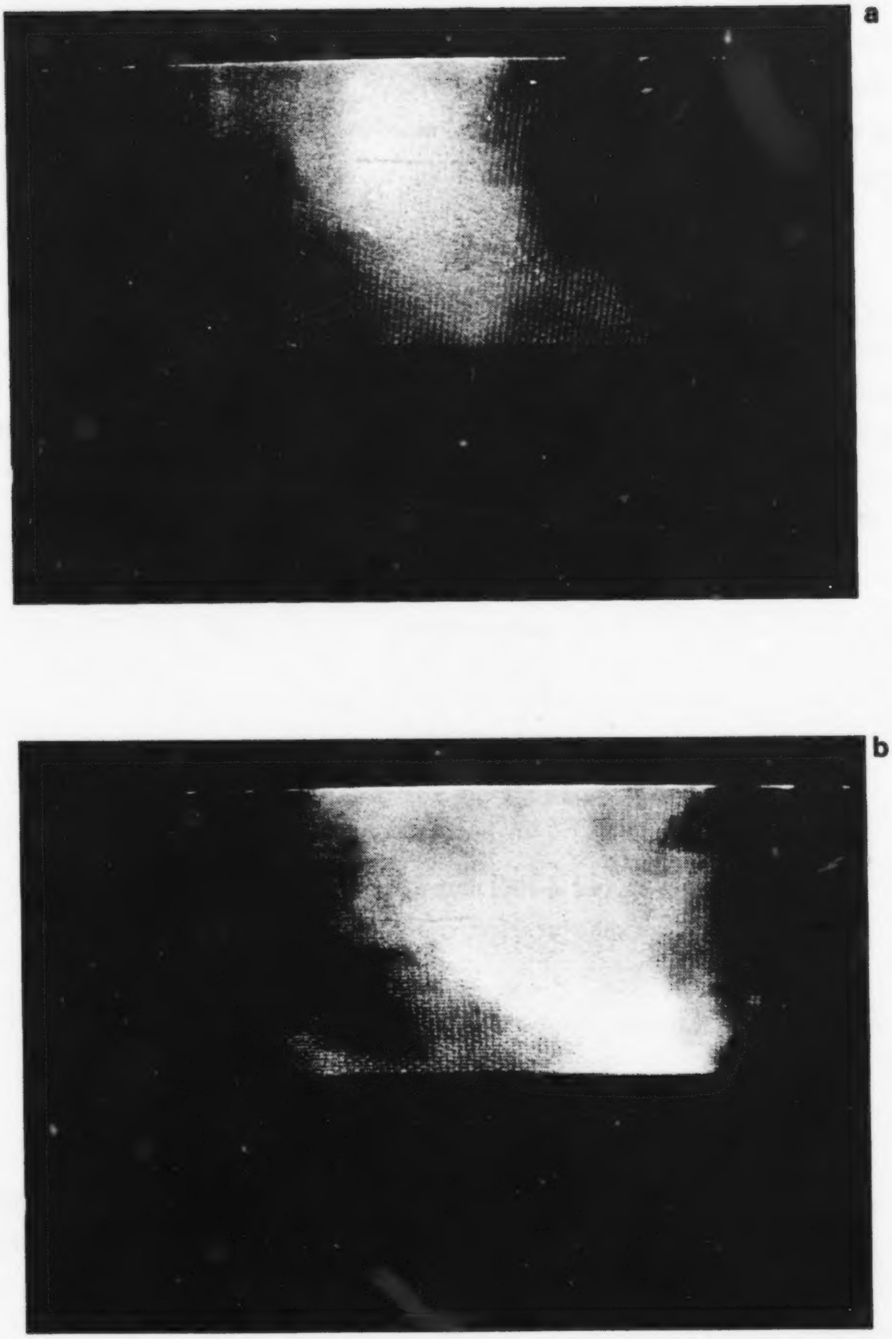

Figure 2.8: Spatial low-pass filtered version of the original image data using the filter impulse response shown in figure 2.7. (a) Frame 1; (b) Frame 10;

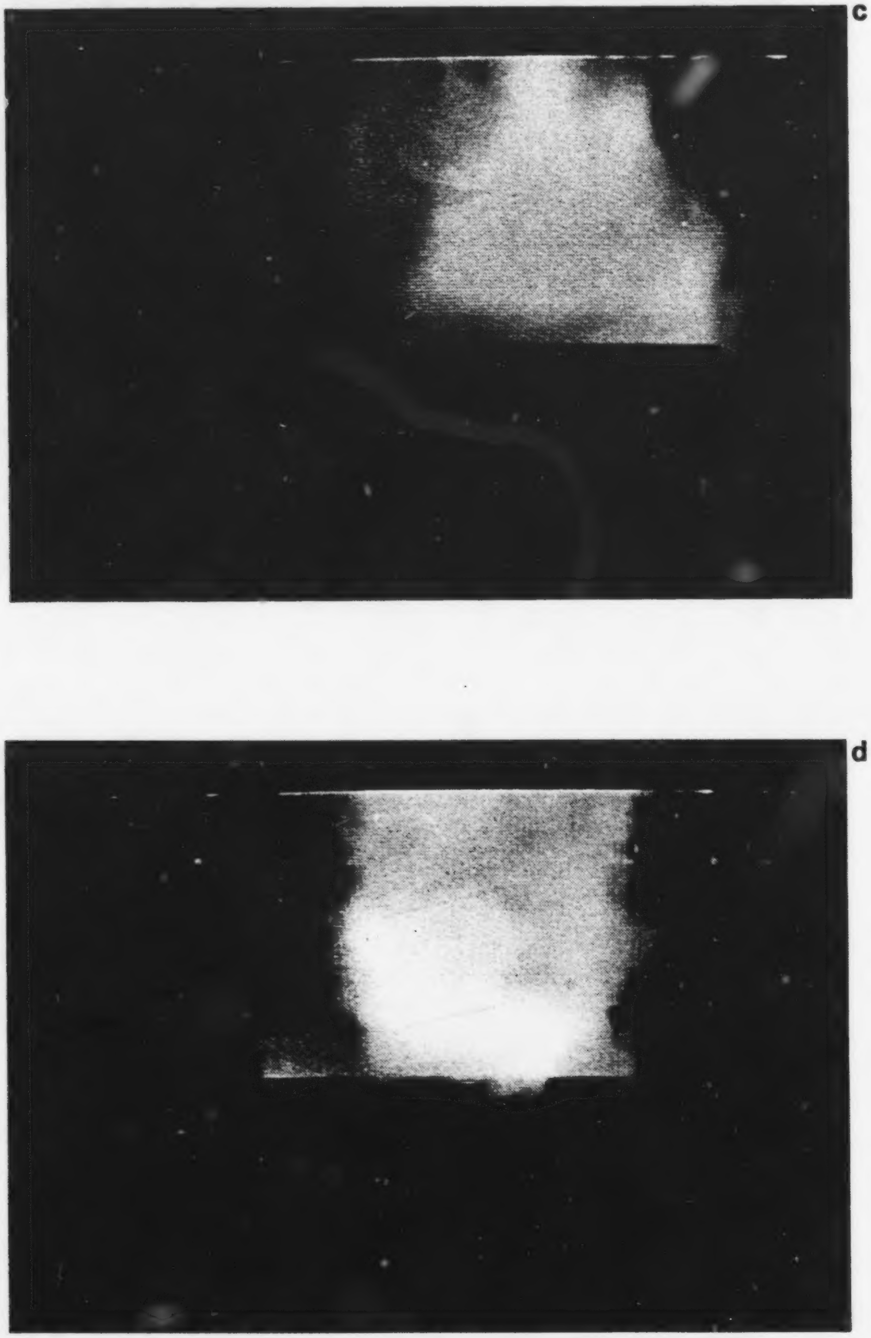

Figure 2.8: (c) Frame 20; (d) Frame 30.

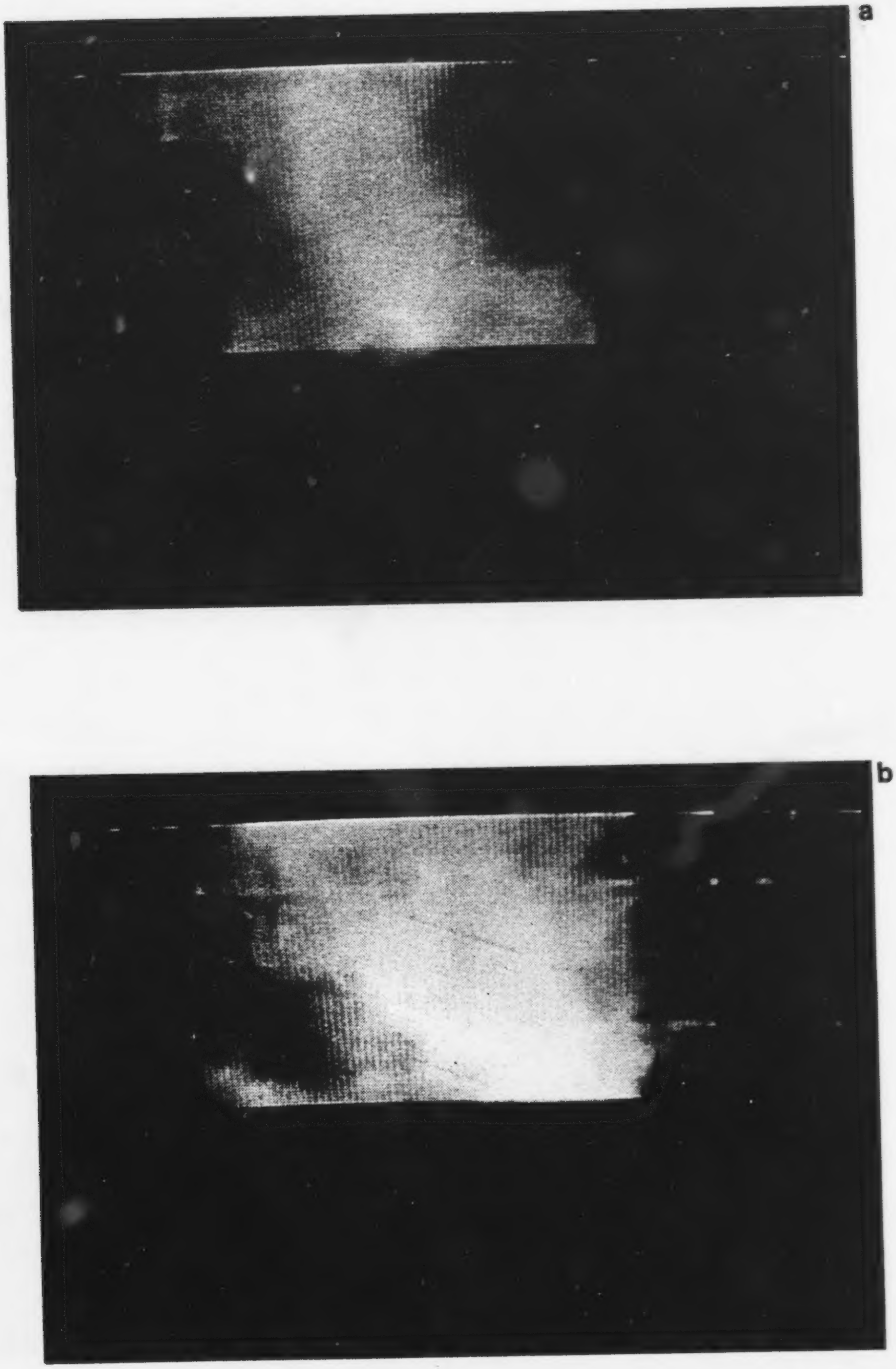

Figure 2.9: Temporal low-pass filtered version of figure 2.1 using eq. (2.8) with a window size W=3.
(a) Frame 1; (b) Frame 10;

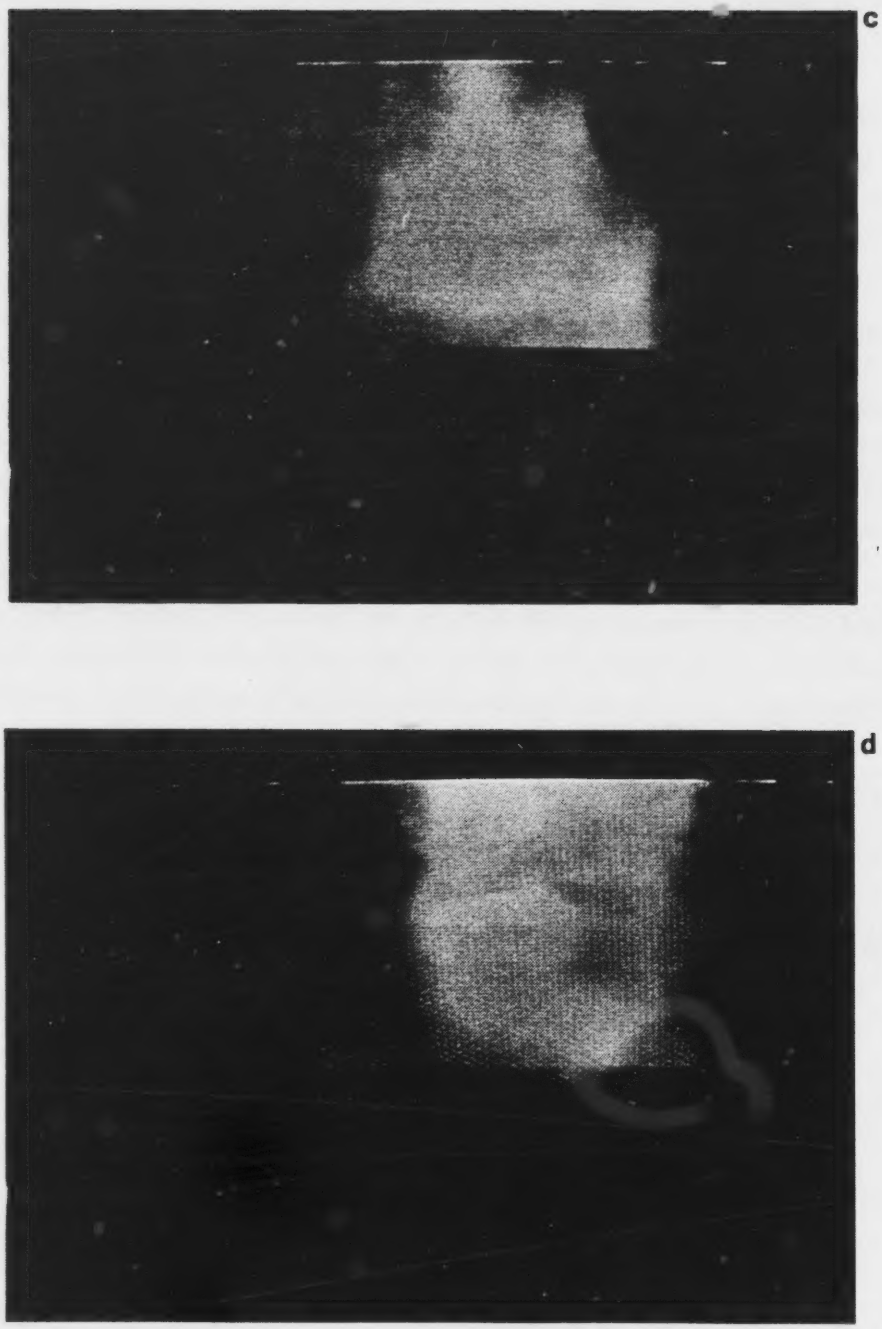

Figure 2.9: (c) Frame 20; (d) Frame 30.

replaced by the median of the pixels contained in the window W.

$$y(m,n,p) = median[g(m-j,n-k,p-l), (j,k,l) \in W] \tag{2.9}$$

Potential advantages of the median filter include the fact that it does not perform signal averaging, it can reduce the impact of multiplicative noise sources, and it is useful for removing out-of-range pixel values while preserving the spatial resolution. A disadvantage is that it performs poorly if the number of noise pixels (pixels containing random fluctuations due to noise) in the window is greater than half the number of pixels in the window.

We applied a 2-D median filter using a 5x5 window to the image data. The results are shown in figure 2.10. It can be seen that the median filtered image data has had the noise reduced and at the same time appears sharper than spatially low-pass filtered data shown in figure 2.8. In addition, the median filter has also more effectively reduced the artifacts due to the background grid pattern. It should be noted that a median filter was also applied in the temporal direction, but did not lead to significant improvements in image quality.

In summary, for the set of data we have processed the spatial median filter provides the best technique for reducing unwanted intraframe noise and background artifacts without sacrificing the edge information in the images. For this set of data, the temporal low-pass filter described by eq. (2.8) yielded more reduction in interframe noise than did a median filter. However, neither seemed warranted for this problem.

2.4 Edge Enhancement

More insight into the data might be gained by first preprocessing the original image intensity information to enhance the "edges" and then consider the temporal characteristics. Since the smoke images do not have well-defined edge information, it is of interest to see what impact spatial filtering to enhance edges will have.

In image processing, edge enhancement is accomplished by performing a spatial high-pass filtering operation, that is enhance the high frequency content of a signal and suppress the low frequency content. The simplest of these 2-D filter structures is based on spatial differencing operations, i.e., a calculation of the spatial gradient. They are generally implemented as non-recursive, finite-impulse response filters (convolution filters) of the form,

$$y(m,n) = \sum_{(k,l) \in W}\sum b(k,l)g(m-k,n-l) \tag{2.10}$$

where y(m,n) is the edge enhanced image, b(k,l) is the filter impulse response, g(m,n) is the recorded image data and W is the local neighborhood on which the convolution filter is applied. Examples of typical impulse responses are shown in figure 2.11.

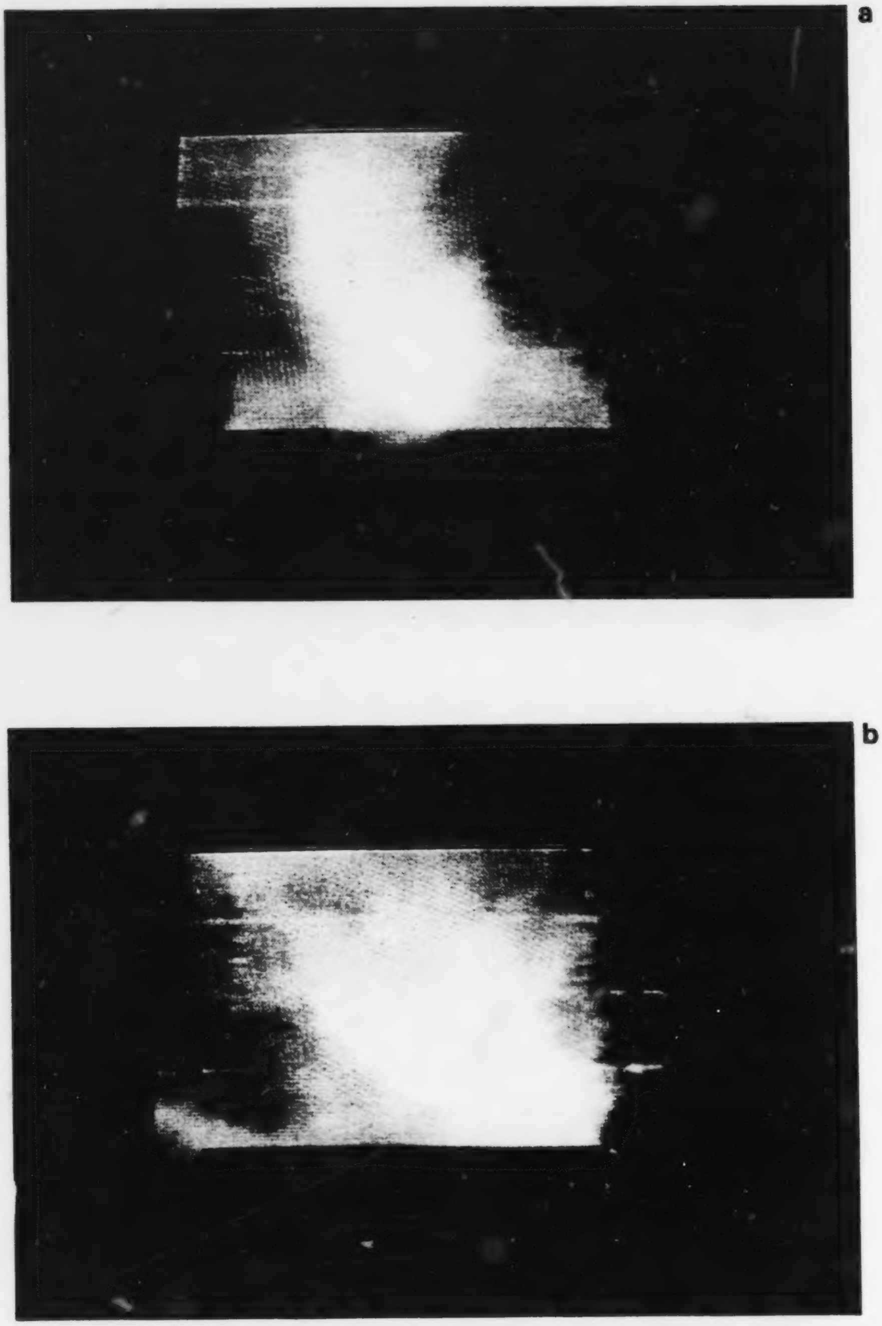

Figure 2.10: Median filtered version of figure 2.1 using a 5x5 window. (a) Frame 1; (b) Frame 10;

Reproduced from best available copy.

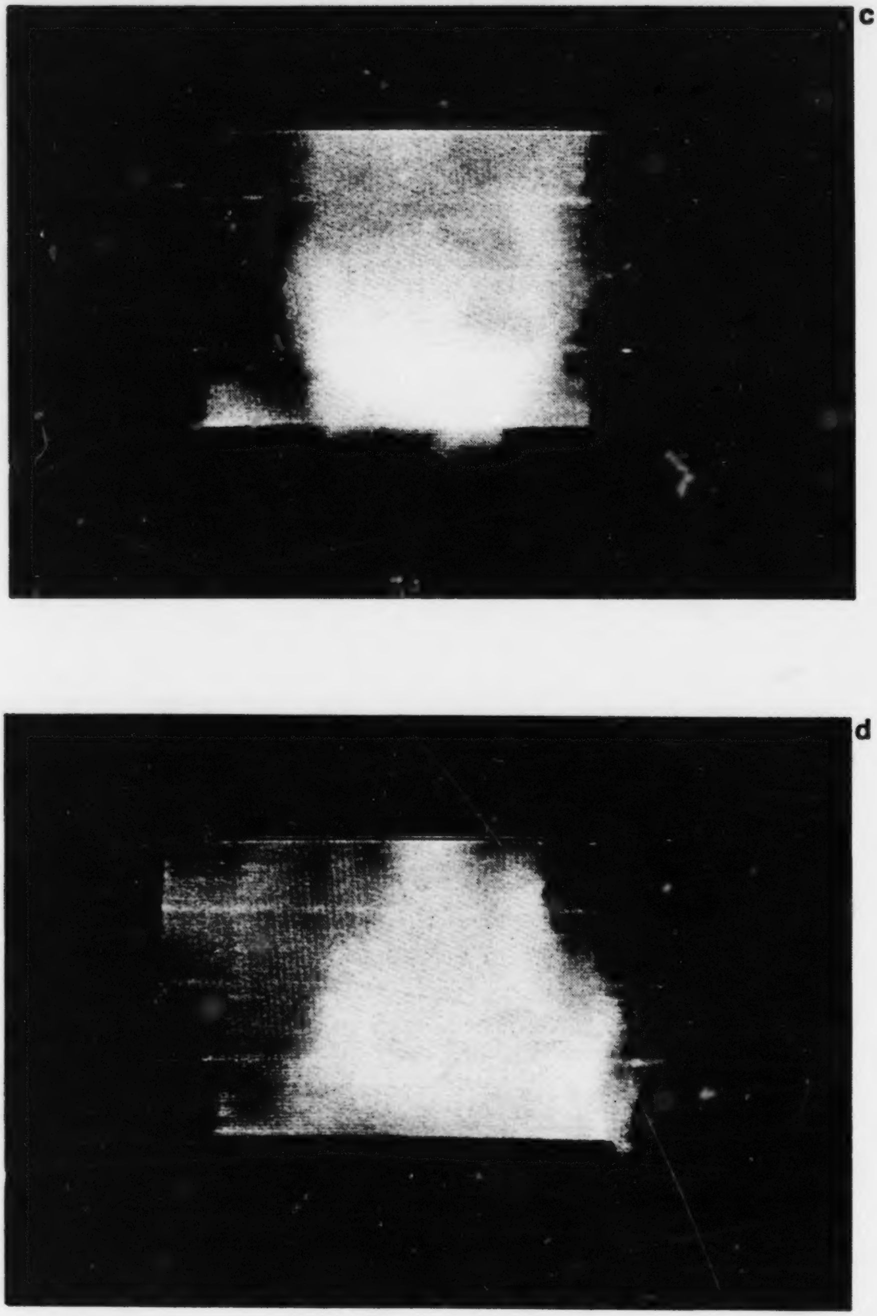

Figure 2.10: (c) Frame 20; (d) Frame 30.

0	-1	0
-1	5	-1
0	-1	0

Figure 2.11: Example of a spatial high-pass filter impulse response.

The results of applying the filter shown in figure 2.11 to the image data are shown in figure 2.12. What can be seen in figure 2.12 is that the higher frequency information (e.g., the pixels around the edges) has indeed been enhanced and the low frequency information (e.g., the pixels in low contrast regions) has been compressed. The histogram of an edge enhanced frame is shown in figure 2.13. The difficulty that is encountered here is the trade-off between enhancing the "edge" information and enhancing the noise. Even if the amount of noise is small, it can be greatly magnified during edge enhancement.

In summary, for low contrast images, such as we have in this data set, edge enhancement does not appear to be extremely beneficial. Initially, it was thought that it might be easier to segment an edge enhanced image than the original data. The difficulty that is encountered is that the edge enhancement process also enhances the background. If the images were higher contrast and there was less reflection of the background, edge enhancement might be more beneficial. It should also be noted that the histograms have been modified. If one chooses, as we do in section 3, a histogram-based segmentation technique, it would be useful to know if edge enhancement helps or hinders the segmentation process. In this case, it hinders more than helps. We have been primarily interested in segmenting the image data into two pieces, smoke and background. To do this, one would like to have bimodal histograms. Edge enhancement on this data tends to make the histograms trimodal. This leads one to believe that the data should be separated into three classes. The question is what three classes? If it were smoke, dark background and grid work this might be useful. However, the range of intensity values for the grid work overlaps with the range of values for the smoke. Thus it did not appear that this would be effective and was not tried. It should be noted, however, the segmentation approach based on optimal thresholding that is described in section 3 could be generalized for trimodal histograms.

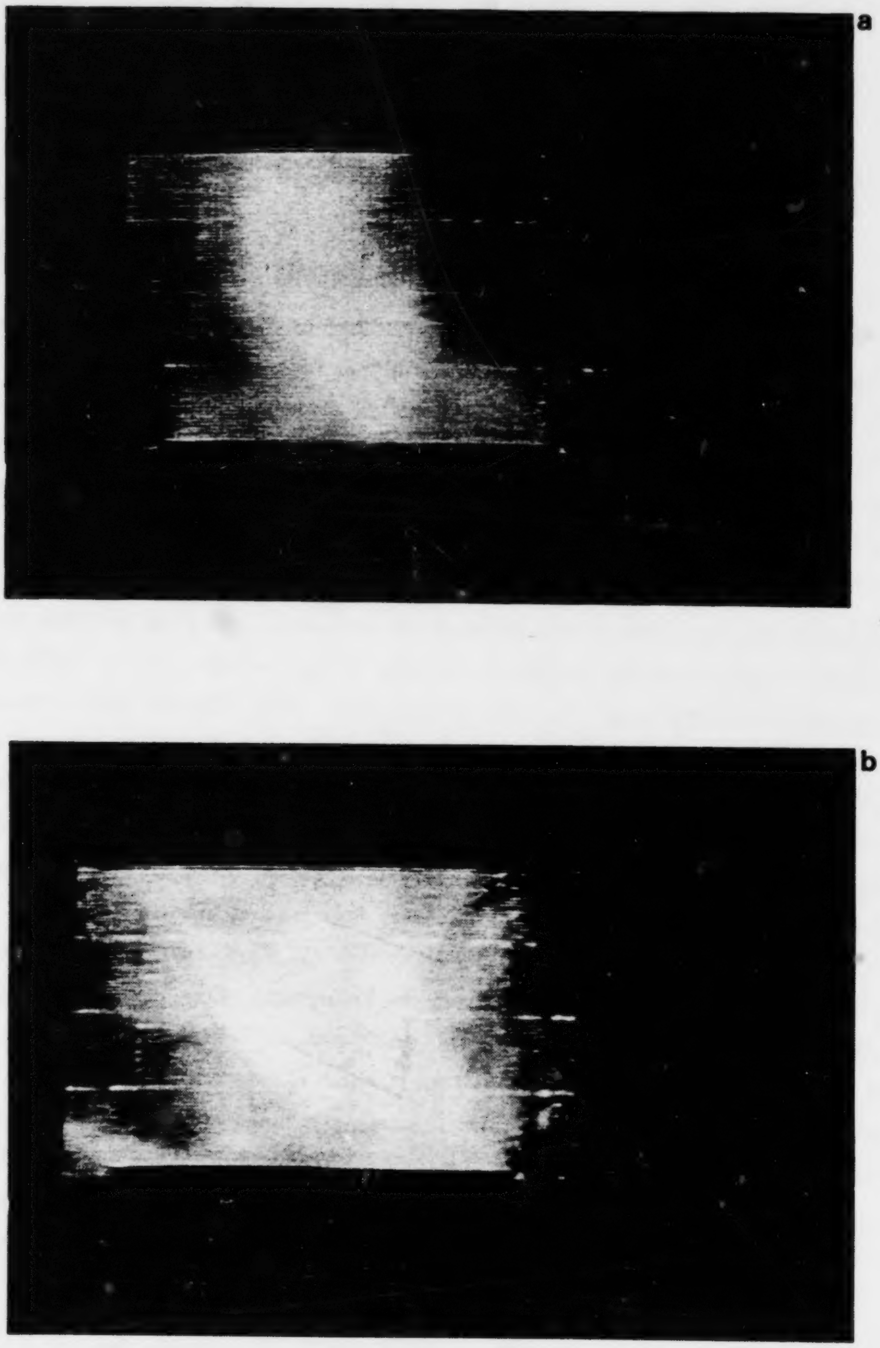

Figure 2.12: Spatial high-pass filtered version of figure 1 using the impulse response shown in figure 2.11.
(a) Frame 1; (b) Frame 10;

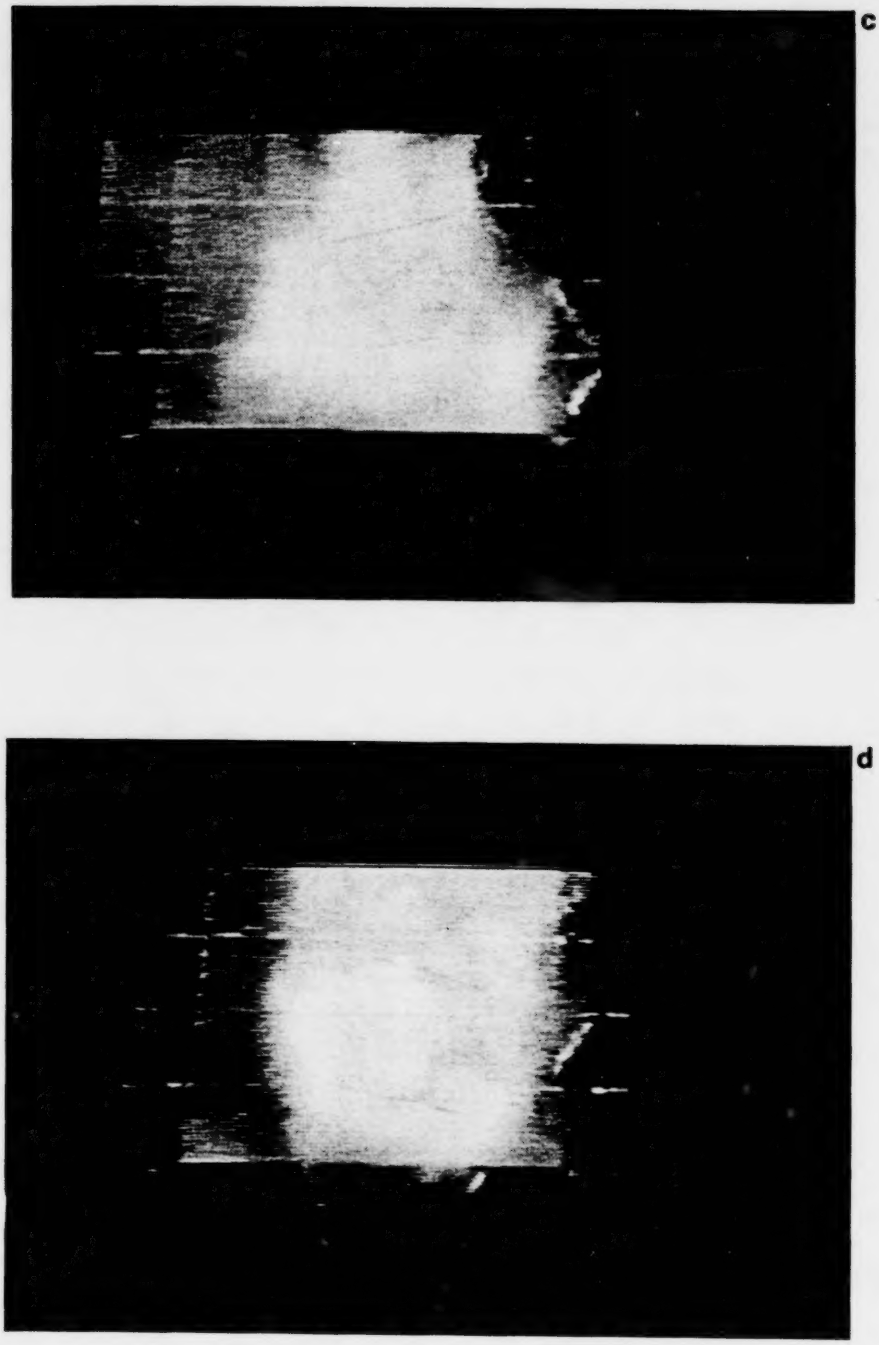

Figure 2.12: (c) Frame 20; (d) Frame 30.

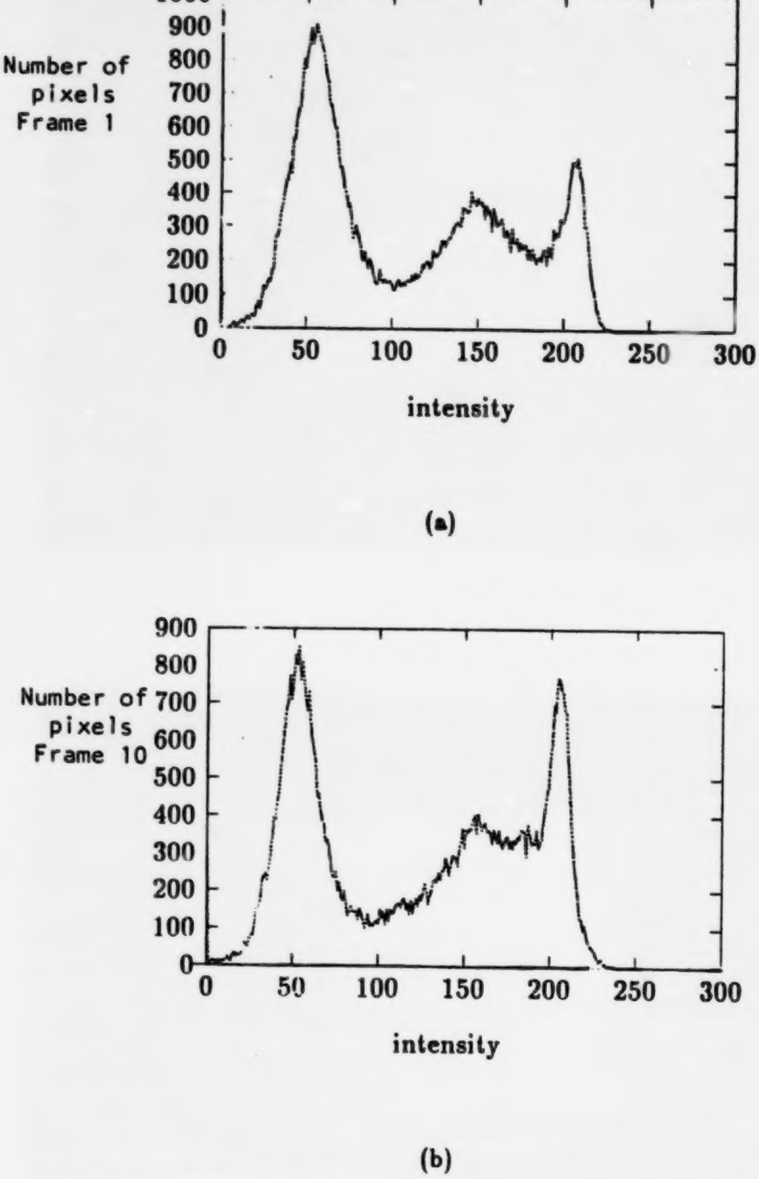

Figure 2.13: Histograms of the high-pass filtered image data shown in figure 2.12.
(a) Frame 1; (b) Frame 10;

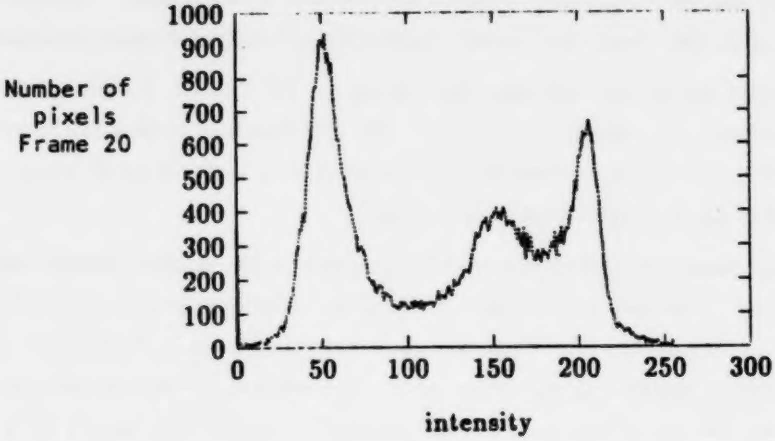

(c)

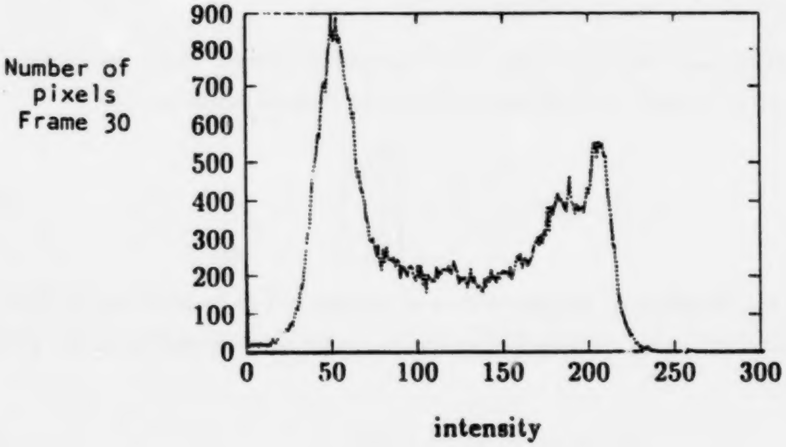

(d)

Figure 2.13: (c) Frame 20; (d) Frame 30.

2.5 Edge Detection

The principal motivation for these techniques is the detection of discontinuities in the image. The discontinuity defines a boundary between two regions in the image. There are two basic approaches to edge detection, frequency domain techniques and spatial domain techniques.

The frequency domain techniques use high pass filters in the Fourier domain to extract specific high frequency content, i.e., edges, of an image. The disadvantage is that in the process of extracting the edges the noise is also enhanced. Furthermore with some types of image data, it may be impossible to find an acceptable passband frequency.

More often, the edge detection techniques are implemented in the spatial domain and are based on gradient detection. The idea underlying most of these techniques is the computation of a local derivative operator. Significant edges are extracted from the image by thresholding after applying a linear or nonlinear operator to the image data. The concept is easily illustrated with the aid of figure 2.14. At the top of figure 2.14 is an image of a simple light object on a dark background. The gray-level profile in the horizontal direction and the first and second derivatives are shown directly below the image. The first derivative information is zero, unless there is a transition in gray level. The second derivative is zero in all locations, except at the onset and termination of a gray-level transition. Hence, the first derivative information can be used to indicate the presence of an edge, while the sign of the second derivative can be used to indicate whether the transition is from dark to light or light to dark.

The gradient operators are most commonly implemented as simple linear operators. The gradient of an image f(x,y) at location (x,y) is defined as the two-dimensional vector

$$\mathbf{G}\,[f(x,y)] = \begin{bmatrix} G_x \\ G_y \end{bmatrix} = \begin{bmatrix} \dfrac{\delta f}{\delta x} \\ \dfrac{\delta f}{\delta y} \end{bmatrix} \tag{2.11}$$

The vector G points in the direction of maximum rate of change of f at location (x,y). For edge detection, we are interested in the magnitude of this vector, generally referred to as the *gradient* and denoted $\mathbf{G}\,[f(x,y)]$.

$$\mathbf{G}\,[f(x,y)] = [G_x^2 + G_y^2]^{1/2} \tag{2.12}$$

In practice, it is common to approximate the magnitude of the gradient by

$$g[f(x,y)] = |G_x| + |G_y| \tag{2.13}$$

The *direction* of the gradient vector is important in some analysis problems and is defined as

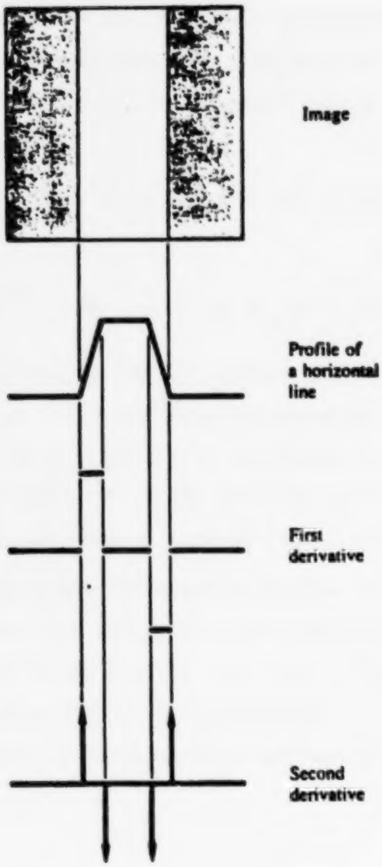
Image
Profile of a horizontal line
First derivative
Second derivative

Figure 2.14: An example of edge detection using first and second derivative operators.

$$\alpha(x,y) = \tan^{-1}(\frac{G_y}{G_x}) \qquad (2.14)$$

The angle is measured with respect to the x axis.

From eq. (2.11), we see that the computation of the gradient is based on obtaining the partial derivatives $\delta f/\delta x$ and $\delta f/\delta y$ at every pixel location. There are a number of ways to digitally estimate the partial derivative information. One approach is to use first-order differences in a 2 x 2 region of the image. Alternatively, a slightly more complicated approach involves pixels in a 3 x 3 neighborhood about the point x_5 (see Figure 2.15). The x-direction component of the gradient is

$$G_x = (x_7 + 2x_8 + x_9) - (x_1 + 2x_2 + x_3) \qquad (2.15)$$

and the y-direction component is

$$G_y = (x_3 + 2x_6 + x_9) - (x_1 + 2x_4 + x_7) \qquad (2.16)$$

Using a 3 x 3 area to compute the gradient has the advantage of increased smoothing over the 2 x 2 operators. This tends to make the estimate of the gradient less sensitive to noise. Modifications to the 3 x 3 gradient operators have been proposed by many people. The basic difference is the weight assigned to the pixels in the 3 x 3 neighborhood. Figure 2.15 illustrated the 3 x 3 neighborhood as well as the linear operators (masks) described by eqs. (2.15) and (2.16).

Several gradient operators were applied to the smoke image data. The 3 x 3 gradient operators provided edges that were less sensitive to random fluctuations in the image data. An example output of the gradient operation using eq. (2.12) is shown in figure 2.16. Although it is difficult to extract any quantitative information about the motion of the smoke from these images, they have the potential for yielding useful qualitative information about the smoke flow when viewed as a temporal sequence.

x_1	x_2	x_3
x_4	x_5	x_6
x_7	x_8	x_9

(a)

−1	−2	−1
0	0	0
1	2	1

(b)

−1	0	1
−2	0	2
−1	0	1

(c)

Figure 2.15: (a) 3x3 neighborhood on which a 3x3 gradient is performed. (b) Mask used to compute G_x at the center pixel (x_5) of the 3x3 neighborhood. (c) Mask used to compute G_y at the center pixel (x_5) of the 3x3 neighboorhood.

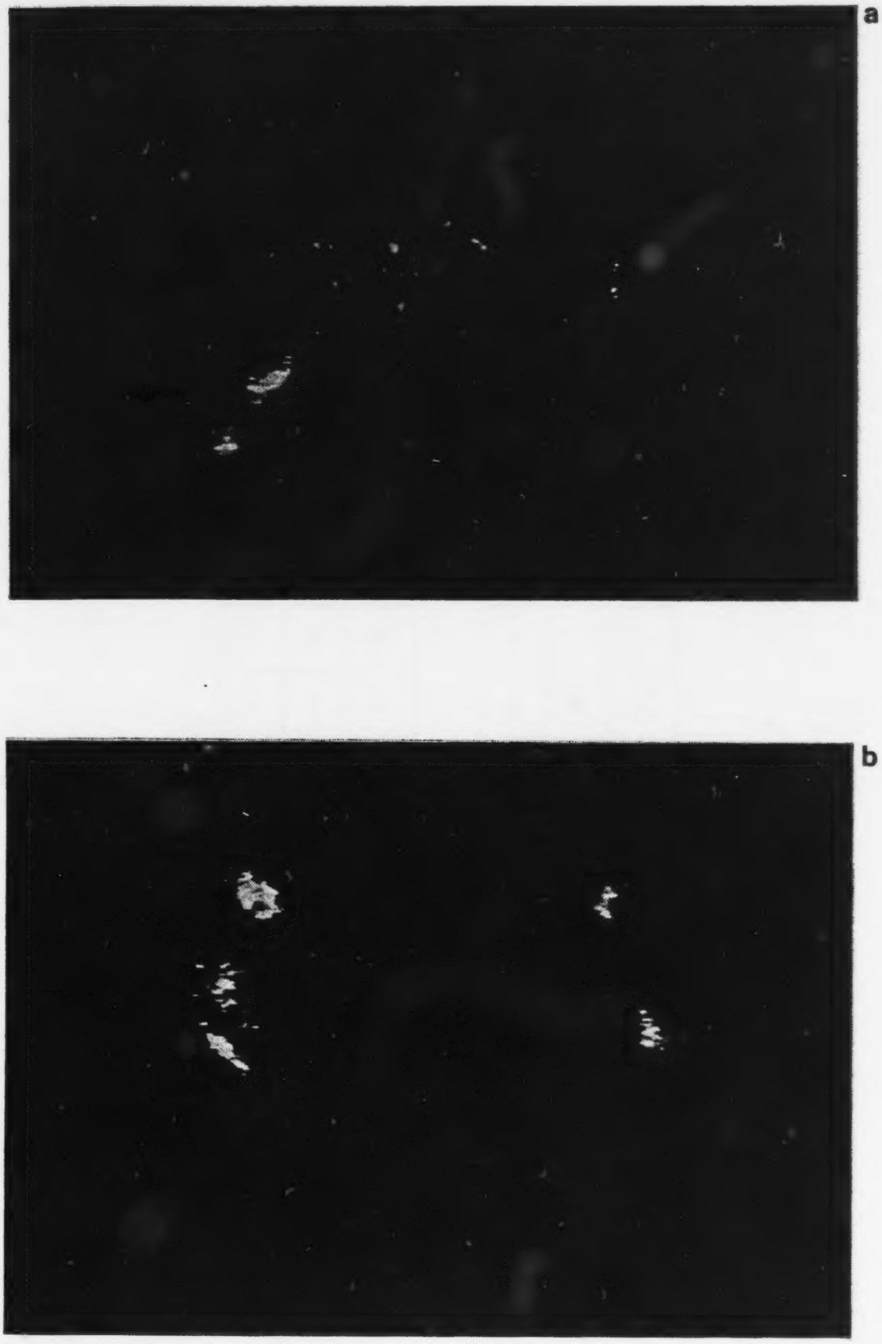

Figure 2.16: The magnitude of the gradient (as calculated by eq. (2.12)) of the original data (figure 2.1). The gradient in the x-direction and y-direction are calculated using eqs.(2.15) and (2.16), respectively. (a) Frame 1; (b) Frame 10;

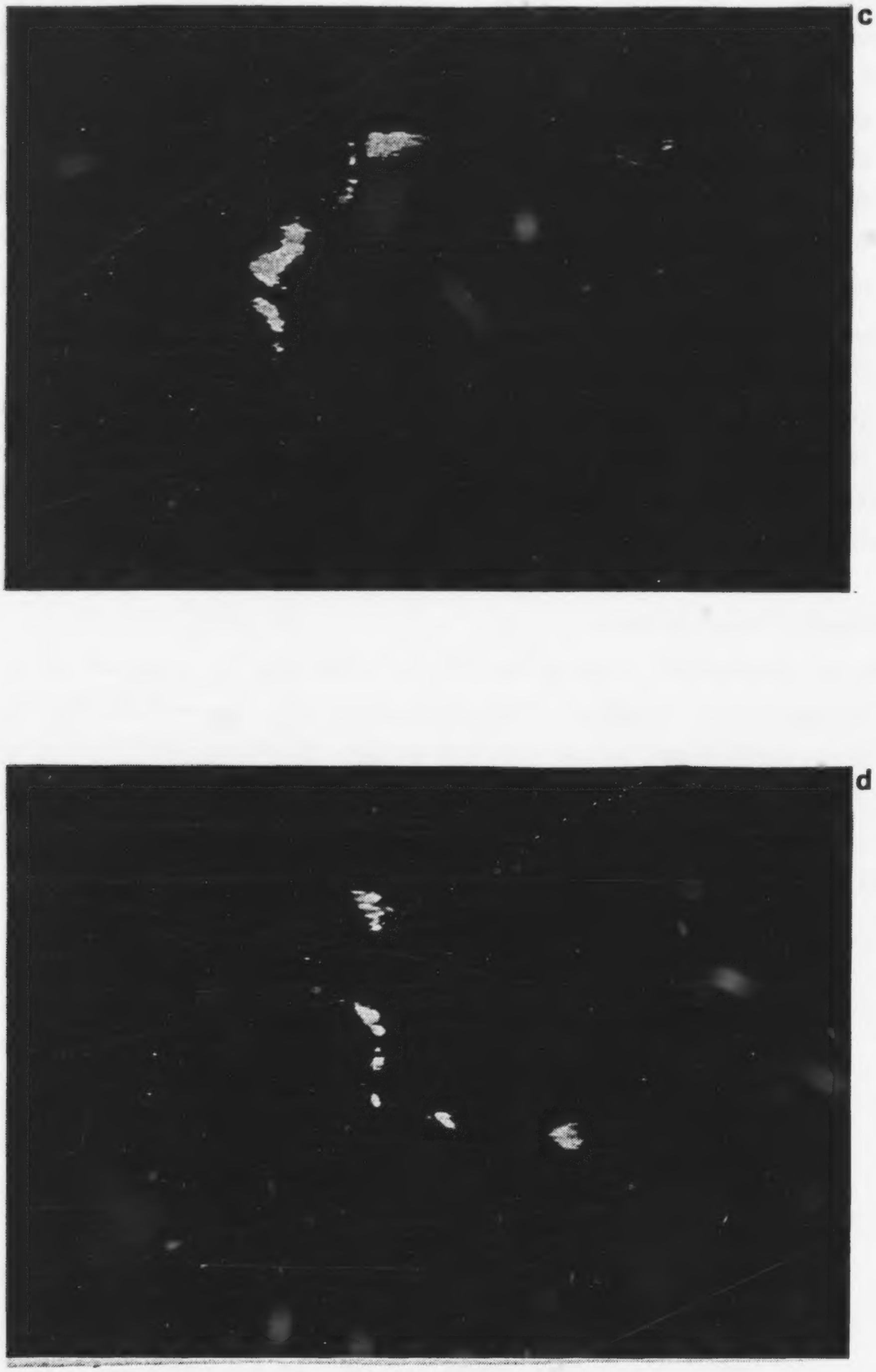

Figure 2.16: (c) Frame 20; (d) Frame 30.

3 VIDEO IMAGE SEGMENTATION

Segmentation is defined as the process of partitioning an image into disjoint regions which are uniform and homogeneous with respect to some characteristic. Image characteristics which have been shown to be useful include gray-level, texture and motion. Over the years, many segmentation algorithms (Haralick and Shapiro, 1985) have been developed and can be classified into the following five categories: pixel clustering, edge detection, region growing, relaxation and segmentation from motion information. In this report, we present the results of using pixel clustering and edge detection techniques.

Segmentation by pixel clustering implies the classification of pixels into a set of classes based on the properties of the image. It is in general the simplest approach, yet one of the most important for segmenting an image. The most straightforward method for pixel clustering divides the gray scale into bands and uses one or more thresholds to determine the regions. This approach assumes that regions are uniquely defined by the gray-levels. The simplest approach is referred to as amplitude thresholding.

3.1 Amplitude Thresholding

Amplitude thresholding (Gonzalez and Wintz, 1988) uses the histogram of an image to determine the separability of one area of interest from another. For example, suppose the image of interest is composed of dark objects on a light background, that is, object and background pixels have gray levels grouped in two distinct portions of the range of amplitude values. To separate the objects from the background, a threshold T is selected to define a boundary between the two classes. See figure 3.1. Any image point (x,y) for which $f(x,y) < T$ is called an object point.

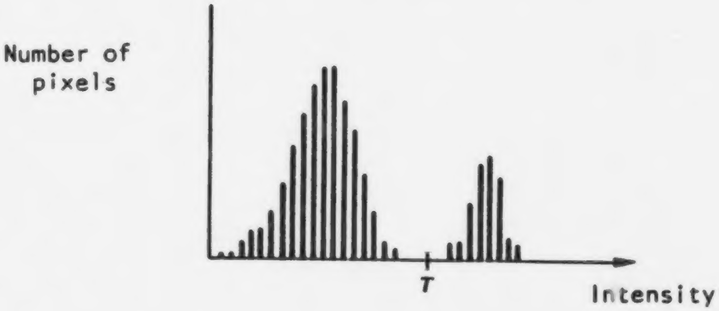

Figure 3.1: Gray-level histogram that can be partitioned by a single threshold, T.

The histogram thresholding technique was evaluated to determine its applicability for the smoke image data. The histograms for frames 1, 10, 20 and 30 of the original image data were shown in figure 2.2. In addition, histograms of various windows of the image data were tested to determine the variation in the characteristics of the histogram to different regions of the image. The image data was windowed as shown in figure 3.2.

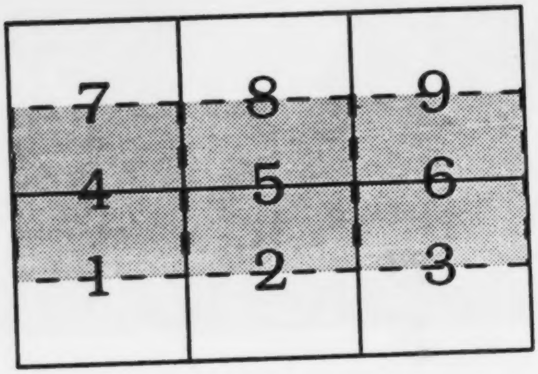

Figure 3.2: Subdivision of images into 9 subimages with 50 percent overlap.

After viewing these histograms, it was clear they could have one or more modes. After testing several different threshold levels, it became clear that it was going to be difficult to arbitrarily choose a threshold to segment this type of image data. If we let the threshold value equal 185, the segmented images that result are shown in figure 3.3.

The problem with this method is that if a histogram of the entire image is generated, it may not be clearly bi-modal. Furthermore, the choice of one threshold value for the entire image may not yield a good segmentation. An alternative is optimal thresholding.

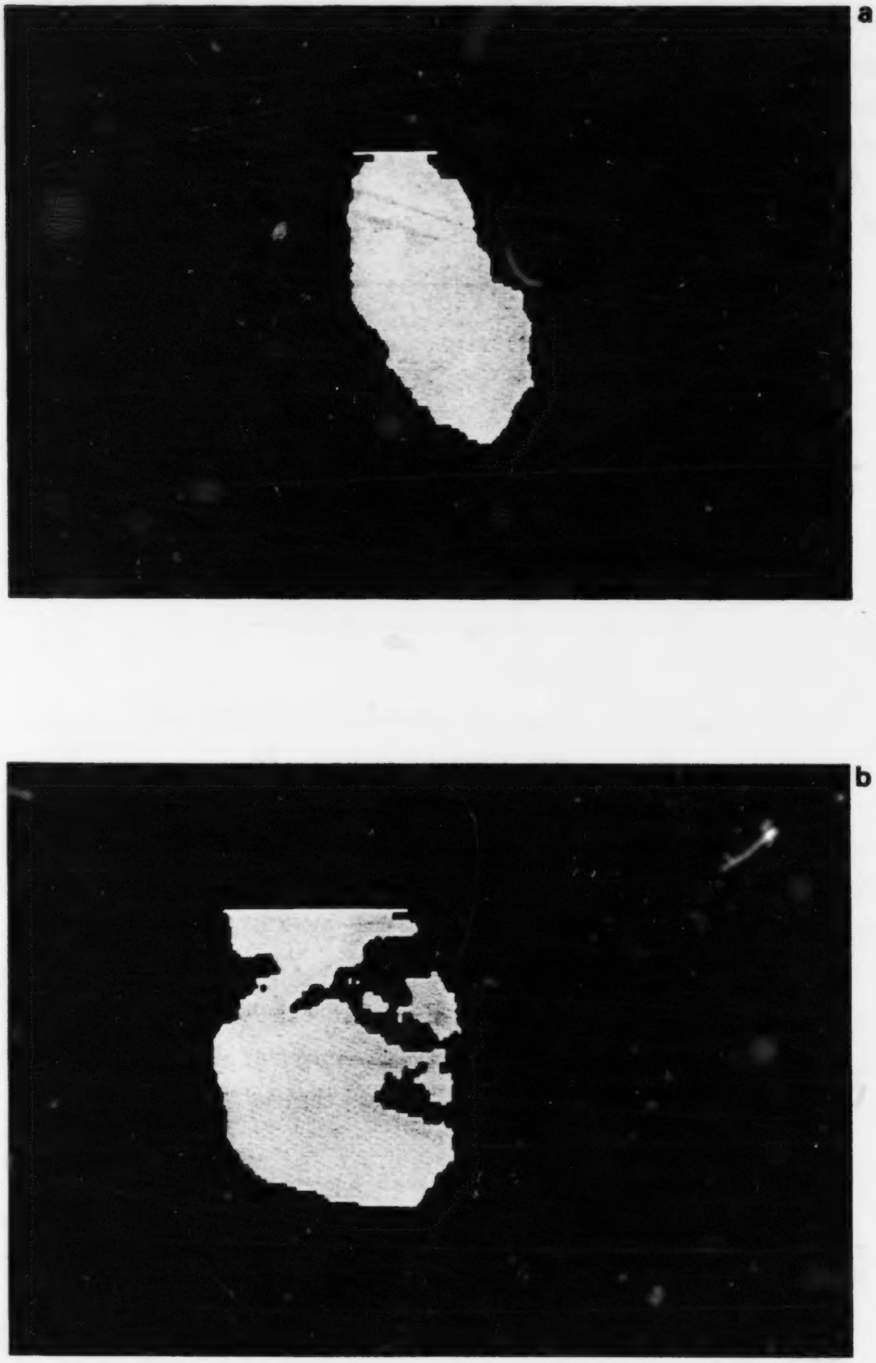

Figure 3.3: The image data segmented at a fixed threshold value of T=185. (a) Frame 1; (b) Frame 10;

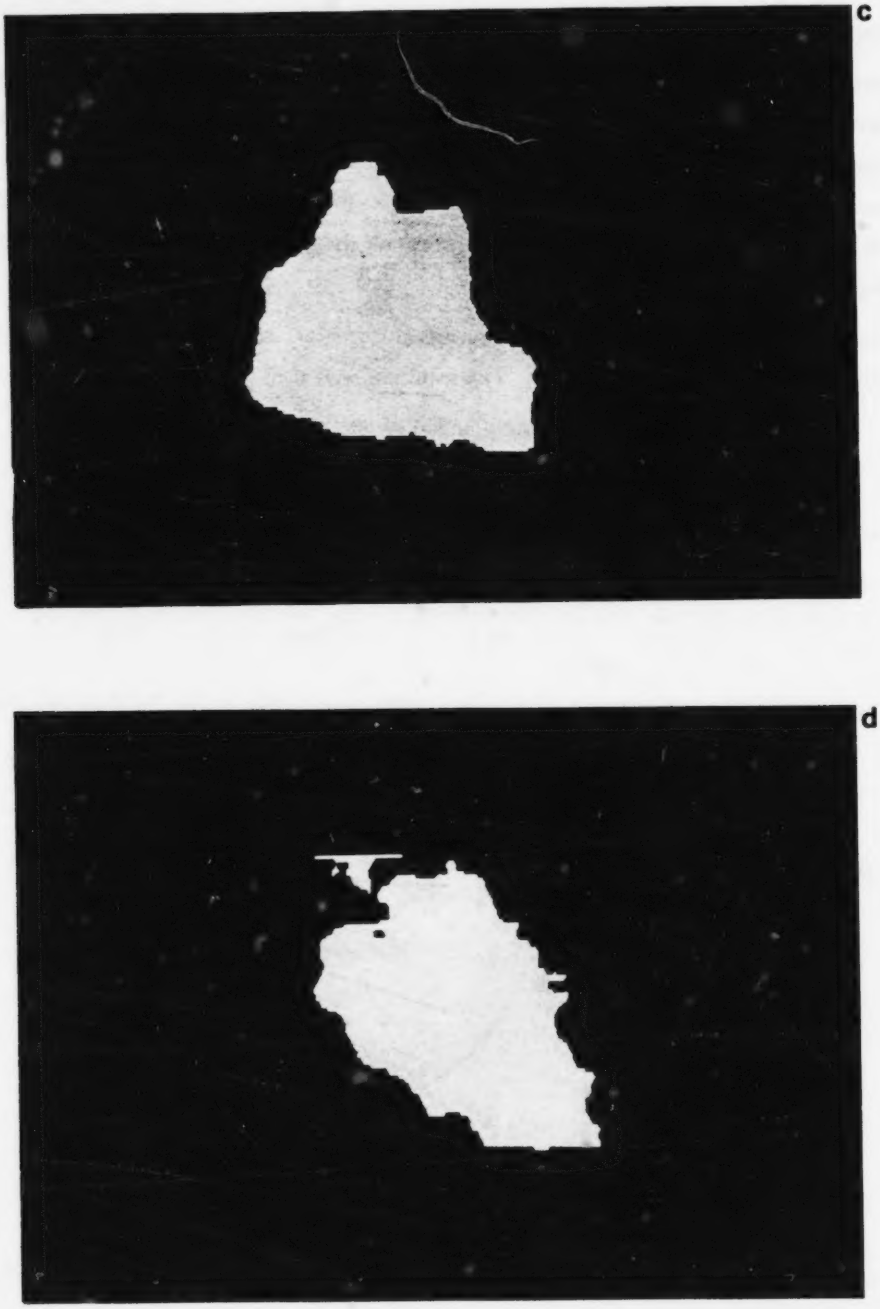

Figure 3.3: (c) Frame 20; (d) Frame 30;

3.2 Optimal Thresholding

3.2.1 Theory (Chow and Kaneko, 1972; Gonzalez and Wintz, 1988)

Suppose an image contains only two primary brightness regions, object and background. The histogram of such an image may be considered as an estimate of the brightness probability density function, p(x). Assume that the probability density function can be modeled as a sum of two unimodal densities, one for the light region and one for the dark region. If the form of the densities is known, then it is possible to determine an optimal threshold that will minimize the error for segmenting the image.

For example, assume that a given histogram is bimodal and can be modeled as a superposition of two probability density functions. The mixture probability density function is given by

$$p(x) = P_1 p_1(x) + P_2 p_2(x) \tag{3.1}$$

P_1 and P_2 are the prior probabilities of the two modes and $P_1 + P_2 = 1$ and the $p_i(x)$ are the pdfs for each mode. For the case where both $p_1(x)$ and $p_2(x)$ are Gaussian,

$$p(x) = \frac{P_1}{\sqrt{2\pi\sigma_1}} \exp\left[-\frac{(x-\mu_1)^2}{2\sigma_1^2}\right] + \frac{P_2}{\sqrt{2\pi\sigma_2}} \exp\left[-\frac{(x-\mu_2)^2}{2\sigma_2^2}\right] \tag{3.2}$$

where μ_1 and μ_2 are the mean values of the two brightness levels and σ_1 and σ_2 are the standard deviations about the means. See figure 3.4

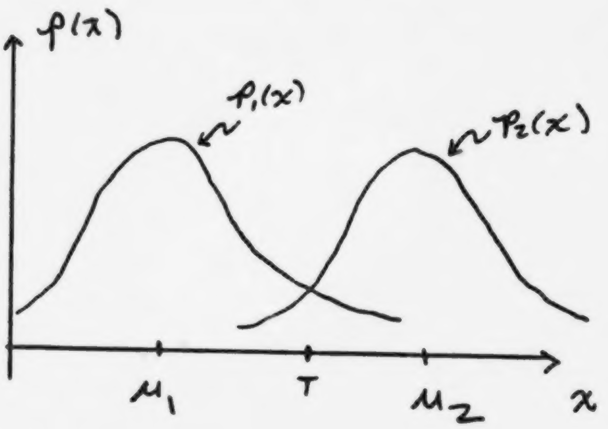

Figure 3.4: Gray-level histogram modeled by a sum of two Gaussian probability density functions.

Suppose the light regions correspond to the objects and the dark regions correspond to the background. We want to define a threshold T such that all pixels below T are classified as background and all pixels above T are classified as object. T is chosen to minimize the error of misclassification in the following way. The probability of classifying an object point as a background point is

$$E_1(T) = \int_T^{\infty} p_2(x)\, dx \tag{3.3}$$

and the probability of classifying a background point as an object point is

$$E_2(T) = \int_{-\infty}^{T} p_1(x)\, dx \tag{3.4}$$

The overall probability is then given by

$$E(T) = P_1 E_1(T) + P_2 E_2(T) \tag{3.5}$$

To find the optimal threshold value for which this error is minimal, we differentiate E(T) with respect to T, equate the result to zero and solve for T. If $\sigma^2 = \sigma_1^2 = \sigma_2^2$, the result is

$$T = \frac{\mu_1 + \mu_2}{2} + \frac{\sigma^2}{\mu_1 - \mu_2} \ln\left(\frac{P_2}{P_1}\right) \tag{3.6}$$

If the objects to be delineated, e.g., regions of the smoke, do not have well defined boundaries, optimal thresholding combined with windowing produces satisfactory results.

3.2.2 Optimal Thresholding of the Smoke Flow Data (Forgety, 1989)

We applied the optimal thresholding technique to the problem of segmenting the smoke images. The first stage in this process is to generate the histogram of the image data and to determine an appropriate model to use as an estimate of the probability density function (pdf). The image data was windowed as indicated in figure 3.2 and histograms generated for each window in each frame of data. What we found, was that if the window was in a region that was all background or all smoke the histogram was unimodal. If the window contained a combination of background and smoke, then the histograms were typically bimodal. It should be noted, however, that there were a few cases that were not clearly unimodal or bimodal. The histograms for these cases were considered to be outliers and were ignored. Hence, it is possible to model the overall probability density function as a combination of the pdf for the background and for the object (the smoke).

The second step is to determine an appropriate analytical model to represent the pdfs for the background and the object. There are any number of possible models one could choose for this representation, including Gaussian, Laplacian, Rayleigh, Chi square, etc. The approach we used is to find the simplest functional form that gave a good fit to the data. As it turns out two classes of histograms are needed to adequately model these data. In some of the windows, a combination of a Rayleigh distribution for the background and a Gaussian distribution for the object provided the best fit, for example windows 1 - 3. In other cases, the best fit was obtained using two Rayleigh distributions, for example windows 5 - 7. The pdf for the Rayleigh is modeled by:

$$p_1(x) = \frac{1}{b}(1-a)e^{-(1-a)^2/2b} \tag{3.7}$$

where a is the offset from zero and b is the function's spread. The pdf for the Gaussian is modeled by:

$$p_2(x) = \frac{1}{\sqrt{2\pi\sigma}}e^{-(1-\mu)^2/2\sigma^2} \tag{3.8}$$

where μ is the mean and σ^2 is the variance.

The overall probability density function for the case when the background was Rayleigh and the smoke was Gaussian is given by:

$$p(x) = \frac{P_1}{b}(x-a)e^{-(x-a)^2/2b} + \frac{P_2}{\sqrt{2\pi\sigma}}e^{-(x-\mu)^2/2\sigma^2} \tag{3.9}$$

where $a < \mu$. For the case when both the background and the smoke are modeled by Rayleigh distributions, the overall probability density function is given by:

$$p(x) = \frac{P_1}{b_1}(1 - a_1)e^{-(x-a_1)^2/2b_1} + \frac{P_2}{b_2}(1 - a_2)e^{-(x-a_2)^2/2b_2} \tag{3.10}$$

To find the optimal threshold, we must differentiate E(T) with respect to T, the threshold value, set the equation equal to zero and solve for T. Using the model for the pdf given in eq. (3.5), the total probability of error becomes

$$E(T) = P_1 \int_T^\infty p_2(x)dx + P_2 \int_{-\infty}^T p_1(x)dx \tag{3.11}$$

In order to estimate the parameters of the mixture density from the histogram, we use a minimum mean square error approach. The mean square error between $p(i)$ and h(i), the histogram values, is given by:

$$M = \frac{1}{N}\sum_{i=1}^{N}[p(i) - h(i)]^2 \tag{3.12}$$

where N is the total number of pixels. The minimization was done by estimating the parameters of $p(x_i)$ using Newton's method.

3.2.3 Results (Forgety, 1989)

The results of applying the optimal thresholding procedure to the smoke image data is described in the following.

Upon investigation of the histograms of several images, it became clear that the distribution of the background was best fit with a Rayleigh function. Moreover, the distribution of the smoke in some subimages could be modeled as a Gaussian and in other subimages was best modeled as a Rayleigh function (see figures 3.5 - 3.8). The reason for the two different mixture densities seems to depend on the position of the very high intensity smoke in each subimage. In a subimage where the smoke was very diffuse with relatively low gray level pixels, the mixture density was that of two Rayleighs. In areas where there were many pixels with high gray levels, the mixture density was that of a Rayleigh plus a Gaussian.

Before the optimal threshold can be found, the parameters that describe the pdf models (Gaussian or Rayleigh in this case) must be found. Once found, the mean square error between the mixture density model and the data is minimized by taking partial derivatives with respect to each model parameter, in turn, and setting each derivative equal to zero. For the densities given in equations (3.9) and (3.10), each required five parameters to be estimated. P_1 is a function of P_2. The parameter estimation was accomplished using Newton's method since the function was differentiable.

The continuous form of the Gaussian and Rayleigh functions was used for the purpose of calculating the first derivatives, but the gradient was used to estimate the second derivative due to the complexity of the analytic second derivative. The gradient is an approximation of the derivative and is used for discrete functions:

$$\delta M(d)/\delta d = M(a,b,c,d+\Delta d) - M(a,b,c,d) \tag{3.13}$$

The iterations were allowed to continue until satisfactory convergence was achieved. Generally four iterations were enough to achieve convergence. The time it took to achieve satisfactory convergence depended on the initial estimates used to start the process. The initial estimates were obtained by calculating them from the data.

To minimize the probability of misclassification when finding the optimal threshold, the background probability distribution function was set equal to the object probability distribution function. For the mixture density containing a Rayleigh and a Gaussian the following equation results:

$$\frac{P_1}{b}(i - a)e^{-(i-a)^2/2b} = \frac{P_2}{\sqrt{2\pi\sigma}}e^{-(i-\mu)^2/2\sigma^2} \tag{3.14}$$

Take the natural log of both sides of eq. (3.14), let $i = T$ where T is the optimal threshold value,

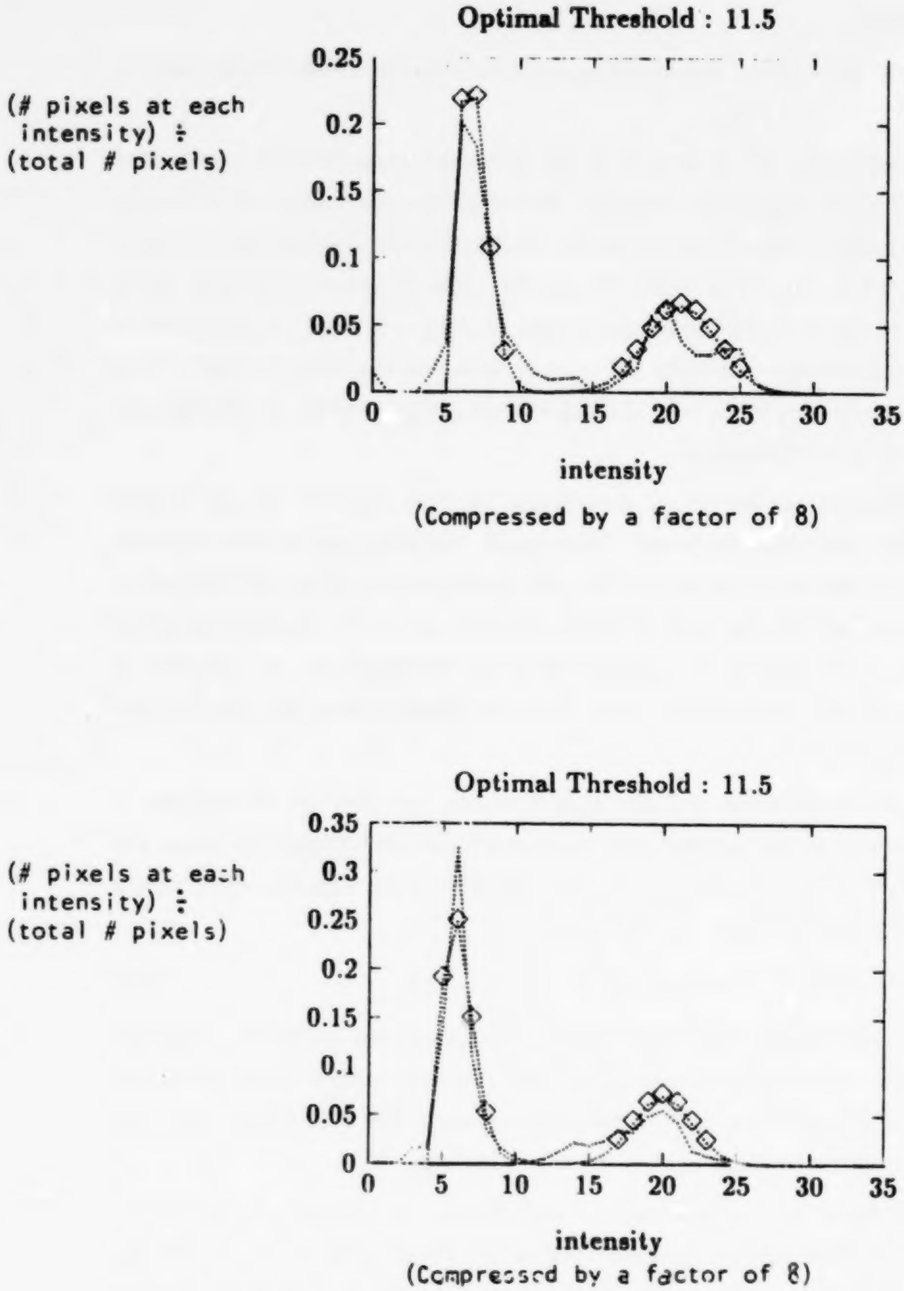

Figure 3.5: Curve fits: subimage 2 of frame 1 and subimage 1 of frame 10

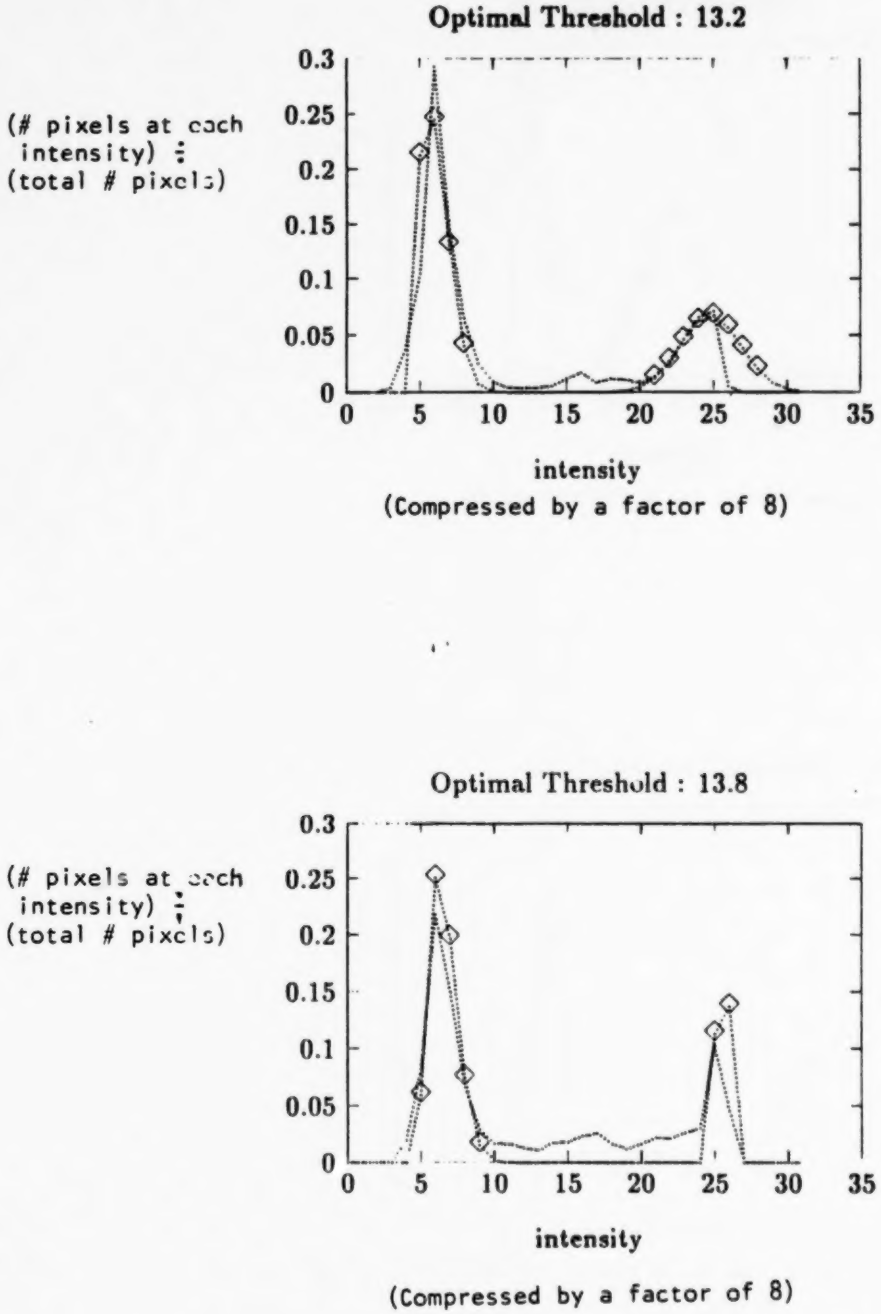

Figure 3.6: Curve fits: subimage 3 of frame 20 and subimage 2 of frame 30

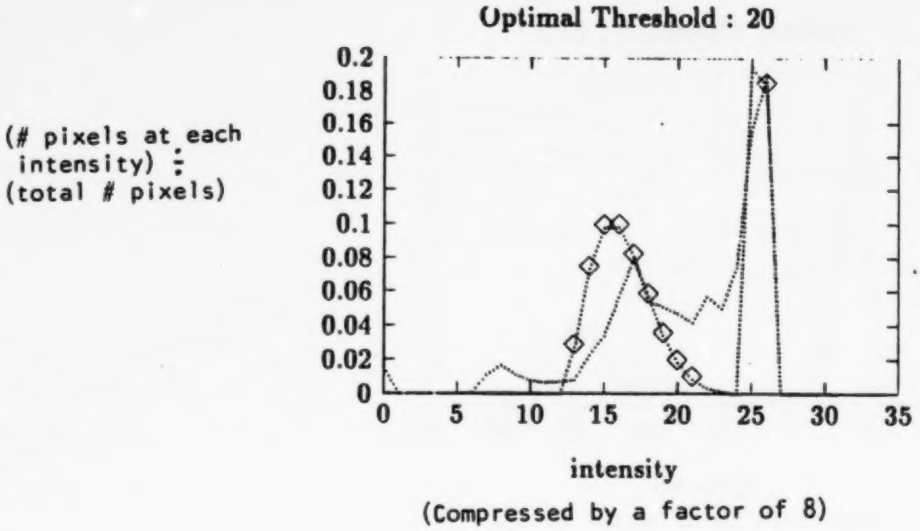

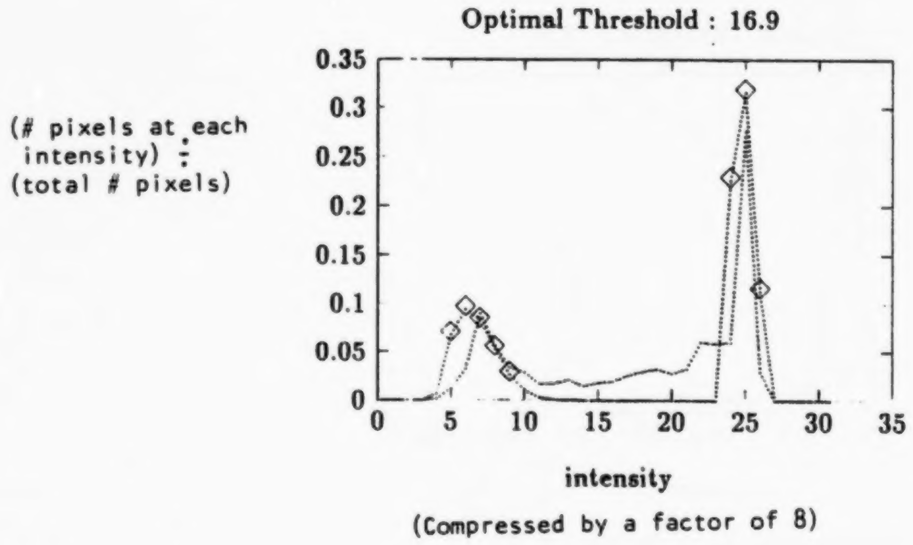

Figure 3.7: Curve fits: subimage 7 of frame 1 and subimage 6 of frame 10

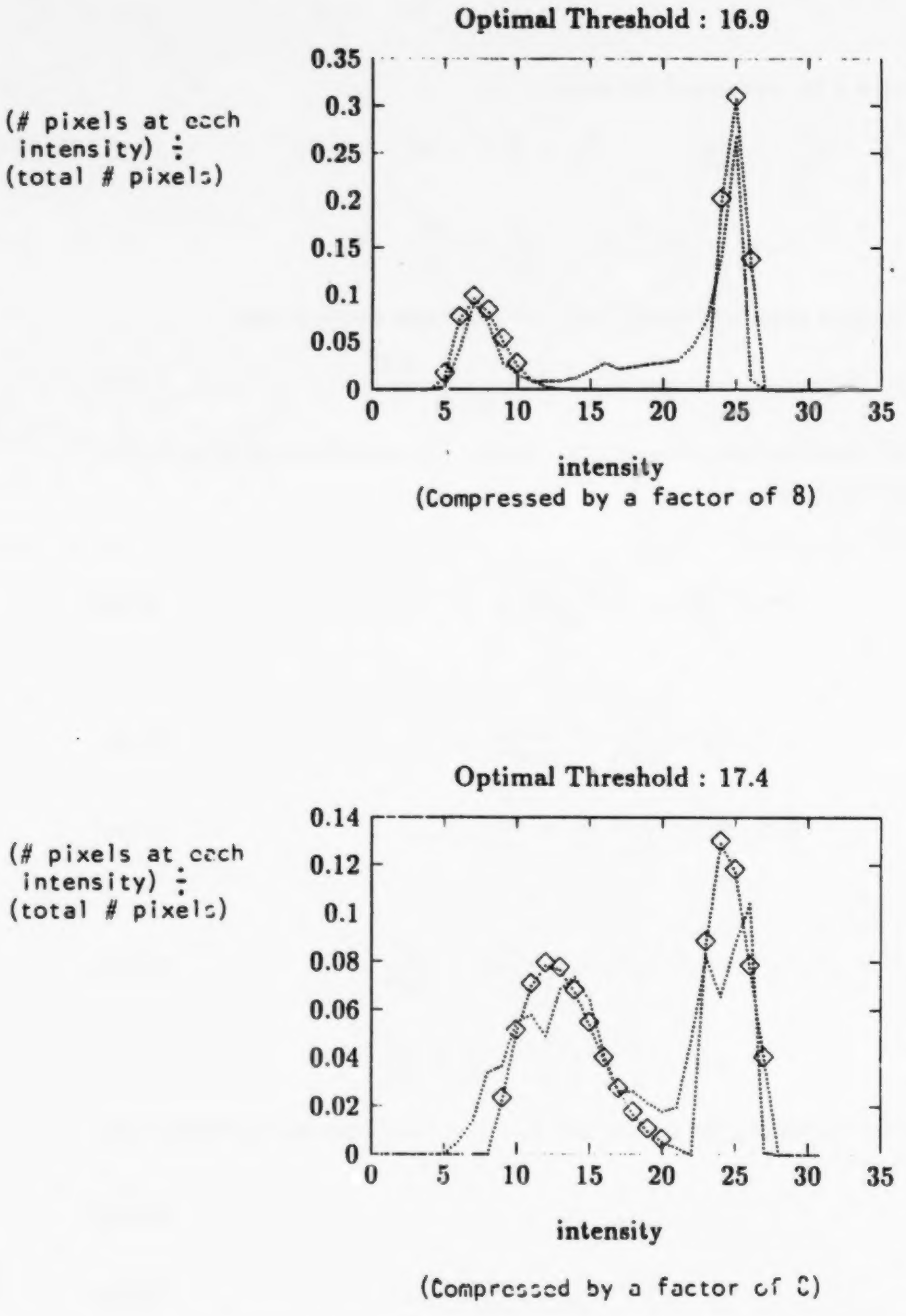

Figure 3.8: Curve fits: subimage 6 of frame 20 and subimage 7 of frame 30

and solve for T. The result is a transcendental equation:

$$ln(T - a) = [\frac{1}{2b} - \frac{1}{2\sigma^2}]T^2 + [\frac{\mu}{\sigma^2} - \frac{a}{b}]T - \ln P_1 + \ln P_2 \tag{3.15}$$

$$+ \ln b - \ln(\sqrt{2\pi}\sigma) - \frac{\mu^2}{2\sigma^2} + \frac{a^2}{2b}$$

Expressing $ln(T - a)$ as a power series and keeping only the first three terms, yields:

$$\ln T = \ln N + \frac{T - a - N}{N} - \frac{[T - a - N]^2}{2(N^2)} \tag{3.16}$$

for $0 < T \leq 2N$ where $2N$ would be the maximum pixel value. The result after substituting eq. (3.16) into (3.15) is a quadratic equation.

$$T = \frac{-A}{2C} \pm \frac{\sqrt{B^2+4AC}}{2C} \tag{3.17}$$

where

$$A = \frac{1}{2b} - \frac{1}{(2\sigma^2)} + \frac{1}{(2N^2)} \tag{3.18a}$$

$$B = \frac{\mu}{\sigma^2} - \frac{a}{b} - \frac{2}{N} + \frac{a}{N^2} \tag{3.18b}$$

and

$$C = -\ln P_1 + \ln b + \ln P_2 - \ln\sqrt{2\pi}\sigma - \frac{\mu^2}{2\sigma^2} \tag{3.18c}$$

$$- \ln N + \frac{3}{2} + \frac{a^2}{2N^2} + \frac{a}{N} + \frac{a^2}{2b}$$

For the mixture density containing the sum of two Rayleigh functions, the quadratic equation has the following parameters:

$$A = \frac{1}{2b} - \frac{1}{2d} \tag{3.19a}$$

$$B = -\frac{a}{b} + \frac{c}{d} + \frac{c}{N^2} - \frac{a}{N^2} \tag{3.19b}$$

and

$$C = -\ln P_1 + \ln b + \ln P_2 - \ln d - \frac{c^2}{2d} + \frac{s^2}{2N^2} + \frac{a}{N} + \frac{a^2}{2b} - \frac{c^2}{2N^2} - \frac{c}{N} \tag{3.19c}$$

Good results were achieved using this method for all parameters except P_1. The estimate of the second derivative with respect to P_1 using the gradient approximation precluded convergence toward an estimate of P_1. Therefore, the analytic second derivative was used. Convergence was then reached and an estimate of P_1 was obtained. Figures 3.5 through 3.8 show the results of the curve fits and the resulting optimal thresholds for a number of subimages in several frames.

All of the subimages yielded, with small variation, one or two optimum threshold values: either 12 or 17 on a 0 to 32 pixel scale which corresponds to a value of 96 or 136 on a pixel scale of 0 to 255. Each subimage with an optimum threshold of 96 came from rows 0 to 63 of the original image, the area including a portion of the building and some smoke. Each subimage with an optimum threshold of 136 came came from rows 64 to 127 in the original image, the area containing the most concentrated smoke. In general, there was consistency across frames with regard to the optimal threshold applied to these two different regions. Small variations from frame to frame in the optimal threshold for a given region appeared due to the placement and distribution of the very concentrated smoke in the particular frame. On average, however, the optimal thresholds were 96 and 136. Therefore, these two optimal thresholds were applied to the original frames using linear interpolation to provide a smooth transition between the thresholds. Figure 3.9 shows the results of segmenting frames 1, 10, 20, and 30.

In summary, we considered both global thresholding and optimal thresholding as techniques for segmenting the image data into two regions. From our experiments, we concluded that it is difficult to heuristically find a single global threshold that would segment this image data. We did find that the optimal thresholding provided us with a robust means for segmenting the image data into two regions. We calculated optimal thresholds for nine subimages for each frame of image data and found consistency from frame-to-frame. The segmented image data has the potential for providing useful qualitative insight about the outer boundary of the smoke dispersion when viewed as a sequence and has proven useful for estimating motion parameters (see section 4).

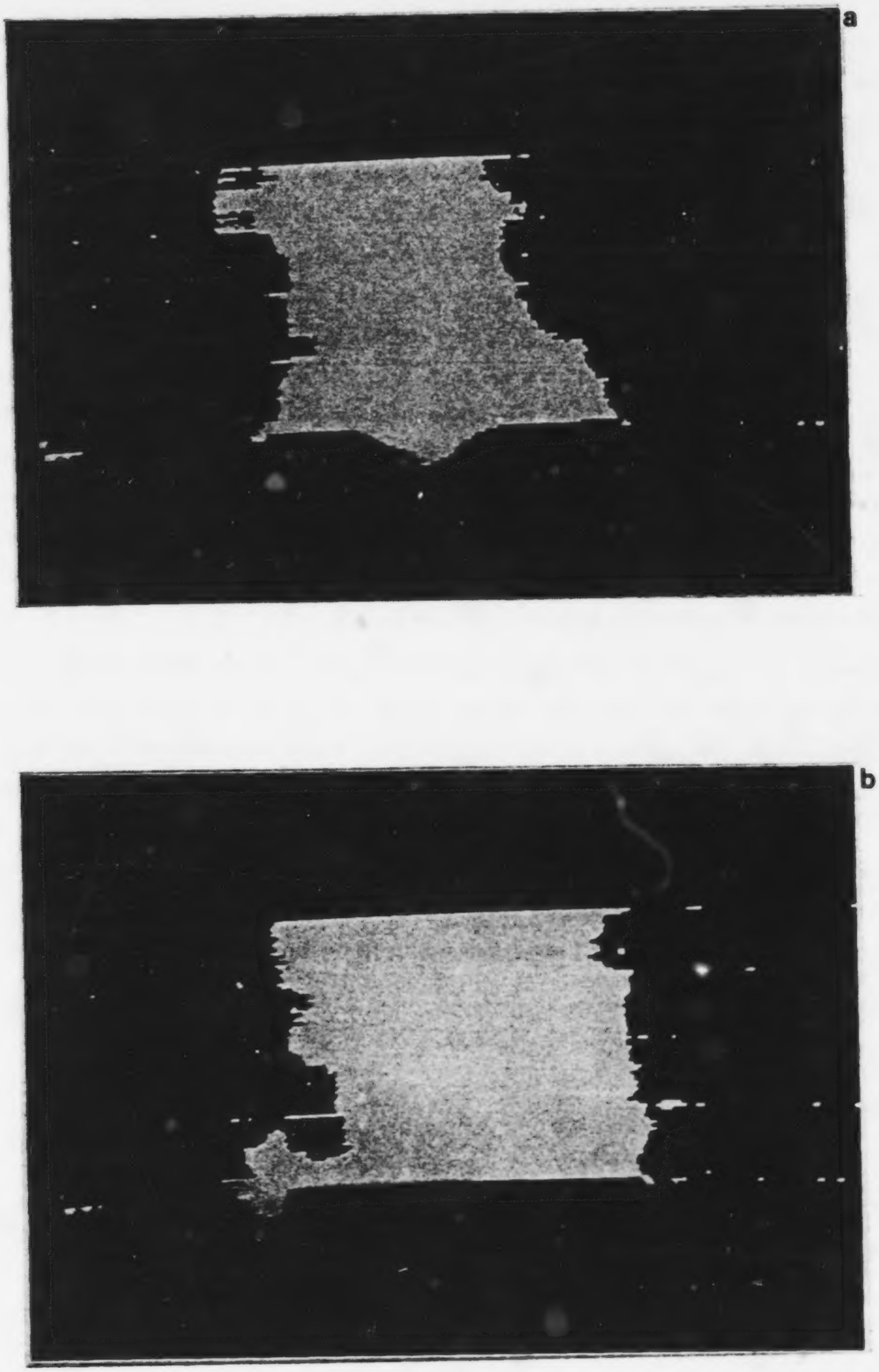

Figure 3.9: The segmented image data using the optimum threshold values calculated for each subimage. (a) Frame 1; (b) Frame 10;

Reproduced from
best available copy.

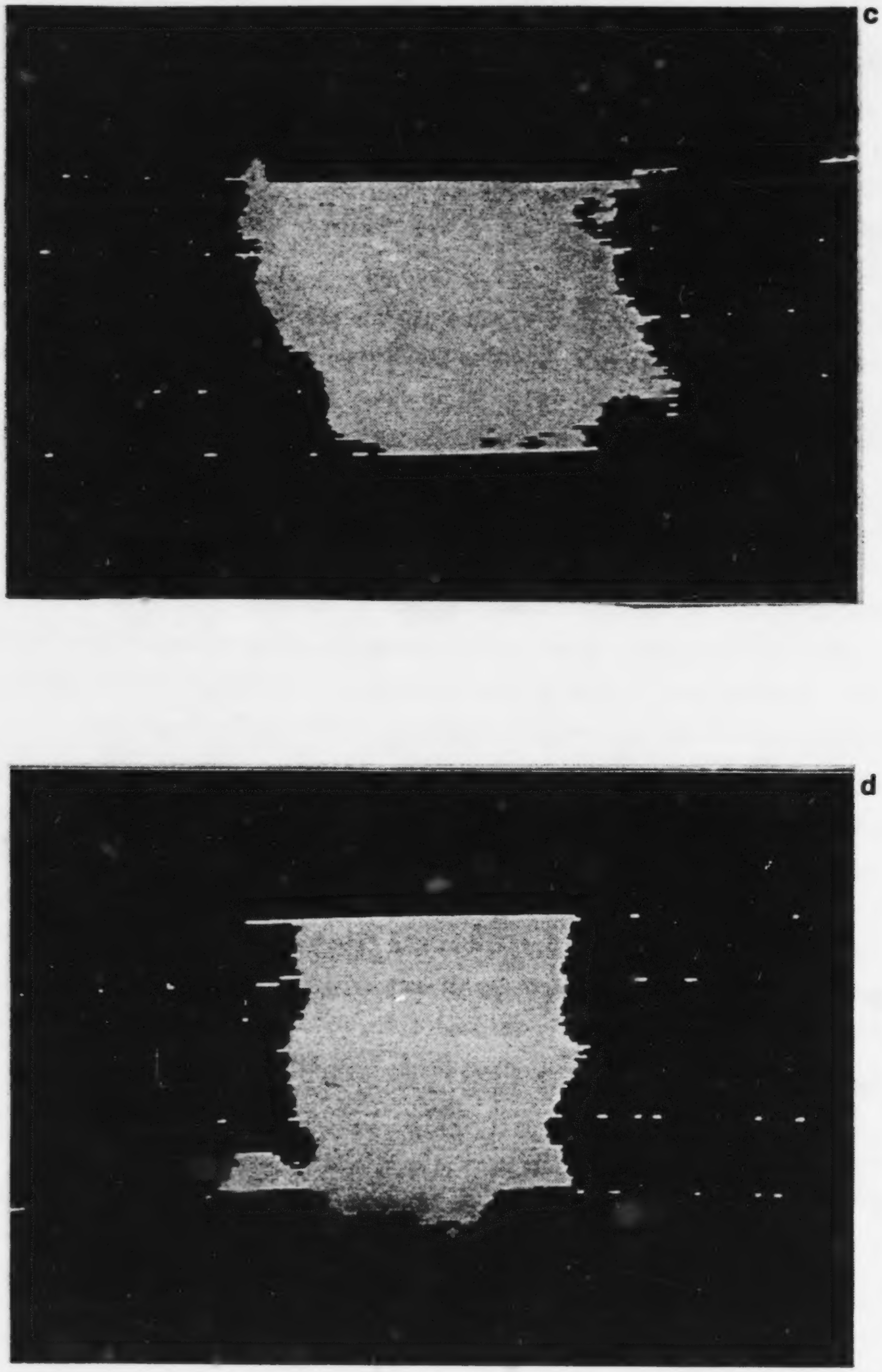

Figure 3.9: (c) Frame 20; (d) Frame 30.

Reproduced from
best available copy.

4 MOTION DETECTION

4.1 Introduction

A very simplistic approach to motion detection involves the subtraction of adjacent frames in a sequence of image data. The idea is that stationary objects will subtract out and leave pixel values of zero, and in areas where motion has occurred, there will be nonzero pixel values (Martin, et al., 1982). A fundamental assumption of this method is that all the images are spatially registered from frame to frame.

A body of work in the field of image coding exploits the idea that in stationary areas the image information stays the same from frame to frame (Netravali, et al., 1980). From a coding point of view, only the moving areas need to be updated during the coding process (Limb and Murphy, 1975). The techniques developed to estimate the amount of motion occurring from frame to frame have also been utilized in image analysis problems (Ballard and Brown, 1982) and (Gonzalez and Wintz, 1988). Netravali and Robbins (1979) use a gradient operation to estimate the displacement of the moving objects on a pixel by pixel basis. Other schemes estimate displacement by correlating the information between blocks in adjacent frames. Another approach attempts to relate the information in adjacent frames by matching correspondence points (Sethi and Jain, 1987). Assumptions for most of these algorithms is that the objects in motion be rigid bodies, the motion is linear and the motion is in a plane parallel to the image plane.

In more recent years the rigid body requirement has been relaxed by some approaches. One such approach tracks points based on the assumption of smoothness of motion. That is, due to inertia the motion of an object cannot change instantaneously. Uniform motion is assumed. A shortcoming of this technique is that colliding objects require a much more complicated algorithm to analyze the motion. Another method determines motion by numerically calculating particular line or surface integrals contained in the image (Kanatani, 1984). No correspondence of points is required, but the surface of the object is assumed to be a closed contour. This approach might prove useful for further study of the thresholded smoke boundary deformation.

4.2 Frame differencing

One of the motivations of this research was to understand the motion characteristics of the image data. The first operation we considered was frame differencing (Ballard and Brown, 1982). A difference operator applied along the temporal axis produces information about the changes that occur in intensity with respect to time. The simplest form for frame differencing is the first-order difference:

$$d_1(x,y) = f_1(x,y) - f_2(x,y) \tag{4.1}$$

where the subscript denotes the frame number of the image or difference frame. The new image, $d_1(x,y)$, has nonzero values at all locations where the intensity has changed value between frame 1 and frame 2. If the background lighting conditions do not change from frame to frame while recording the original image data and there is not a significant amount of noise degradation, the nonzero values can be attributed to the temporal changes in the smoke. Figure 4.1 illustrates the results of performing a first-order difference on a sequence of frames from the original data. Figure 4.1(a) is the difference between frames 1 and 2, 4.1(b) is the difference between frames 10 and 11, 4.1(c) is the difference between frames 20 and 21 and 4.1(d) is the difference between frames 30 and 31. Clearly one can see the temporal variations.

Since the first-order difference operation is sensitive to temporally correlated noise degradations, it is of interest to consider alternatives. The first-order difference calculation can be generalized to an nth-order difference as follows.

$$d_k^n(x,y) = d_k^{n-1}(x,y) - d_{k-1}^{n-1}(x,y) \tag{4.2}$$

where d_k^n is the nth-order difference at frame k. Alternatively, eq. (4.2) can be written as,

$$d_k^n(x,y) = \sum_{i=0}^{n}(-1)^i \binom{n}{i} f_{k-i}(x,y) \tag{4.3}$$

where $d_k^0 = f_k$. The advantage of an nth-order difference is its decreased sensitivity to low frequency time-correlated noise. Another way to interpret the nth-order difference is as a high pass filter with an increasing cutoff frequency as n increases. This is illustrated in figure 4.2 (Cowart, 1986) with a comparison of the frequency response for a first-order and third-order difference. It should also be noted that since a difference filter is basically a high-pass filtering operation, any temporally uncorrelated white noise gets amplified. Hence, a trade-off must be made.

We performed first, second, and third-order differencing on the image data. We believe there is potential for obtaining qualitative insight when viewing the first-order difference images as a video sequence. Little insight was gained for this data from second and third-order differencing because of the amplification of interframe noise. Perhaps if a better means for suppressing the interframe noise was found, the second and third-order differencing would be more useful. Alternatively, if cleaner image data is recorded all three difference sequence may prove to be useful both for qualitative and further quantitative assessment of the motion characteristics.

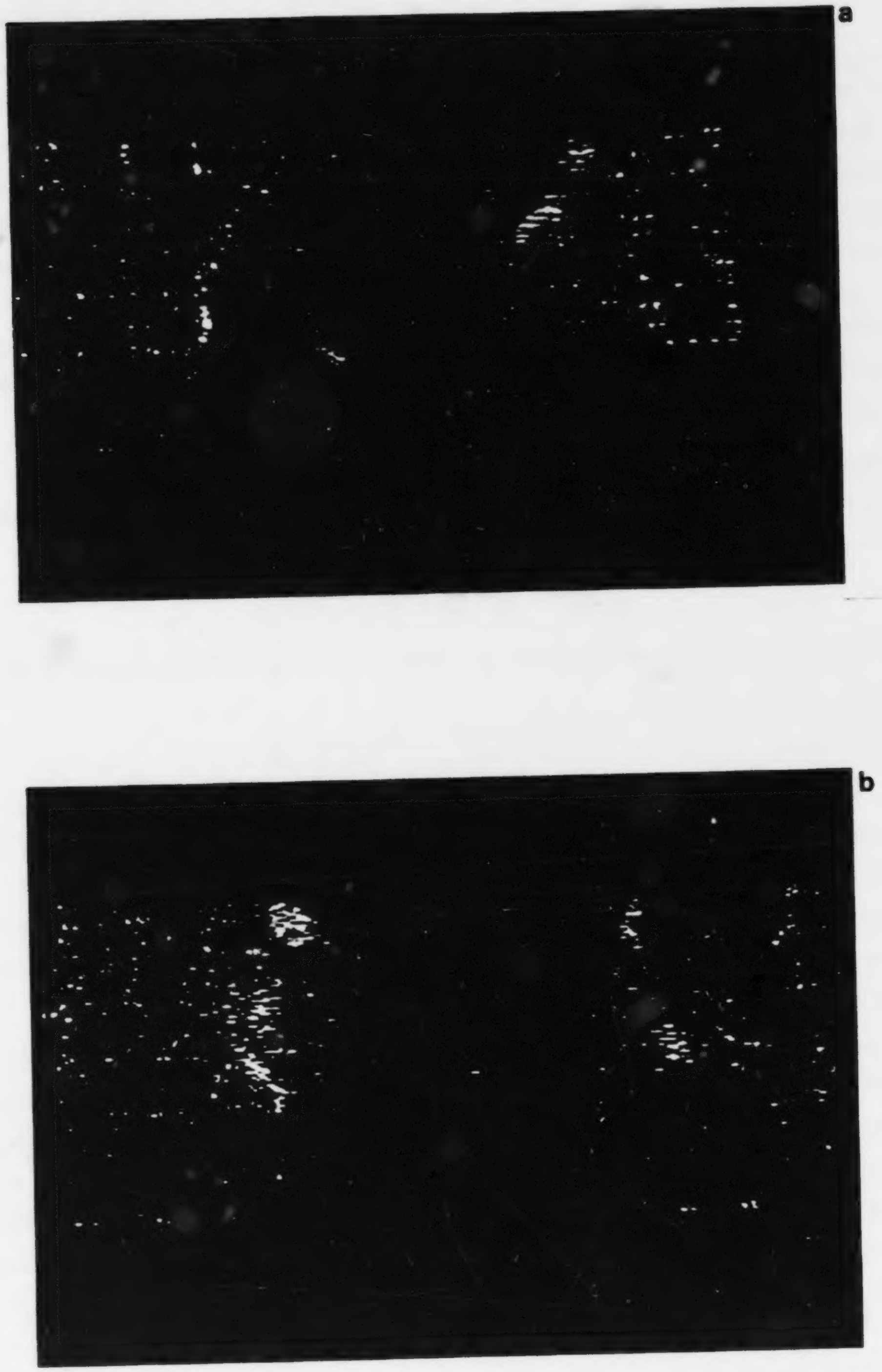

Figure 4.1: Absolute value of the first-order temporal difference of the original image data. (a) Difference between frames 1 and 2; (b) Difference between frames 10 and 11;

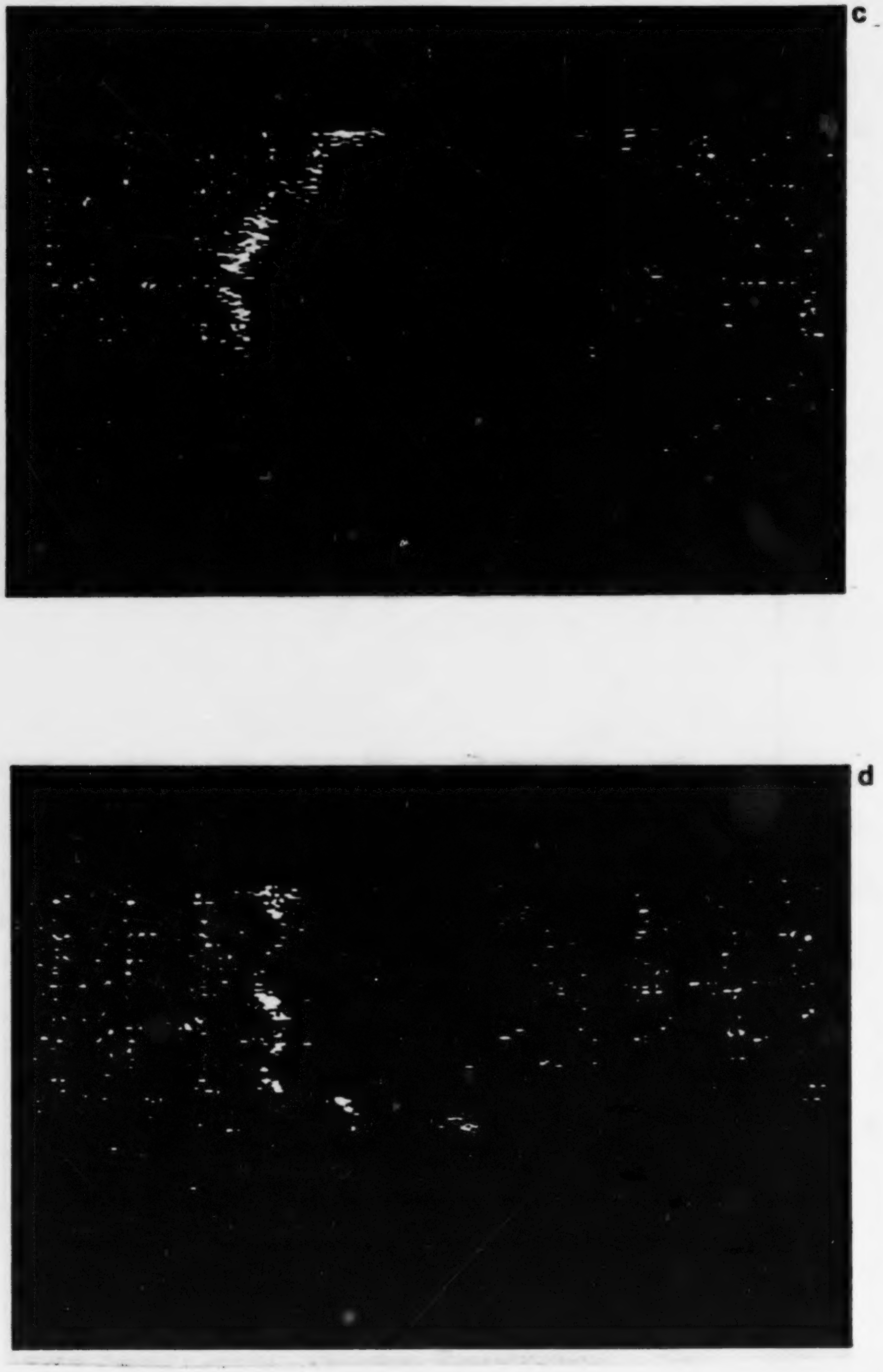

Figure 4.1: (c) Difference between frames 20 and 21;
(d) Difference between frames 30 and 31.

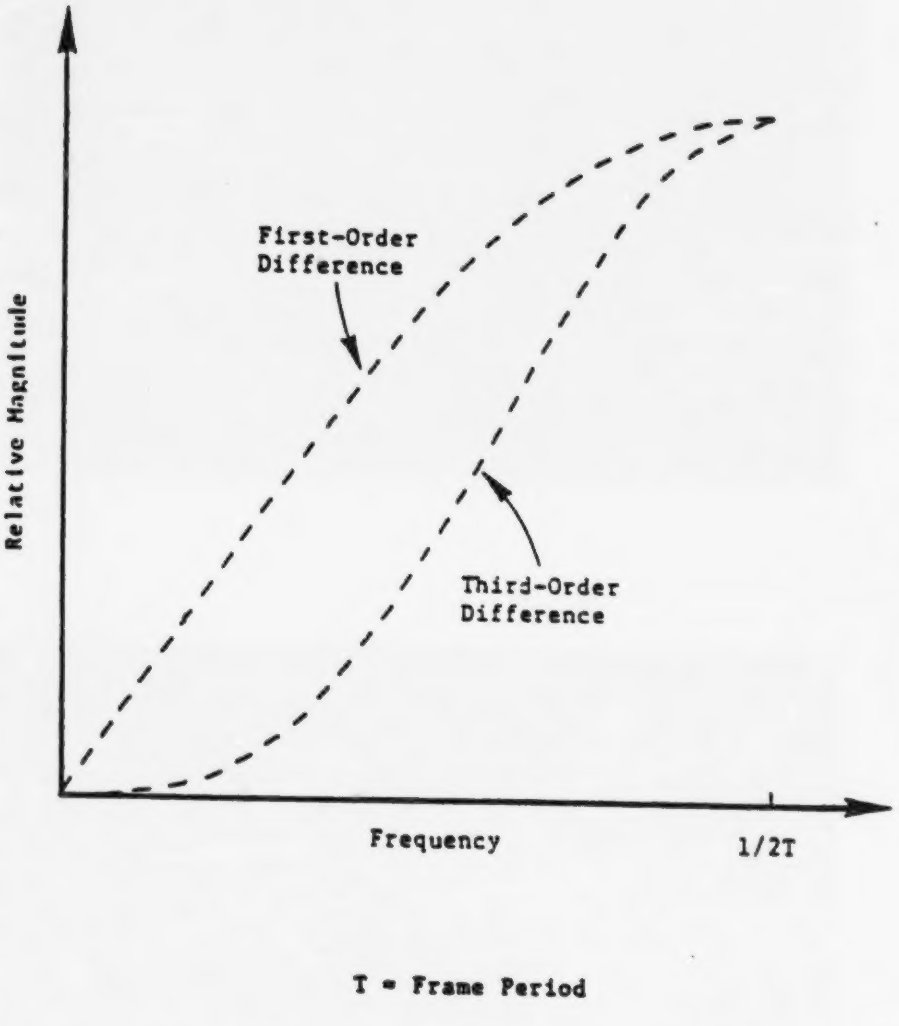

Figure 4.2: Frequency response of a first-order and third-order difference filter.

4.2 Center of Mass

Assuming the boundaries of the regions in the segmented image data reasonably describe regions containing the smoke, they can then be treated as an object with mass and area. The integrated optical density (IOD) is a measure of the mass contained in each thresholded image of smoke (Castleman, 1987). Its equation is given by the following:

$$IOD = \sum_{i=1}^{N} \sum_{j=1}^{M} p(i,j) \tag{4.4}$$

It is simply a sum of all pixel values. The assumption is that the accumulation of much smoke in a region, as opposed to a small amount of smoke, is characterized by higher pixel values in that region and therefore yields a higher mass. The IOD was found for each of the segments in frames 1 - 30 of the segmented image data using the optimal thresholding technique. The results are displayed in Table 4.1 and Table 4.2. Note the mass increases and then decreases. This change of mass is caused by the accumulation of smoke in the area of the building and by the subsequent sweeping away of the built up smoke reported by Huber (1988a).

The equation for the coordinates of the center of mass are given by:

$$x = \frac{\sum_{i=1}^{N} \sum_{j=1}^{M} ip(i,j)}{IOD} \tag{4.5a}$$

$$y = \frac{\sum_{i=1}^{N} \sum_{j=1}^{M} jp(i,j)}{IOD} \tag{4.5b}$$

The center of mass was calculated for each of the thresholded images. A plot of the row/column coordinates of the center of mass is given in Figure 4.3. This action is confirmed in Huber (1988a).

The normalized area of the thresholded smoke images is simply the number of pixels in or on the boundary of the image assuming each pixel covers one unit. Refer to Table 4.1 and Table 4.2 to see the change in area of the smoke over time. Note a periodic increase in area followed by a decrease. This phenomenon is similar to that of the integrated optical density. Changes in area and integrated optical density generally reveal the stages of smoke accumulation observed by Huber. An increase in area and optical density would imply the end of the cycle of smoke accumulation, and a decrease in area would be expected to follow. An increase in optical density and a decrease in area might imply that the smoke is beginning its cycle of accumulating.

frame	iod (mil)	area
1	2.27	95
2	2.22	94
3	2.19	90
4	2.19	89
5	2.24	87
6	2.36	88
7	2.54	90
8	2.74	90
9	2.27	95
10	2.85	93
11	2.90	95
12	2.84	95
13	2.76	96
14	2.50	98
15	2.31	97

Table 1: Integrated optical density and area: frame 1 to 15

frame	iod (mil)	area
16	2.19	94
17	2.21	93
18	2.42	93
19	2.63	92
20	2.80	91
21	2.89	89
22	2.79	88
23	2.77	87
24	2.76	87
25	2.77	87
26	2.77	87
27	2.71	93
28	2.70	93
29	2.61	94
30	2.50	95

Table 2: Integrated optical density and area: frame 16 to 30

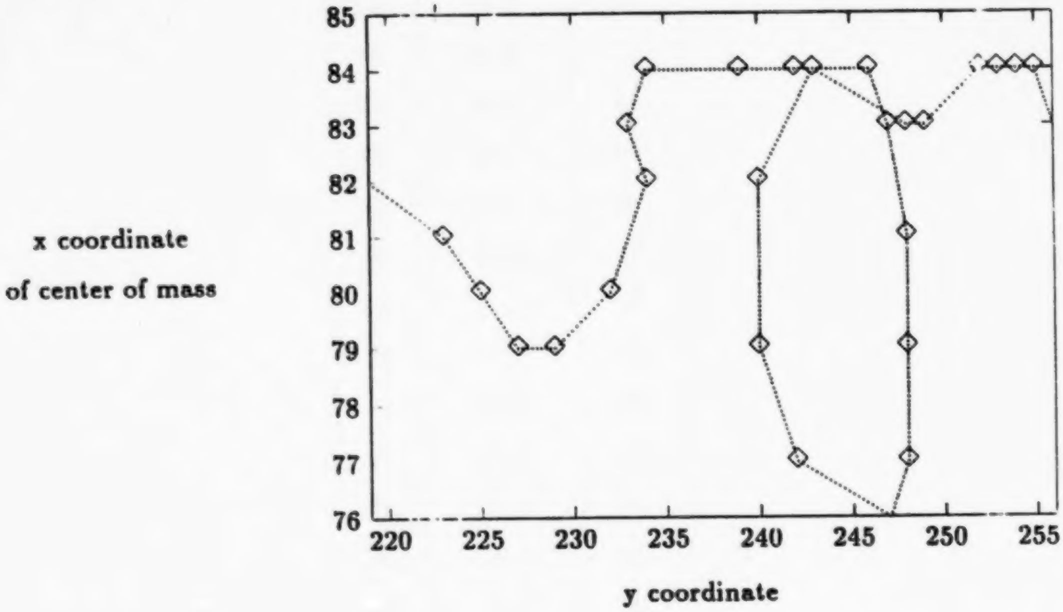

Figure 4.3: Plot of the center of mass over 30 frames.

4.3 Boundary Deformation

Using the thresholded images, the boundary of each image was extracted in a binary image. Only the points on the boundary contour have a nonzero pixel value. Refer to figure 4.4. By overlaying these binary images, a comparison of the deformation of the boundaries over time may be made. At this time only a qualitative comparison has been made, but future work could consider the boundary deformation more quantitatively. Attributes of shape and size could be computed and compared. This same process could be performed inside the smoke to characterize the boundary between diffuse and more concentrated smoke. Further work in this area would possibly derive significant information about changes in concentration of the smoke.

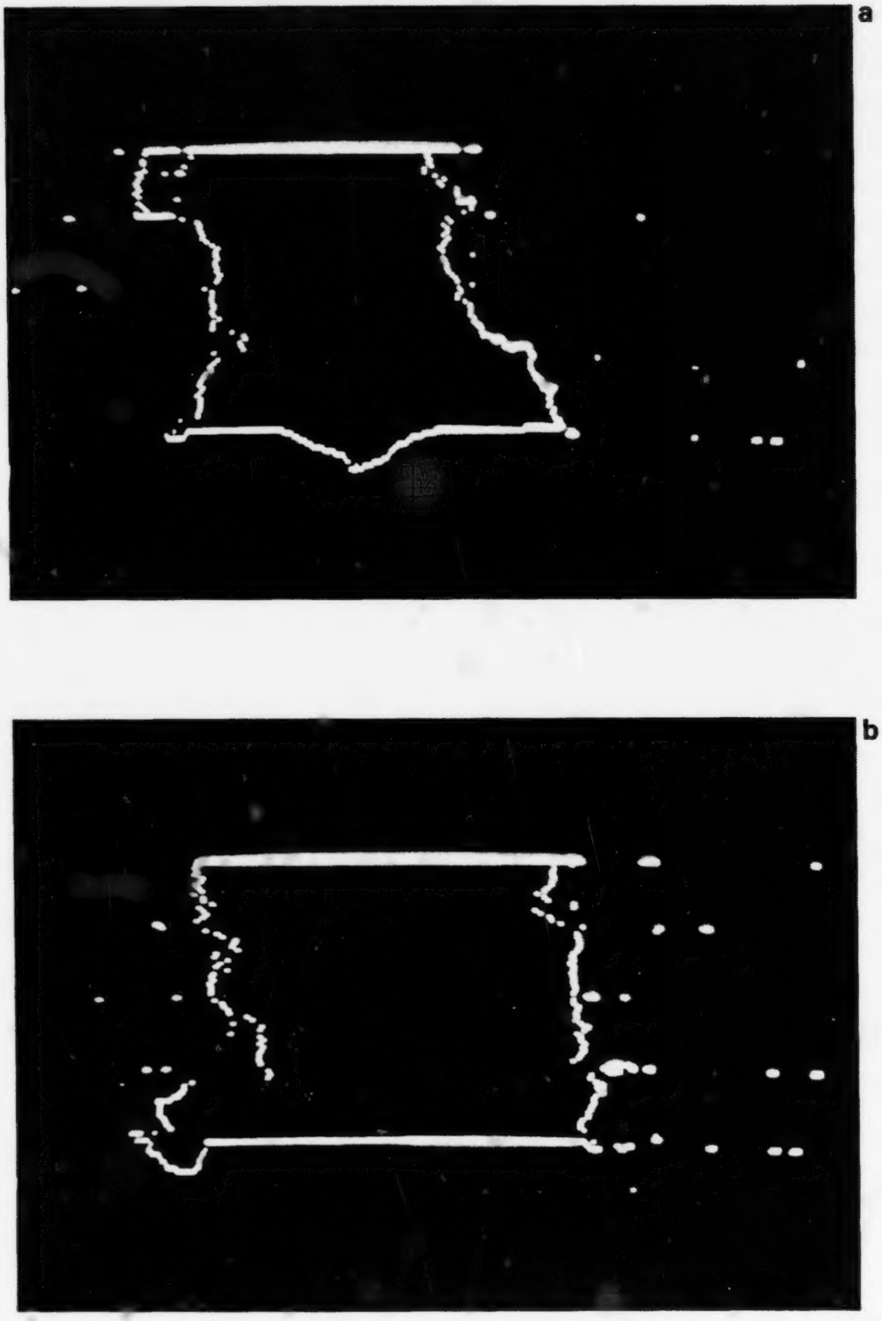

Figure 4.4: Binary image of the boundary contour of the segmented image data using the optimal threshold values. (a) Frame 1; (b) Frame 10;

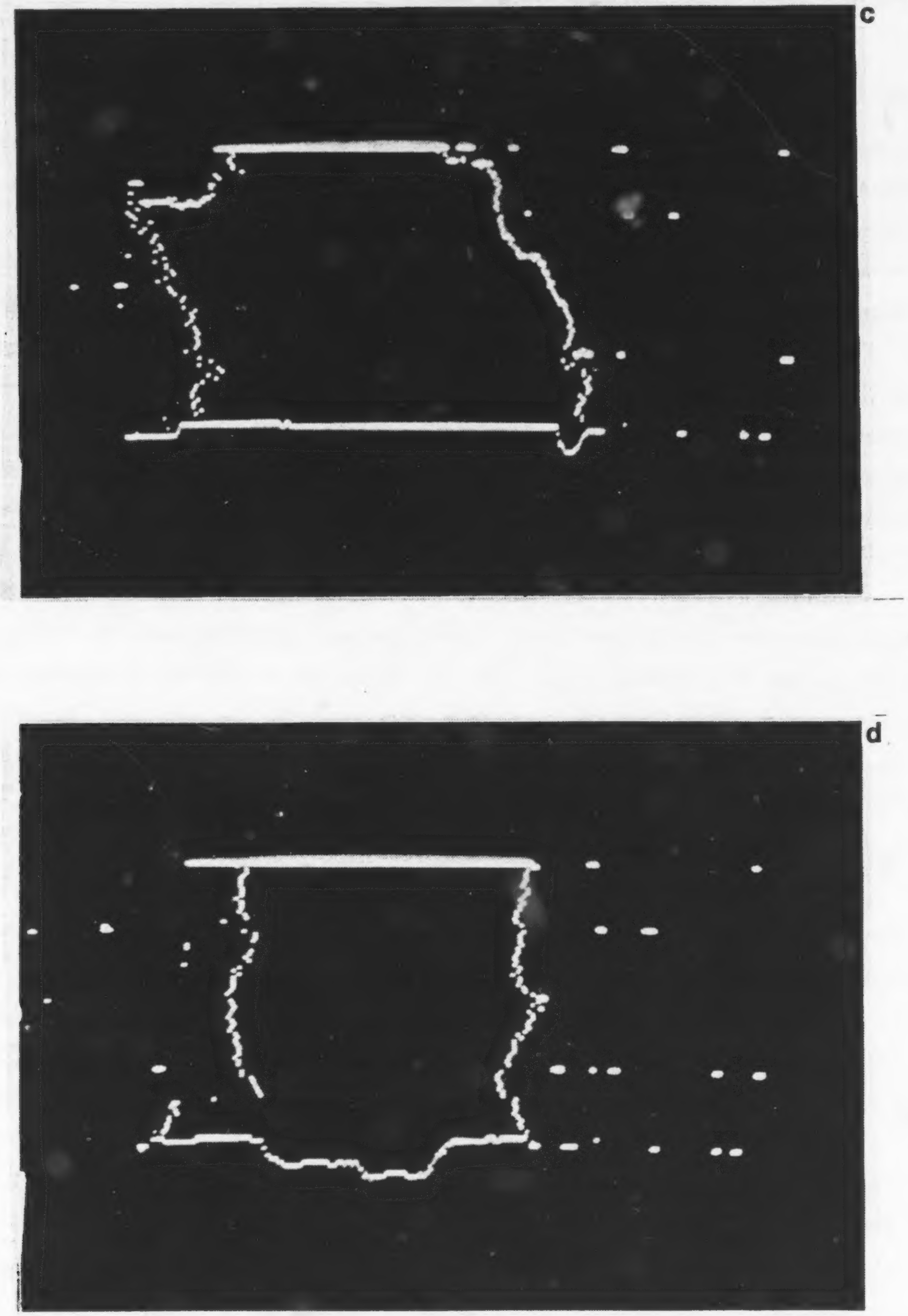

Figure 4.4: (c) Frame 20; (d) Frame 30.

- Euclidean geometry provides a concise accurate description of man-made objects but is inappropriate for natural shapes and textures. Fractals provide a good means for describing natural shapes and textures.

- Euclidean shapes are usually described by a simple algebraic formula. Fractal shapes are often the result of a construction procedure or algorithm.

Mandelbrot (1983) used the term *fractal dimension* as a numerical measure of the degree of boundary irregularity or surface roughness of an object. *Fractal dimension* can be illustrated by considering the measurement of the length of a coastline with a ruler of length k and then counting the number of rulers it takes to cover the coastline. The result will be an estimate of the length L(k) of the coastline. As the ruler length k is decreased, smaller features are included in the measurement and L(k) increases. An analytic formula for the function L(k) is given by Mandelbrot (1983)

$$L(k) = Ck^{1-D} \tag{5.1}$$

where C is a constant equal to the length obtained for $k=1$ and D is the fractal dimension with $D \geq 1$.

A large number of methods have been developed for generating fractal sets. Lovejoy and Mandelbrot (1985) used a technique called fractal sum of pulses for generating rainfall intensity statistics. They represented the time series of rainfall intensity as a summation of rectangular pulses with random heights (rainfall intensity) with random widths (rainfall duration). The centers of the rectangular pulses were randomly distributed according to a Poisson process with constant rate λ.

The majority of fractal functions in the field of computer vision are modeled stochastically using fractional Brownian motion (Pentland, 1984), (Peitgen and Richter, 1986). For a fractional Brownian motion (fBm) $I(t)$, the variations $\Delta I = I(t_2) - I(t_1)$ are zero mean Gaussian with variance proportional to the magnitude of the time difference $\Delta t = |t_2 - t_1|$ raised to the power $2H$ (Peitgen and Richter, 1986).

$$E[\Delta y^2] \propto \Delta t^{2H} \tag{5.2}$$

where $E[\cdot]$ is the statistical expectation. If $H = 1/2$, we have standard Brownian motion and $E[\Delta y^2] \propto \Delta t$.

In the remainder of this section, we describe the a new fractal-based algorithm for extracting motion information from a sequence of smoke image data. We describe how the fractal dimension and related measures are affected by the spatial-temporal distributions of the smoke in time-varying image sequences. The concept of fractals is combined with image analysis techniques to develop two models for the purpose of investigating the atmospheric dispersion of hazardous air pollution as recorded in video imagery.

5.2 Derivation of a New Model

In this work, we were not concerned with obtaining the fractal dimension explicitly. Instead, two fractal parameters were computed, the dynamical horizontal fractal parameter (HFP) and the dynamical vertical fractal parameter (VFP). These two parameters play an important role in the analysis of our natural data. In general terms, one is interested in describing how a fractal or near-fractal object can be represented by a measure. Physically, HFP and VFP describe the complexity and variability of a surface. Even though the fractal parameters are the key for the present research, the fractal dimension is easily derivable. If the topological dimension is given by T, the fractal dimension D is:

$$D = T - p_j(\mathbf{v}) \tag{5.3}$$

where $p_j(\mathbf{v})$ is the dynamical fractal parameter.

Let us define a random function $I(r)$ (Mandelbrot, 1983) as a fractal Brownian function if for all r and variations $\Delta_i r$ $(i=1, 2, 3, \ldots)$:

$$P_r\left[\frac{[I(r+\Delta_i r) - I(r)]}{|\Delta_i r|^{(1 - p_j(\mathbf{v}))}} < \theta\right] = F(\theta) \tag{5.4}$$

$F(\theta)$ is the cumulative distribution function, $\Delta_i r$ is the variation, $\Delta_i r = r(x_{i+1}) - r(x_i)$ and is the ith element of the vector quantity $\Delta \mathbf{r}$, and $p_j(\mathbf{v})$ is the dynamical fractal parameter which is a function of the variable vector $\mathbf{v}$ (vector $\mathbf{v}$ may have several variables). In this study we limited ourselves to the case where the vector $\mathbf{v}$ is composed of three variables; time, the nominal velocity of smoke, and the concentration of smoke. The index j represents either the horizontal or vertical fractal parameter. The parameters $p_j(\mathbf{v})$ describe how the surface of an object varies and indicate how complex the surface is (measure of fragmentation).

Equation (5.4) can be rewritten to obtain,

$$< \Delta I_{\Delta_i r} > |\Delta_i r|^{p_j(\mathbf{v})-1} = < \Delta I_{\Delta_i r} > \tag{5.5}$$

where $< \Delta I_{\Delta_i r} >$ is the mean value of the change in intensity over distance $\Delta_i r$. Using equation (5.5), we solve for $p_j(\mathbf{v})$ as follows:

$$\log\left[< \Delta I_{\Delta_i r} > \mid \Delta_i r \mid^{p_j(\mathbf{v})-1} \right] = \log\left[< \Delta I_{\Delta_1 r} > \right] \tag{5.6}$$

from which

$$(p_j(\mathbf{v})-1) \log \mid \Delta_i r \mid = \log < \Delta I_{\Delta_1 r} > - \log < \Delta I_{\Delta_i r} >$$

and

$$p_j(\mathbf{v}) = 1 + \frac{\log < \Delta I_{\Delta_1 r} > - \log < \Delta I_{\Delta_i r} >}{\log \mid \Delta_i r \mid} \tag{5.7}$$

Equation (5.7) defines a method for evaluating the dynamical fractal parameters. To evaluate $p_j(\mathbf{v})$, we need to compute the quantities $< \Delta I_{\Delta_i r} >$ for different spatial separations $\Delta_i r$ $(i=1,\ldots)$. In the two-dimensional case, these spatial separations $\Delta_i r$ may be viewed as concentric pulses representing straight cylinders whose base is a circle. The cylindrical integration method is the same approach used by (Mandelbrot, 1983). If we consider a reference point $I(i,j)$ in two-dimensional Euclidean space, we then define $\Delta_i r$ as the distance between $I(i,j)$ and its neighbor $I(k,l)$ as

$$\Delta_i r = \sqrt{(m-k)^2 + (n-l)^2} \tag{5.8}$$

5.3 Methodology for Evaluating $p_j(\mathbf{v})$

As mentioned above, equation (5.7) defines a method for evaluating the dynamical fractal parameters. These fractal parameters are proportional to the difference between two means, $< \Delta I_{\Delta_1 r} >$ which is the mean value of the change in intensity at one-unit distance and $< \Delta I_{\Delta_i r} >$ is the corresponding mean at an i-unit distance. Defining the fractal parameters in this way, permits us to process only the additional information required at an ith-unit distance. There is no need to reprocess redundant information. The difference of the means of intensity provides us with information about the surface characteristics in a local neighborhood of the pixel.

For the remainder of this section, denote the intensity of a pixel at location $\mathbf{r} = (\mathrm{m},\mathrm{n})$ to be $I(\mathbf{r}) = \mathrm{I}(\mathrm{m},\mathrm{n})$. In general, the image to be analyzed is defined on a $M \times N$ rectangular grid. Let $\mathrm{m} = \{ 1,2,\ldots\ldots,M \}$ represent the horizontal direction and $\mathrm{n} = \{1,2,\ldots\ldots,N\}$ the vertical direction. Let $\mathrm{G} = \{ 1,2,\ldots\ldots,N_g \}$ be the finite set of the N_g quantized gray levels. For each pixel $(i,j) \epsilon M \times N$, there is one and only one gray level value $G_{i,j}$.

Figure 5.1 shows a block diagram of the fractal model-based algorithm we developed. There are two main branches to this algorithm. One branch computes $<\Delta I_{\Delta_1 r}>$ and the other

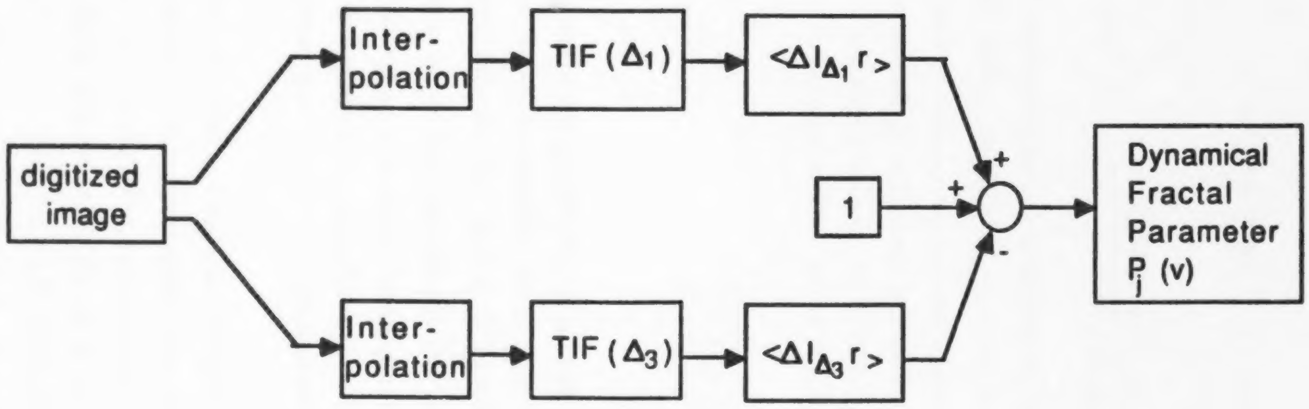
digitized image
Inter-polation
TIF (Δ_1)
$<\Delta I_{\Delta_1} r>$
Inter-polation
TIF (Δ_3)
$<\Delta I_{\Delta_3} r>$
1
+
+
-
Dynamical Fractal Parameter P_j (v)

Figure 5.1 Block diagram of the fractal parameter model.

computes $<\Delta I_{\Delta_i r}>$ for $i=3$. In the first stage interpolation was done to obtain the intensity values of points not lying on the rectangular sampling grid. These are required for the subsequent calculation of $<\Delta I_{\Delta_i r}>$. The second stage generates a set of intermediate images, referred to as the transfer images of the fractal (TIF). Each pixel in a TIF represents a sum of the absolute value of differences in gray level of that pixel and its neighbors. The third stage computes the $<\Delta I_{\Delta_i r}>$ using the results of stage three. The fourth stage combines the information from the two branches to calculate the $p_j(\mathbf{v})$.

Stage One: Interpolation

Consider a circular neighborhood with radius $\Delta_i r$ around a pixel (m,n). Figure 5.2 shows the first-order circular neighborhood configuration. It is used to calculate $<\Delta I_{\Delta_i r}>$, the mean of the differences of the gray levels between adjacent pixels and is an indicator of the fractal behavior of the time-varying object flux (smoke). The circular neighborhood configuration consists of eight pixels, each of which is placed on a circle in the image plane centered at (i,j). For all pairs (i,j), the quadruplets $\{(i,\ j+1),\ (i,\ j-1),\ (i+1,\ j)$ and $(i-1,\ j)\}$ are the pixels corresponding to grid corners (rectangular grids) and, hence, their intensities are known. As can be seen in figure 5.2, these four pixels are immediately to the north, south, east, and west of the pixel under consideration. The remaining four diagonal and off-diagonal locations are not positioned on grid points and their intensity values need to be interpolated (these "interpolated" pixels are marked an 'x'). This configuration was chosen because a circle is the largest disk that can be inscribed in the eight nearest neighbor square on a rectangular grid. Also, each intensity $I(\mathbf{r})$ is located at the same distance from the reference pixel $I(m,n)$ (Castwell, 1986). Other configurations such as an ellipse or a hyperbolic could be utilized, as suggested by Lovejoy (1986).

Let $v = (a,b)$ be one of the interpolated pixels and $q^{(i)}$, $i=1, 2, 3, 4$ be the coordinates of the four nearest grid points encircling v. The intensity value at v is then defined as a linear combination of the intensity values of $q^{(i)}$ multiplied by normalized inversed Euclidean distances between the interpolated pixel v and its neighbors $q^{(i)}$ $(i=1, 2, 3, 4)$.

$$d_i = ||v - q^{(i)}||^{-1} \qquad i=1,\ 2,\ 3,\ 4 \tag{5.9}$$

Let $h(i,j)$ denote the image function at point (i,j); then the intensity value at the interpolated pixel v is $h(v(a,\ b))$ and is given by

$$h(v(a\ \ b)) = \left[\sum_{i=1}^{4} d_i\right]^{-1} \left[\sum_{i=1}^{4} d_i\ h(q^{(i)})\right] \tag{5.10}$$

Figure 5.3 shows how the interpolated pixels are expanded in terms of their four neighbor grid

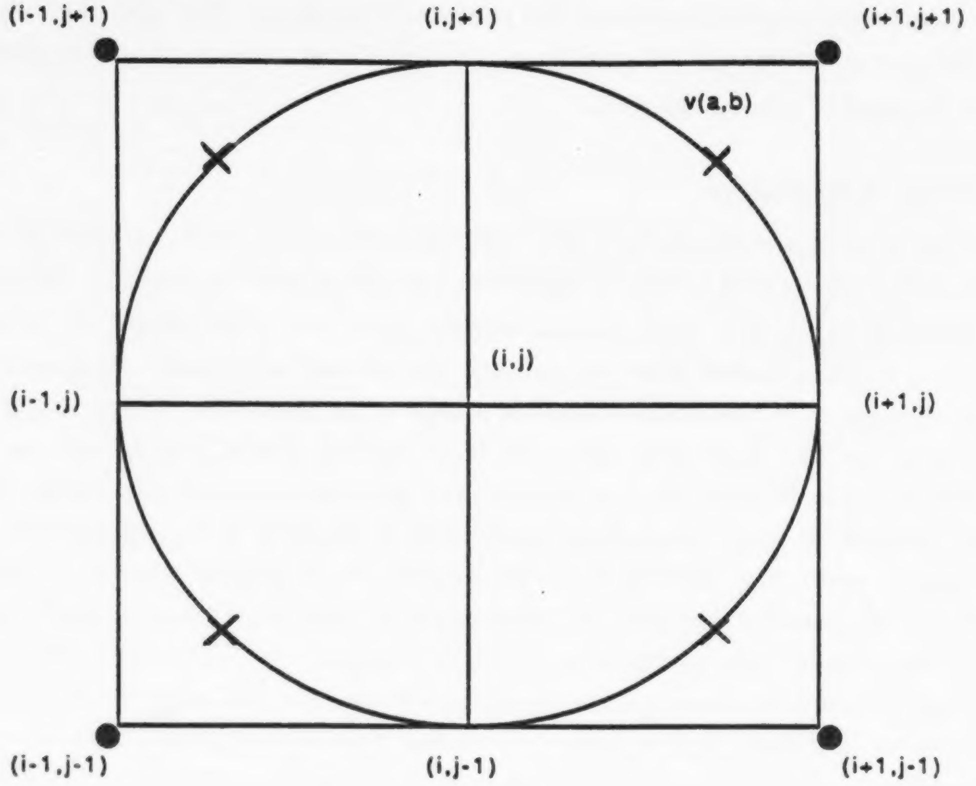
(i-1,j+1)
(i,j+1)
(i+1,j+1)
v(a,b)
(i,j)
(i-1,j)
(i+1,j)
(i-1,j-1)
(i,j-1)
(i+1,j-1)

Figure 5.2 **First-order circular neighborhood configuration**
● real pixel
x interpolated pixel

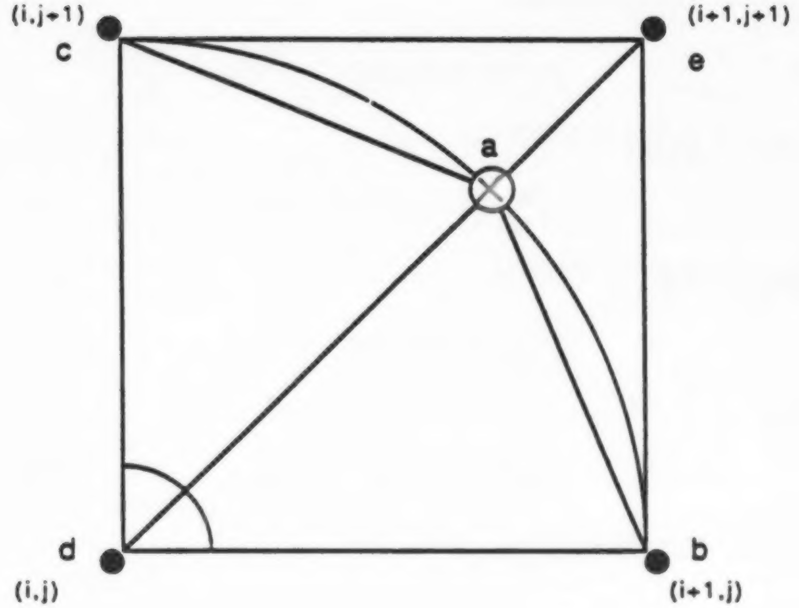
(i,j+1)
c
(i+1,j+1)
e
a
d
(i,j)
b
(i+1,j)

Figure 5.3 **Interpolated pixels**

cd = 1 unit pixel distance

ae = (sqrt - 1) unit pixel distance

ab = ac = 2 sin $\frac{\phi}{2}$ unit pixel distance

da = 1 unit pixel distance

• real pixel

x interpolated pixel

points.

Assuming unit distance (norm) between pixels $(i,\ j)$ and $(i\ \pm 1,\ j)$ and unit distance (norm) between pixels $(i,\ j)$ and $(i,\ j \pm 1)$, then the linear combination coefficients may be given by the following:

$$d_1 = \frac{1}{||v - q^{(1)}||} = \frac{1}{0.7653} = 1.3065$$

($q^{(1)}$ is the pixel at $(i+1,\ j)$)

$$d_2 = \frac{1}{||v - q^{(2)}||} = \frac{1}{0.7653} = 1.3065$$

($q^{(2)}$ is the pixel at $(i,\ j+1)$)

$$d_3 = \frac{1}{||v - q^{(3)}||} = \frac{1}{\sqrt{2} - 1} = 2.4142$$

($q^{(3)}$ is the pixel at $(i+1,\ j+1)$)

$$d_4 = \frac{1}{||v - q^{(4)}||} = \frac{1}{1} = 1$$

($q^{(4)}$ is the pixel at $(i,\ j)$)

$$\frac{1}{\sum_{i=1}^{4} d_i} = \frac{1}{1.3065 + 1.3065 + 2.4142 + 1.0} = 0.1659$$

Let $\frac{1}{\sum_{i=1}^{4} d_i} = \beta$, and from the above we conclude the following:

- the contribution of pixel $(i,\ j)$ to v is $\beta d_4 = \alpha_1$
- the contribution of pixel $(i+1,\ j)$ to v is $\beta d_1 = \alpha_2$
- the contribution of pixel $(i,\ j+1)$ to v is $\beta d_2 = \alpha_3$
- the contribution of pixel $(i+1,\ j+1)$ to v is $\beta d_3 = \alpha_4$

where $\sum_{i=1}^{4} \alpha_i = 1$.

Stage Two: Generation of the TIF's

A set of intermediate images, referred to as transfer images of the fractal (TIF's) are generated in stage two. These intermediate images are generated by computing the sum of the absolute values of the difference in gray level at each pixel (m,n) and its neighbors on the chosen disk. The absolute value metric defines the magnitude for each pixel of the transfer image of the fractal. The sum of the absolute values of the difference in gray levels defines a measure of the grayness variation in the image. The measure of the grayness variation represents a length. This length, which is a fundamental measure in fractal theory, is important because it characterizes the complexity and variability of an image surface.

Let $f^{(\Delta_i r)}$ be the transfer image of the fractal (TIF) for *ith*-unit circular neighborhood. For the one-unit neighborhood $(\Delta_1 r)$, we have

$$f_{(m,n)}^{(\Delta_1 r)} = \sum_{t=1}^{5} |s_t| \ , \tag{5.11}$$

where

$$s_1 = \Big[I(m,n) - I(m+1,n)\Big]$$

$$s_2 = \Big[I(m,n) - I(m,n-1)\Big]$$

$$s_3 = \Big[I(m,n) - I(m-1,n)\Big]$$

$$s_4 = \Big[I(m,n) - I(m,n+1)\Big]$$

and the s_t for the interpolated pixel locations are

$$s_5 = \Big[(1-\alpha_1)I(m,n) - \alpha_2\, I(m+1,n) - \alpha_3\, I(m,n+1) - \alpha_4\, I(m+1,n+1)\Big].$$

$$s_6 = \Big[(1-\alpha_1)I(m,n) - \alpha_2\, I(m,n+1) - \alpha_3\, I(m-1,n) - \alpha_4\, I(m-1,n+1)\Big].$$

$$s_7 = \Big[(1-\alpha_1)I(m,n) - \alpha_2\, I(m-1,n) - \alpha_3\, I(m,n-1) - \alpha_4\, I(m-1,n-1)\Big].$$

$$s_8 = \Big[(1-\alpha_1)I(m,n) - \alpha_2\, I(m+1,n) - \alpha_3\, I(m,n-1) - \alpha_4\, I(m+1,n-1)\Big].$$

Using the same procedure, the second transfer image of the fractal, $f_{(m,n)}^{(\Delta_3 r)}$, for a 3-unit circular neighborhood $(\Delta_3 r)$ is generated. Again, the intensity values of the pixels which do not fall on grid points are interpolated using the weighting coefficients α_1, α_2, α_3, and α_4. Then, $f_{(m,n)}^{(\Delta_3 r)}$, is given by

$$f_{(i,j)}^{(\Delta_3 r)} = \sum_{\Omega_1} |h(i,j) - h(m,n)| + \sum_{\Omega_2} |h(i,j) - h(m,n)| \ , \tag{5.12}$$

where Ω_1 represents the set of pixels such that
$\Omega_1 = \{(m,n) \mid \text{2-unit pixel} < \sqrt{(m,i)^2 + (n,j)^2} \leq \text{3-unit pixel}\}$. The set Ω_2 is one set of points which does not fall on the grid points.

Stage Three: Calculation of $<\Delta I_{\Delta_i,r}>$

In stage three, the $<\Delta I_{\Delta_i,r}>$ are calculated.

$$<\Delta I_{\Delta_1,r}> \;=\; <TIF(\Delta_1)> \;=\; \frac{1}{M} \sum_{(m,n \in M \times n)} f^{(\Delta_1,r)}_{(m,n)} \tag{5.13}$$

and

$$<\Delta I_{\Delta_3,r}> \;=\; <TIF(\Delta_3)> \;=\; \frac{1}{M} \sum_{(m,n \in M \times n)} f^{(\Delta_3,r)}_{(m,n)} \tag{5.14}$$

Stage Four: Calculation of $p_j(\mathbf{v})$

In stage four, $<\Delta I_{\Delta_1,r}>$ and $<\Delta I_{\Delta_3,r}>$ are substituted into eq. (5.7) to calculate for the $p_j(\mathbf{v})$.

In this research, we limited our study to considering the difference between the two means $<\Delta I_{\Delta_1,r}>$ and $<\Delta I_{\Delta_3,r}>$. This technique can be extended to other unit distances by creating several transfer images of the fractal. In each case, the intensity values of the pixels that do not fall on grid points can be estimated by interpolation.

5.4 Spatio-temporal Characteristics of Smoke

Experimental results are presented in this section. We relate the fractal parameters to the transient nature of a pollutant first by exploiting the spatio-temporal characteristics of smoke particles and second by relating the nominal velocity of the smoke to the fractal parameters. Finally, some interpretations and discussions of the findings are reported.

5.4.1 The Experiments

The goal of these experiments was to better understand the bahavior and the variability of the computed fractal parameters with respect to time and their dependence on window size and location. The experiments were performed using three different side view image sequences (Huber and Arya, 1985). Each sequence has 200 frames, a spatial resolution of 120 x 350, and each pixel is quantized to 8 bits. The experiments were first run for the two windows shown in figure 5.4. We chose two windows, one horizontal and one vertical, because of the non-isotropic nature of the data. The horizontal fractal parameter was computed using a window of size 15x240. This window is a horizontal section across the image frame. The vertical fractal parameter was computed using a window of size 100x15 pixels. This window is a vertical section across the image frame. The background, the region without smoke, was not permitted in the horizontal and vertical windows since our objective was to analyze the smoke.

Values of the horizontal and the vertical dynamical fractal parameters were computed for a each frame (from frame 1 to frame 200) of the image sequence using equation (5.7). Figures 5.5-5.7 show the temporal variability of the vertical fractal parameter for sequences of smoke whose velocity was one, two, and four meters per second, respectively. These curves were used as a smoke descriptor. The curves were plotted as a function of time (frame number). For comparison purposes, figure 5.8 displays all three curves. As can be seen in figure 5.5, the dimensionless vertical fractal parameter fluctuates between (0.862501) and (0.727101), in figure 5.6, between (0.855822) and (0.753397), whereas in figure 5.7, it is located between (0.887980) and (0.810155). A temporal oscillation in the flow can be seen in the figures. Even though the temporal variability is complicated, it displays a near-cyclic nature. These fluctuations of almost similar magnitude reflect the fluctuations of similar magnitude that have been observed in the near wake of the model building.

Similarly, figures 5.9-5.11 show the temporal variability of the horizontal fractal parameter for sequences of smoke whose velocity was one, two, and four meters per second respectively. As can be noticed, the curves in figures 5.9-5.11 display larger fluctuations than those in figures 5.5-5.7. In figure 5.9, the dimensionless horizontal fractal parameter swings between (0.963429) and (0.617555), in figure 5.10, between (1.017728) and (0.651562) and in figure 5.11, between

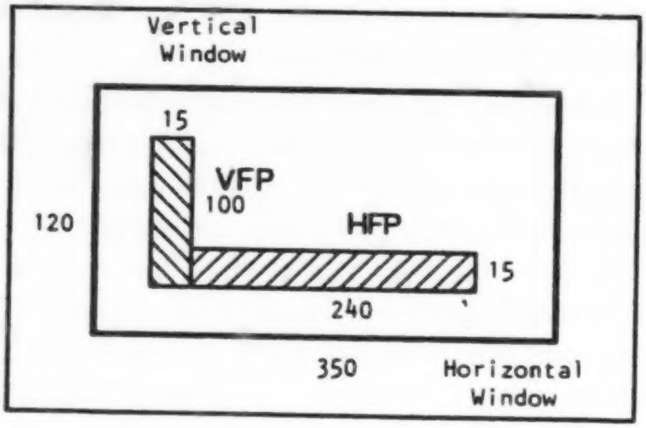
Vertical
Window
15
VFP
100
120
HFP
15
240
350
Horizontal
Window

Figure 5.4 Position, size and orientation of the two spatial windows that are used to calculate the horizontal and vertical fractal parameters. The horizontal window is 15 rows by 240 columns and the vertical window is 100 rows by 15 column.

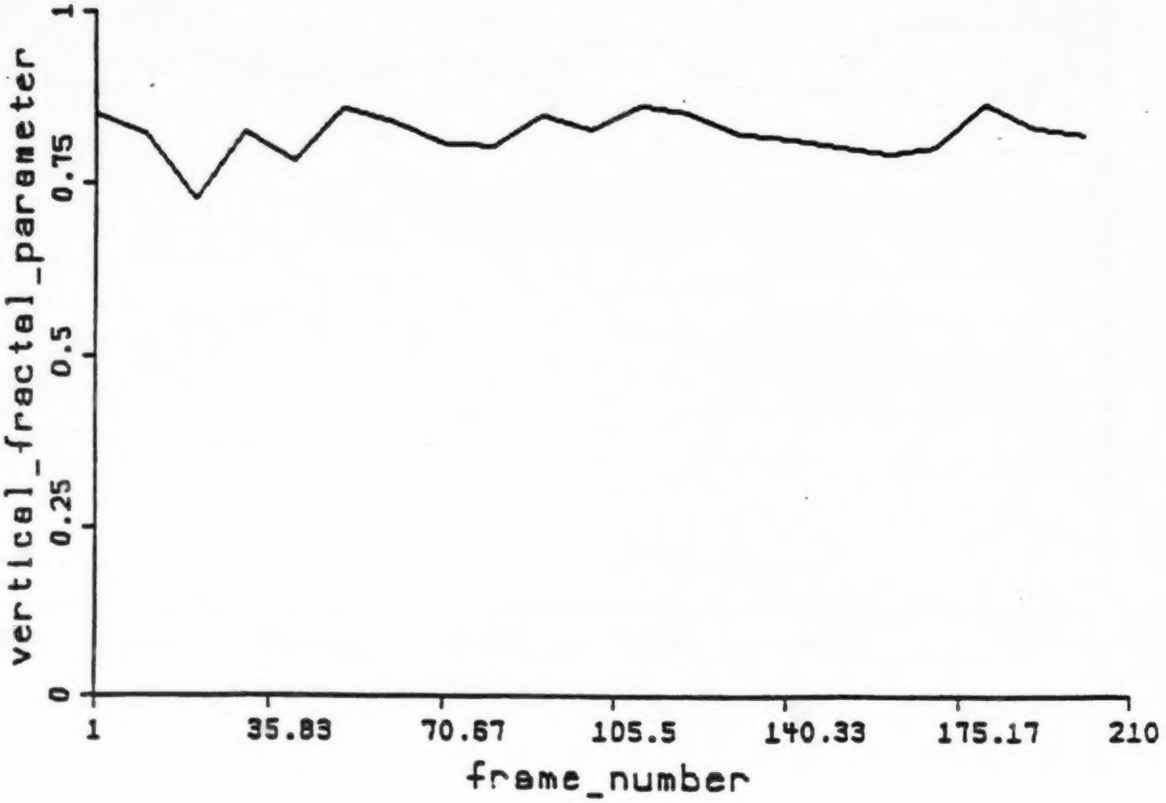

Figure 5.5 Vertical fractal parameter versus frame number (time) freestream wind speed of 1 m/s.

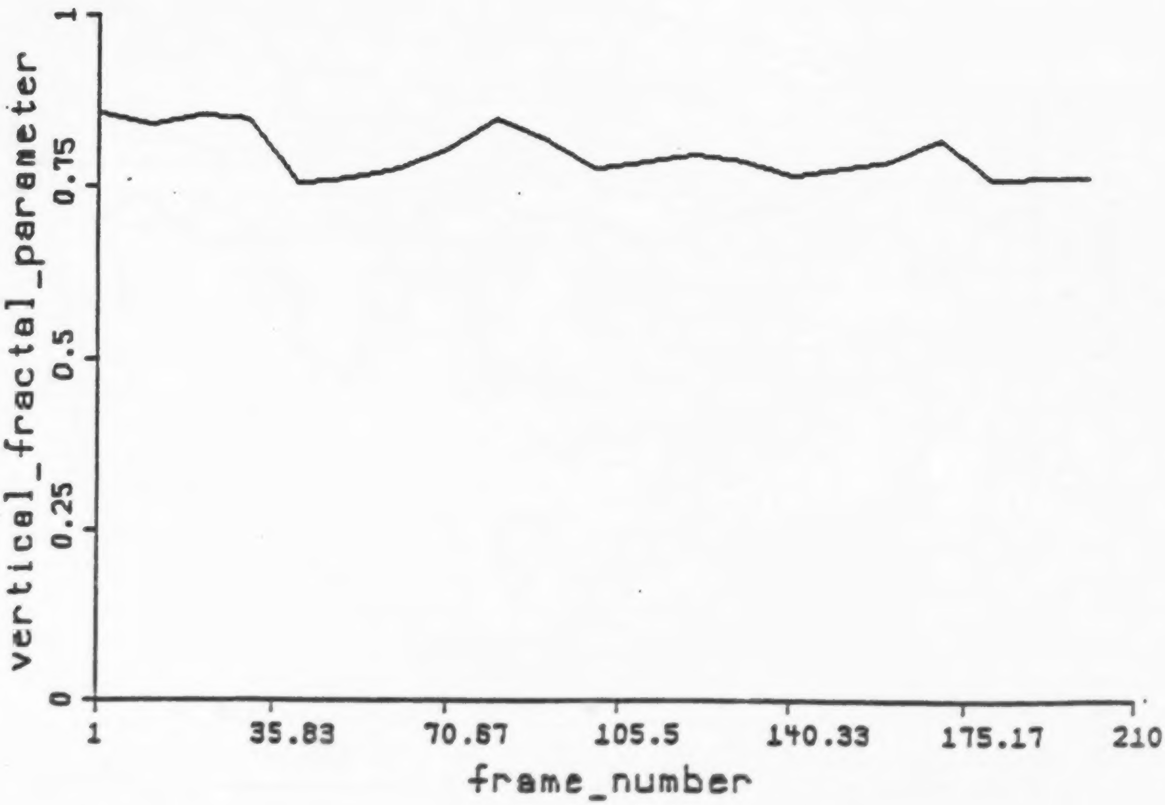

Figure 5.6 Vertical fractal parameter versus frame number (time) freestream wind speed of 2 m/s.

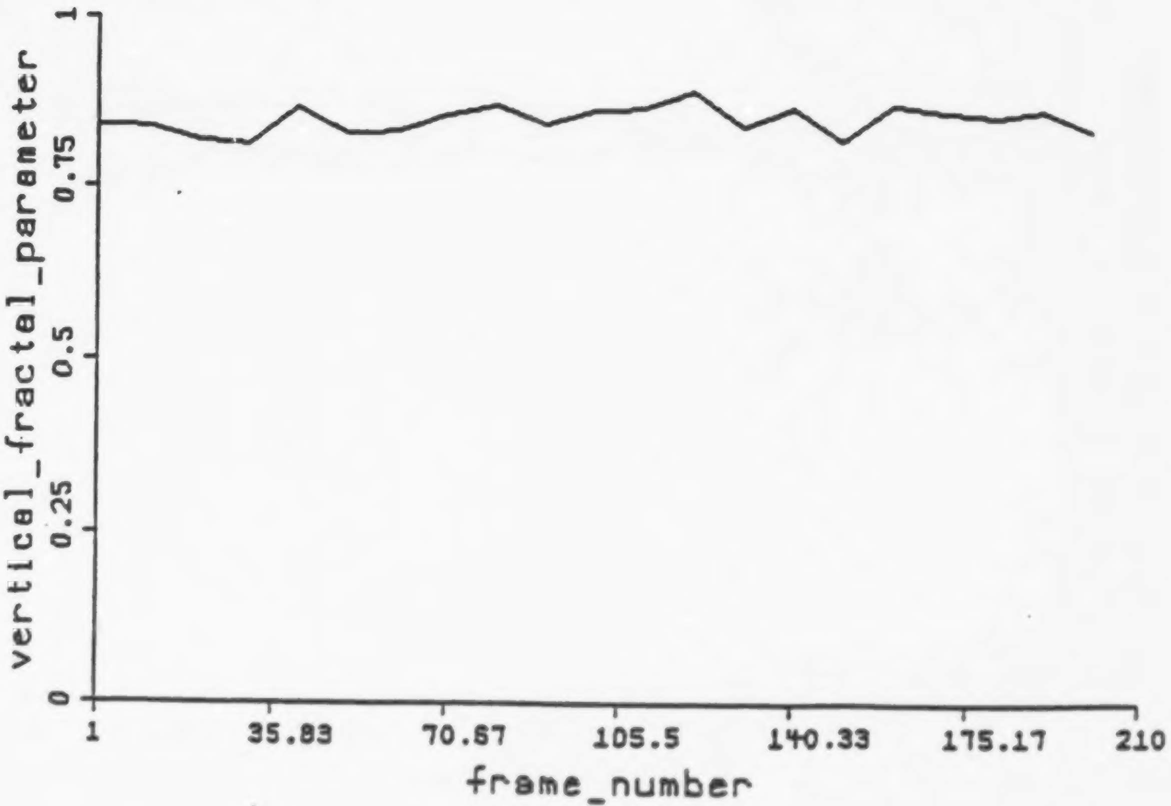

Figure 5.7 Vertical fractal parameter versus frame number (time) freestream wind speed of 4 m/s.

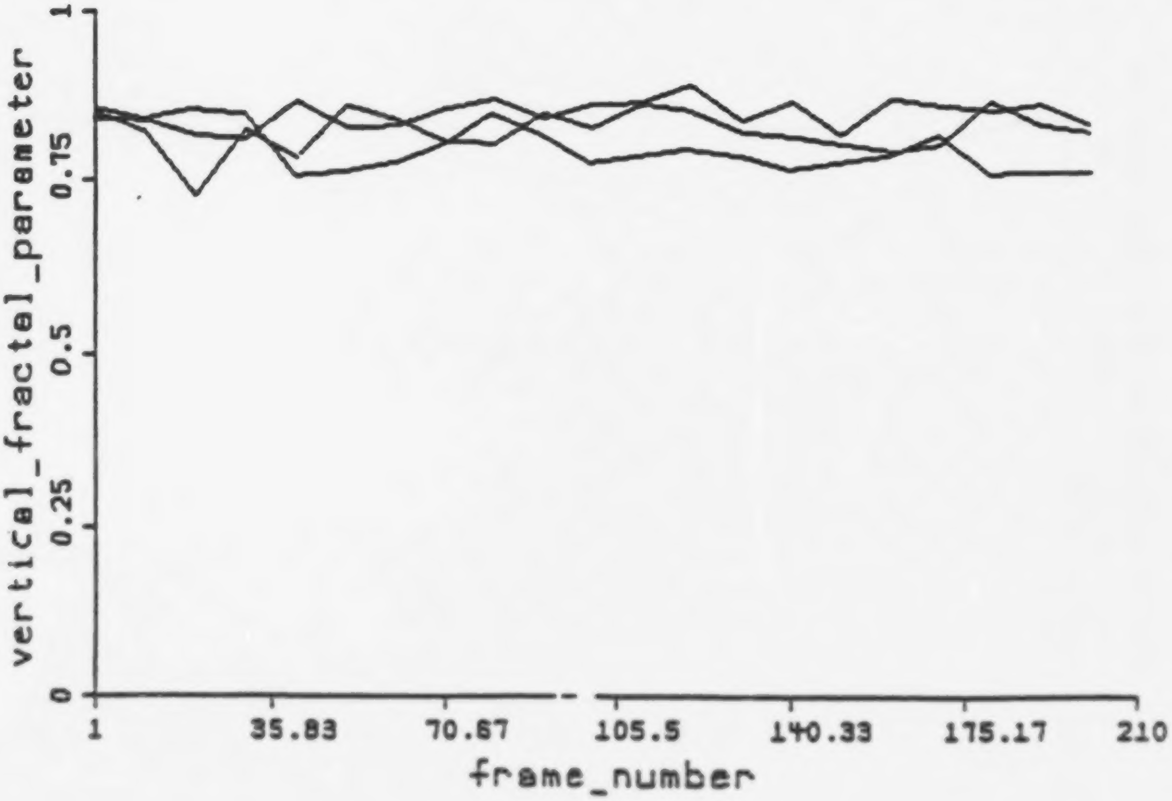

Figure 5.8 Vertical fractal parameter versus frame number (time) overlay of the three freestream wind speeds of (1 m/s, 2 m/s, 4 m/s).

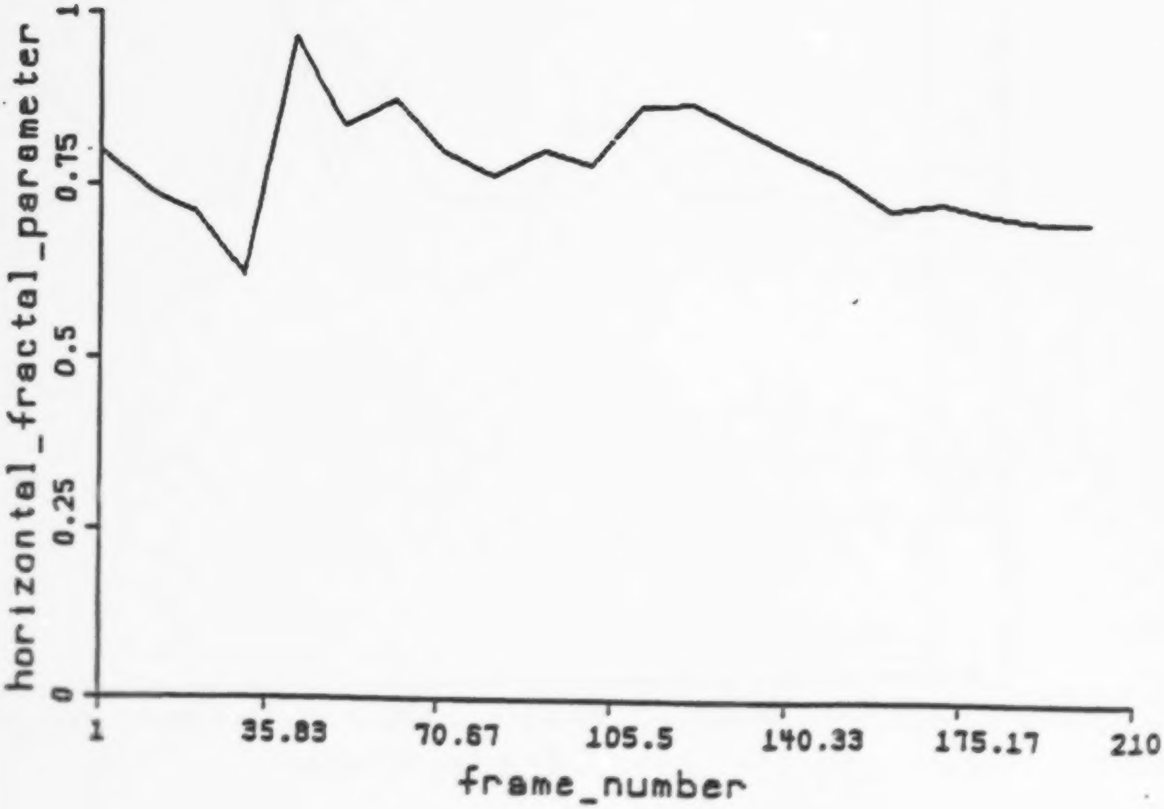

Figure 5.9 Iorizontal fractal parameter versus frame number (time) reestream wind speed of 1 m/s.

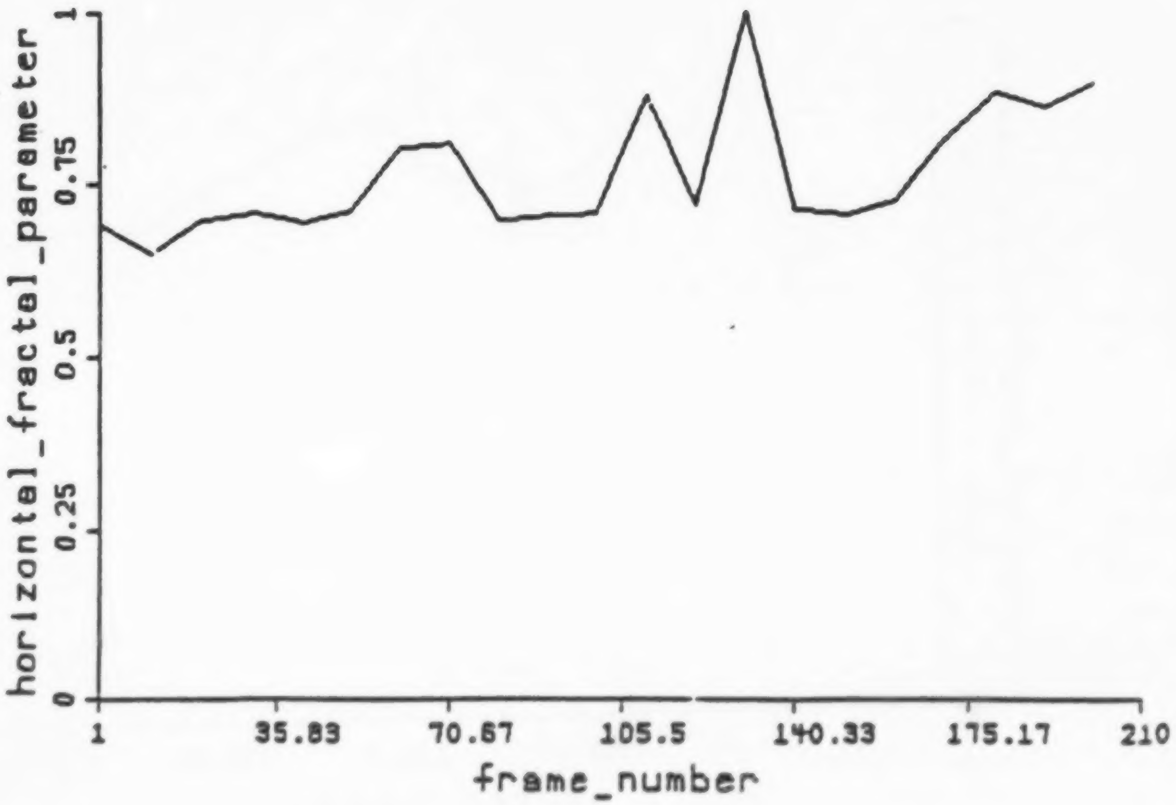

Figure 5.10 Horizontal fractal parameter versus frame number (time) freestream wind speed of 2 m/s.

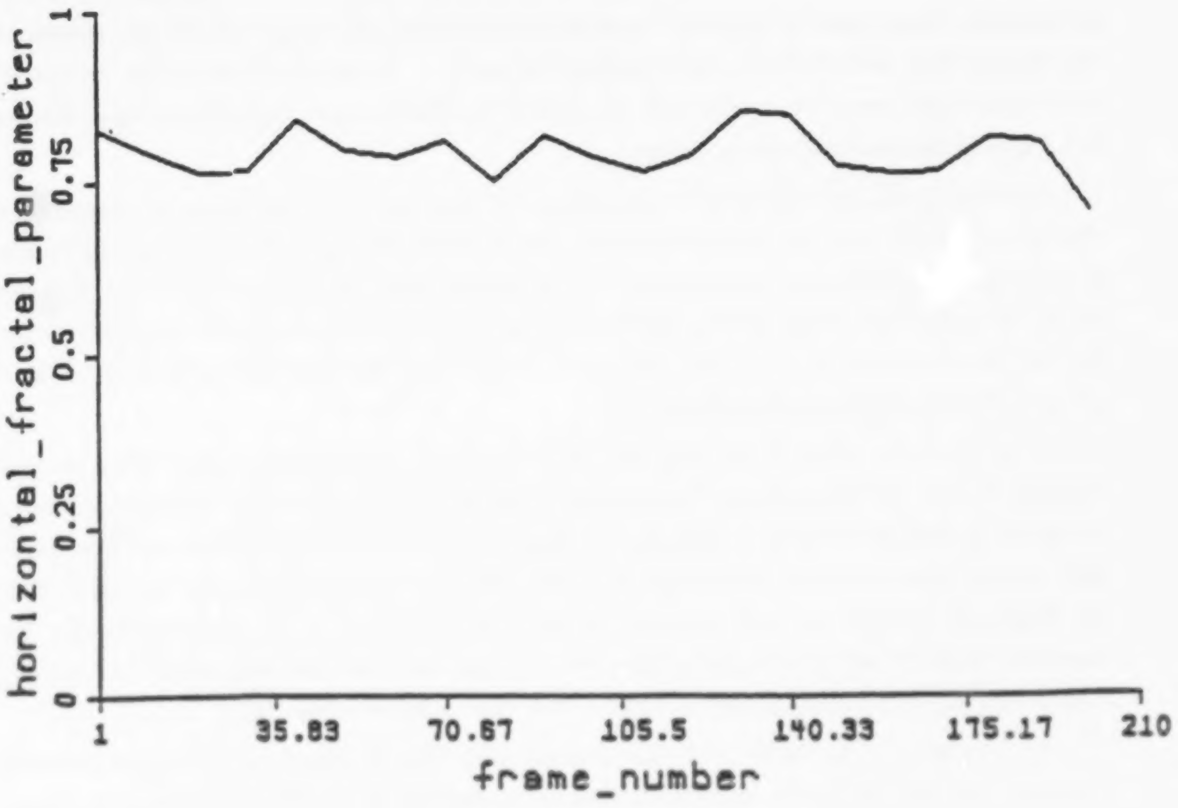

Figure 5.11 Horizontal fractal parameter versus frame number (time) freestream wind speed of 4 m/s.

(0.848785) and (0.706663). Hence, for any chosen frame (time) it is interesting to note a fundamental difference between the dimensionless horizontal and vertical fractal parameters. This can be explained by the anisotropic characteristics of the pollutant. Figure 5.12 displays the three curves of the horizontal fractal parameter for different velocities. As can be seen, a clear difference exists from one velocity set-up to another. As before, the temporal oscillation of the dimensionless horizontal fractal parameter is nearly-cyclic. However, the fluctuations do not always show approximate repetitions of a single shorter cycle; they do not exhibit movements of any known, fixed periodicity (in the mathematical sense). The lengths of the cycles, as well as their amplitudes, may vary considerably as opposed to periodic movements displaying a definite recurrence of fluctuations in given periods.

Additional tests were performed in an attempt to understand how the fractal parameters are affected by window size and window location. The windows were also selected to determine the actual spatial and temporal characteristics of the smoke particles and to confirm the multiple scaling of turbulence. These results appear to be significant not only to the smoke investigators but also to other researchers in geophysics, meteorology, and medicine. The disposition of these different windows is illustrated in figure 5.13.

A large window of 90 × 230 was selected at the center of the entire picture whose spatial dimensions were 120 ×350 pixels. This technique was employed for the three different sequences. Values of the fractal parameters were again computed for 21 frames each (from frame 1 to frame 200) of each image sequence utilising eq. (5.7). The time interval between frames was again 0.33 sec. Figures 5.14, 5.15, and 5.16 illustrate the temporal variability of the fractal parameter for sequences of smoke particles whose nominal velocity was one, two, and four meters per second, respectively. For comparison purposes, figure 5.17 shows the three curves.

As can be seen in figure 5.14, the dimensionless fractal parameter fluctuates between (1.064992) and (0.724770), in figure 5.15, between (1.052762) and (0.707913), whereas in figure 5.16, it is estimated between (1.082521) and (0.931597). As discussed for previous figues, the temporal oscillation of the flow is plainly shown. Again, the near cyclic nature can be observed from figures 5.14 and figure 5.15. Nevertheless, figure 5.16 shows an almost fuzzy straight line at the beginning and then starts to vary with very small fluctuations. This is not surprising since we have chosen a large window in the center of each frame. The window, in fact, includes a large portion of the background, that is regions which do not contain smoke particles. This violates the assumption that the background is not included in the window.

The same technique was used to analyse of smoke data with a reduced size of window. The size of these "middle range" window is 60 × 110. Figures 5.18, 5.19, and 5.20 show the temporal variability of the fractal parameter for sequences of smoke whose nominal velocity was one, two,

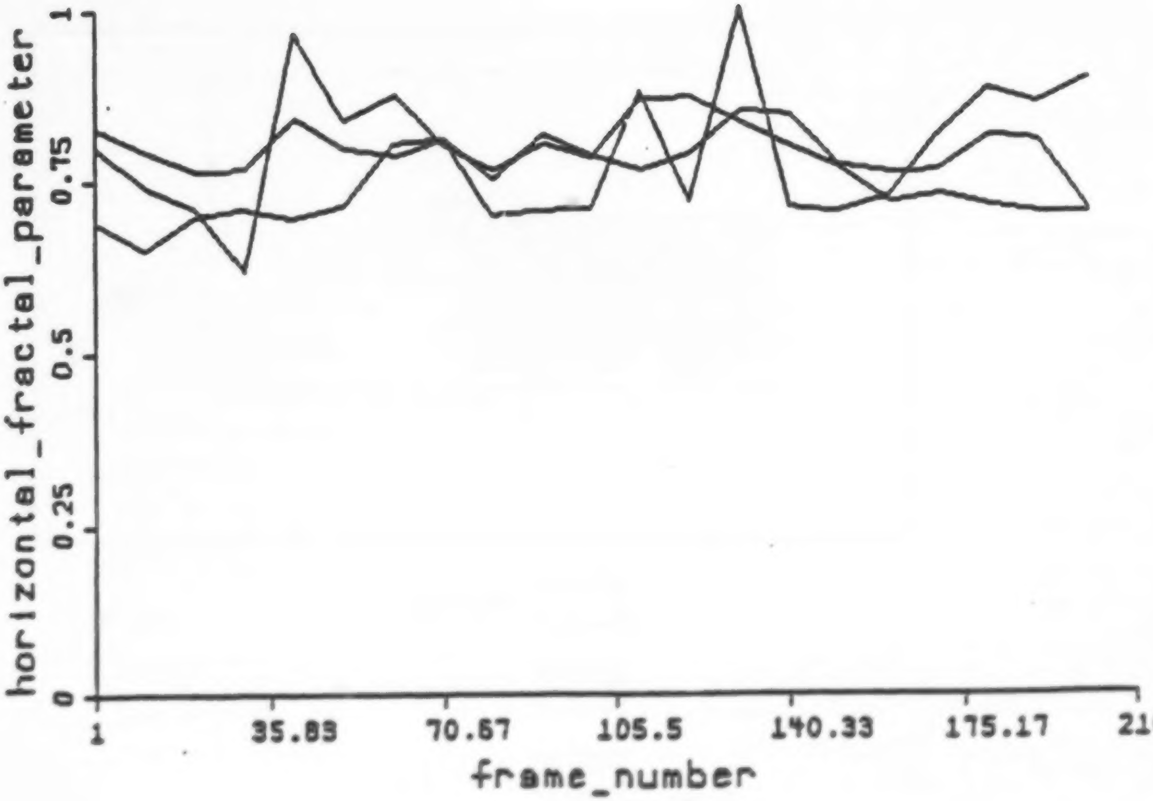

Figure 5.12 Horizontal fractal parameter versus frame number (time) overlay of the three freestream wind speeds of (1 m/s, 2 m/s, 4 m/s).

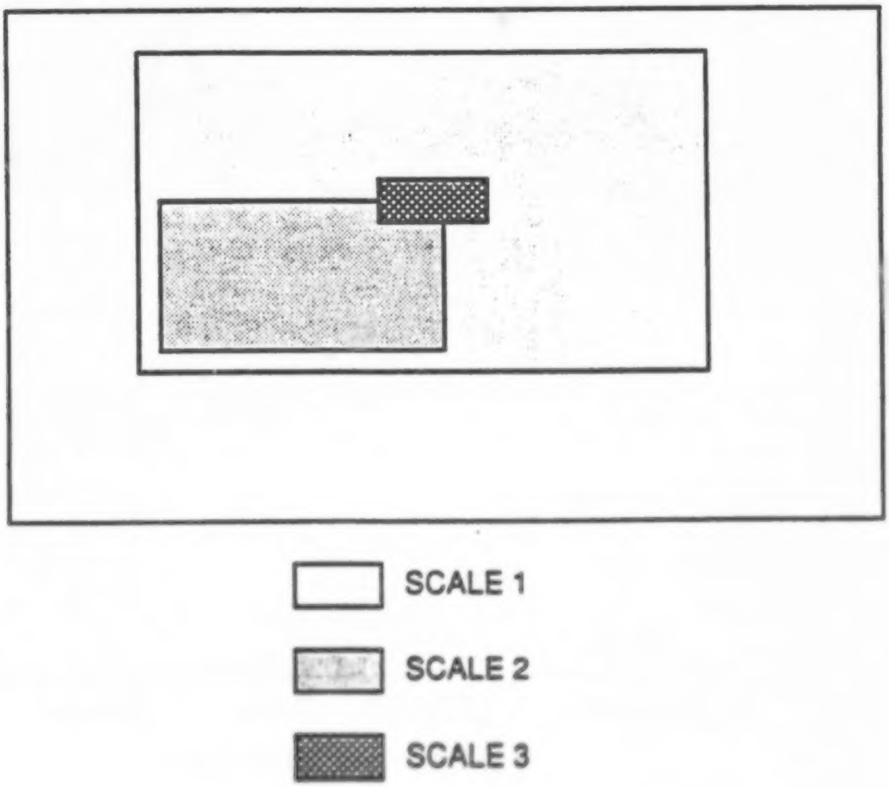
▭ SCALE 1
▨ SCALE 2
▩ SCALE 3

Figure 5.13 Disposition of the large, middle and small size windows. (scale 1, scale 2, scale 3, respectively).

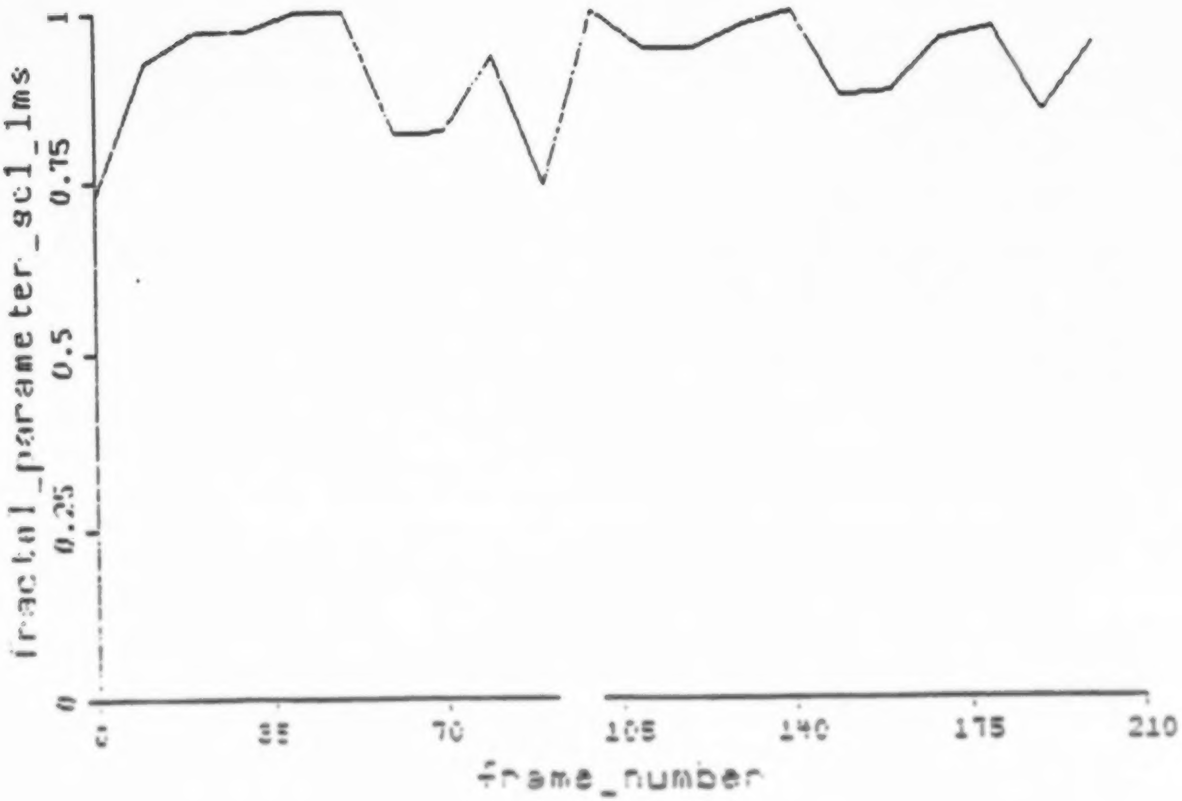

Figure 5.14 Fractal parameter versus frame number (time). scale 1. freestream wind speed of 1 m/s.

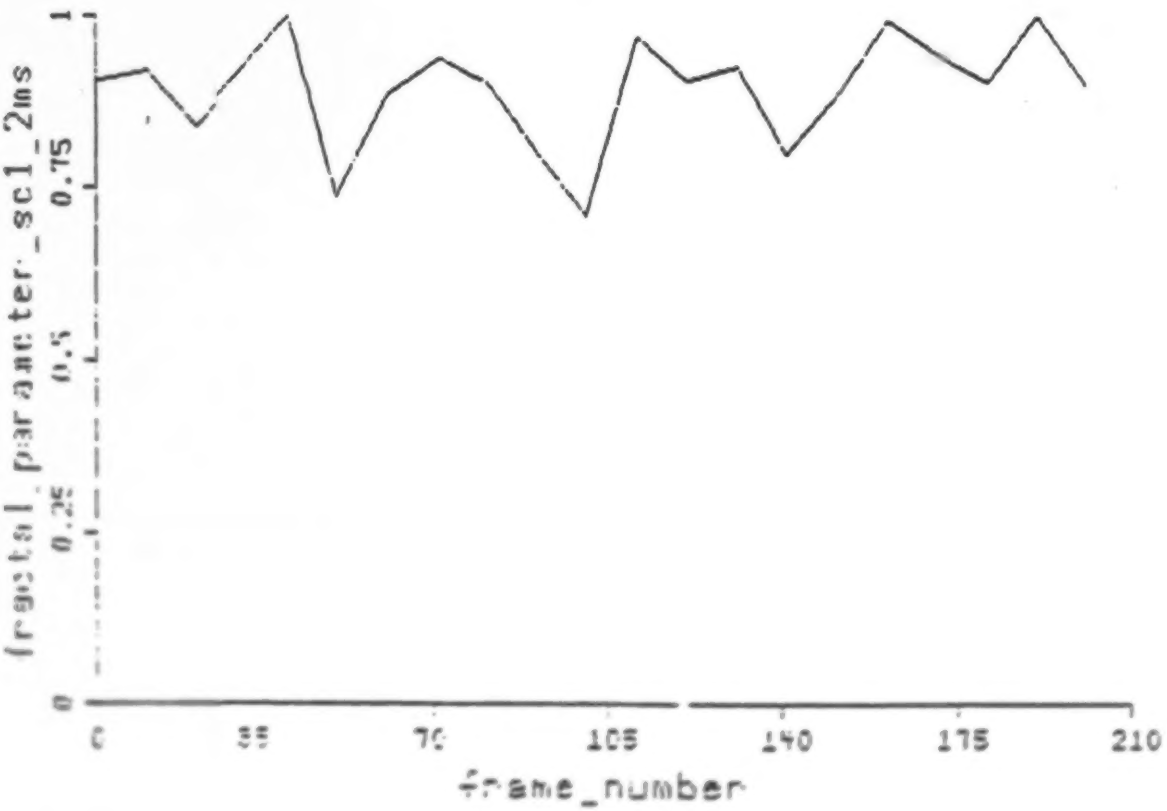

Figure 5.15 ractal parameter versus frame number (time), scale 1. eestream wind speed of 2 m/s.

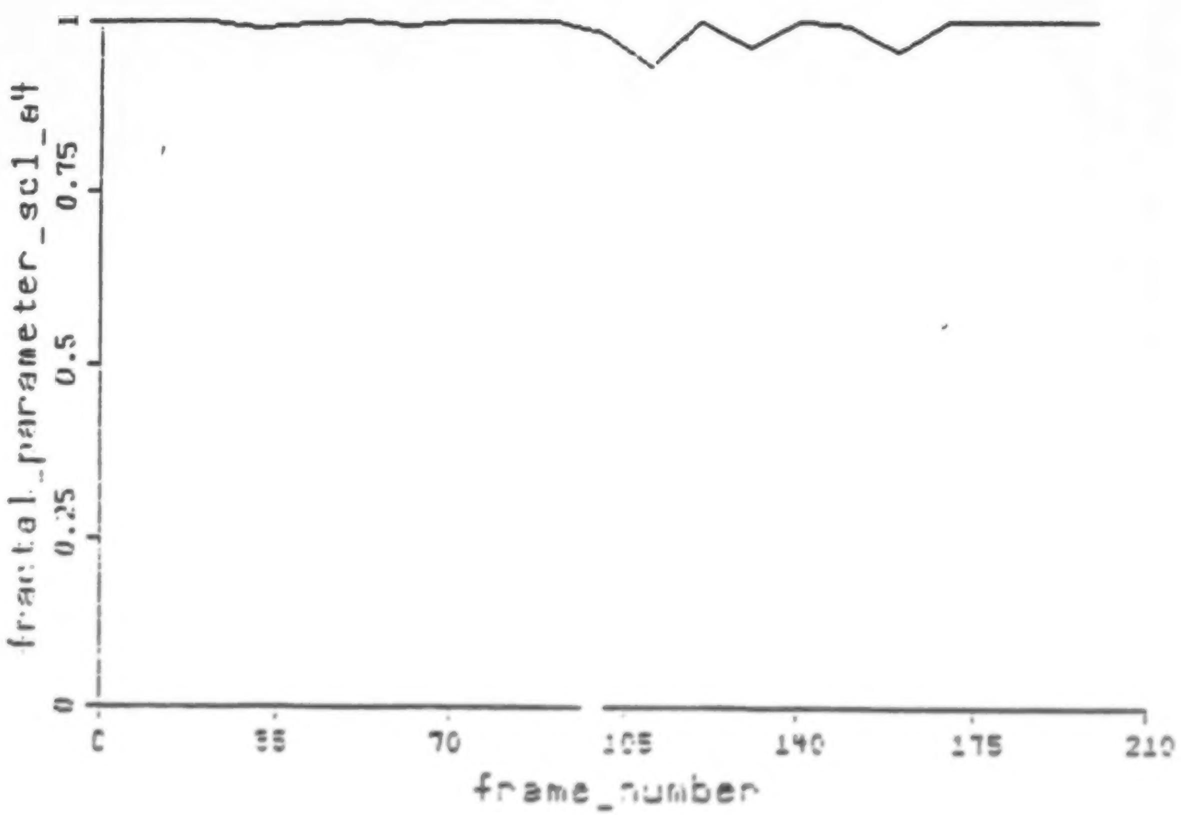

Figure 5.16 Fractal parameter versus frame number (time), scale 1, freestream wind speed of 4 m/s.

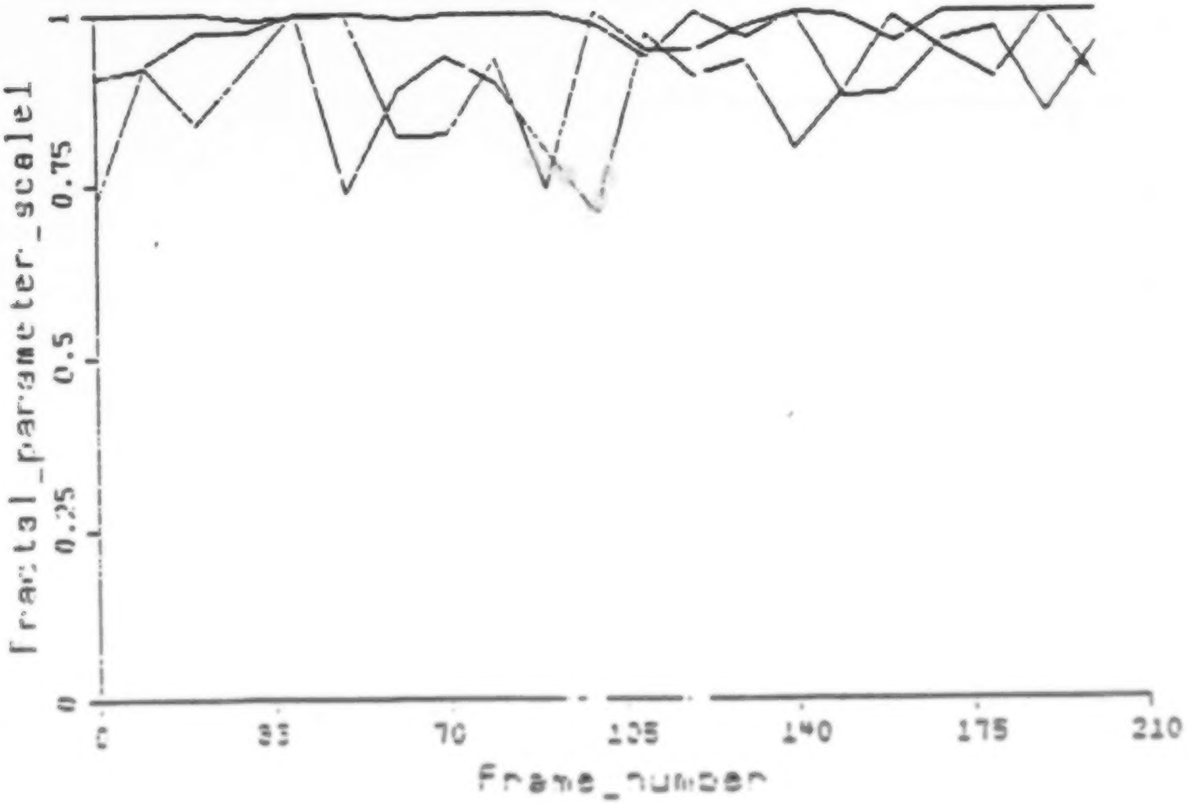

Figure 5.17 Fractal parameter versus frame number (time), scale 1, overlay of the three freestream wind speeds (1 m/s, 2 m/s, 4 m/s).

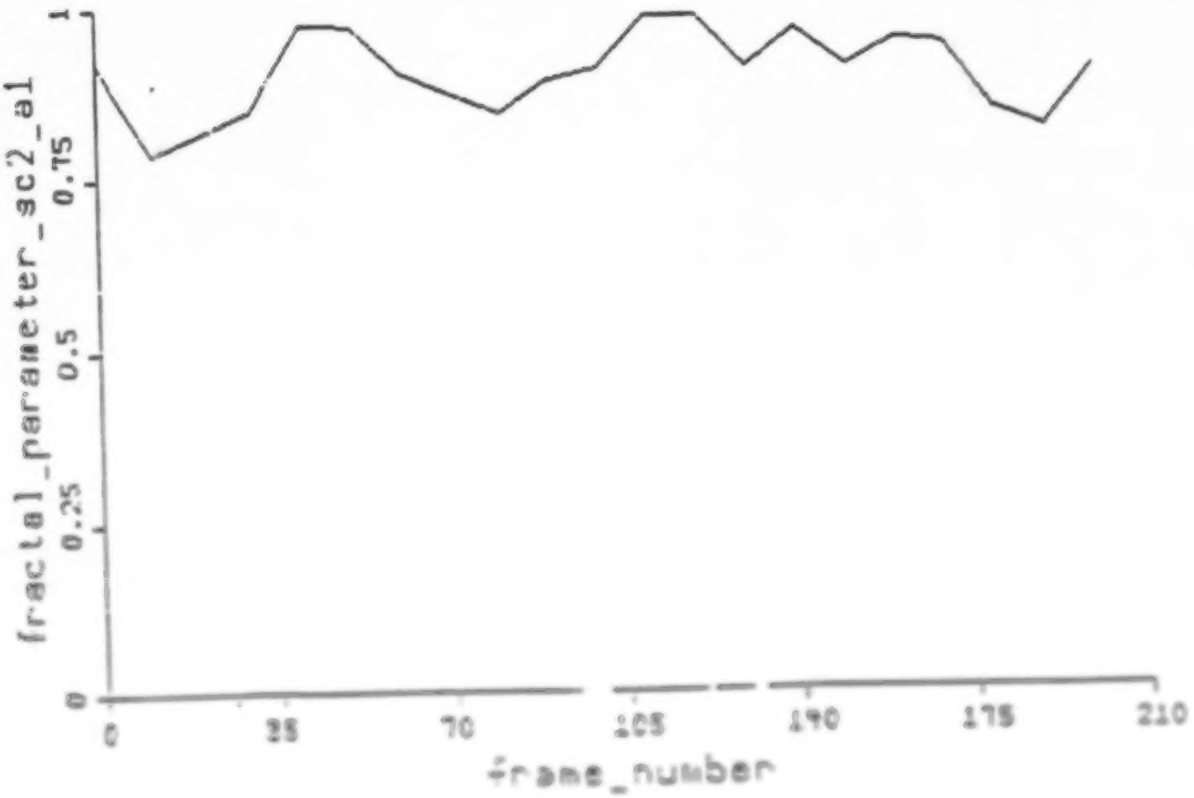

Figure 5.18 Fractal parameter versus frame number (time), scale 2, freestream wind speed of 1 m/s.

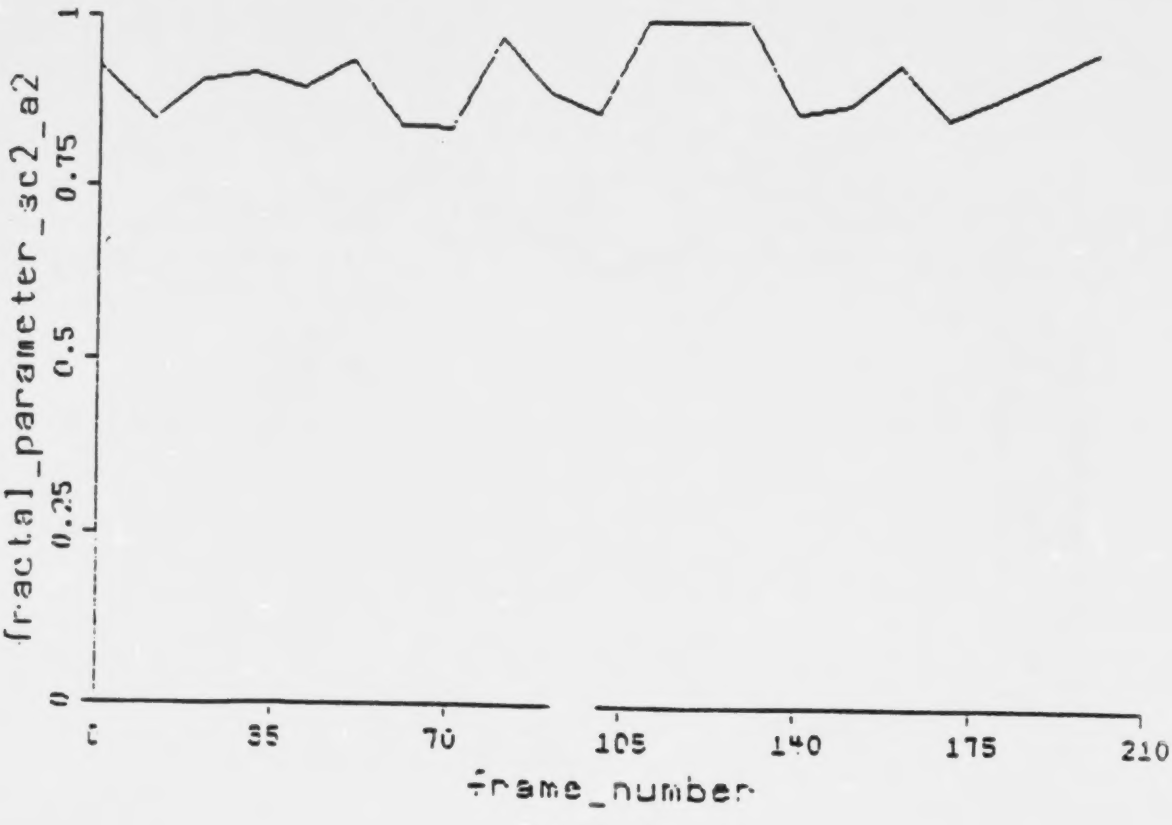

Figure 5.19 Fractal parameter versus frame number (time), scale 2, freestream wind speed of 2 m/s.

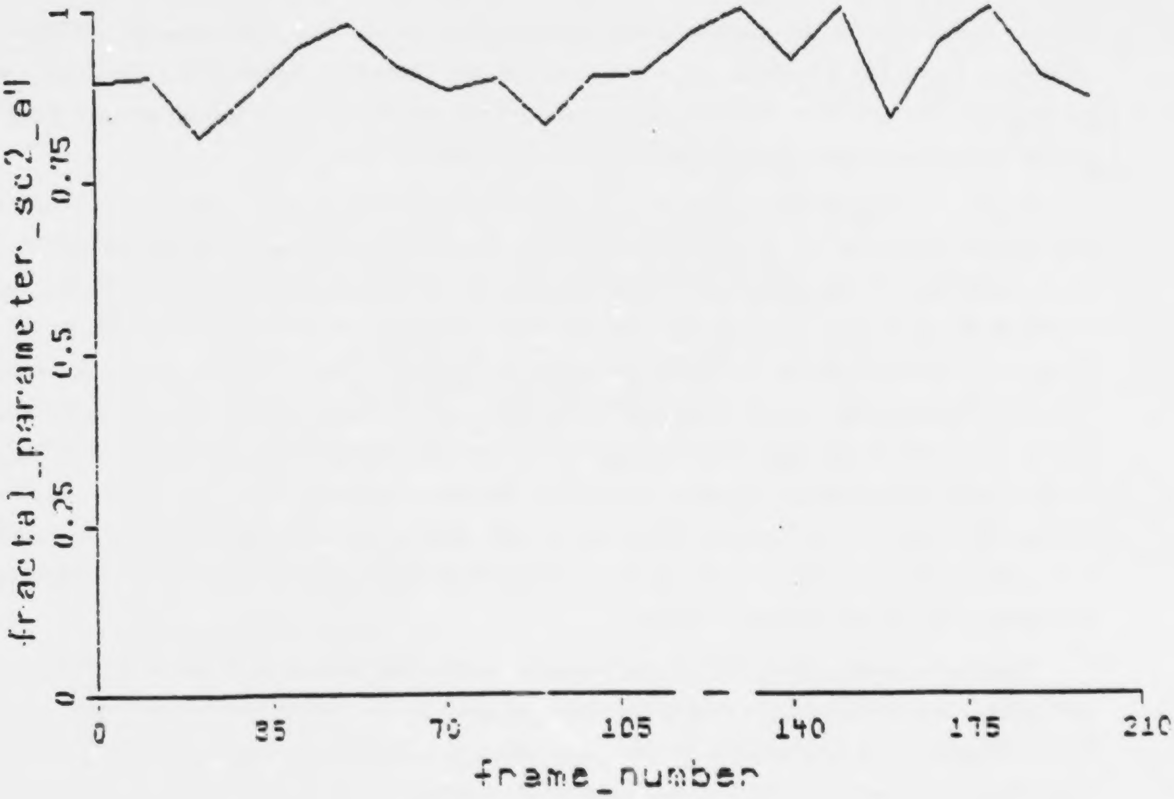

Figure 5.20 Fractal parameter versus frame number (time), scale 2, freestream wind speed of 4 m/s.

and four meters per second, respectively. Again figure 5.21 illustrates the three curves for comparison purposes. As can be seen from these figures, the smoke behaves in an almost similar fashion. In figure 5.18, the dimensionless fractal parameter varies between (0.981817) and (0.785444), in figure 5.19, between (1.035891) and (0.837033), whereas in figure 5.20, it fluctuates between (1.015673) and (0.812122). The oscillations behave in a similar manner but with a slight reduction in the dynamic range of the amplitudes as compared to the large-sized window. However, an exception must be mentioned for the case where smoke data were taken at a nominal velocity of 4m/s. The differences between figure 5.16 and figure 5.20 (taken at the same nominal velocity but with different window sizes) resulted from the fact that in the latter case, background was not included inside the medium range windows.

Finally, we studied the smoke data using smaller windows. These "small range" windows had spatial dimensions of 15×50 pixels. Similarly, figures 5.22, 5.23, and 5.24 display the temporal variability of the fractal parameter for the three different sequences of smoke, that is, sequences of smoke data taken at one, two, and four meters per second respectively. Figure 5.25 displays the three curves of the fractal parameter for different nominal velocity set ups. In figure 5.22, the dimensionless fractal parameter varies little, and its values are in the vicinity of one. Similar observations and arguments may be used for figures 5.23 and 5.24. This is not surprising, because pixel intensities as discussed previously, express integrated counts of smoke particles through the field of view. Near the plume center, one expects that the largest pixel values result from large coherent patches of dense smoke. This produces small variations in gray-level resulting in almost equal fractal parameter values.

The above results tell us that if one examines smoke data, variability exists at all scales; in particular it is known that this variability continues down to the smaller field measurement scale. These variations are fundamental in that they reflect the internal processes controlling smoke. Furthermore, it leads us to believe that some of the analyses done on the images may be redundant. This is not surprising because if one observes smoke flow, one can see patches of a given shape that are geometrically similar when they can be obtained from one another by changing the spatial dimensions. Hence, it may suffice to fix one characteristic length to qualitatively specify the behavior of smoke particles. Although the quantitative features are somewhat sensitive to the window size but the qualitative features may be not. This in fact mirrors exactly the properties of fractal concepts. That is, qualitatively speaking, the fluctuations in a field that is "scaling" look the same despite the magnification. In other words, the large scale fluctuations are qualitatively similar to the middle scale fluctuations embedded within them. Those middle scale features are in turn the same as the still smaller fluctuations superimposed upon them.

A last attempt consists of choosing an appropriate subimage (window) and moving it on the

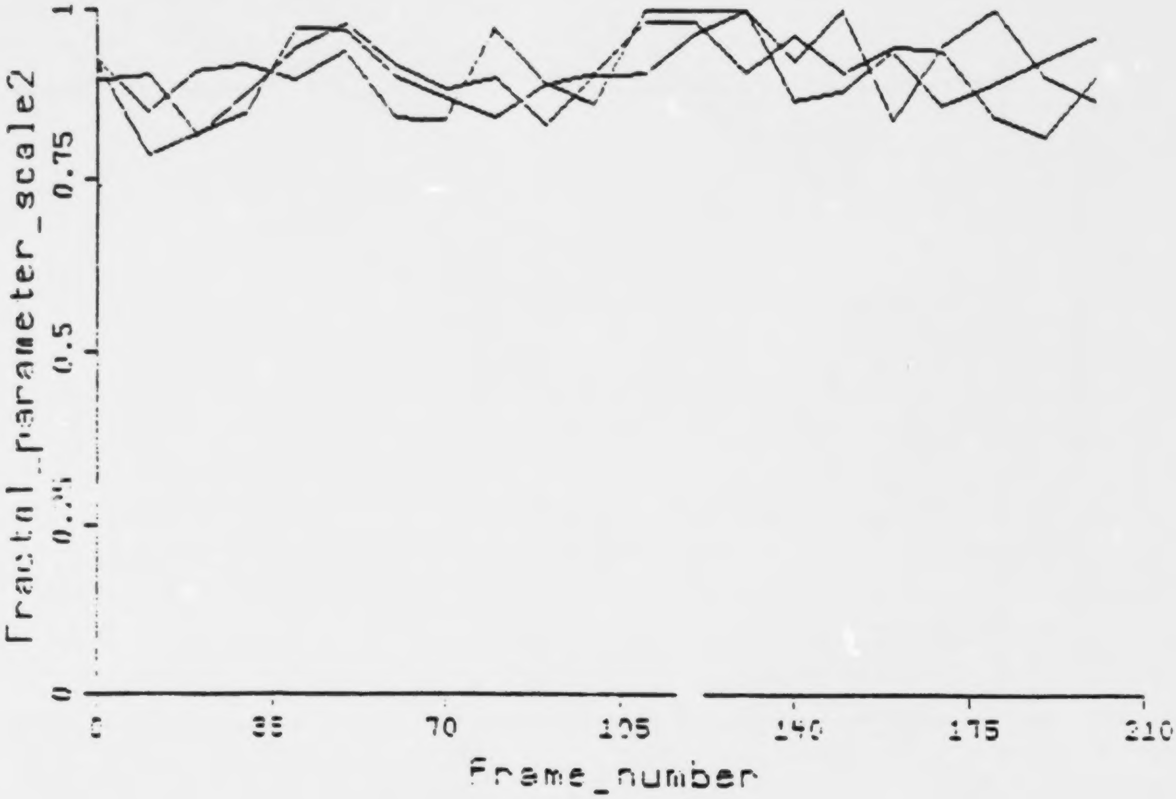

Figure 5.21 Fractal parameter versus frame number (time), scale 2, overlay of the three freestream wind speeds (1 m/s, 2 m/s, 4 m/s).

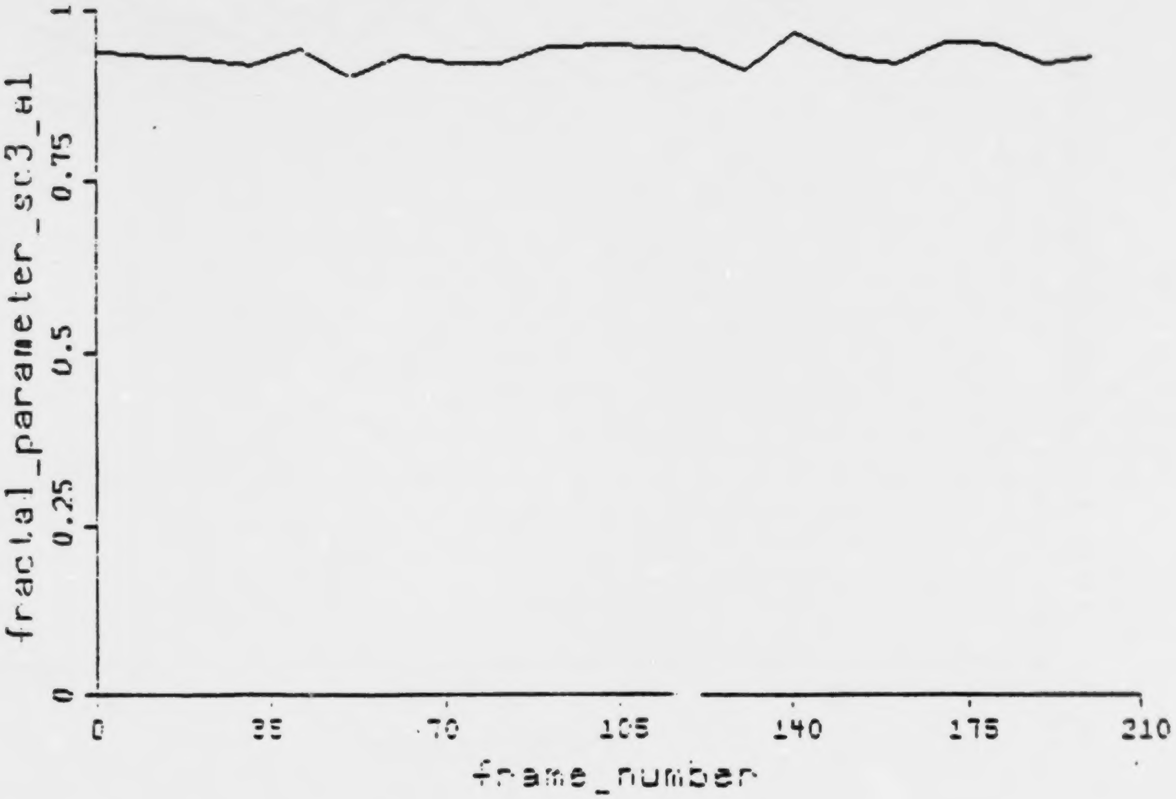

Figure 5.22 Fractal parameter versus frame number (time), scale 3, freestream wind speed of 1 m/s.

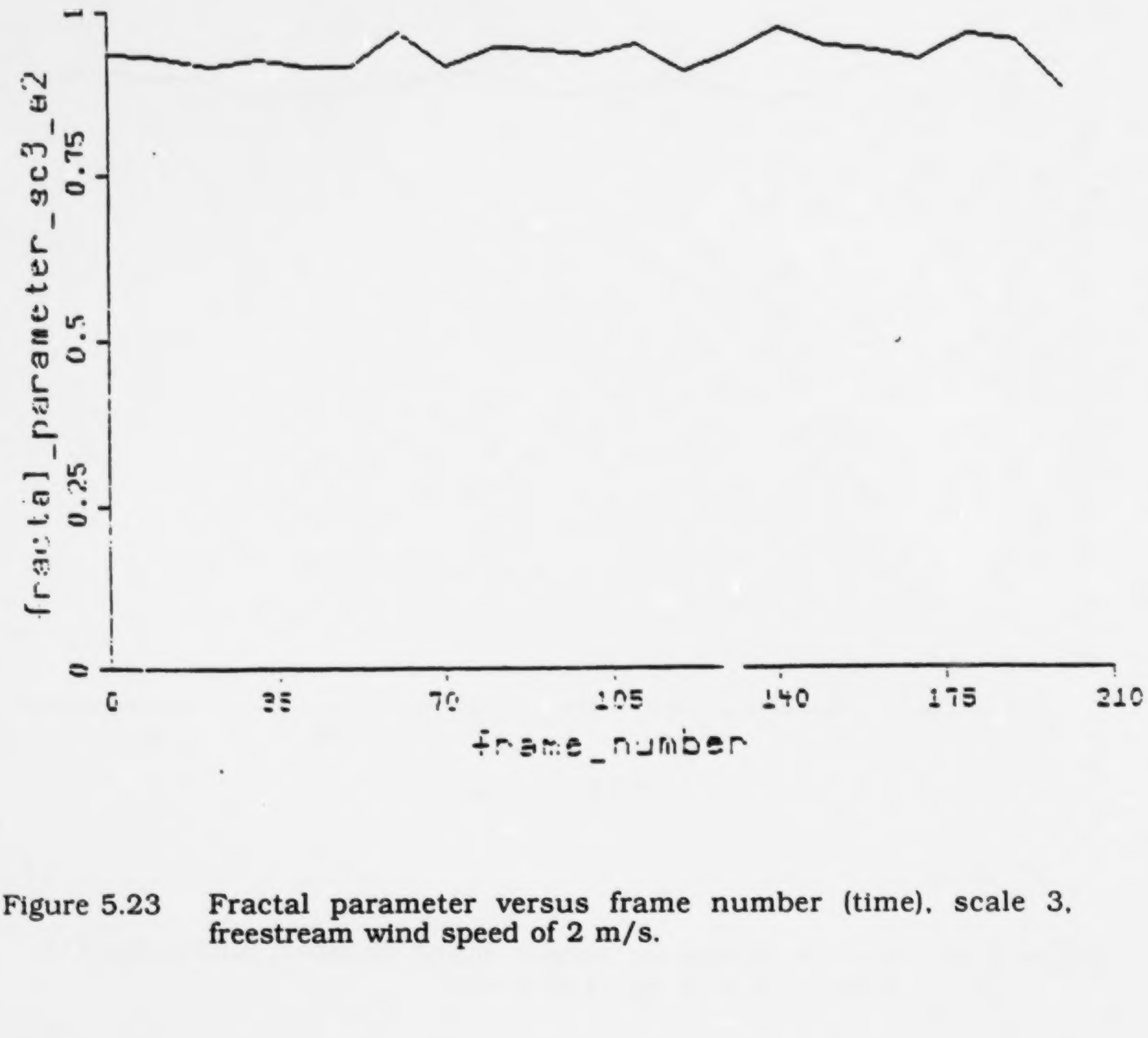

Figure 5.23 Fractal parameter versus frame number (time), scale 3, freestream wind speed of 2 m/s.

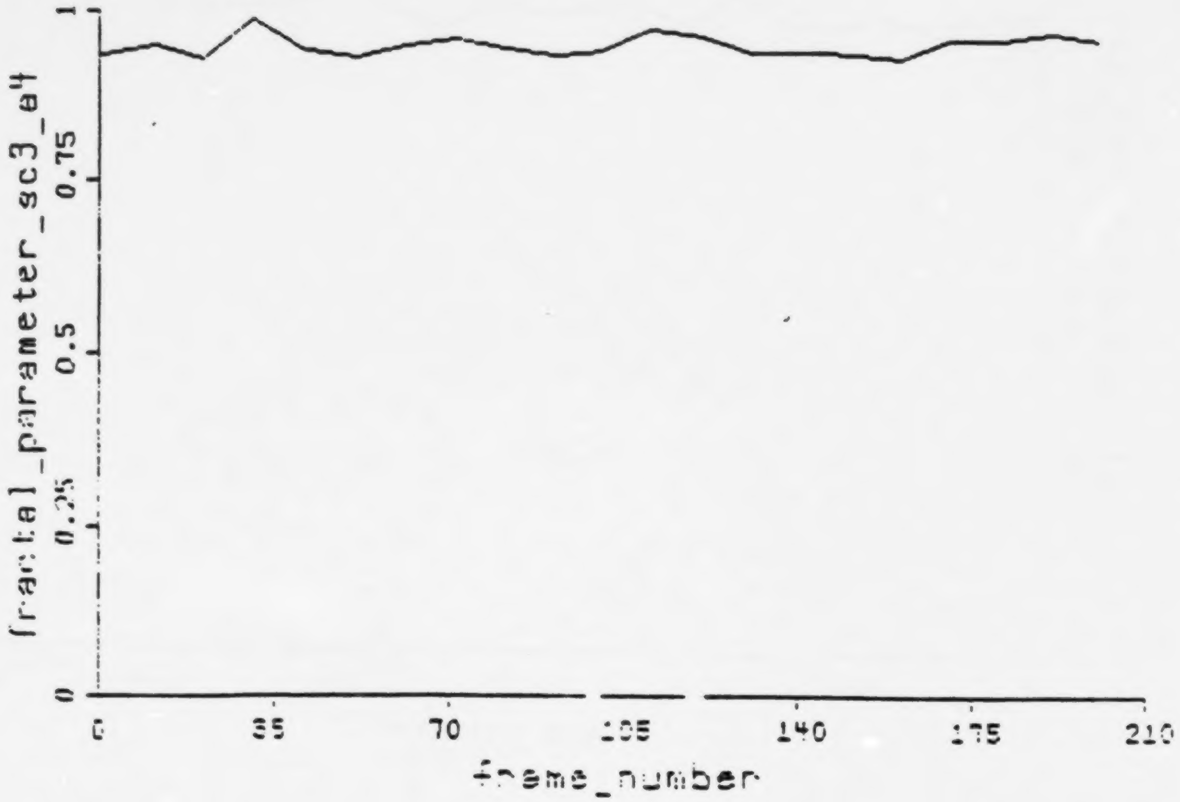

Figure 5.24 Fractal parameter versus frame number (time), scale 3, freestream wind speed of 4 m/s.

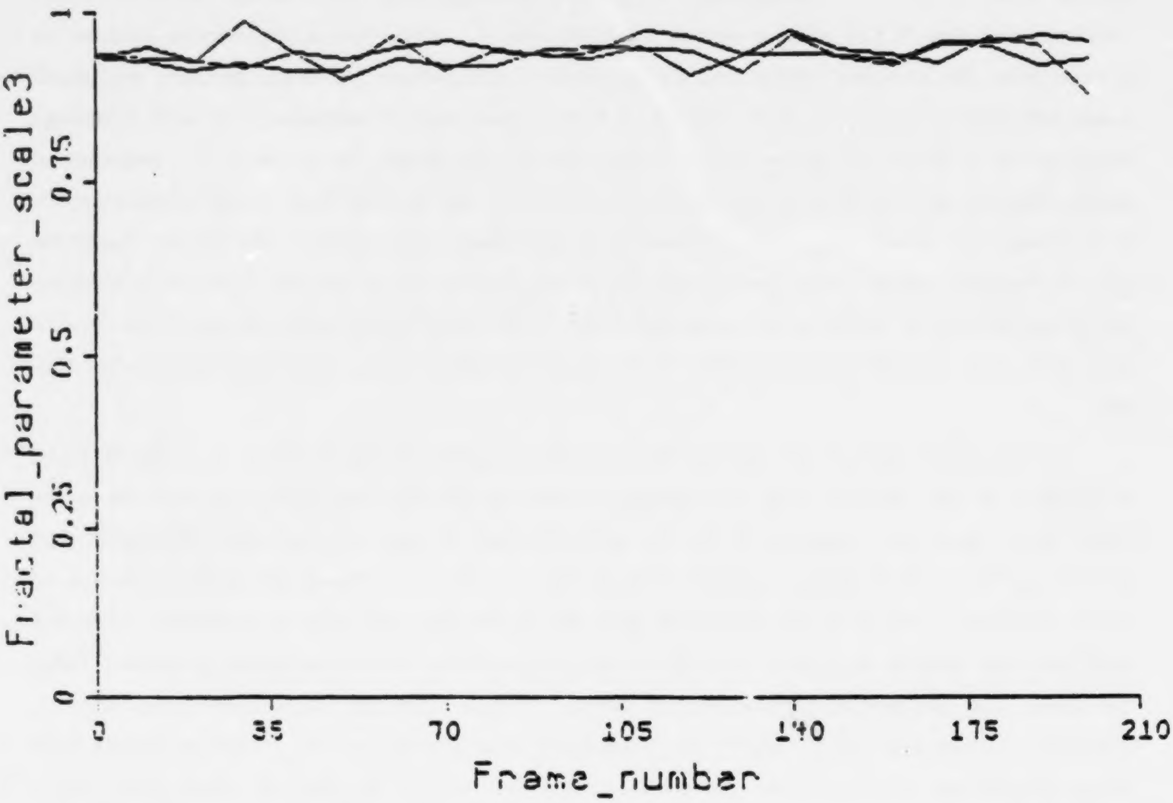

Figure 5.25 Fractal parameter versus frame number (time), scale 3, overlay of the three freestream wind speeds (1 m/s, 2 m/s, 4 m/s).

spatial and temporal locations of smoke images. As discussed earlier, we wish to relate the dynamical fractal parameter to the concentration of smoke. The technique is again used for a typical frame of a sequence of smoke data taken at a freestream wind speed of one meter per second. First, a picture is divided into 21 (3×7) subimages with 0% overlap. Each subimage (window) contains 40×50 picture elements. The choice of the window is appropriate because we learned from the previous results that the qualitative fluctuations for large, medium, and small range windows (cf. figure 5.13) are similar. A fractal parameter is computed over each subimage using eq. (5.7). Table 5.1 shows the computed fractal parameters for a frame of a sequence of smoke data whose velocity was one meter per second. As can be seen from the set of parameters, it is not easy to obtain a complete understanding and relate these values to the smoke concentration. A few low values of the fractal parameters are located at the ground level, some medium values are located in between the upper and lower levels. Some other values appear to be close to each other even though they are separated by an important distance in the field plane (wind tunnel).

At the upper level of the picture, the fractal parameter fluctuates between (1.031197) and (0.786724), at the medium level it fluctuates between (0.997460) and (0.744282) whereas in the lower level (near the background of the wind tunnel) it oscillates between (0.890921) and (0.680110). From the previous analysis of the smoke data based on the large, medium, and small range windows (cf. figure 5.13), we learned that the qualitative fluctuations are similar. This fact indicates that further attempts using the whole picture would not be necessary. However, Table 5.1 shows that the fractal parameters are affected by the locations where there are computed. Similarly, Tables 5.2 and 5.3 show the computed fractal parameters for frames of smoke data whose freestream wind speed set ups were two and four meters per second, respectively. Same arguments and explanations may also be given to such results.

Next, we applied the same procedure but the frames were separated from the previous ones by a reasonable amount of time (1.66 sec). Note that this choice was not to compute the fractal parameters for each time but to understand how the computed values of the fractal parameters are affected by the time event. Therefore, this amount of time can be made short or long but still the values are changed. Tables 5.4, 5.5, and 5.6 show the computed fractal parameters for smoke image taken at freestream wind speeds of one, two, and four meters per second, respectively. As indicated in the previous analysis, the fractal parameters are always affected by the locations of their computed values either in space or in time. These variations are logical since as mentioned before, in a smoke plume there are at least two regions of different concentration that are distinguishable. One appears as haze on the outside edges of the plume and background is readily visible through it. The other constitutes the "main body" of the plume that from time to time contains "holes". These results also indicate that the velocity of the motion depends on the location

0.843354	0.786724	0.793549	1.031197	0.834878	0.852109	0.822097
0.889231	0.744282	0.997460	0.823986	0.856985	0.895521	0.885181
0.873503	0.680110	0.700828	0.867945	0.890921	0.842690	0.689607

Table 5.1 **Fractal parameters for each subimage in a typical frame time t, freestream wind speed of 1 m/s.**

0.781816	0.818754	0.836754	0.895241	0.803783	0.834996	0.790347
0.838411	0.792348	0.914231	0.873417	1.007961	0.906911	0.844161
0.807486	0.716240	0.696812	0.814416	0.920698	0.836422	0.724987

Table 5.2 Fractal parameters for each subimage in a typical frame time i, freestream wind speed of 2 m/s.

0.956931	0.872486	0.856986	0.874674	0.814139	0.894113	0.863041
0.899597	0.858217	0.896297	0.885981	0.896510	0.903176	0.926413
0.803450	0.757603	0.749851	0.793109	0.806897	0.836651	0.881154

Table 5.3 **Fractal parameters for each subimage in a typical frame time *t*, freestream wind speed of 4 m/s.**

0.831198	0.794330	0.776292	0.958621	0.810851	0.890331	0.802690
0.876321	0.763891	1.008914	0.799346	0.795846	0.913462	0.829633
0.889718	0.700935	0.756524	0.849924	0.900321	0.806470	0.714591

Table 5.4 Fractal parameters for each subimage in a typical frame time t + 1.66 seconds, freestream wind speed of 1 m/s.

0.803860	0.799646	0.861110	0.896367	0.896367	0.699603	0.706831
0.796687	0.846873	0.896348	0.856362	0.971109	0.701238	0.737246
0.843386	0.734136	0.706633	0.859210	0.876377	0.797390	0.729451

Table 5.5 Fractal parameters for each subimage in a typical frame time *i* + 1.66 seconds, freestream wind speed of 2 m/s.

0.990389	0.904986	0.814416	0.814416	0.845184	0.863293	0.913289
0.936710	0.796121	0.706711	0.741116	0.805164	0.933189	0.816413
0.790486	0.766428	0.656033	0.703670	0.800770	0.794487	0.890068

Table 5.6 Fractal parameters for each subimage in a typical frame time i + 1.66 seconds, freestream wind speed of 4 m/s.

in the frame. Because of the inherent ambiguities in this approach, a new algorithm based on higher-order fractals is described in the subsequent section. Prior to presenting the new algorithm, however, attempt to verify the near-cyclic nature of the temporal variability of both dynamical horizontal and vertical fractal parameters is the next section.

5.4.2 Statistical Interpretation

In general, a object such as smoke moves in a turbulent motion; therefore the spatial distribution, the concentration, the plume shape, and possibly the temperature are continually changing. For instance, the concentration of a pollutant at a cluster of points in a highly turbulent plume varies with time. This variation may be explained by the varying plume sizes and the turbulent eddies causing dispersion. Assuming that the eddies are comparable in size to the plume, they produce a local disturbance of the plume and interleave the clean air and the pollutant causing concentration variations within the instantaneous plume.

Our interest in this subsection is in expressing the characteristic properties of the variations of some quantity (smoke) which continually varies. As illustrated in the previous subsection, the chaotic and complicated behavior of smoke is reflected by the complexity and irregularity of figures 5.5-5.12. In fact, these figures display fluctuations which occur in a succession of rise, peak, fall, and trough. There is no mathematical regularity about the wave-like motion. The peak in one cycle may be twice as high as in the succeeding cycle; while in one cycle the rise may be gradual and the subsequent decline very sharp, in another the rise may be rigorous and the decline less precipitous. This lack of uniformity, in respect to length, amplitude, and shape, that makes difficult the mathematical interpretation of figures 5.5-5.12. In other words, the periodicity and the constancy of the amplitude variation are not easily seen as opposed to periodic movements showing a definite recurrence of fluctuations in given periods, or at stated intervals. However, some distinguishing features of the curves can be specified. In the following, we attempt to explain the previously described results using the language of fractals and statistical theory.

For simplicity, consider figures 5.5-5.8. The deviation of the vertical fractal parameter from its mean value during a period of time (say 200 frames) appears to be nearly constant from frame to frame. Throughout the remaining subsection, we shall restrict our attention to the case where the fractal parameters vary only with respect to time. Let the dynamical vertical fractal parameter be denoted, here, by a variable x and its mean by $\bar{x}$. If ϵ represents the deviation from the mean value of the vertical fractal parameter such that $\epsilon = x - \bar{x}$, the standard deviation is given by

$$\sigma = (<(x-\bar{x})^2>)^{\frac{1}{2}} = (<(\epsilon)^2>)^{\frac{1}{2}} \qquad (5.15)$$

where $< . >$ indicates a time average. One property of the curve (in our case vertical fractal parameter vs. time) which we can define, is the constancy of $(<(\epsilon)^{\frac{1}{2}}>)^2$ during successive number of frames. The statistical properties of the curve are by no means completely determined by this. Therefore, it is possible to envision an infinite variety of curves (vertical fractal parameter vs. time) with a given standard deviation of ϵ. These curves may possess either a large or a small number of peaks, with the passage of time as discussed previously. In the case of a large number of peaks, the standard deviation of $\epsilon^{(1)}$ ($^{(1)}$ means the first derivative with respect to time; in general, $^{(k)}$ will stand for the kth derivative) might be anticipated to be larger than in the case of a small number of peaks. Consequently, the features of the curve may be better described by specifying the standard deviations of $\epsilon^{(1)}$.

In the following we show the existence of some relationships between the standard deviations for ϵ, $\epsilon^{(1)}$, $\epsilon^{(2)}$, $\cdots$ and the curve. Assume that we are able to observe the time-sample values of ϵ, i.e, $\epsilon(t_1) = \epsilon_1$, $\epsilon(t_2) = \epsilon_2$, $\cdots$ $\epsilon(t_k) = \epsilon_k$. Upon a perturbation, the time-sample becomes

$$\epsilon(t_1 + \delta t) = \epsilon_1 + \delta\epsilon_1,\ \epsilon(t_2 + \delta t) = \epsilon_2 + \delta\epsilon_2,\ \ldots.,\ \epsilon(t_k + \delta t) = \epsilon_k + \delta\epsilon_k$$

where δt is a small amount of time. Therefore, we have

$$< (\epsilon)^2 > = \frac{1}{k} \sum_{i=1}^{k} (\epsilon_i)^2 \tag{5.16}$$

Since we are considering a curve in which $< (\epsilon)^2 >$ is constant, $< (\epsilon)^2 >$ is also constant to the first order terms of each term $(\epsilon_i)^2$ (Taylor series expansion), that is:

$$< (\epsilon)^2 > = \frac{1}{k} \sum_{i=1}^{k} \left(\epsilon_i + \epsilon_i^{(1)}\delta t\right)^2 = < (\epsilon)^2 > + 2 < \epsilon\epsilon^{(1)} > \delta t \ .$$

To guarantee the constancy of the mean $< (\epsilon)^2 >$, we must have.

$$< \epsilon\epsilon^{(1)} > = 0 \tag{5.17}$$

Therefore, there is no correlation between ϵ and $\epsilon^{(1)}$. Differentiating (10), we have

$$< \epsilon\epsilon^{(2)} > + < (\epsilon^{(1)})^2 > = 0 \ . \tag{5.18}$$

Consequently, using the definition of a correlation coefficient, there is a correlation attribute between ϵ and $\epsilon^{(2)}$ given by:

$$\rho = - \frac{< (\epsilon^{(1)})^2 >}{< (\epsilon)^2 >^{1/2} < (\epsilon^{(2)})^2 >^{1/2}} \ . \tag{5.19}$$

A consequence of the existence of this correlation coefficient ρ is that $< (\epsilon^{(1)})^2 >$ cannot be greater than $< (\epsilon)^2 >^{\frac{1}{2}} < \epsilon^{(2)})^2 >^{\frac{1}{2}}$.

The assumption of the near-constancy of the standard deviation of $\epsilon^{(1)}$ allows us to use the same logic as for the standard deviation of ϵ, hence differentiating $< (\epsilon^{(1)})^2 >$ yields

$$< \epsilon^{(1)} \epsilon^{(2)} > = 0 \tag{5.20}$$

Differentiating (5.20) once more, will give

$$< \epsilon^{(1)}\epsilon^{(3)} > + < (\epsilon^{(2)})^2 > = 0$$

From (5.18), we have upon differentiating,

$$< \epsilon\epsilon^{(3)} > + 3 < \epsilon^{(1)}\epsilon^{(2)} > = 0 \tag{5.21}$$

From (5.20) and (5.21), we conclude:

$$< \epsilon\epsilon^{(3)} > = 0$$

Proceeding in this way it can be shown that

$$< \epsilon\epsilon^{(2k)} > = (-1)^k < (\epsilon^{(k)})^2 > \tag{5.22a}$$

and

$$< \epsilon\epsilon^{(2k+1)} > = 0 \tag{5.22b}$$

The idea behind the use of these standard deviations is to specify some statistical attributes of the curve. In order to facilitate the matter as much as possible, we suppose as before, that a time-sample of ϵ can be observed ($\epsilon(t_i) = \epsilon_i$ $i = 1, 2, \cdots k$). Next, is to correlate the ϵ_i's with time-sample values ϵ_j such that $\epsilon_j = \epsilon(t_i + \tau)$ for ($i = 1, 2, \cdots k$), and where τ is a small amount of time. Then let ρ_τ be the correlation coefficient so obtained.

Letting $\epsilon(t)$, $\epsilon(t + \tau)$ be the values of ϵ at time t and time $t + \tau$, respectively, then we would by definition have

$$\rho_\tau = \frac{< \epsilon(t)\epsilon(t + \tau) >}{< (\epsilon(t))^2 >^{1/2} < (\epsilon(t + \tau))^2 >^{1/2}} \tag{5.23}$$

If we assume the near-constancy of the standard deviation of ϵ, (5.23) becomes

$$\rho_\tau = \frac{< \epsilon(t)\epsilon(t + \tau) >}{< (\epsilon(t))^2 >} . \tag{5.24}$$

This is valid since

$$< (\epsilon(t + \tau))^2 > \approx < (\epsilon(t))^2 >$$

Further, $\epsilon(t + \tau)$ may be expanded in power of τ as:

$$\epsilon(t + \tau) = \epsilon(t) + \sum_{i=1}^{k} \frac{\tau^{i}\epsilon^{(i)}}{i!} \quad ,$$

from which (5.24) is rewritten as:

$$\rho_{\tau} = 1 - \frac{\tau^{2}}{2!} \frac{< (\epsilon^{(1)})^{2} >}{< (\epsilon)^{2} >} + \frac{\tau^{4}}{4!} \frac{< (\epsilon^{(2)})^{2} >}{< (\epsilon)^{2} >}$$

$$- \cdots + \frac{(-1)^{(k)}\tau^{2k}}{(2k)!} \frac{< (\epsilon^{(k)})^{2} >}{< (\epsilon)^{2} >} \qquad (5.25)$$

To give a flavor for eq. (5.25), we envisage $\epsilon = \sin(t + \xi)$, where $\xi \in R$. It is well known that

$$< (\epsilon)^{2} > = < (\epsilon^{(1)})^{2} > = \cdots = < (\epsilon^{(k)})^{2} > = 0.5$$

from which (64) yields:

$$\rho_{\tau} = \sum_{k=0}^{\infty} (-1)^{(k)} \frac{\tau^{2k}}{(2k)!} = \cos \tau$$

This confirms the temporal variability of the vertical fractal parameter, for if we approximate its deviation ϵ from its mean value by a sinusoidal curve, then the correlation coefficient is also oscillatory. This further supports that on the continuous motion of smoke, there is a correlation between the movement in any one period of time and the next.

Nevertheless, it is clear that both vertical and horizontal fractal parameters are not conservative properties. This is not surprising since our input data were sequences of images and our pollutant (smoke) is a time-varying (deformable) object presenting fluctuations due to some factors such as the vortex-shedding and external perturbation. The frames can be envisioned as surfaces formed by different processes, hence, having different fractal parameters.

5.4.3 Discussions

From the previous results, one notices that the curves obtained in analyzing smoke data fluctuate throughout the set of frames of the whole sequences and change in a near-cyclic manner. The fluctuations are due to the fact that smoke particle concentrations are not the same for every frame of the sequence and for every freestream wind speed set up. Expressed in another way, an image surface would have a different structure and form (variation of brightness over its surface); hence, a different outcome (a different fractal parameter). The observation that both vertical and horizontal fractal parameters within a given region change over space, or time scale, indicates that the region of analysis is an image of multiple turbulent flows (Babloyantz, 1986). Smoke data supports a multi-fractal model in which the fractal parameter is a function of fluctuations in the intensity. It is clear that the fluctuations in intensity are caused by variations in the time event, nominal velocity and concentration of smoke particles. In conjunction with the concepts of fractal parameters, scaling, and intermittency are the tools needed to understand the extreme variability of the transient smoke data over a range of space and time scales. Furthermore, smoke data can be qualitatively evaluated as having one or more of the properties of particle coarseness, irregularity and chaotic flow, monodispersed or polydispersed particle structure.

Additionally, our fractal parameters represent a difference between two means, one mean produced at one-unit distance $<\Delta I_{\Delta_1}>$, and another mean produced at three-unit distance $<\Delta I_{\Delta_3}>$. This difference of the means of intensity, defined over a local neighborhood at each pixel, provides information about the environment in the immediate vicinity of the pixel. The fractal parameter is the difference of means of the intensity values inside each window. A high value of the fractal parameter indicates that the two means are close each other; that is, it would indicate that the pixel is in an environment where gray levels of smoke data do not change much. A low value of the fractal parameter would imply that the pixels of the original image are in an environment where the mean at three-unit distance is much greater than the mean obtained at one-unit distance. This means that a smoke image has drastic grey level change (reflecting chaotic motion). This high variation of grey level is evident, since as might be expected, the condition of monodispersion is extremely rare in nature. Hence, we unquestionably assume that smoke particles are polydispersed. For the same smoke environment, the fractal parameter measures would be statistically close.

If the smoke is concentrated, it is possible that an element (a pixel of smoke data) and its neighboring elements have similar gray level values. This means that the TIF pixel values would be small for both one-unit distance and three-unit distance; hence, the fractal parameter would be in the vicinity of one. In general, however, this case would have a small probability of occurance since the smoke flow undergoes turbulent motion. In the majority of cases in the original image and its neighboring elements have different gray level values. It is worth noting, however, that a physical variation in smoke data may not always give rise of intensity variations.

In summary, high values of the fractal parameters relate to weak gray level variations at a distance of three-unit pixel and strong gray level variations at a distance of one-unit pixel. On the other hand, low values of the dynamical fractal parameters relate the strong gray level variations at a distance of three-unit pixel and weak gray level variations at a distance of one-unit pixel.

5.5 Velocity Considerations

Depending on conditions of the smoke flow, thin smoke puffs may form a continuous packet, several packets, or many separate packets. Furthermore, flow visualization shows that packet surfaces can be extremely rough and therefore difficult to characterize. With all these complexities in mind, we attempt to understand the relationship existing between the fractal parameters and the motion of the smoke. The difficulties that we have faced in attempting to understand the motion phenomenon from figures 5.5-5.12 due to the fluctuations, prompted us to generate three pictures by averaging the three different sequences separately. The strategy of averaging over a sufficient time period represents a "steady state picture". For example, an average of the side view of a picture for an average of 120 frames (4 sec) corresponding to a smoke velocity of 2m/s was taken. The same technique for computing the two fractal parameters (HFP) and (VFP) was used for the three averaged sequences, i.e. equation (5.7). Figure 5.26 shows the flow-speed dependence of the vertical fractal parameter in the motion of the smoke; likewise figure 5.27 illustrates the variations of the horizontal fractal parameter in terms of the different speeds.

As can be seen in figure 5.27, with increasing speed, the horizontal fractal parameter decreases slowly; this may be attributed to the fact that the gray-level of the image is also decreased due to the dilution of the smoke. In general, speed and direction play a key role in the dilution of smoke. For example, assuming that the smoke in the wind tunnel is swept away from its origin at a certain measured quantity per unit of time (say, Q_p/s), then the quantity of smoke in distance d of the plume would be inversely proportional to the wind speed, i.e., $Q_p\, d/U$ where U is the wind speed (m/s). However, figure 5.26 shows a slight increase of the vertical fractal parameter with respect to the increasing velocity.

These results demonstrate that both fractal parameters differ from one type of flow to another (different freestream wind speeds). The deflection shown between figure 5.26 and figure 5.27 is explained by the non-uniform and turbulent motion that smoke undergoes. In effect, vortices move at different velocities; hence, they merge and unite and their size augments in the downstream direction. This is due to the presence of the obstacle (building) and to the complicated variability of the velocity in the vertical direction. The presence of the building is crucial in flow considerations and leads to major transformations of the wake flow. The horseshoe vortex that forms around the model building is one of the possible means of interaction between the wake and the mean flow regions. Physically speaking, the dimensions of the building and the boundary conditions of the flow play a major role in the aerodynamic wake flow. Furthermore, this resulted from the strong vertical and horizontal recirculation within the cavity region.

In addition to the above, more complicated unsteady secondary flow patterns in which large fluctuations of the recirculating zone exist. Transport of smoke material to and from the cavity

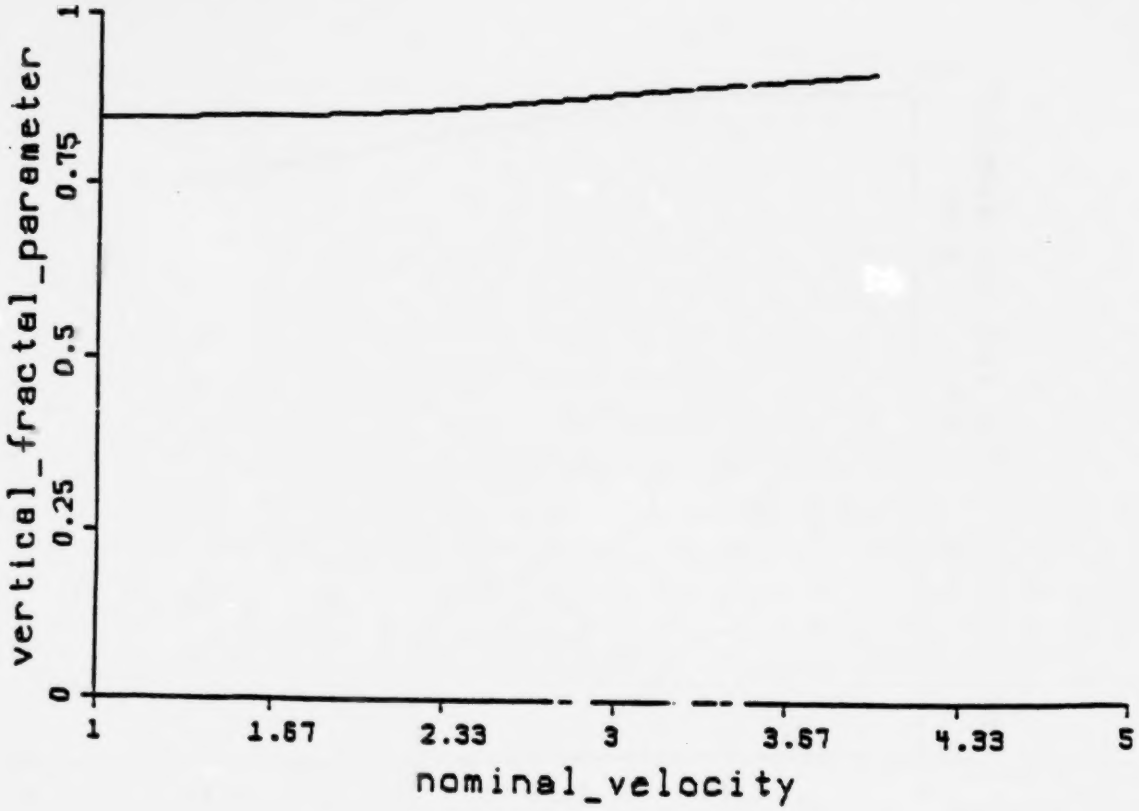

Figure 5.26 Vertical fractal parameter versus nominal velocity (freestream wind speed).

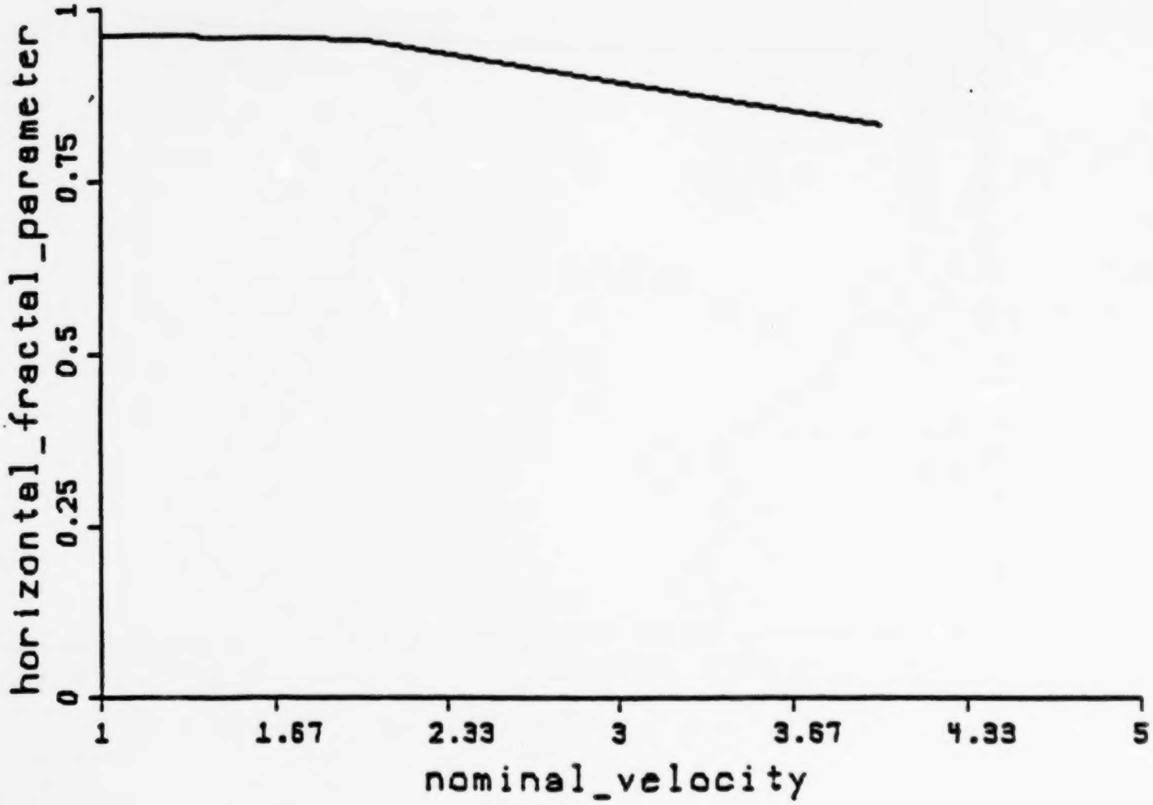

Figure 5.27 Horizontal fractal parameter versus nominal velocity (freestream wind speed).

is, hence, not limited to turbulent transport across the closed surface. Material can therefore be both advected into and removed from the recirculation region by turbulent diffusion or by secondary flows, such as the rising spiral vortices generated behind the lateral building edges. Bursting, strong oscillations and intermittent collapsing and reforming as the smoke flows into and out of the cavity continually varies with time.

Next, we utilized three different time-averaged pictures whose nominal velocity was one, two, and four meters per second respectively. These time-averaged pictures represent 120 frames (4 sec) as before. We investigated the variation in the horizontal fractal parameter in terms of the location of the boundary layer flow. The window size for this analysis was selected to be 10 × 275. The height of 10 was chosen so a reasonable number of values could be plotted. The horizontal fractal parameter was computed from the top of each steady state picture to the bottom by intervals of 10 pixels. Figures 5.28, 5.29, and 5.30 show the spatial variability of the horizontal fractal parameter for the steady state picture of smoke whose velocity was one, two, and four meters per second respectively as a function of vertical position in the image. The length 275 is adequate for smoke data taken at freestream wind speeds of one and two meters per second. However, this length may include a portion of the background for smoke data whose velocity was four meters per second. To avoid this inaccuracy, the length of 275 was reduced to 180 for the data taken at four meters per second. Figure 5.31 show the spatial variability of the horizontal fractal parameter for the steady state picture of smoke whose velocity was four meters per second with the window size of 10×180.

As can be seen, the horizontal fractal parameters are different for all three different cases. Nevertheless the values of the horizontal fractal parameter are decreasing from the top to the ground level. These features fit a simple parabolic configuration similar to the one pointed out in figure 5.32. In summary, this analysis appears consistent with the type of measurements taken by the traditional technique of hot-wire anemometry instruments. Furthermore, as can be seen in figure 5.33, the horizontal fractal parameter values are nearly the same at the ground level, but can be distinguished at both medium and high levels.

In a similar fashion, the spatial variability of the vertical fractal parameter is investigated. We used the three different time-averaged pictures whose nominal velocity was one, two, and four meters per second, respectively. We studied the variation of the vertical fractal parameter in terms of the location of smoke data from its original source. The window size for this analysis was chosen to be 100×30. This choice is good because the heights of our original pictures are 120 pixels. The vertical fractal parameter was calculated from the position of the source of smoke (close to the model building) of each steady state picture to the downstream of the building by intervals of 30 pixels. Figures 5.34, 5.35, and 5.36 show the spatial variability of the vertical

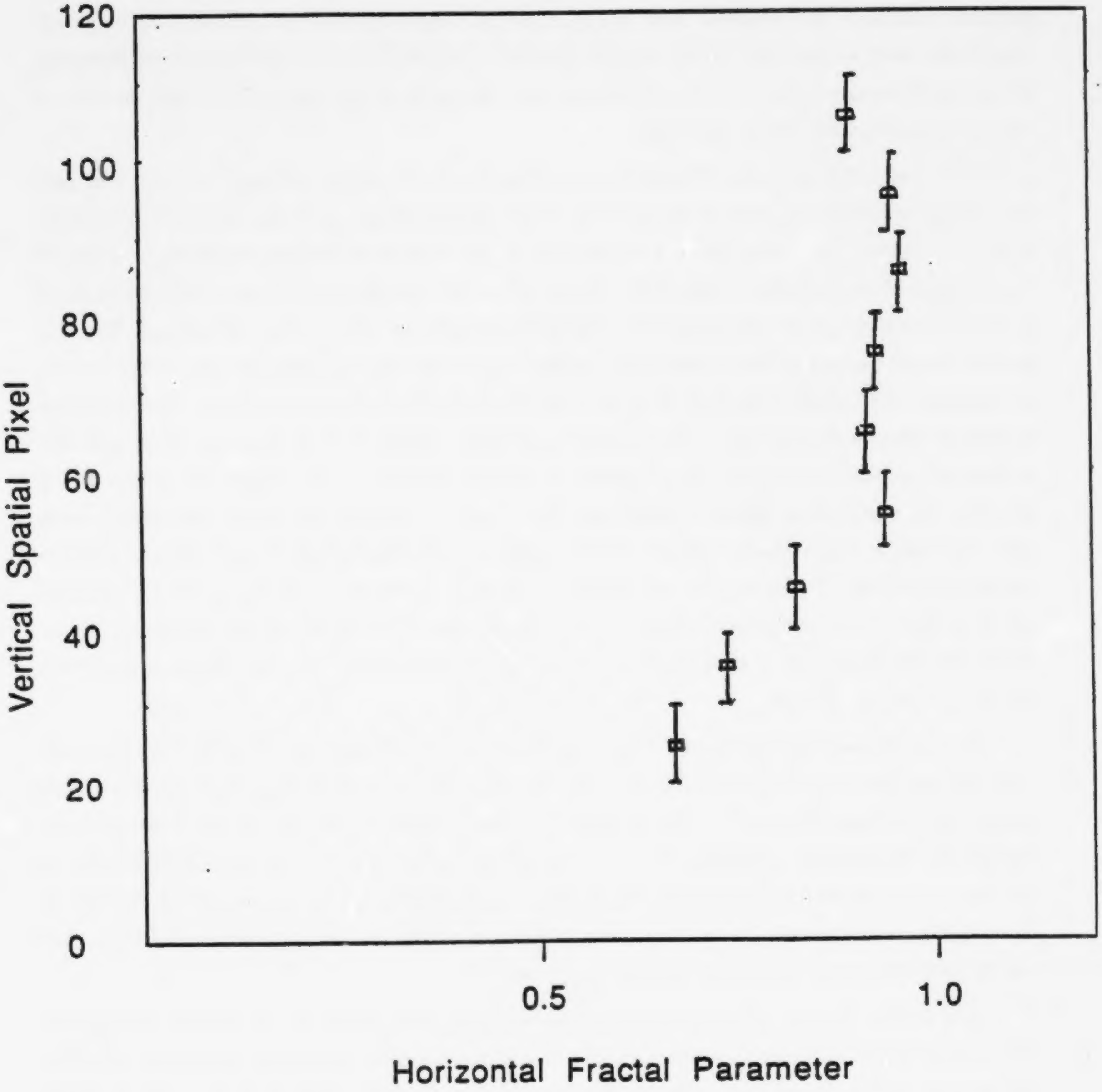

Figure 5.28 Vertical position (in pixels) versus the horizontal fractal parameter window 10x275, freestream wind speed of 1 m/s.

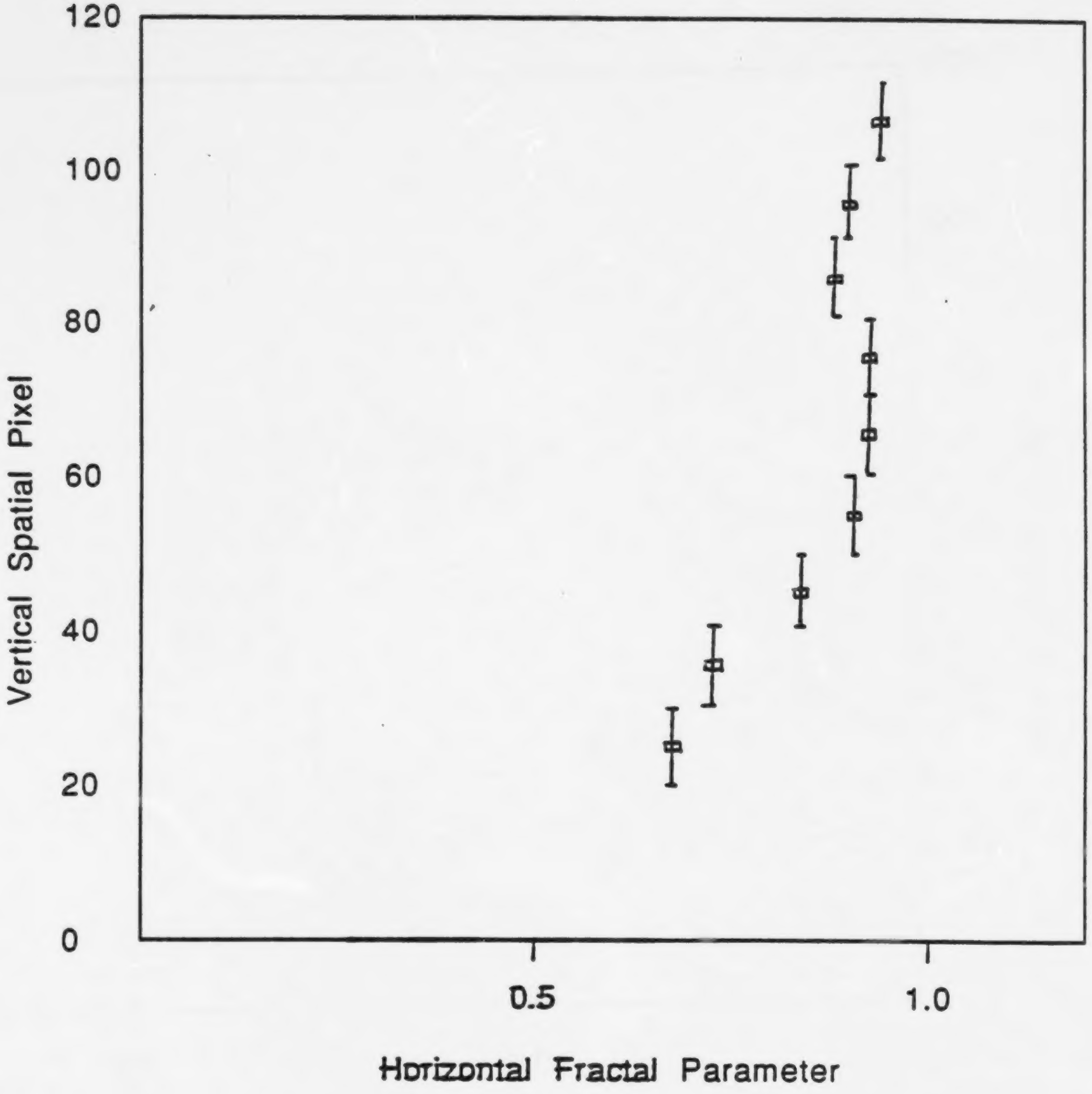

Figure 5.29 **Vertical position (in pixels) versus the horizontal fractal parameter window 10x275, freestream wind speed of 2 m/s.**

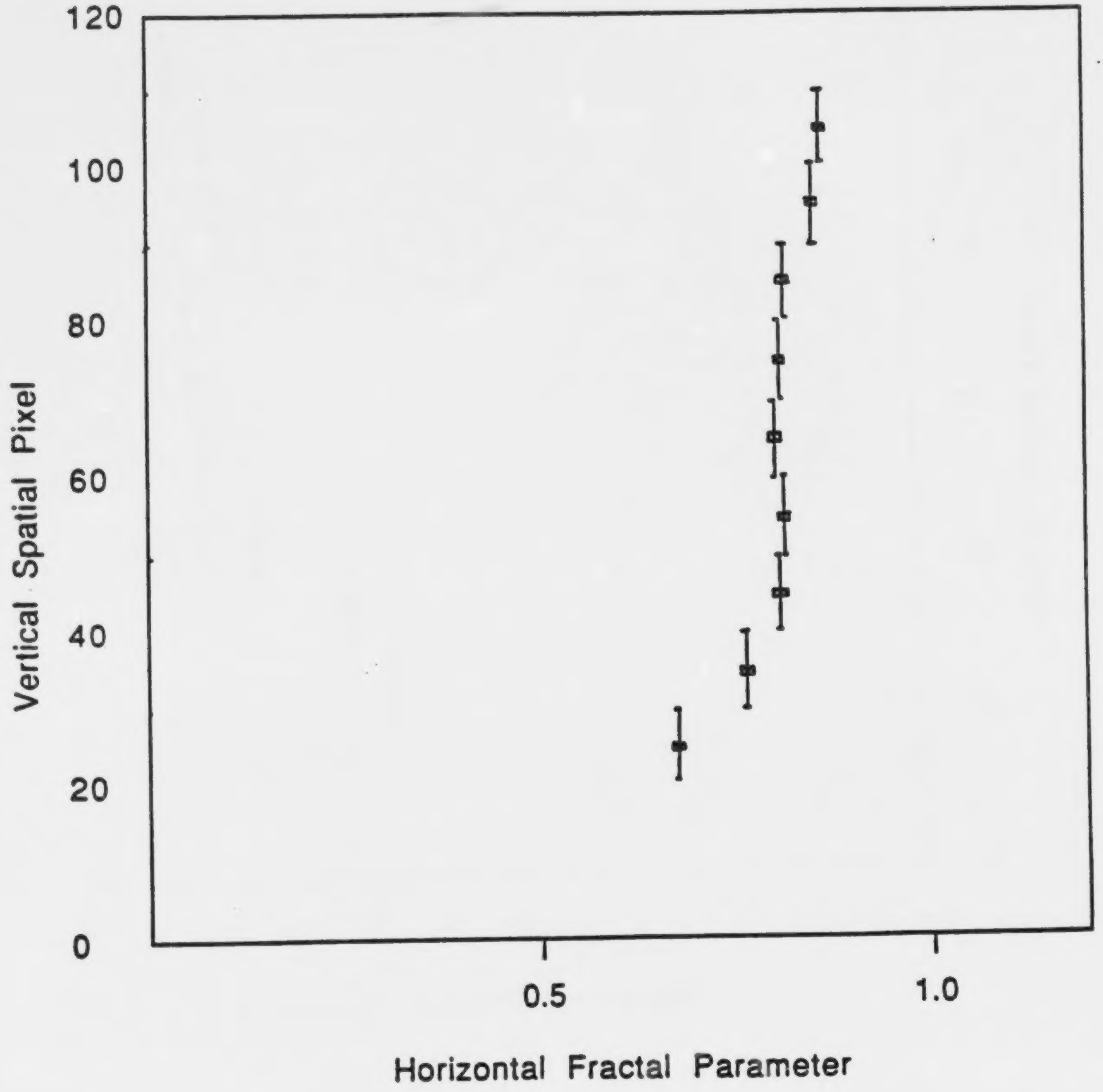

Figure 5.30 Vertical position (in pixels) versus the horizontal fractal parameter window 10x275, freestream wind speed of 4 m/s.

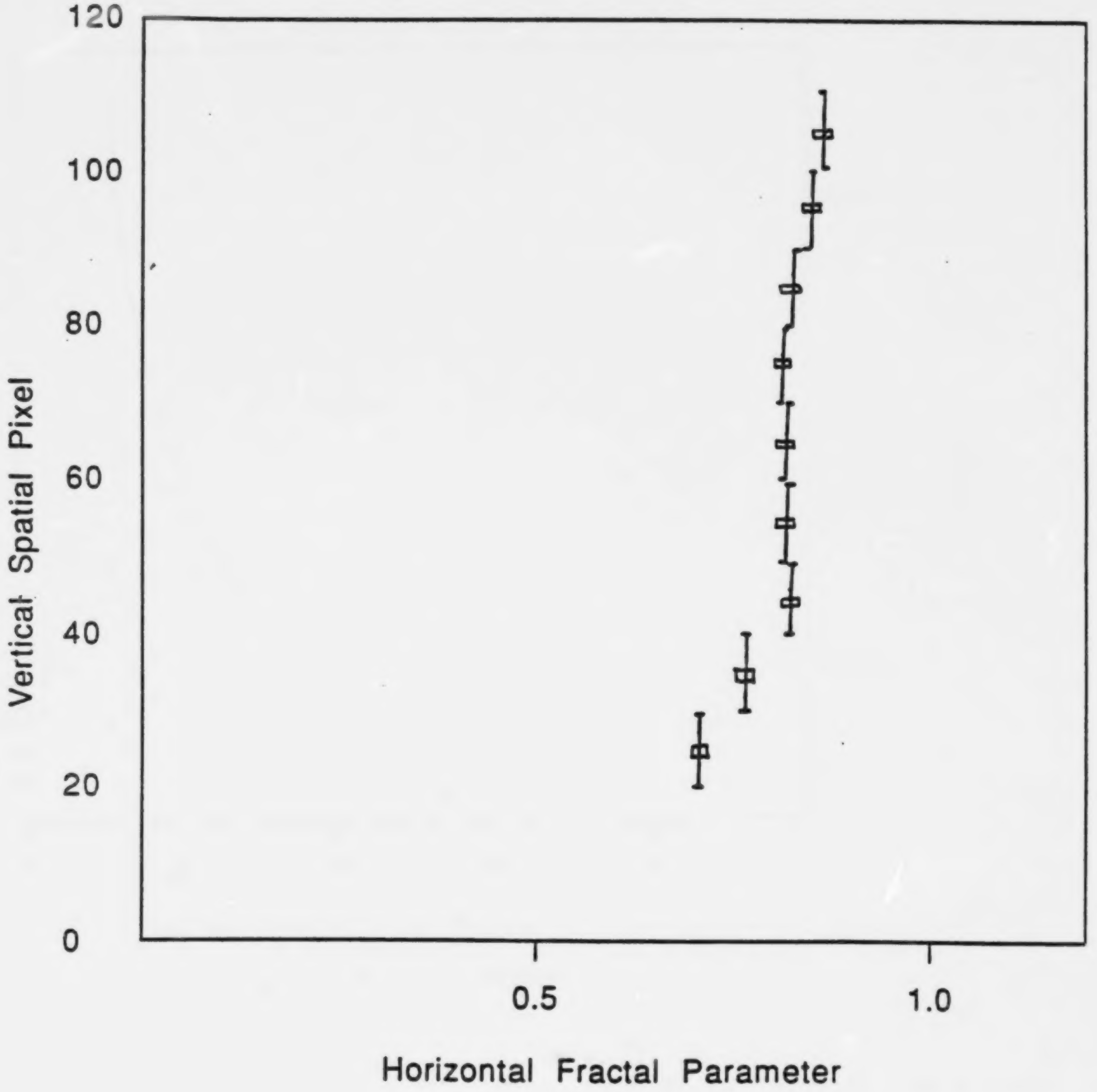

Figure 5.31 Vertical position (in pixels) versus the horizontal fractal parameter window 10x180, freestream wind speed of 4 m/s.

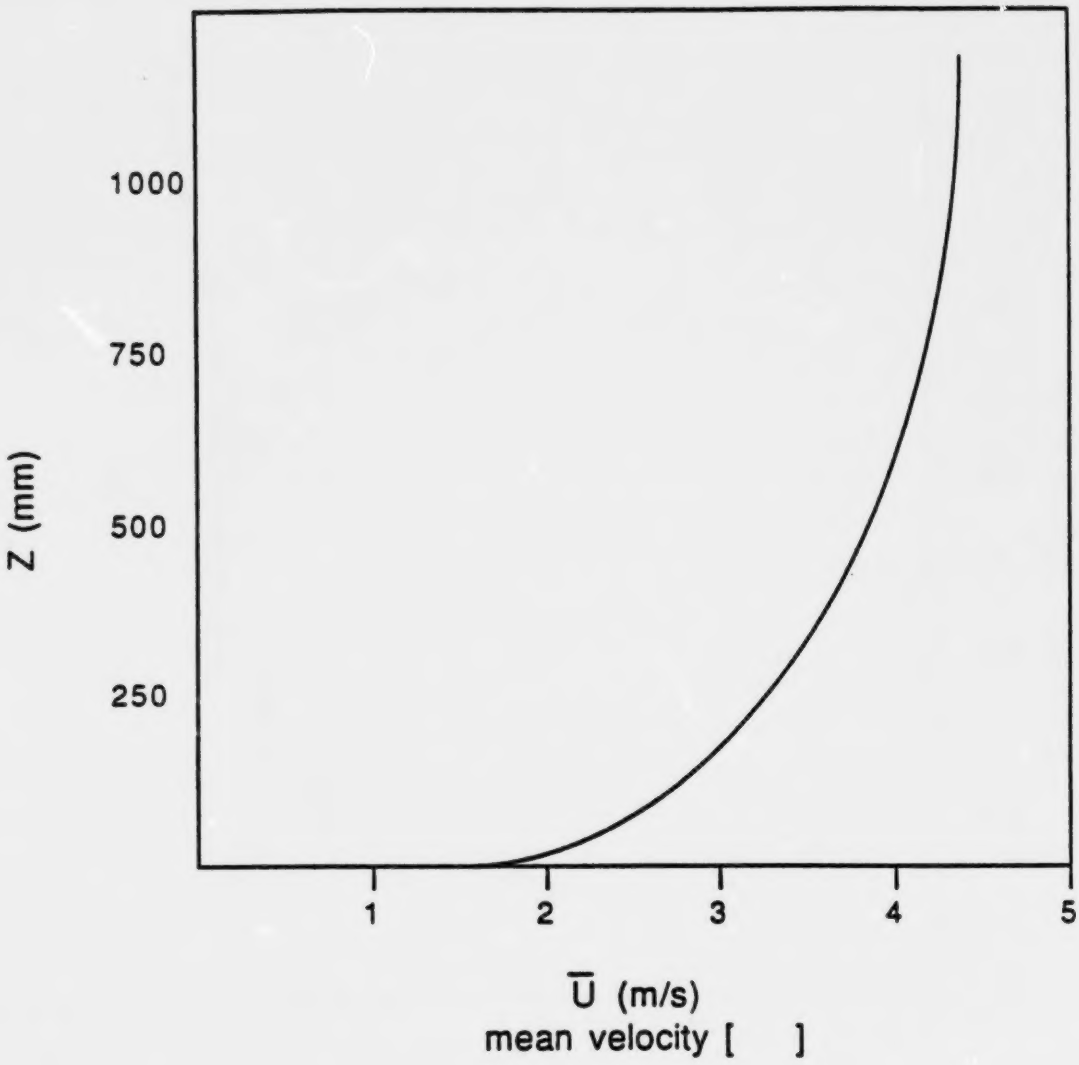

Figure 5.32 Vertical profile of mean velocity (height versus mean velocity).

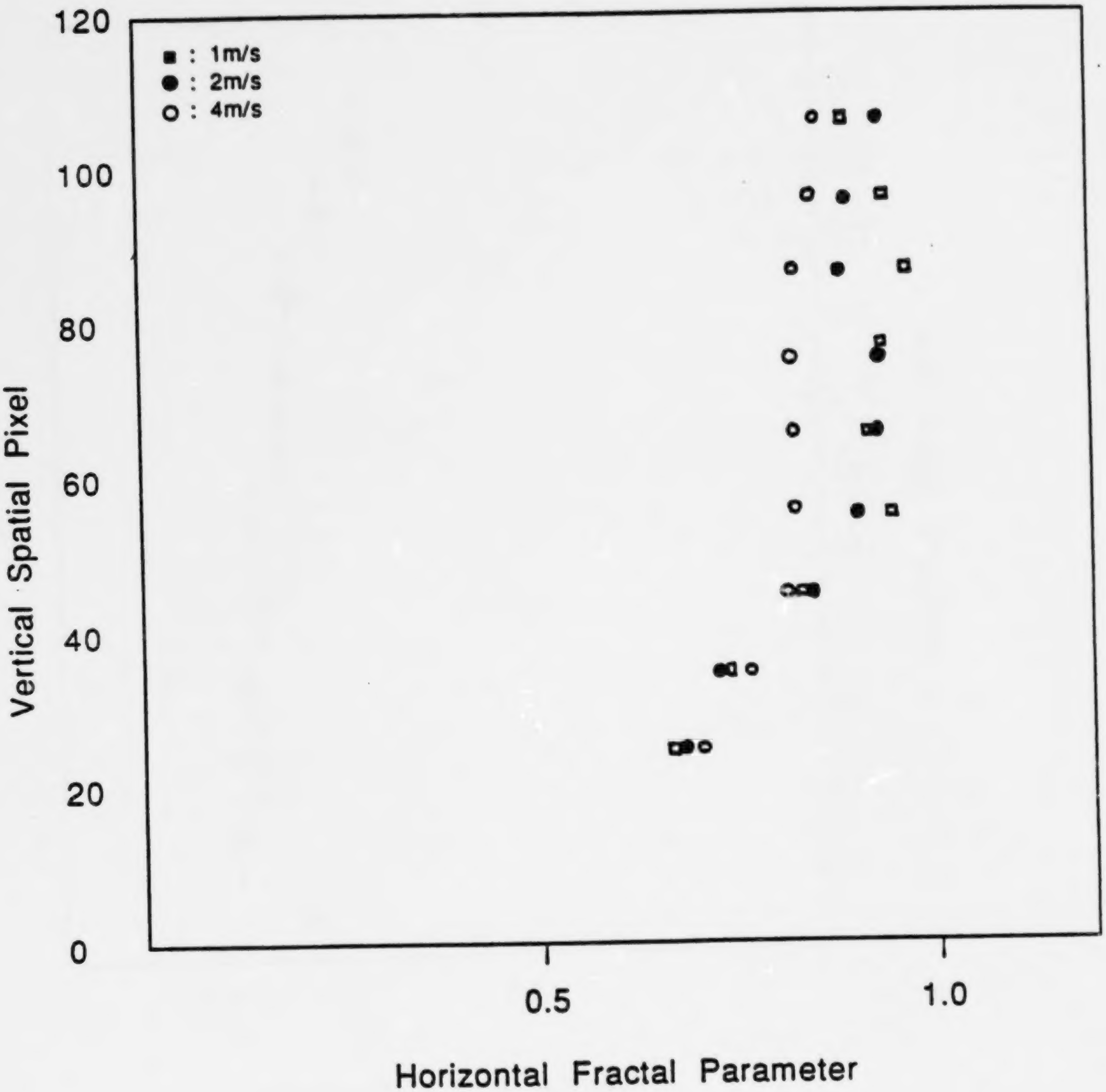

Figure 5.33 Vertical position (in pixels) versus the horizontal fractal parameter overlay of the three freestream wind speeds (1 m/s, 2 m/s, 4 m/s).

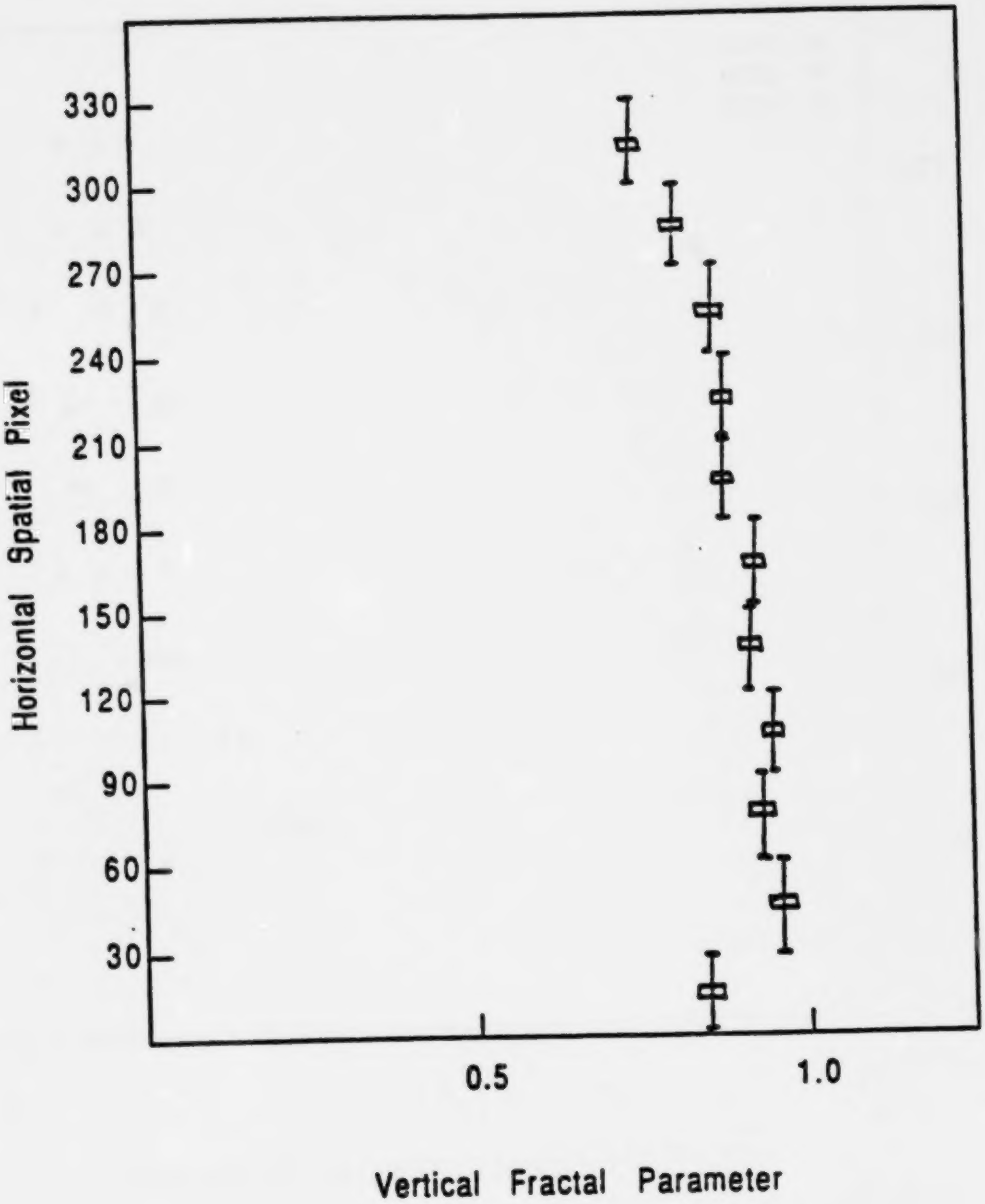

Figure 5.34 Horizontal position (in pixels) versus the vertical fractal parameter window 100x30, freestream wind speed of 1 m/s.

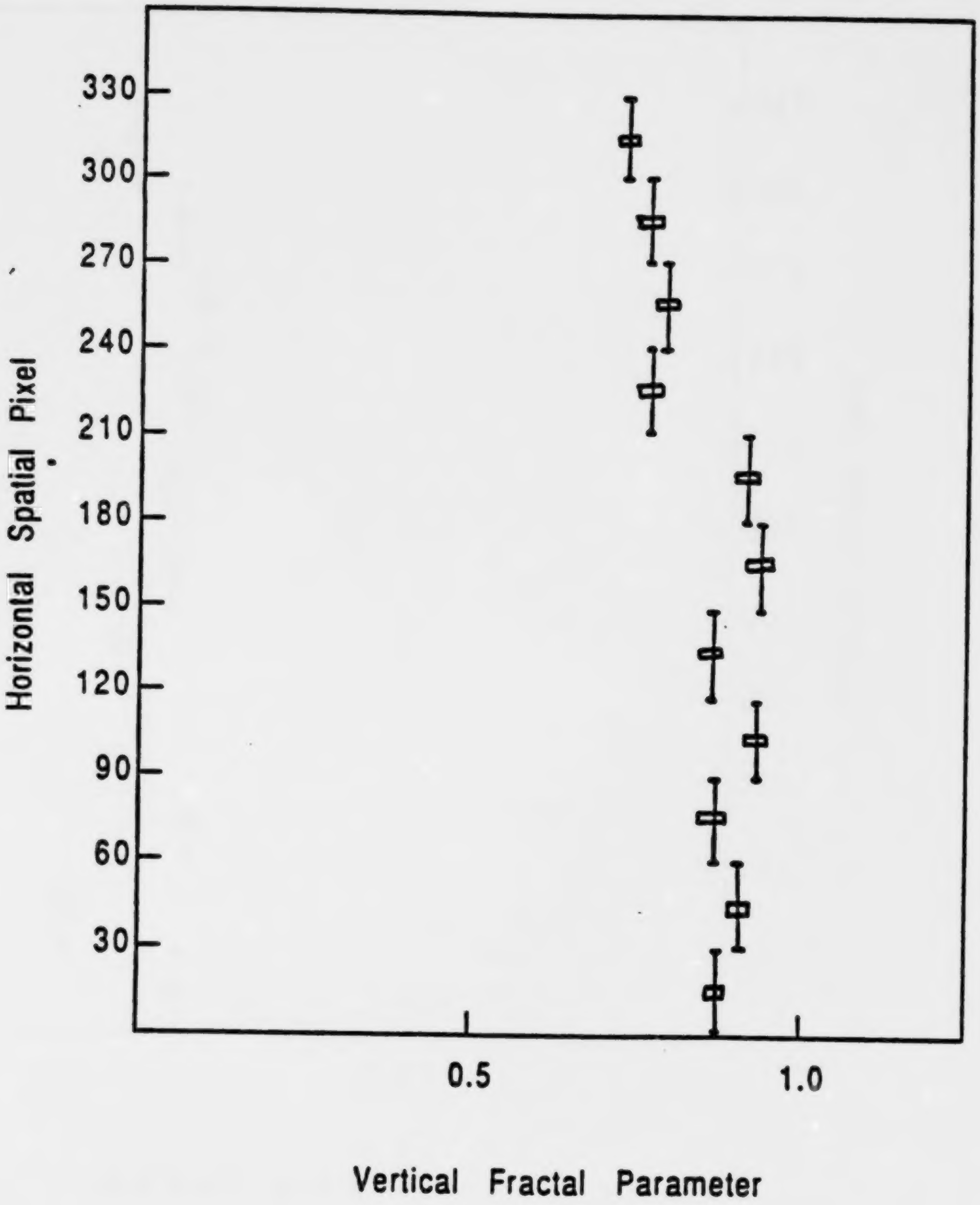

Figure 5.35 Horizontal position (in pixels) versus the vertical fractal parameter window 100x30, freestream wind speed of 2 m/s.

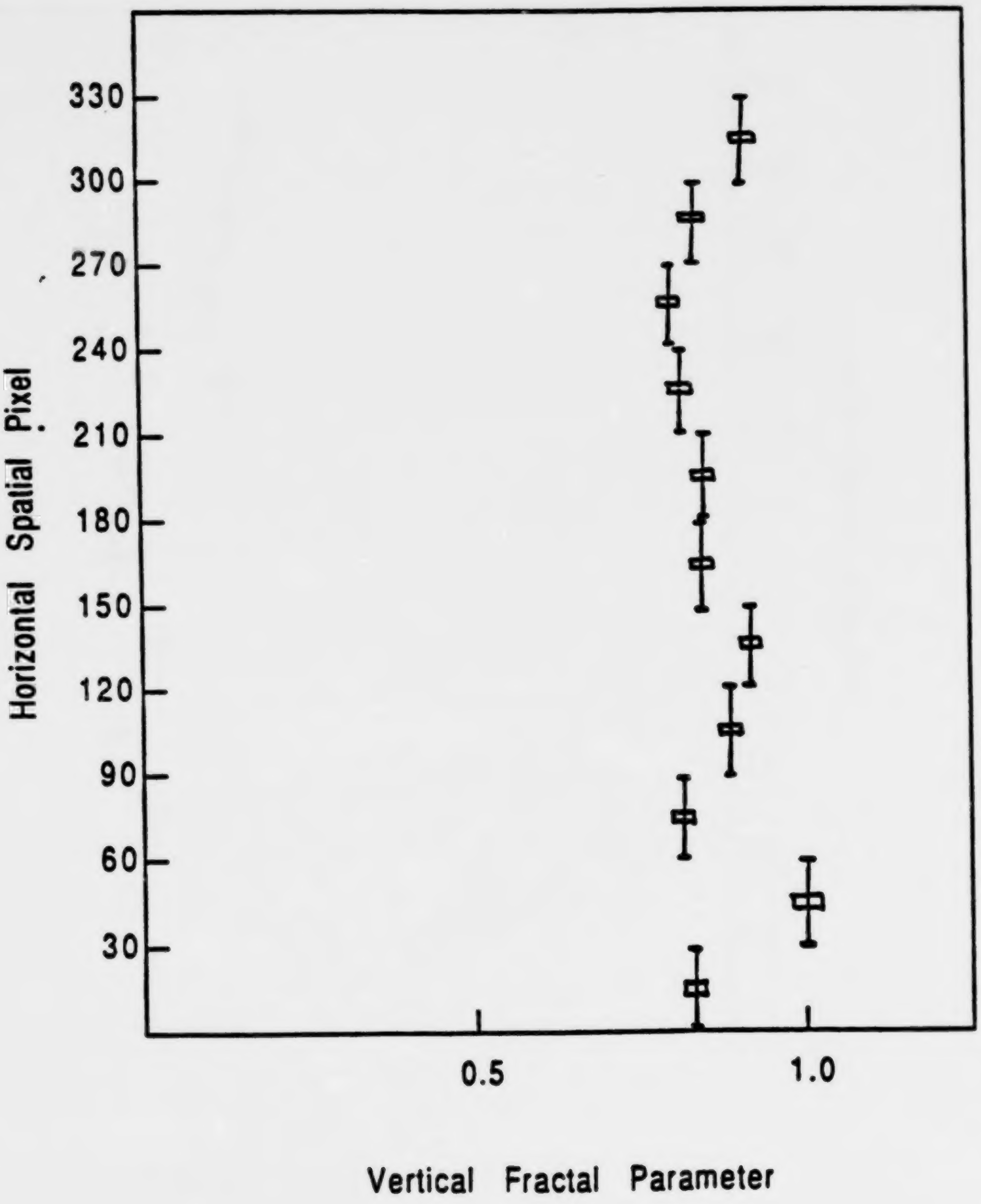

Figure 5.36 Horizontal position (in pixels) versus the vertical fractal parameter window 100x30, freestream wind speed of 4 m/s.

fractal parameter for the steady state picture of smoke whose velocity was one, two, and four meters per second respectively. As shown in figures 5.34, 5.35, and 5.36, the horizontal spatial pixel represents the location of pixels in the horizontal direction of a given picture. The horizontal spatial pixel represents the location of smoke downstream the model building. The vertical fractal parameters are different for all three cases. Figure 5.34 shows that the values start to increase near the source location and then slightly decreases far away from the source (downstream of the model building). Figure 5.35 starts to increase slightly near the source location then undergoes weak oscillations (at four to six times the building height downstream of the position of the leeward edge of the model building and finally decreases far away from the source (downstream of the model building). Finally, figure 5.36 oscillates throughout the set of measurements. Even though these results are interesting, it is not clear how to fit the data. As in the previous results concerning the vertical spatial pixel and for the same reasons, we reduced the height from 100 to 70 for the case of smoke data whose velocity was four meters per second. Figure 5.37 illustrates the output of the analysis using the same procedure as for obtaining figure 5.36. The qualitative behavior of figure 5.37 is comparable with the one shown in figure 5.36.

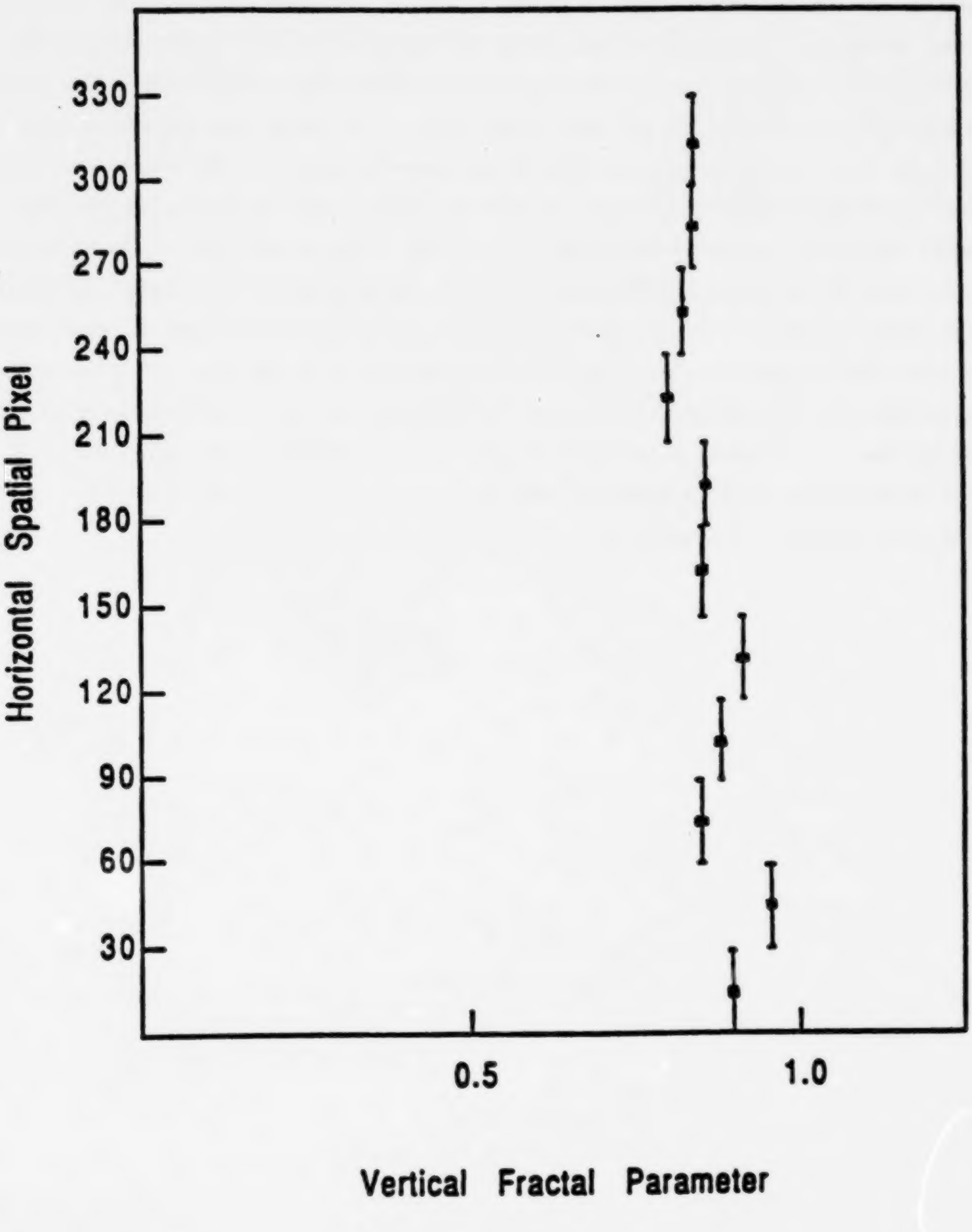

Figure 5.37 Horizontal position (in pixels) versus the vertical fractal parameter window 70x30, freestream wind speed of 4 m/s.

5.6 Spatial Fluctuations of Concentration in Smoke Plumes

The concentration of an air pollutant may be regarded as a random variable $C(x,y,z,t)$. Here the triplet (x,y,z) is to be interpreted as a vector locating the point of observation in a three-dimensional space. Generally, the outcomes of $C(x,y,z,t)$ are correlated in space and in time.

Physically speaking, air pollutant concentrations also exhibit turbulent fluctuations. According to Chatwin and Sullivan (1979), instantaneous releases of smoke particles are torn apart by the actions of boundary layer flows and the presence of model buildings, with the result that there are patches of smoke interspersed with clear air patches. Continuous smoke plumes also display variability in smoke density, especially during periods when there are numerous large, well developed turbulent eddies. In fact, as we will see later, air pollutant concentration displays plume intermittency as well as in-plume concentration fluctuations. Hanna (1984) provides a review of some basic theories of concentration fluctuations and analytical methodologies for practical estimation of the fluctuations. Current models do not adequately account for flow bounded at the top and bottom, which nearly always happens in the boundary layer of the atmosphere. From these efforts and investigations, it appears that the concentration patterns within a plume are the most difficult problem still to be solved.

In the following, we develop a new model based on higher-order fractal dimensions to characterize the concentration pattern. Further, we relate it to the prevailing wind tunnel conditions such as wind nominal velocity. The motivation for using higher-order fractal dimension is to distinguish phenomena that are easily recognizable and separable perceptually but have the same fractal dimension (Ait-Kheddache and Rajala, 1988; Medioni and Yasumoto, 1984). The higher-order fractal dimensions (H-OF) have been recently introduced in physics to characterize chaotic dynamical systems (Mandelbrot, 1986; Halsey, et al., 1986). The H-OF dimensions are composed of the fractal dimension, the correlation dimension, and the information dimension. These H-OF dimensions concern strange attractors, but the last two are extended in this research to the context of smoke analysis.

The first use of H-OF (Ait-Kheddache and Rajala, 1988) in image classification turned out to be successful. We briefly describe the aspects in Ait-Kheddache and Rajala (1988) that are relevant to this work. Specifically, we address the definitions of the H-OF dimensions and the ways in which they were implemented for our analysis.

5.6.1 Smoke Particle Concentration

Following Friedlander (1977), smoke particle concentration at a point – expressed as the number of particles per unit volume of gas – is defined in a manner similar to gas density.

Suppose ∂M to be the number of particles in an initially rather large volume ∂V surrounding the point Q in the gas. Then the ratio $\partial M/\partial V$ is the average (number) concentration of the particles within the volume ∂V. As the volume ∂V shrinks toward the point Q, the average concentration can either increase or decrease depending on the concentration gradient in V. Usually, however, it would approach a constant value over a range of values of the quantity ∂V in which the gradient is small but various smoke particles are still present. This constant value is defined as the particle concentration at the point Q. As the volume keeps on shrinking, the number of particles will be so small that the average concentration fluctuates noticeably. In general, concentration field depends on several parameters which include the density, the viscosity, the distance from the source of emission, the release rate, the reference velocity, the concentration of the release material itself.

5.6.2 H-OF Dimensions: Theoretical Background

A primary objective in theoretical investigations is to look for new methods for characterizing questions related to a specific problem and to understand their interrelationships. There is an infinite number of distinct and pertinent generalized dimensions that characterize a phenomenon. In particular, a complete understanding of the "finite" set of dimensions is coequal to a complete characterization of the fractal. Although there exist a large number of distinct definitions of dimension, the relevant definitions may be divided into two categories, those which only depend on metric properties (the Hausdorff or fractal dimension) and those which are based on metric and probability properties (for example, the information dimension).

A set of generalized dimensions which have recently been introduced by Hentschel and Procaccia (1983) is given by:

$$D_f = \lim_{l \to 0} \left[\frac{1}{(f-1)} \frac{Log(X(f))}{Log(l)} \right] \tag{5.26}$$

$$X(f) = \sum_{i=0} p_i^f \tag{5.27}$$

where p_i denotes the probability of finding points ("bins") of the set in the $l-$ th box; an easy new way to compute p_i's is found in Procaccia (1986).

The intuitive meaning of these results is that f serves to choose a subset of singularities that find out D_f. It is clear from eq. (5.26) that for high values of f, D_f indicates the scaling behavior of the more concentrated parts of the measure. For lower f, the more rarefied region is quantified. Regarding the above classification, f plays a role similar to temperature in physics and statistical mechanics where an ensemble of energy levels corresponds to any given temperature (Procaccia, 1986).

A more general definition of the set D_f for any set A embedded in a d-dimensional Euclidean space is created by segmenting the set into M disjoint subsets A_1, A_2, ..., A_M such that each subset possesses a measure p_i and it lies within a ball of radius l_i where ($l_i < l$) (Halsey, et al., 1986). Eq. (5.26) can be rewritten as (Hentschel and Procaccia, 1983)

$$D_f = \frac{1}{(f-1)} \lim_{l \to 0} \left\{ \frac{\log \sum_{i=0} p_i \exp(f-1) log p_i}{log(l)} \right\} \tag{5.28}$$

The measures D_f are defined for any $f \geq 0$; when f is an integer, D_f has a physical meaning. Hentschel and Procaccia (1983) have shown that:

$$\lim_{f \to 0} D_f = D_0 \tag{5.29}$$

$$\lim_{f \to 1} D_f = D_1 \tag{5.30}$$

$$D_{f=2} = D_2 \tag{5.31}$$

D_0 is the fractal dimension, D_1 is the information dimension, and D_2 is the correlation dimension.

The information dimension D_1 provides a measurement of the exponential rate (see eq. (5.28)) of increase of the information obtained by measuring the shape of the phenomenon with increasing resolution. Mandelbrot (1986) and Procaccia (1985) applied the above theory to static invariants and defined the generalized information of order f, H_f as in Balatoni and Renyi (1976). The original theory of Grassberger and Procaccia (1984) concerning the correlation dimension calculated how the number of pairs of vectors which are separated by distances less than a specified value (say l), changes as a function of l.

$$H_1 = - \sum_i p_i \log p_i \tag{5.32}$$

$$H_f = \frac{1}{(1-f)} \log \sum_i p_i^f \qquad f \neq 1 \tag{5.33}$$

It has been shown in Balatoni and Renyi (1976), that

$$\lim_{f \to 1} H_f = H_1 \tag{5.34}$$

and $H_f \geq H_f{}'$ for any $f' > f$.

5.6.3 Pseudo Matrices of the Fractal

Having presented the relevant background information, the development of the approach taken in this research may now be described. The algorithm is based on pseudo matrices. The features of the phenomenon and higher-order fractal dimensions are obtained explicitly through interscale matrices, which we call the pseudo matrices of the fractal (PMF).

5.6.3.1 Derivation of the PMF

The pseudo matrix of the fractal (PMF) is a two-dimensional representation of image primitives. The entries in the PMFs are frequency counts of variations in gray level of an image. Assume that an image to be analyzed is defined on a $M \times N$ rectangular grid. The grid has M resolution elements in the horizontal direction and N resolution elements in the vertical direction. Let $\mathrm{m} = \{ 1,2,......,M \}$ be the horizontal spatial domain, and $\mathrm{n} = \{ 1,2,.......,N \}$ be the vertical spatial domain. Let $\mathrm{G} = \{ 1,2,.......,N_g \}$ be the finite set of the N_g quantized gray levels. For each position $(m,n) \in M \times N$, $I(m,n)$ represent its gray level, e.g., one of the 256 values. $I_{m,n} = I(m,n)$ represents the function of assigning gray level $g \in G$ to each pair of coordinates in $M \times N$ such that $I{:}M \times N - G$. The pseudo matrix of the fractal $Fr^{(\Delta_\alpha)}$ of an image is obtained by applying a transformation $T(.)$ to the image. The formulation of $Fr^{(\Delta_\alpha)}$ is given by:

$$Fr^{(\Delta_\alpha)}(G,\sigma) = Card\{(m,n)|I_{m,n} = g \ AND \ N_{\Delta_\alpha} = BETA\}\,, \tag{5.35a}$$

for $BETA = 0,1,...,16$, $m = 2,3,...,M-1$, and $n = 2,3,...,N-1$, where

$$N_{\Delta_\alpha} = \sum H(TF - |I_{m,n} - I_{k,l}|) \tag{5.35b}$$

subject to $(k,l)|d((m,n),(k,l) \le \Delta_\alpha$. $H(.)$ is the Heaviside function, equal to 1 for positive or null argument, and equal to 0 for negative argument. Here $(m,n),(k,l)$ are pairs of spatial coordinates in $M \times N$. Card { } refers to the number of elements in a set. $d((m,n),(k,l))$ is the distance between the elements (m,n) and (k,l). Δ_α is the size of the local mask, (see figures 5.38 and 5.39). Figure 5.38 shows a 3×3 annular mask defined when $\Delta_\alpha = \Delta_1$ and figure 5.39 shows a 5×5 annular mask defined when $\Delta_\alpha = \Delta_3$. Δ_α is a positive integer that is selected according to the complexity of the image. TF is the fixed threshold value and N_{Δ_α} contains the information on the rate of change of the gray scale.

The PMF is a $G \times \sigma$ matrix, where G is defined above and σ represents the surface of the window. The window with its center positioned at a particular spatial location is used for evaluating the rate of change in gray scale about that location. The expression

$$\sum H(TF - |I_{m,n} - I_{k,l}|) \tag{5.36}$$

counts the differences that are less than the threshold function TF. In other words, it is the

n_2	n_3	n_4
n_1	x	n_5
n_8	n_7	n_6

Figure 5.38 3x3 annular mask $\Delta_{\alpha=1}$ (x_1, n_k) is true if k=1, 2, ... , 8.

n_3	n_4	n_5	n_6	n_7
n_2				n_8
n_1		x		n_9
n_{16}				n_{10}
n_{15}	n_{14}	n_{13}	n_{12}	n_{11}

Figure 5.39 5x5 annular mask $\Delta_{\alpha=3}$ (x_1, n_k) is true if k=1, 2, ... , 16.

"correlation integral" which counts how many pairs of pixels are in a σ-square whose absolute difference is less than the threshold function TF. Note that the number N_{Δ_a} produced by this measure contains information on frequency since smoke frequency is characterized by a repetition of rising and falling picture element values.

5.6.3.2 Selection of the Threshold

The number N_{Δ_a} will increase by one each time the absolute difference exceeds the threshold. The process is completed after all the pixels in the window are considered. Appropriate choices of the threshold depend on the granularity of the image. In these studies, we found that a $TF = 6$ was a reasonable value. A final PMF denoted by $FFr^{(\Delta_\alpha)}(g,N_{\Delta_\alpha})$ is obtained by:

$$FFr(g,N_{\Delta_\alpha}) = \frac{1}{\beta}\sum^{\beta} Fr^{(\Delta_\alpha)}(g,N_{\Delta_\alpha}) \tag{5.37}$$

Eq. (5.37) is in fact the "expected" PMF which is also a $G \times \sigma$ matrix obtained by averaging all the outputs according to the values of the threshold function TF.

5.6.4 Image Features Extraction From the PMFs

To establish a PMF from an original picture, the elements inside the selected σ-square are all considered. That is, the neighborhood about a point in all directions is taken into consideration. Hence, the PMFs are formed by using angularly independent features. Eq. (5.36) is used at one time (for each σ-square) in lieu of one direction at a time. This strategy eliminates the angular dependency, while on the other hand diminishes the amount of calculation needed to process a picture. More explicitly, we suppose that the final pseudo matrix of the fractal $FF(g,N_{\Delta_a})$ of an image can sufficiently define the concentration information. All of the considered features can be derived from the final PMF.

As mentioned previously, the entries of the PMFs are regarded as frequency counts of the grayness changeability of a processed picture. More precisely, two closely related measures are considered, from which all of the image features are extracted. These measures are derived from the final pseudo matrix of the fractal as described by eq. (5.37). The measures comprise the information dimension and the correlation dimension and are defined:

$$D_1 = -\frac{\sum_i p_i Log p_i \Big|_{\Delta_\alpha}}{Log(\sigma_{\min}) Log \sum^{G}\sum^{\sigma} FFr(g,N_{\Delta_a})} \tag{5.38}$$

$$D_2 = \tfrac{1}{2} \frac{Log \sum_i p_i^2 \Big|_{\Delta_\alpha}}{Log(\sigma_{\min}) Log \sum^{G} \sum^{\sigma} FFr(g, N_{\Delta_\alpha})} \tag{5.39}$$

where $\sigma_{\min}$ represents the smallest σ-square window. These features are utilized to characterize the smoke data.

5.6.5 Methodology

This portion describes the characterization of small scale spatial fluctuation of concentration within plumes. The description is based on the spatial variation of intensity and hence captures the relevant features of the image. One can take a large picture (full frame of smoke data) and subdivide it into nonoverlapping subimages. We denote such a vector by $X(D_1,D_2)$, where D_1 and D_2 are defined by eqs. (5.38) and (5.39), respectively. Each feature parameter vector was converted to a two-dimensional array where each element of the constructed array corresponds to a scaled value of the feature parameter estimated from the subimage of the original picture. If we denote such a 2-D array by $R(x,y)$, where x and y are the spatial coordinates of the array, then the elements of $R(x,y)$ are obtained by scaling the values of the feature parameters, i.e., kD_i ($i = 1,2$). In this approach several values have been tried, but $k = 100$ was found to be good. Similar smoke regions would have similar feature parameter vectors, but this case is rare since smoke data exhibits a chaotic statistical variation. For example, a simple category of region would be "smoke" (scattered above a specified level or "clear" (less scattered). Other categories include heaviest aerosol concentration, moderate scattered values and so forth.

5.6.6 Image Analysis Based on the Information and Correlation Dimensions

First, the entire area of a picture is divided into a 8 ×19 regions with 0% overlap as presented in figure 5.40. Each subimage contains 15 × 18 picture elements. A PMF is computed over each subimage. Then, the two features namely the information dimension and the correlation dimension were calculated using eqs. (5.38) and (5.39). In general, there is no rule available for choosing a window because the process and analysis depends on the image data.

Based on the methodologies described in the previous subsection, we created six different images from the computed information and correlation dimensions. Figures 5.41, 5.42, and 5.43 are the plots of the evaluated histograms of the information dimension for a typical frame of the sequence of smoke whose velocity was one, two, and four meters per second respectively. Surprisingly, these plots reflect the concentration fluctuations in a plume, illustrating plume intermittency as well as in-plume concentration fluctuations (Hanna, 1984). The peaks ("higher frequency") represent the in-plume turbulent fluctuations, whereas the valleys ("low frequency")

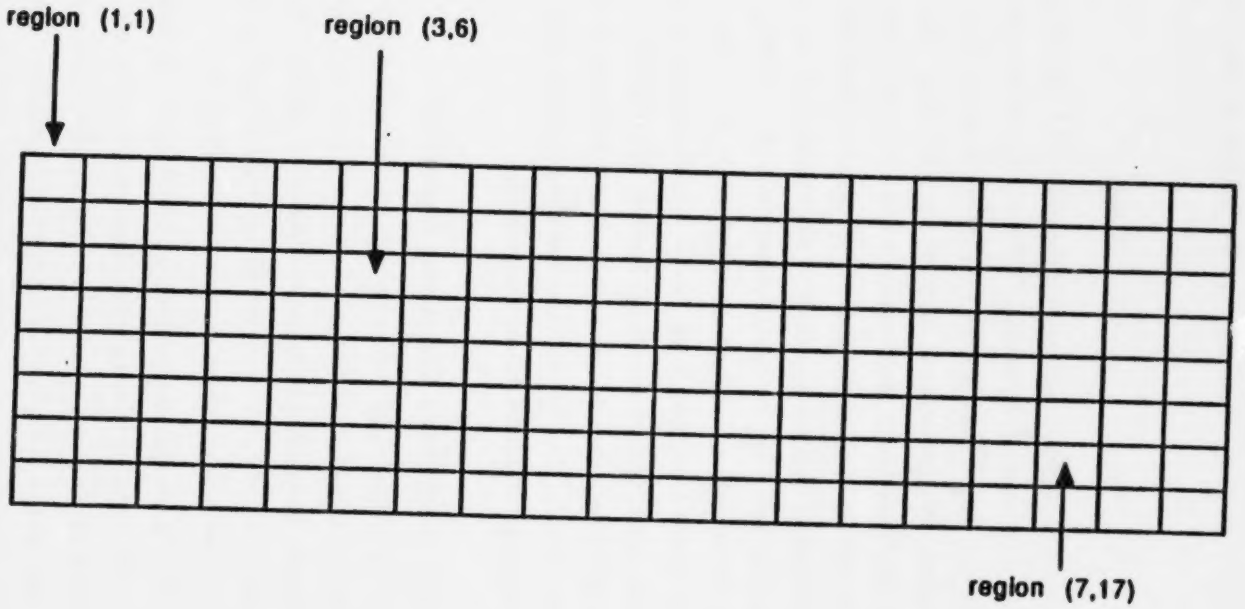
region (1,1)
region (3,6)
region (7,17)

Figure 5.40 Non-overlapping regionalized windows.

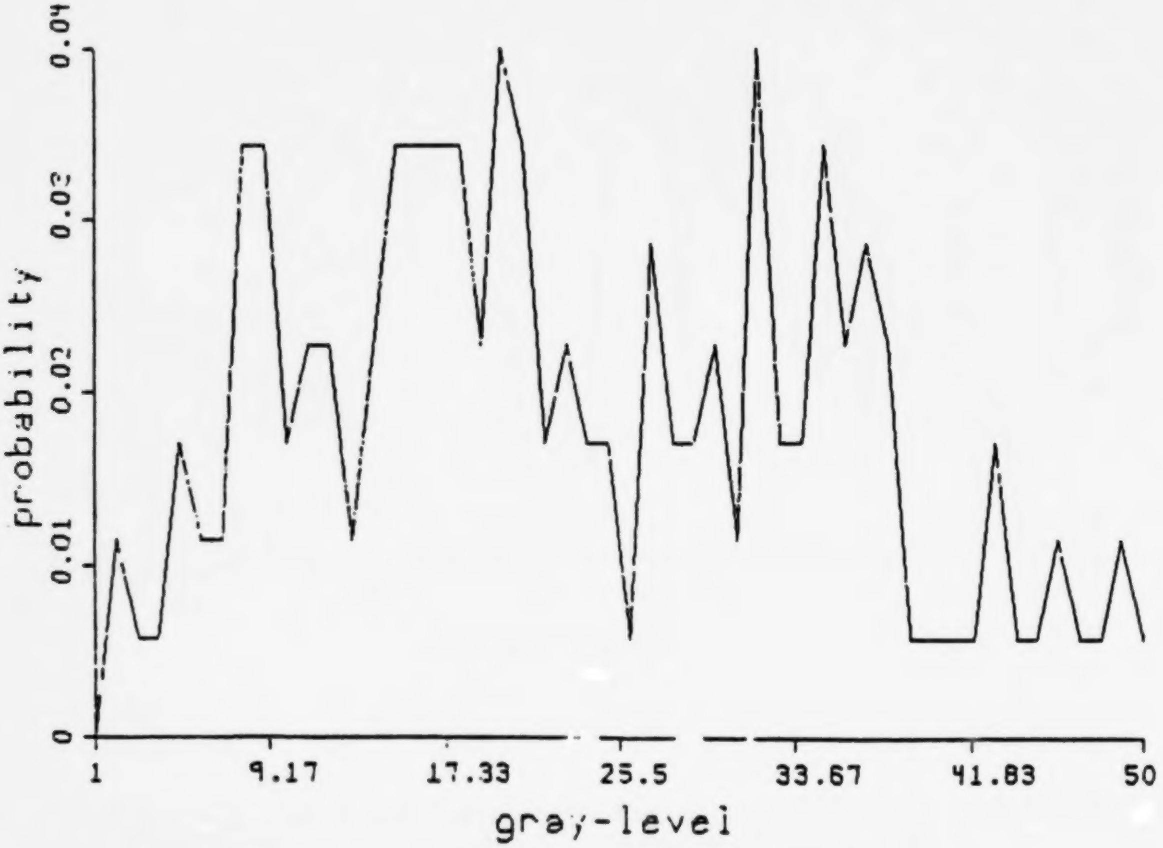

Figure 5.41 Concentration versus space-time information dimension with freestream wind speed of 1 m/s, time separation: 0.033 sec.

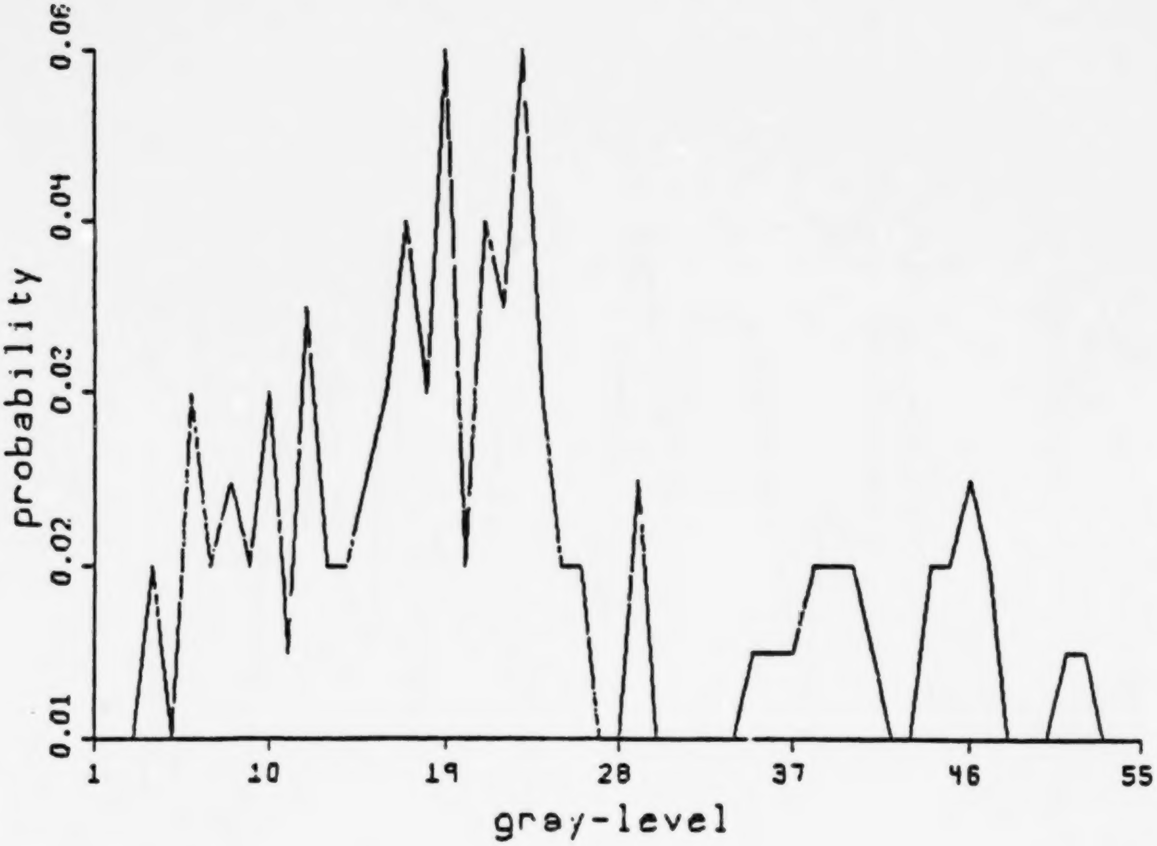

Figure 5.42 Concentration versus space-time information dimension with freestream wind speed of 2 m/s, time separation: 0.033 sec.

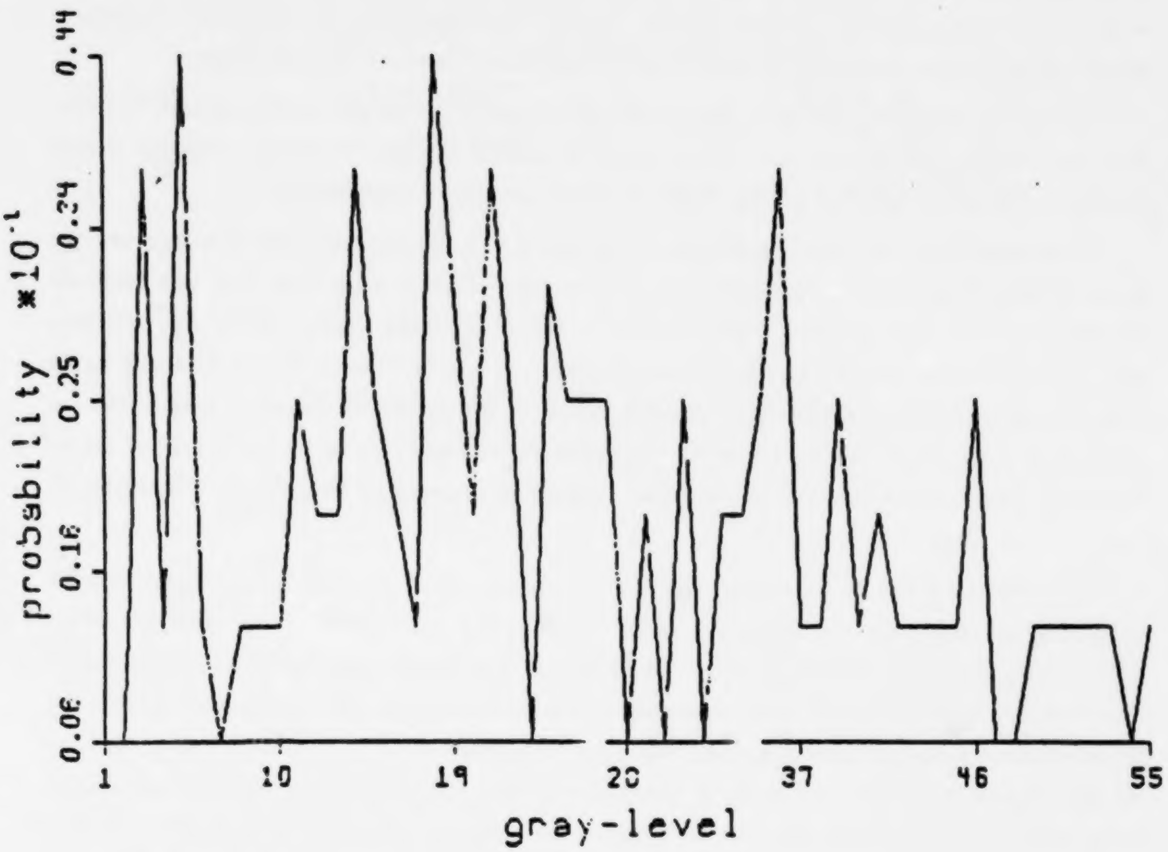

Figure 5.43 Concentration versus space-time information dimension with freestream wind speed of 4 m/s, time separation: 0.033 sec.

represent the periods with clean air or intermittency.

It is a typical of observed time series of concentration fluctuations that the fluctuations are at least as large as the mean (Hanna, 1984). It is worthwhile to mention that part of the fluctuations were probably due to emissions variability which were assumed to be negligible. These new results hence provide concentration fluctuations rather than just mean concentrations.

As can be seen from the three figures, the entire configuration alters with respect to variations in nominal velocity set ups. Hence small or middle changes in nominal velocity induce automatically substantial and sudden effects in smoke particle concentrations.

In the next step, we used the correlation dimension as a fundamental tool to understand the fitted profiles of smoke data as discussed in section 5.6.5. Figures 5.44, 5.45, and 5.46 illustrate the histograms of the correlation dimension for the frames of smoke whose velocity was one, two, and four meters per second respectively. Surprisingly, as can be seen in figures 5.44 and figure 5.45, the plots mirror the best-fitted profiles based on the empirical Gaussian model (Hanna, 1984). The positions of the maximum concentration are obviously closer to the source of smoke than were found downwind. The plot increases sharply to a maximum then decreases suddenly to form a Gaussian shape.

By comparing figures 5.44, 5.45, and 5.46, it is seen, that the smoke particle distribution changes with respect to the nominal velocity set up. The wide width of the Gaussian shape reflects regions closer to the source of smoke. In effect, these regions contains high level concentration. Further downwind, the plume dispersion was controlled by the background turbulence. Hence, these regions will reflect average and low level concentration. We believe these findings are also important because the strategy based on correlation dimension provides both simultaneously temporal and spatial features that cannot be obtained using the Gaussian (or similar) models to describe pollutant concentration distributions.

The same comments may be given as in the case of the information dimension; that is, the probability density function of concentration fluctuations may directly be related to the probability density function of turbulent velocity fluctuations as can be observed in figures 5.41-5.43.

Next, we studied how these two features (the information and correlation dimensions) vary with respect to time. We applied the technique to a sequence of frames separated by a short amount of time (0.66s). Figures 5.47, 5.48 and 5.49 show the plots of the histograms of the information dimension for frames of smoke data whose velocity was one, two and four meters per second respectively. As can be seen, these plots are similar to figures 5.41, 5.42 and 5.43. However, the locations of the plume intermittency and in-plume concentration fluctuations are different. Similarly, figures 5.50, 5.51 and 52. are the plots of the histograms of the correlation dimension for frames of smoke data whose velocity was one, two, and four meters per second,

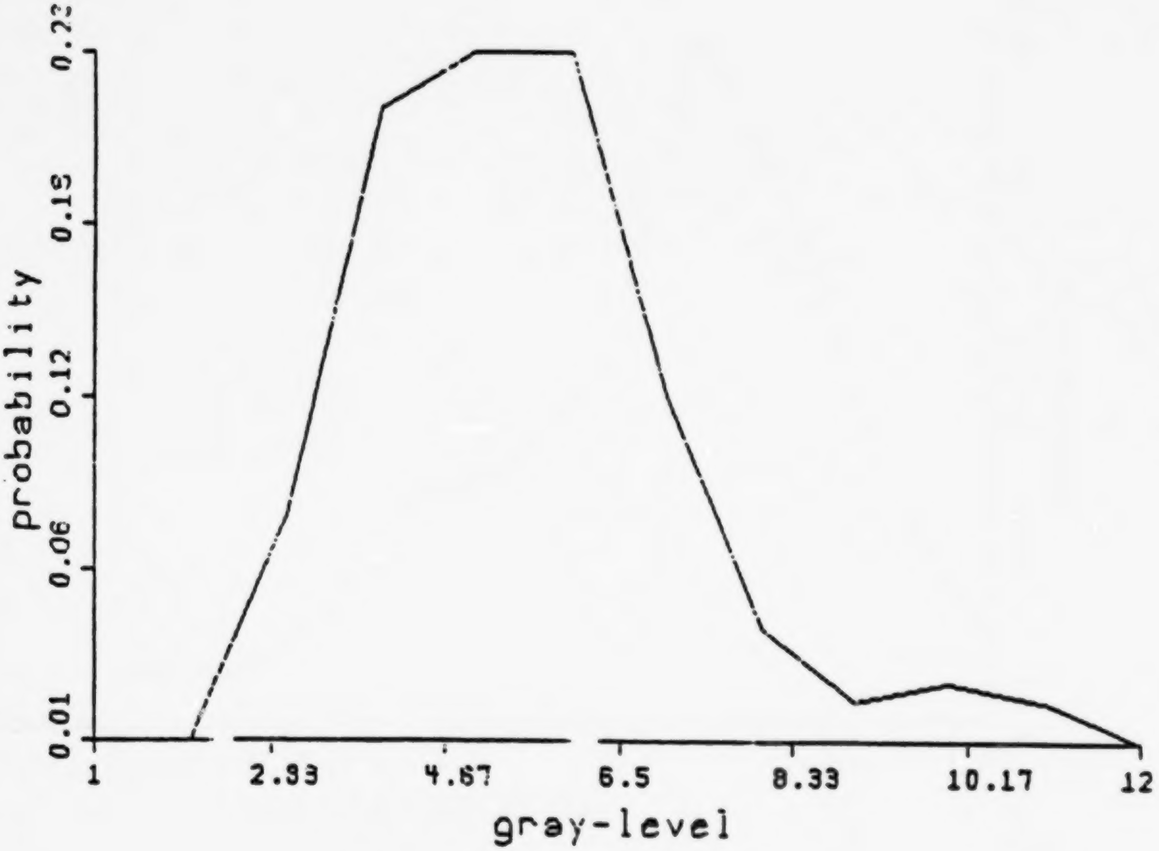

Figure 5.44 Concentration versus space-time correlation dimension with freestream wind speed of 1 m/s, time separation: 0.033 sec.

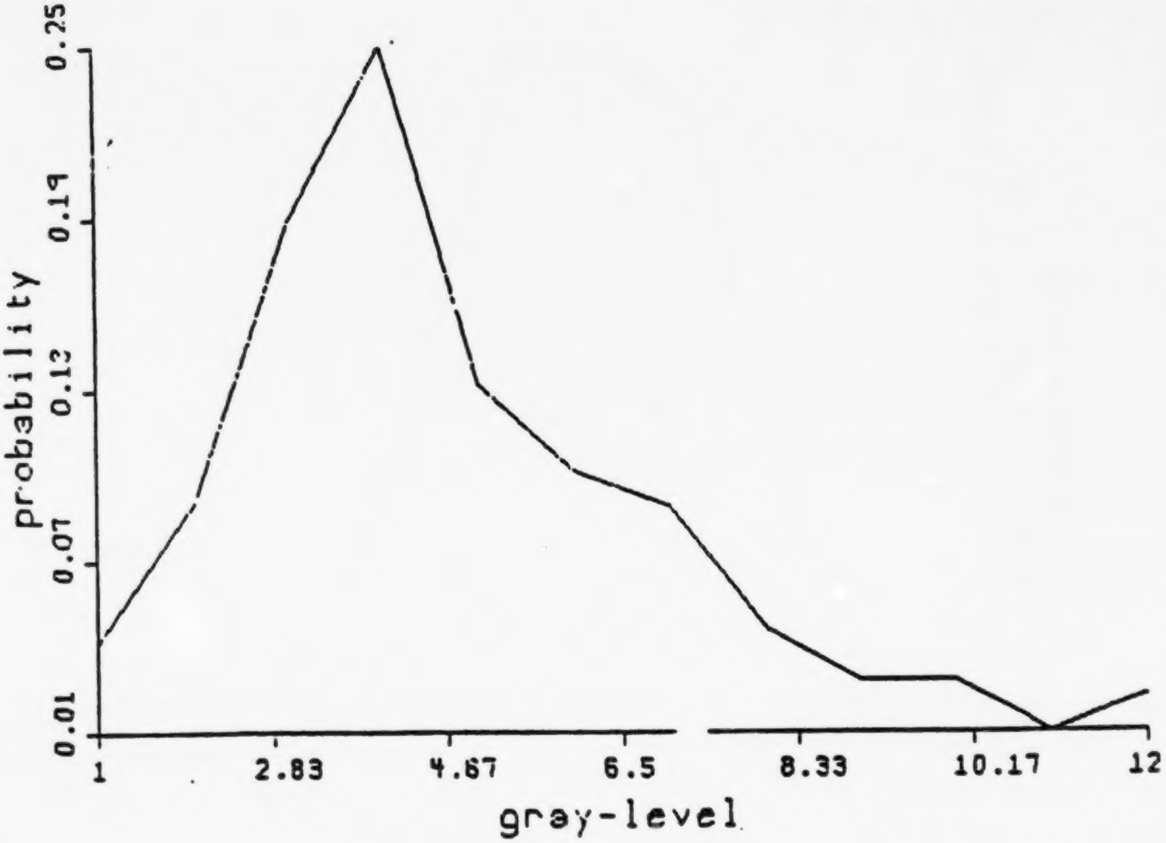

Figure 5.45 Concentration versus space-time correlation dimension with freestream wind speed of 2 m/s, time separation: 0.033 sec.

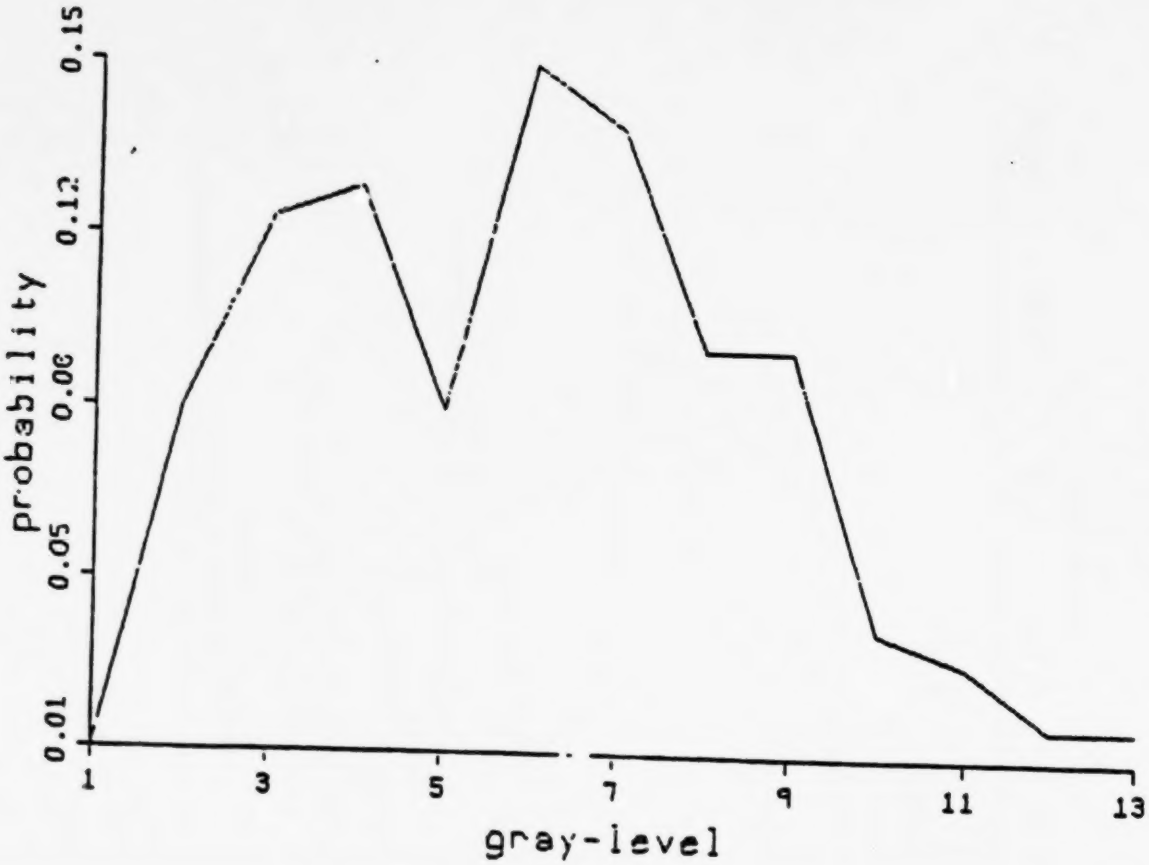

Figure 5.46 Concentration versus space-time correlation dimension with freestream wind speed of 4 m/s, time separation: 0.033 sec.

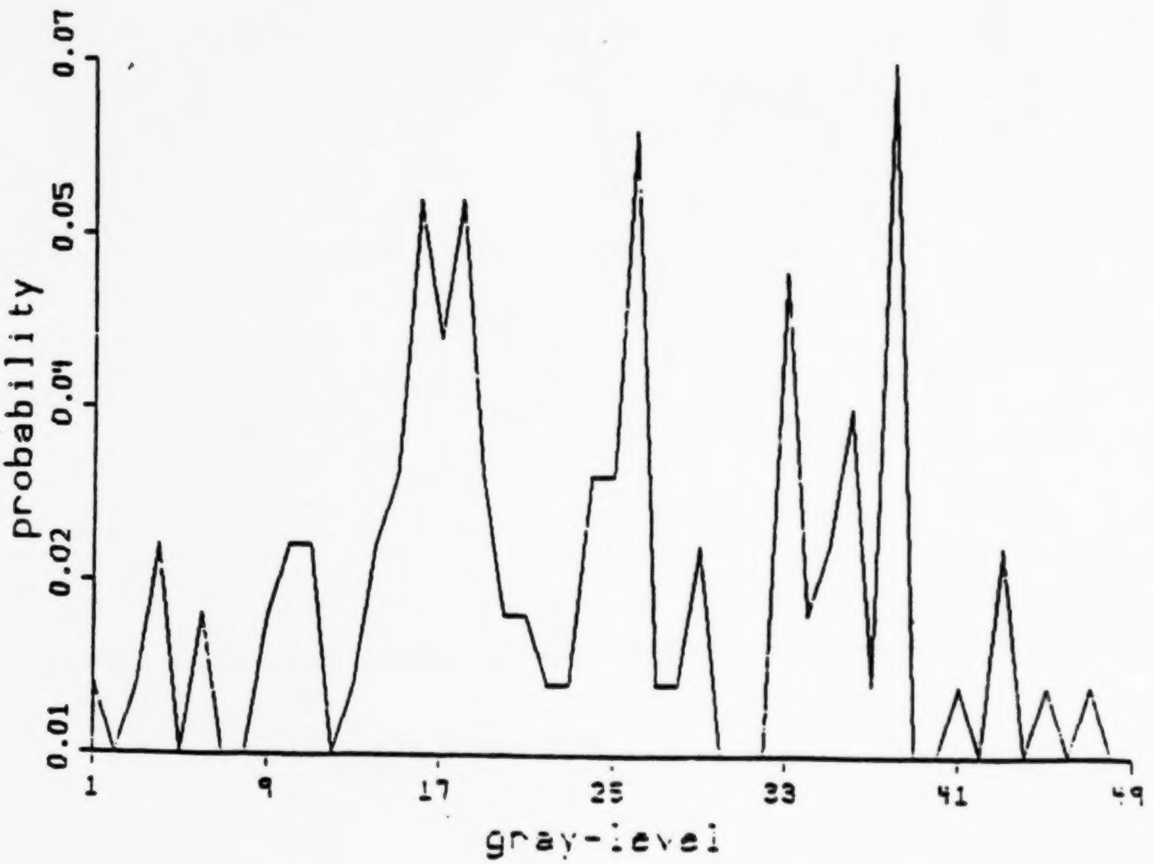

Figure 5.47 Concentration versus space-time information dimension with freestream wind speed of 1 m/s, time separation: 0.66 sec.

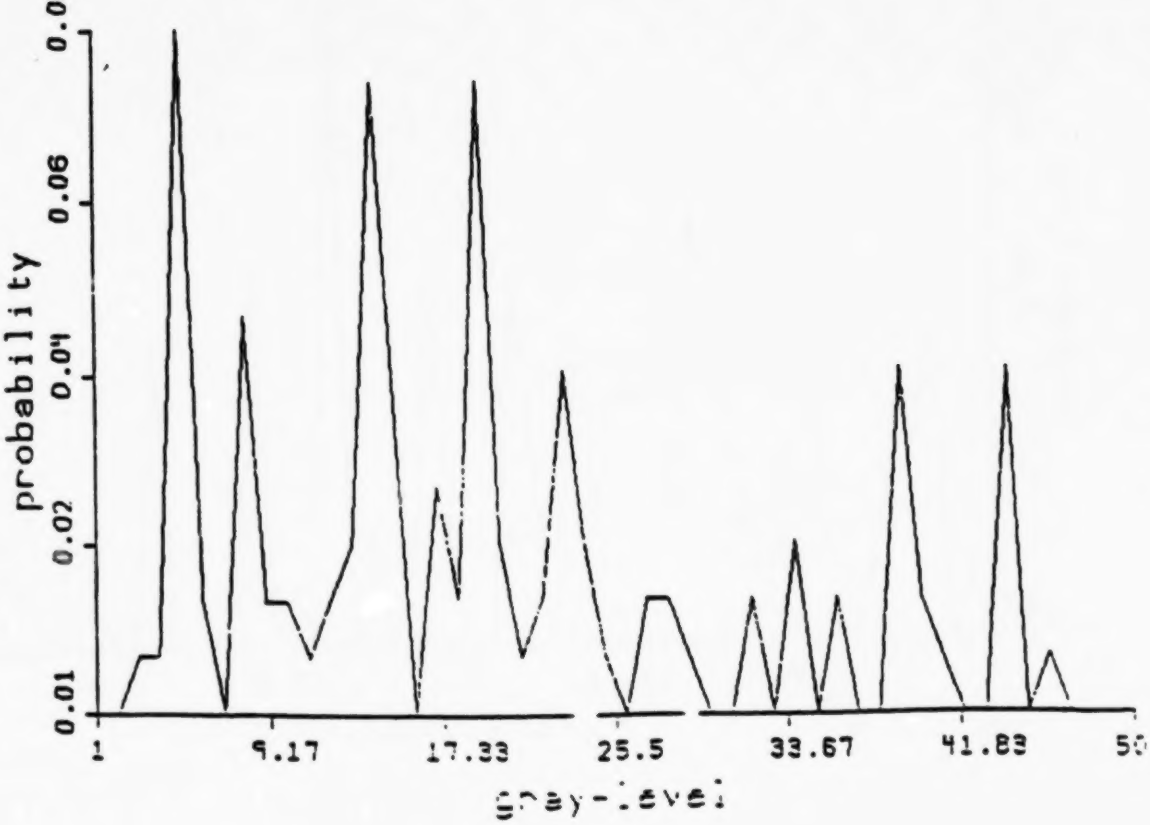

Figure 5.48 Concentration versus space-time information dimension with freestream wind speed of 2 m/s, time separation: 0.66 sec.

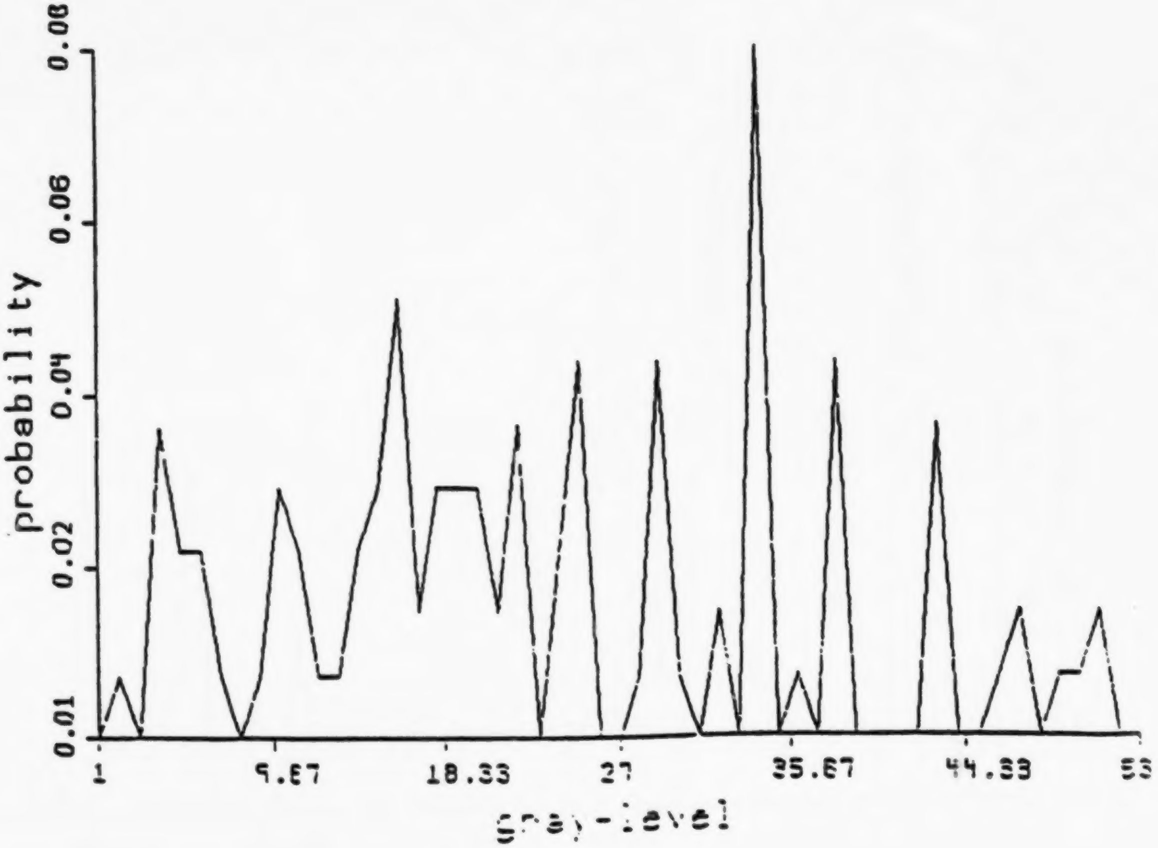

Figure 5.49 Concentration versus space-time information dimension with freestream wind speed of 4 m/s, time separation: 0.66 sec.

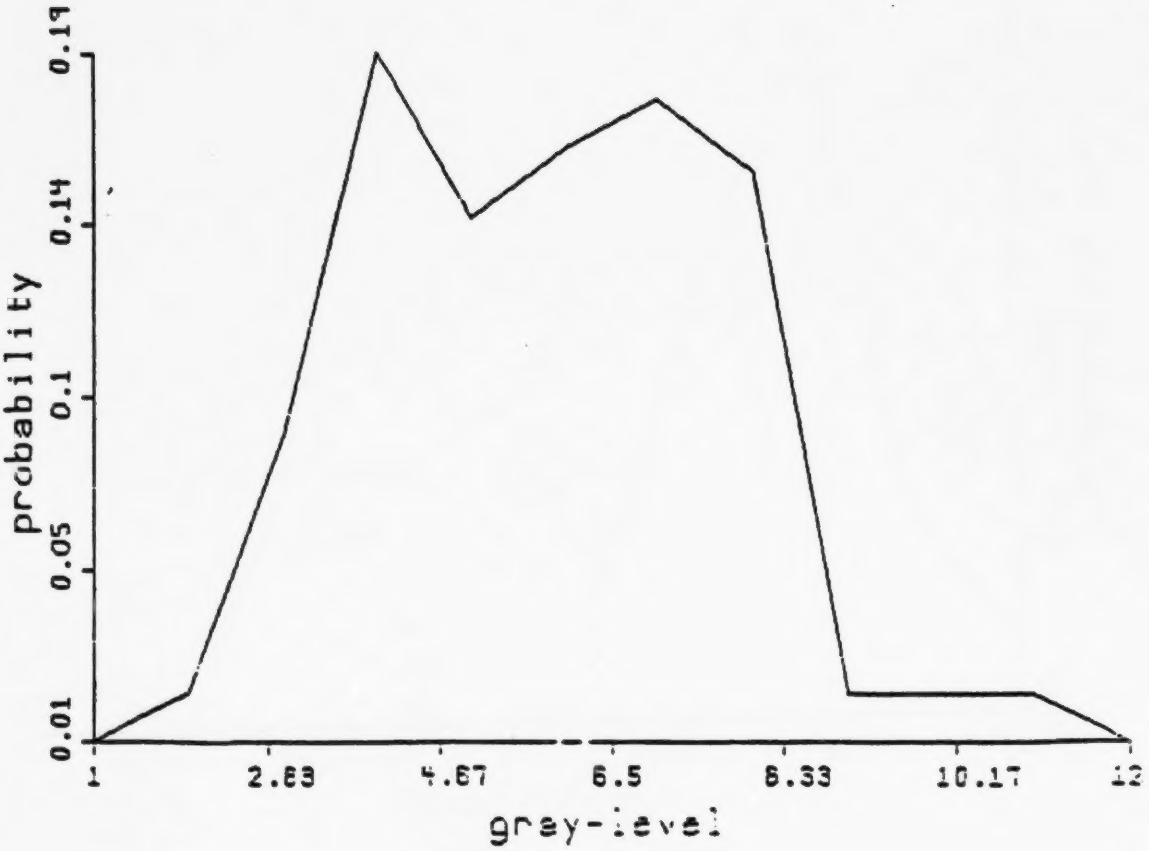

Figure 5.50 Concentration versus space-time correlation dimension with freestream wind speed of 1 m/s, time separation: 0.66 sec.

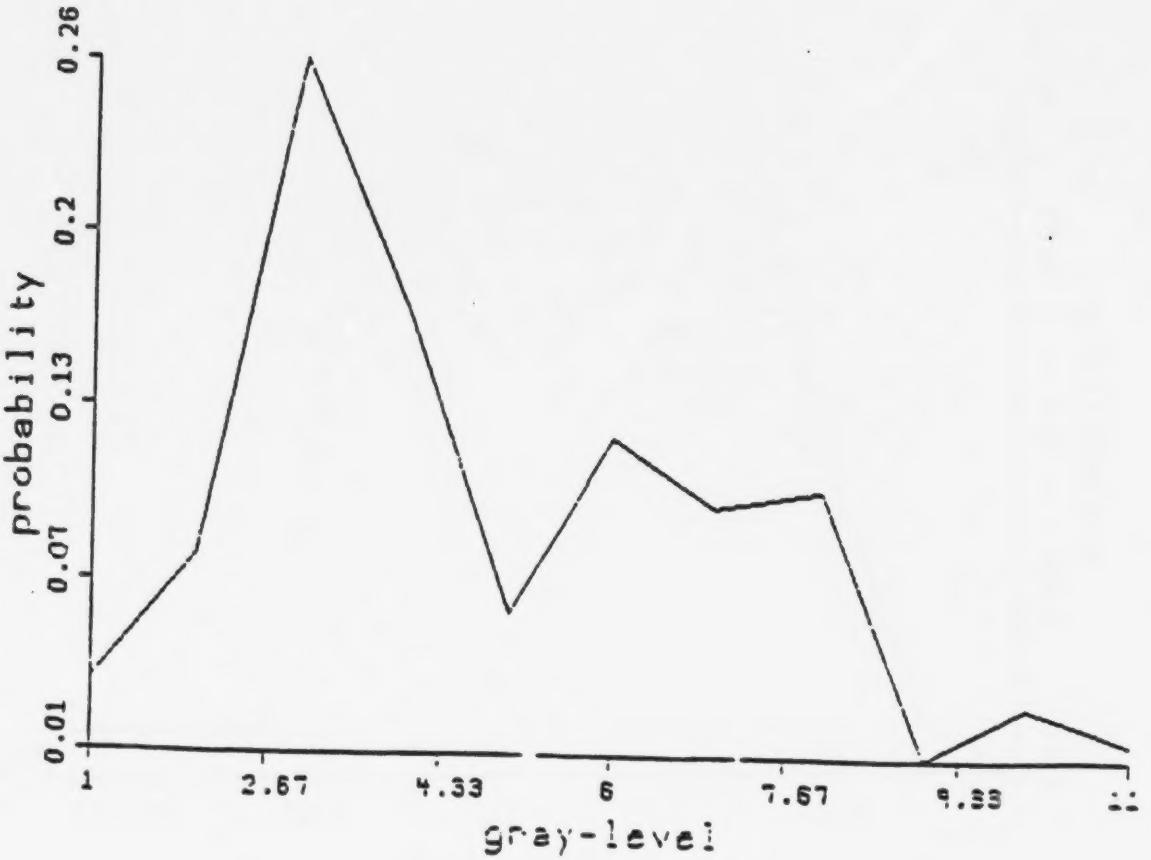

Figure 5.51 Concentration versus space-time correlation dimension with freestream wind speed of 2 m/s, time separation: 0.66 sec.

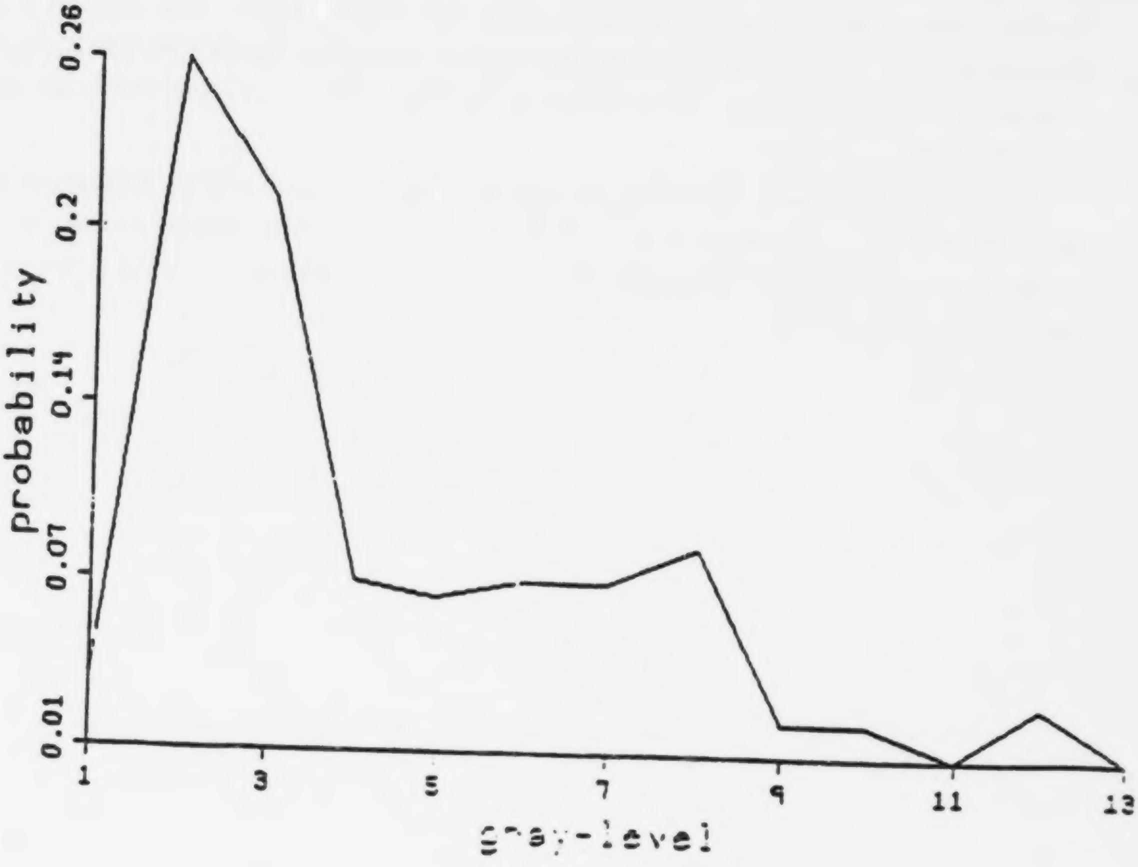

Figure 5.52 Concentration versus space-time correlation dimension with freestream wind speed of 4 m/s, time separation: 0.66 sec.

respectively. These figures also display a Gaussian shape.

Finally, using the same procedure, we investigated the two features but this time frames of the three different image sequences are separated by 2.66 seconds. Figures 5.53, 5.54 and 5.55 illustrate the plots of the histograms of the information dimension and figures 5.56, 5.57 and 5.58 show the plots of the histograms for the correlation dimension. The results are similar to the previous two cases.

There are several factors which may be responsible for the differences in the histograms for either the information dimension or the correlation dimension. These include, meteorological conditions in the wind tunnel and a slight decrease of total particulate matter in the plume with increasing downwind distance.

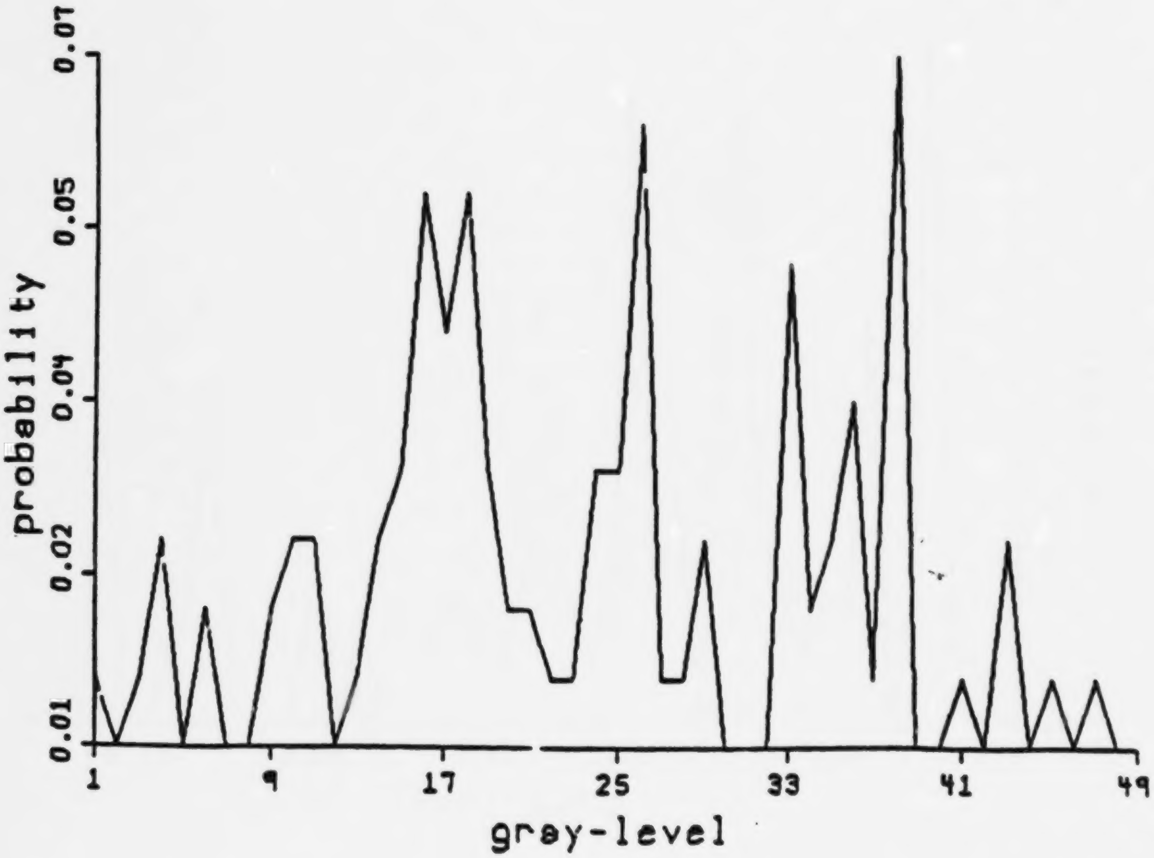

Figure 5.53 Concentration versus space-time information dimension with freestream wind speed of 1 m/s, time separation: 2.66 sec.

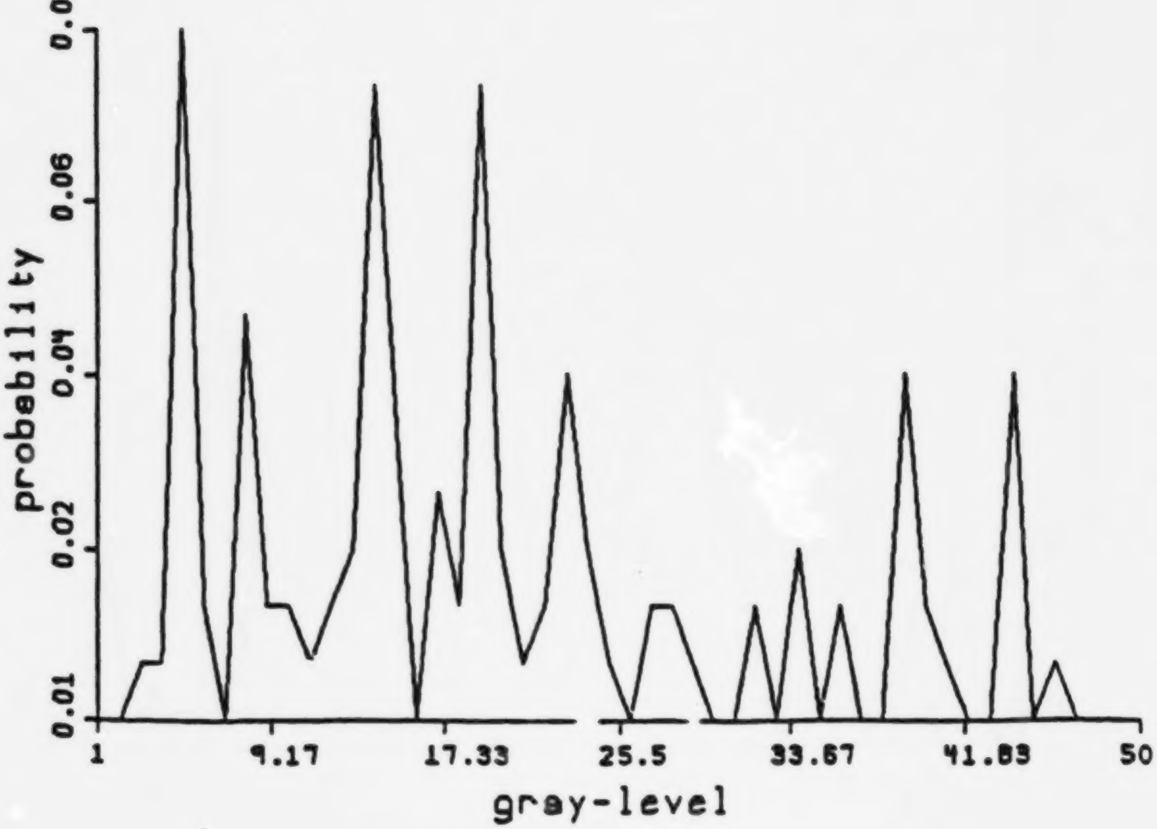

Figure 5.54 Concentration versus space-time information dimension with freestream wind speed of 2 m/s, time separation: 2.66 sec.

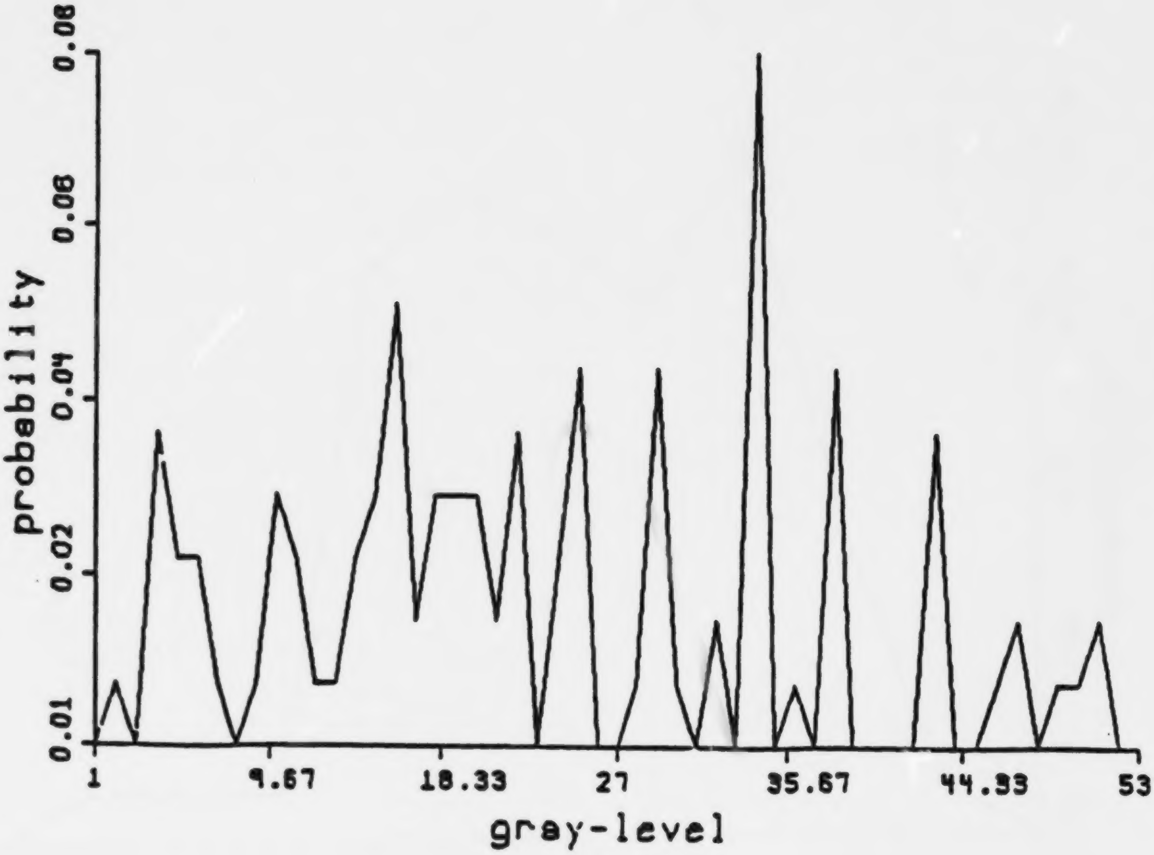

Figure 5.55 Concentration versus space-time information dimension with freestream wind speed of 4 m/s, time separation: 2.66 sec.

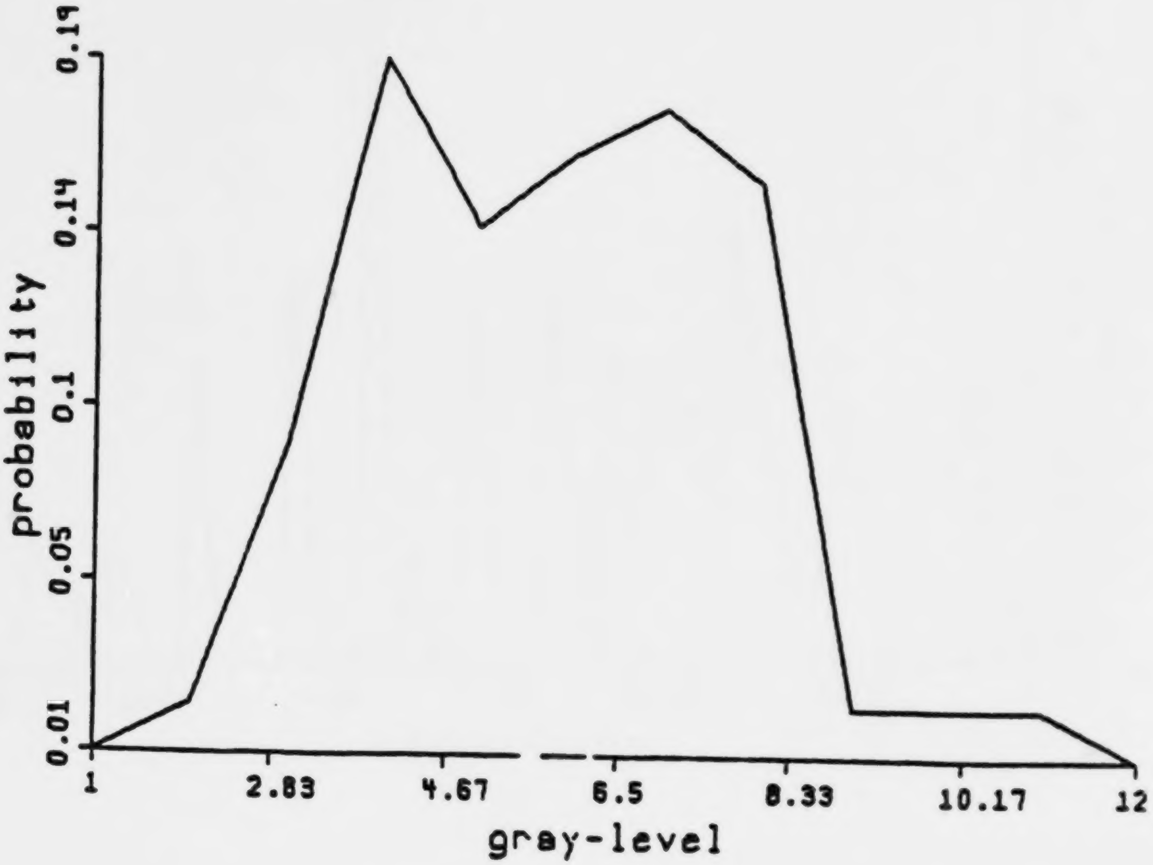

Figure 5.56 Concentration versus space-time correlation dimension with freestream wind speed of 1 m/s, time separation: 2.66 sec.

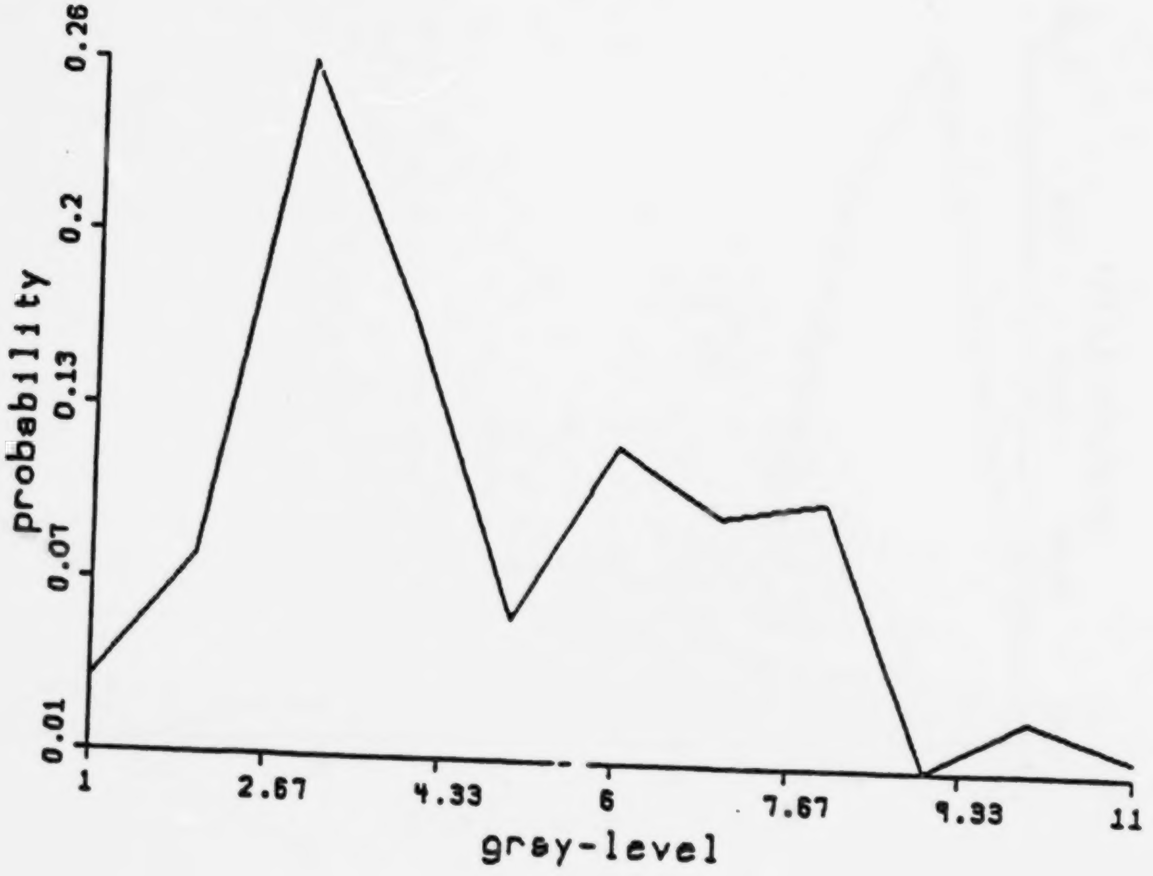

Figure 5.57 Concentration versus space-time correlation dimension with freestream wind speed of 2 m/s, time separation: 2.66 sec.

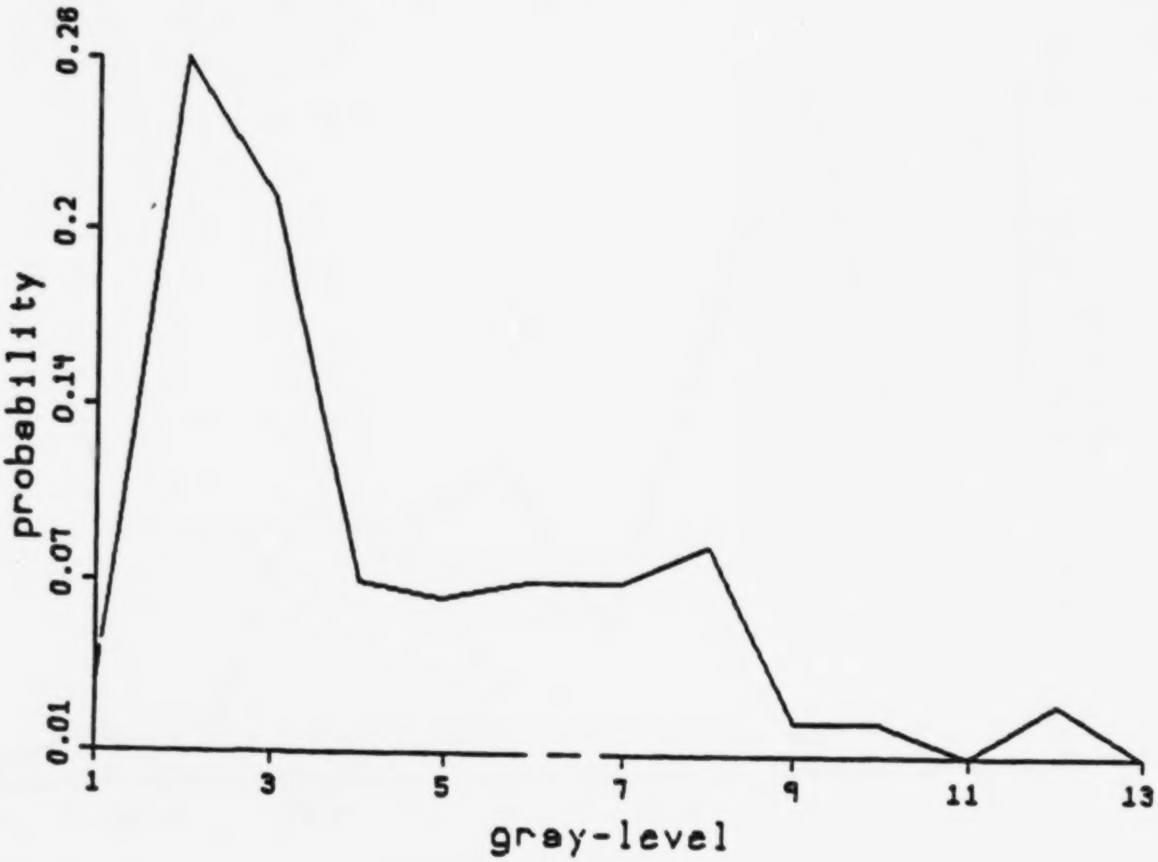

Figure 5.58 Concentration versus space-time correlation dimension with freestream wind speed of 4 m/s, time separation: 2.66 sec.

6 VISUALIZATION OF SMOKE DISPERSION USING LASER LIGHT SHEETS

6.1 Introduction

A popular method of visualizing fluid flow is to illuminate the flow with thin sheets of laser light. This method can be implemented via laser beam divergence techniques (Mueller, 1985; Brandt, 1985; Stanlisas, 1985; Veret, 1985; Porcar et al., 1985; Stapountzis et al., 1987; and Porcar and Prenel, 1982) or laser beam scanning techniques (Porcar et al., 1985; Porcar and Prenel, 1982; Balint et al., 1985; and Prenel et al., 1987). Two of these techniques were utilized for a pollution dispersion study carried out in a wind tunnel. Results of the method as applied in the experiment are presented in this report.

6.2 Experimental Arrangement

The experiment was conducted in the U.S. Environmental Protection Agency's Meteorological Wind Tunnel at Research Triangle Park, North Carolina. The wind tunnel has a test section 3.7 meters wide, 2.1 meters high, and 18.3 meters long. Smoke, generated in the form of vaporized paraffin oil, was released from floor level at the approximate center of the width of the wind tunnel. In order to facilitate referencing positions within the wind tunnel, this smoke source will be designated as the origin of a three dimensional coordinate system. An axis along the length of the tunnel and intersecting the origin will be referred to as the x axis. Positive values of x lie on the downstream side of the origin. The axis along the width of the tunnel and intersecting the origin will be referred to as the y axis. Positive y coordinates extend from the origin away from the source of illumination. The z axis intersects the origin and extends vertically above the floor of the wind tunnel. All z values within the tunnel are positive. See figure 6.1.

The wind tunnel floor was covered with gravel, having diameters smaller than 10mm, except for a section covered by a paper material in the form of honeycomb. The honeycomb, which was flat black, served as a low reflectance background for observations recorded from above. This section covered the rectangular area from approximately $x = 80$ cm to $x = -50$ cm and from $y = -56$ cm to $y = 65$ cm. Throughout this report, it will be referred to as the area of observation or the area of observational interest. Small light colored clay markers with diameters of approximately 1 cm were placed on top of the honeycomb at measured distances to aid in the location and measurement of recorded data.

A building model was placed on the honeycomb with its downstream side at $x = -1$ cm, centered with respect to $y = 0$. A Pulnix Model TM540 CCD camera was mounted looking down through a ceiling window, producing an overhead view of the test section of interest. This experimental arrangement had been set up for a previous series of flow visualization experiments using

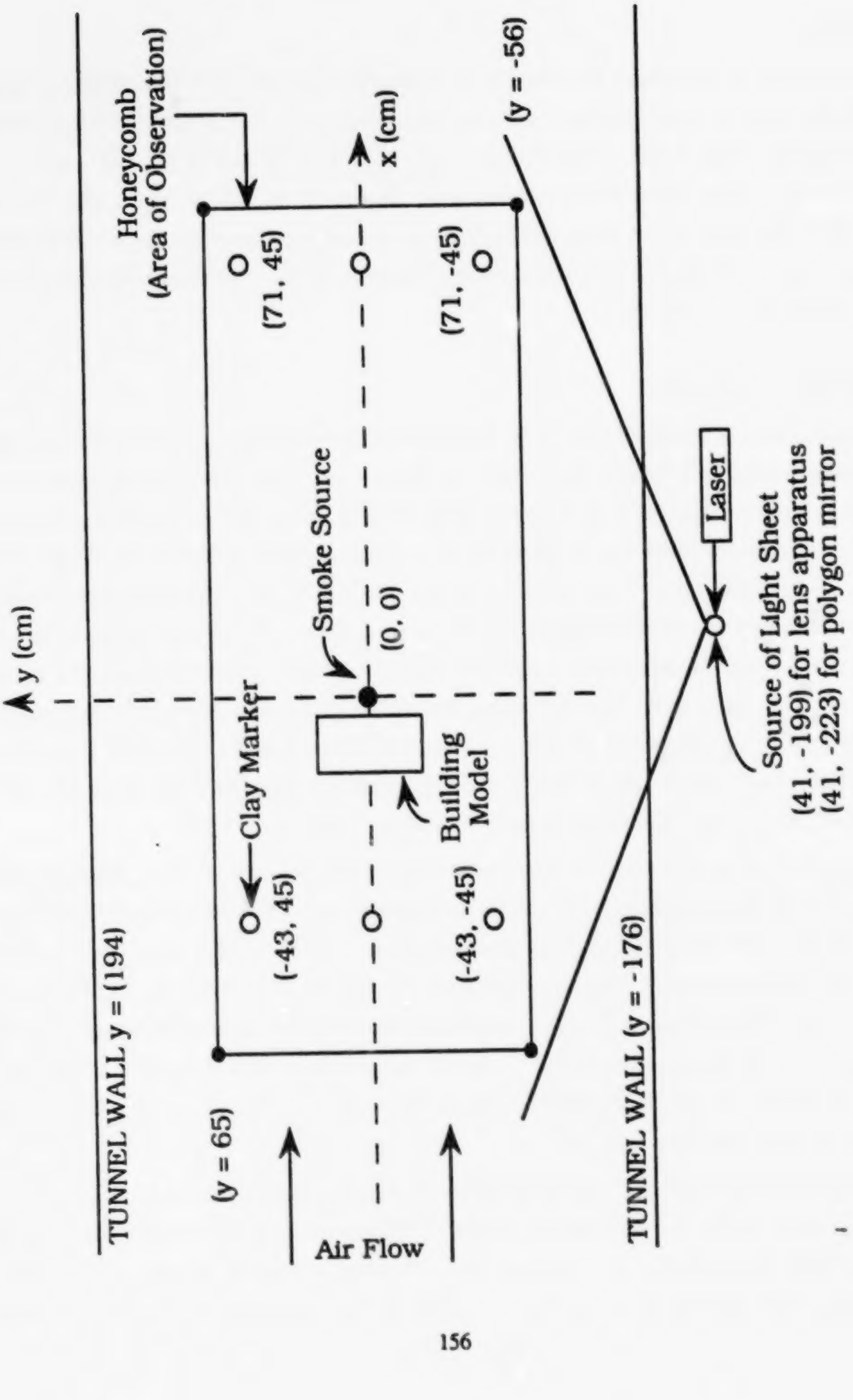
TUNNEL WALL y = (194)
TUNNEL WALL (y = -176)
Honeycomb
(Area of Observation)
x (cm)
y (cm)
(y = 65)
(y = -56)
Air Flow
Clay Marker
(-43, 45)
(-43, -45)
(71, 45)
(71, -45)
Smoke Source
(0, 0)
Building
Model
Laser
Source of Light Sheet
(41, -199) for lens apparatus
(41, -223) for polygon mirror

Figure 6.1. Top view of experiment

fluorescent lighting (Lee et al., 1989). The fluorescent illumination was replaced with laser lighting for the experiments discussed here.

A Spectra-Physics Model 164 argon laser was placed outside of a side window of the wind tunnel. It was a continuous wave laser, capable of producing a beam with a power of five watts. The laser was operated in the multi-line mode, with wavelengths from 488 nm to 514 nm. During the experimentation, it was normally set for a power output of either 2.0 watts or 2.5 watts. The beam has an approximate diameter of 1 mm with a divergence of approximately 0.7 mrad. See figure 6.2.

Two devices which produced horizontal sheets of laser light were developed for use with the laser. The first device contained a polygonal mirror which rotated on a motor shaft. The laser beam struck the rotating polygonal mirror facets and was scanned along a horizontal plane, effectively producing a horizontal sheet of light. The polygonal mirror was positioned outside a side window at a position (x = 41 cm, y = -223 cm). The laser and polygonal mirror apparatus were mounted on a platform which could be raised and lowered to the desired vertical heights (z).

The second device contained a first-surface mirror and several lenses. The laser beam was reflected by the mirror and passed through the lenses. The lenses spread the beam into a horizontal sheet of light. The outermost lens was located at the position (x = 41 cm, y = -199 cm). This system was mounted on a platform which could be raised and lowered.

Both the polygonal mirror and lens arrangements produced light sheets which originated from a point source and spread out in a polar fashion. Theoretically, illumination of this type is inversely proportional to the radial distance from the source. It is not jointly uniform with respect to the x and y axes. Therefore, the recorded image data must be transformed to represent data uniformly illuminated over the entire x-y plane. In addition to correcting for illumination effects, this transformation must also correct for the non-linear recording effects of the camera.

Illumination which is uniform over the x-y plane can sometimes be produced using additional mirrors and lenses (Stanlisas, 1985; Arnold et al., 1987; and Merzkirch, 1974). This type of arrangement requires the mirrors and lenses to be at least as large as one side of the observational area of interest. Consequently, the arrangement is limited to relatively small observational areas. Since the experiment presented here utilized an observational area of approximately 120 cm by 130 cm, such methods were found to be impractical.

The illumination of smoke flows using the polygonal mirror and lens systems is illustrated in figure 6.3. It is seen that the lens system produced a thinner sheet of light than the polygonal mirror system.

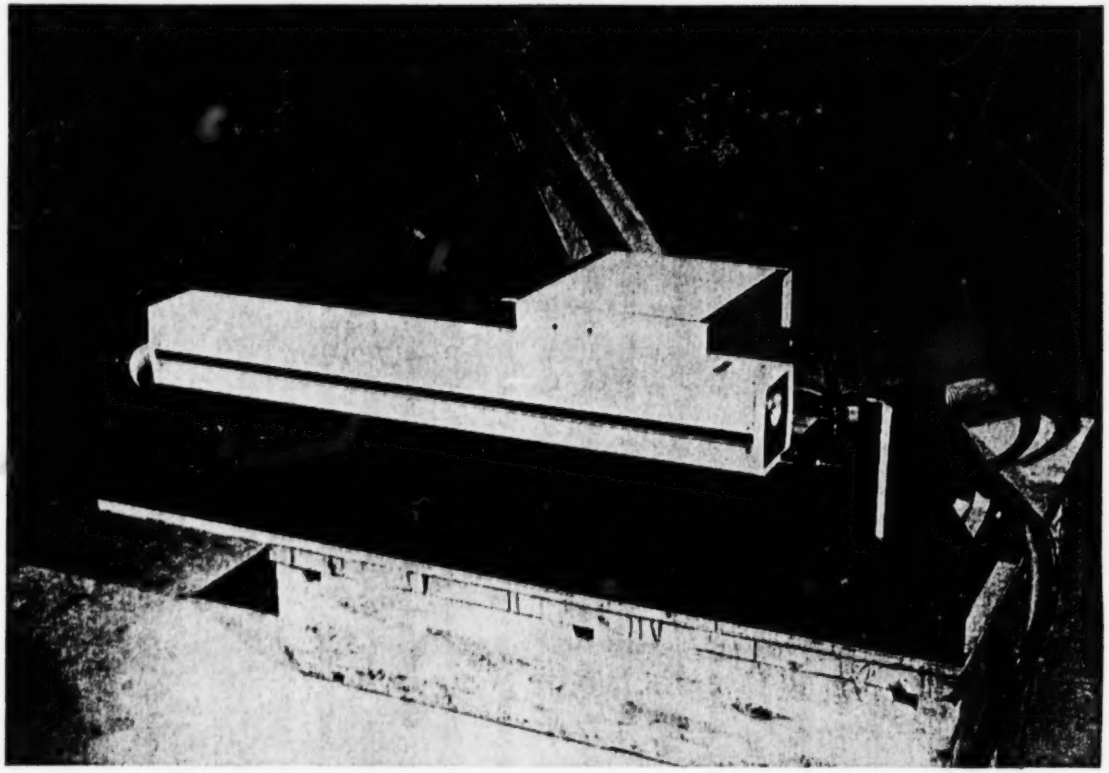

Figure 6.2 Laser system.

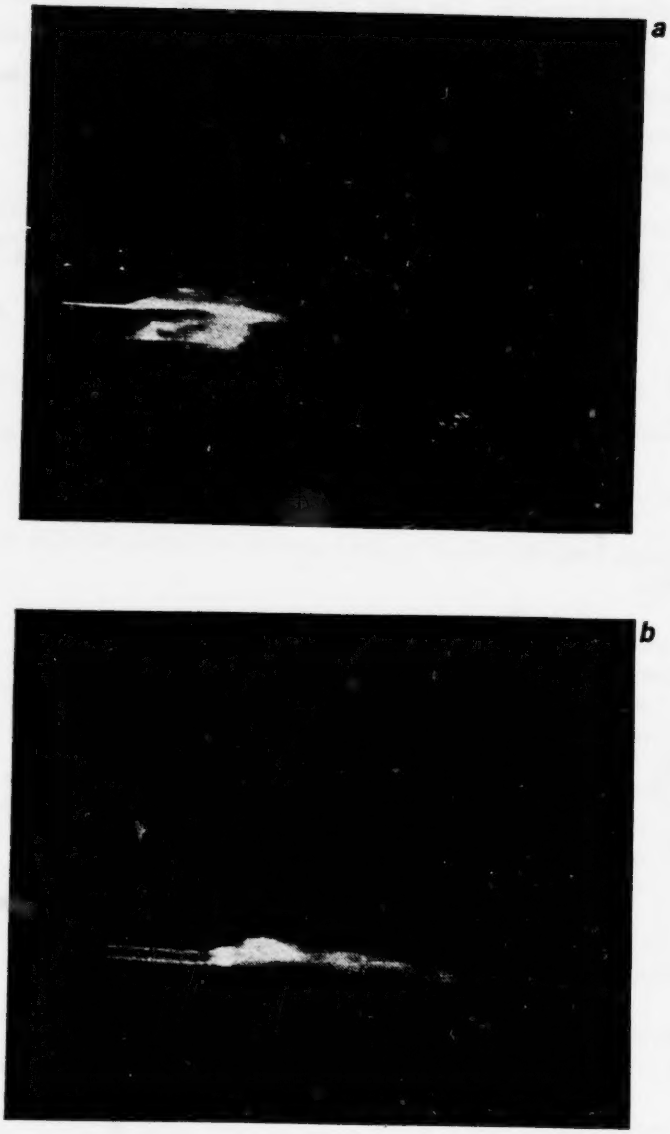

Figure 6.3 Laser light sheet illumination.
(a) Lens system.
(b) Polygonal mirror system.

6.3 Rotating Polygonal Mirror Method of Producing Light Sheets

One common method for producing thin light sheets is to reflect a laser beam off of a rotating polygonal mirror. The polygonal mirror is mounted on a mechanism such as a motor shaft which provides consistent rotation. The laser beam is directed so that it reflects off of the facets of the rotating polygon, which produces sweeps of the laser beam. When rotated at rates much higher than the sampling rate of the observing mechanism, the sweeping beams serve as a continuous sheet of light. See figure 6.4.

Some advantages of a polygonal mirror system are:

* The intensity of the resulting light sheet should be fairly consistent from one angular increment to the next. This, of course, assumes that the frequency of the beam scan is very large.

* Light sheets can be produced with well defined edges.

* Light sheets can be produced which cover large areas at high beam scanning rates.

Some disadvantages of a polygonal mirror system are:

* It requires a motor and some type of electronic speed control.

* The scan frequency must be great enough to prevent aliasing and degradation problems.

* If the motor shaft is not rotating while the laser is on, the laser beam will not sweep. The output power of the laser will be concentrated in the stationary beam, rather than spread out over a large area. Consequently, the danger to humans due to beam exposure is considerable.

* It is difficult to produce light sheets which are adequately thin when the area to be illuminated is large. This depends on the consistency of the facet-to-rotational centerline angle, the straightness of the motor shaft, and the coupling between the polygon and the motor shaft.

* A polygon system which produces horizontal sheets of light is not easily adjusted to produce vertical sheets of light.

* Polygonal mirrors are fairly expensive. Prices range from several hundred dollars to several thousand dollars.

6.3.1 Design Considerations

These polygonal mirrors are typically machined from beryllium, steel, or aluminum. These materials vary in weight, modulus of elasticity, and Poisson's ratio. Consequently, they also have different distortion factors. Beryllium has the best overall physical properties, but it is by far the most expensive choice (Speedring; Beiser, 1974; and Hayosh, 1976).

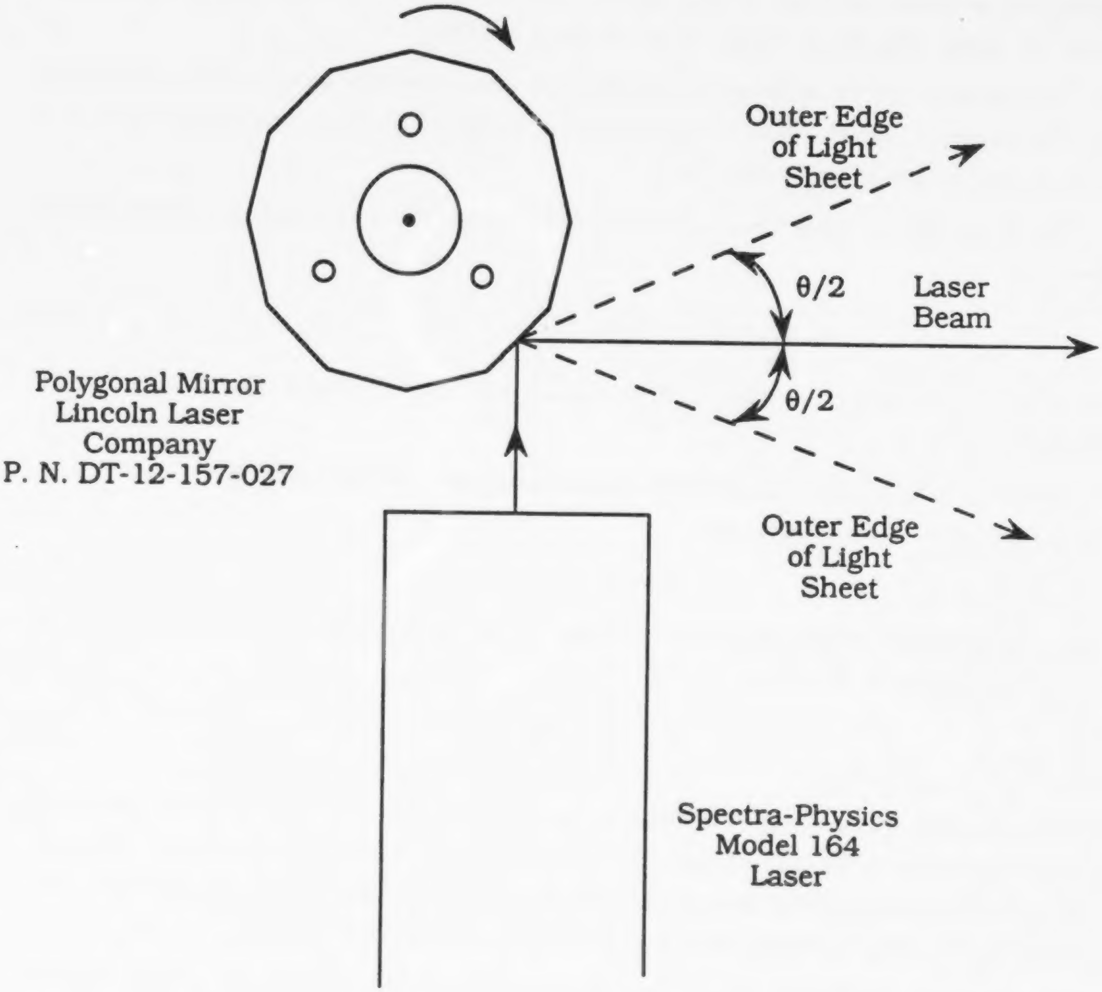
Outer Edge of Light Sheet
θ/2
Laser Beam
θ/2
Polygonal Mirror Lincoln Laser Company P. N. DT-12-157-027
Outer Edge of Light Sheet
Spectra-Physics Model 164 Laser

Figure 6.4. Laser light sheet produced using polygonal mirror

The facets of the polygon are usually plated to improve surface characteristics. The most common plating is electroless nickel. The facets are then polished to the required surface flatness. An alternative to a polished electroless nickel surface is a diamond machined surface. Finally, a coating such as silicon monoxide or magnesium fluoride is applied to enhance the reflectivity and protect the surface (Speedring; Beiser, 1974; and Hayosh, 1976).

The optimum number of facets on the polygonal mirror depends on each particular application. The number of facets affects the maximum sweep angle of the beam, the sweep frequency of the beam, and the size of each mirror facet.

The relationship between the maximum beam sweep angle and the number of polygon facets is given by:

$$\theta = \frac{720^\circ}{n} \tag{6.1}$$

where θ is the maximum sweep angle of the laser beam and n is the number of facets on the polygonal mirror.

Referring to figure 6.5, it is seen that the coverage width of the light sheet at a distance r from the polygonal mirror is given by:

$$c = 2\,[r \tan(\theta/2)] \tag{6.2}$$

where r is the distance from the polygonal mirror along the light sheet centerline and c is the width of the light sheet at a distance r. Thus,

$$n = \frac{720^\circ}{2 \arctan[c/(2r)]} \tag{6.3}$$

The number of facets on the polygon is also related to the size of each facet. Assume for now that the radius of the polygon (i.e., the distance from the center of the polygon to the center of each facet) is given. As the number of facets increases, the size of each facet decreases. And, of course, as the number of facets decreases, the size of each facet increases.

An extremely small facet size is unacceptable. When a laser beam with a finite diameter strikes a corner of the polygon between two facets, a portion will reflect off one facet and the remaining portion will reflect off of the other facet. Consequently, two separate rotating beams will result simultaneously at opposite outer edges of the light sheet. Beiser (1974) refers to the period of time during which this vignetting effect occurs as the retrace interval. This phenomenon will degrade and extend the outer edges of the sheet. Therefore, the length of the polygon facet (from corner to corner) should be considerably larger than the diameter of the laser beam in order to avoid degradation of a significant portion of the light sheet.

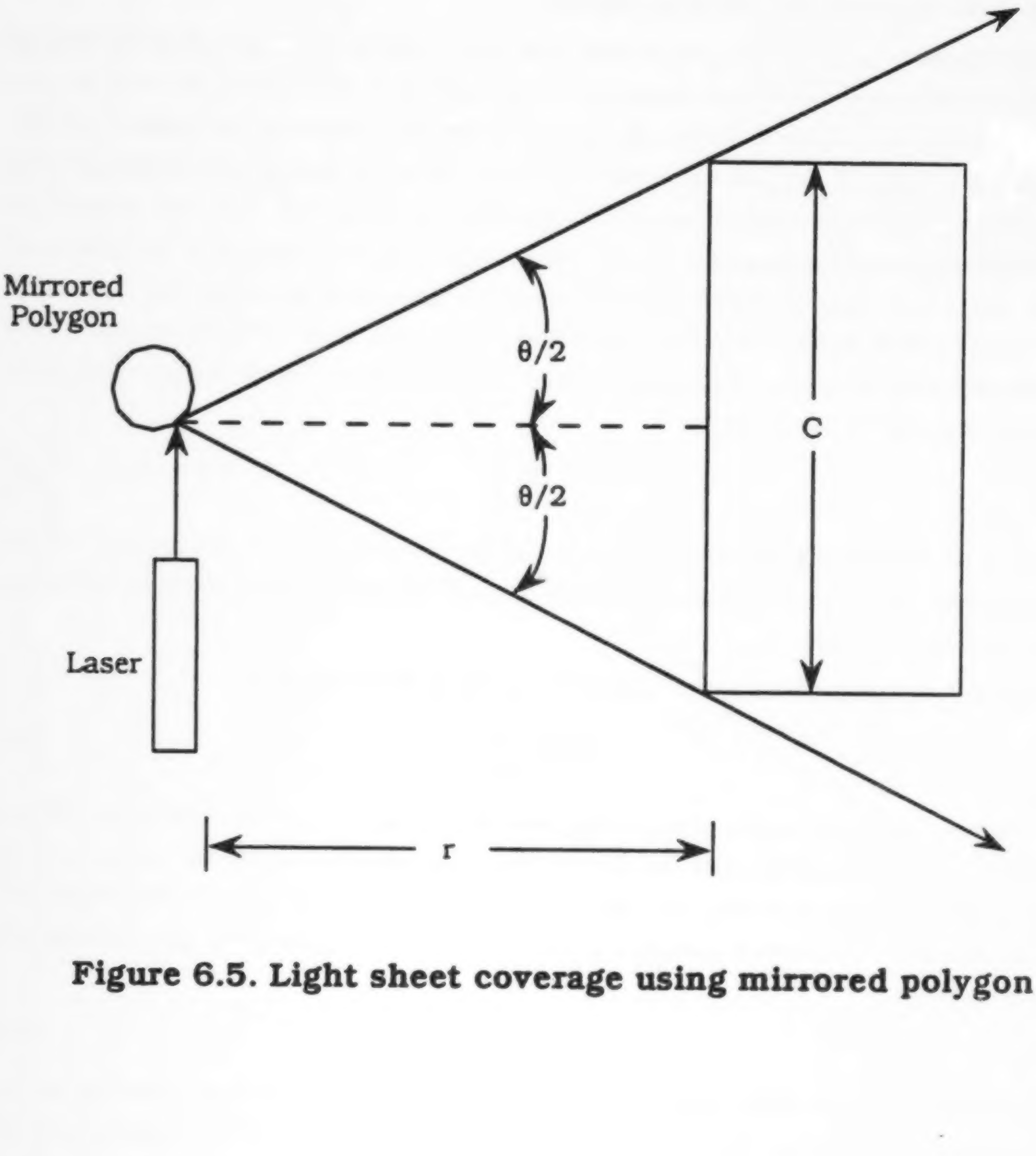
Mirrored Polygon
θ/2
θ/2
C
Laser
r

Figure 6.5. Light sheet coverage using mirrored polygon

A polygon with many facets can have an acceptable facet size if its radius is large enough. Unfortunately, the mass of the polygon increases as its radius increases. As the mass increases, the torque requirement on the motor increases. Consequently, as the polygon radius increases, the size of the required motor usually increases also.

The frequency of the beam sweep is very important. Ideally, the beam will sweep through the area of observation many times during each charge period of the photo elements in the camera. As a result, each frame of the recorded image will appear to have been illuminated by a constant source of light. If the laser sweep period is shorter than, but comparable to, the photo element charge period, each image frame will be inconsistently illuminated. The only exception to this generalization is when the photo element charge period is an exact multiple of the laser sweep period. If the laser sweep period is longer than the photo element charge period, only a portion of the test area will be illuminated in each image field. As a result, aliasing is quite obvious when a sequence of frames is viewed. The number of beam scans per photo element charge period can be calculated from the following relation:

$$s = \frac{nwQ}{60} \tag{6.4}$$

where s is the number of beam scans per photo element charge period, n is the number of facets on the polygon, w is the motor shaft speed, in RPM, and Q is the charge period of the photo elements, in units of seconds.

The required motor shaft speed to prevent aliasing can be found using:

$$w = 60 \, \frac{s}{nQ} \tag{6.5}$$

Another important consideration is the thickness, or wobble, of the light sheet. This is dependent upon the consistency of the facet-to-rotational centerline angle, the accuracy of the motor shaft-to-polygon coupling, and the straightness of the motor shaft. The relationship between the facet-to-rotational centerline angular error and the thickness of the resulting light sheet is given by:

$$t = r \tan(\epsilon) + d \tag{6.6}$$

where t is the thickness of light sheet due to an inconsistent facet-to-rotational centerline angle, r is the distance from the polygonal mirror, ϵ is the maximum difference of the facet-to-rotational centerline angles of two facets, and d is the diameter of the original laser beam (exiting the laser).

Commercially available polygons will often have facet-to-rotational centerline consistencies of 5 arc-seconds or better. This gives a thickness increase of 0.048 mm at a distance of 2 m, which is quite small. Any appreciable wobble in the light sheet can therefore be attributed to problems with the shaft or shaft couplings rather than to polygon inaccuracy.

6.3.2 Implementation

A Model DT-12-157-027 polygonal mirror from Lincoln Laser was used in the experiment. It had twelve facets, each with length 0.42 inch and width 0.295 inch. The facet surfaces were diamond machined, with a flatness better than 1/4 wavelength at 633 nm. The radius (polygon center to facet) dimension was 0.787 inch. The substrate was aluminum. The consistency of the facet-to-rotational centerline angle was less than six arc seconds. See figure 6.6.

The polygonal mirror was coupled to the shaft of a direct current motor. The motor was held by hardware which could be adjusted to align the polygonal mirror with the laser beam. See figures 6.7 and 6.8. The motor was energized with a direct current power supply. The angular speed of the motor shaft was calibrated to the output voltage of the power supply using an Electronic Brazing Co. Model 510-AL stroboscope.

Aluminum was seen to be an adequate polygon substrate material. Its low density, and thus its low inertial load, allowed a very small direct current motor to be used. Aluminum tends to deform more than steel and beryllium, but the deformation of the facets was considered negligible compared to the alignment imprecision due to the motor shaft coupling.

The ratio of the laser beam diameter to the facet length was roughly 0.1. This ratio was large enough that some visible degradation of the light sheet edges was expected.

From eq. (6.1), the maximum beam sweep angle for this twelve faceted polygon is found to be 60°. The polygonal mirror, located at (x = 41 cm, y = -223 cm), was 167 cm from the near side of the area observed (i.e. 167 cm from y = -56 cm). Eq. (6.2) shows that the light sheet should cover 193 cm in the x direction along this near side. Therefore, along the near side of the observed area, the light sheet should be centered at x = 41 cm and span from (x = -55 cm, y = -57cm) to (x = 138 cm, y = -57cm). Since the light sheet expands as the distance from the polygonal mirror increases, the near side coverage determines if the overall coverage is great enough. It is seen that the spread of the light sheet is theoretically adequate to cover the entire area of observational interest. See figures 6.1 and 6.5.

Preliminary tests with the polygonal mirror apparatus showed that the spreading angle of the actual light sheet using the argon laser was approximately 60°. Due to safety concerns, an exact measurement was not made. In order to get a more precise determination of the spread angle, tests were carried out with a .5 mW Helium-Neon laser. As expected, a small portion of the light sheet at the outer edges was visibly degraded. See Table 6.1 for the results. Using eq. 6.2, the observed maximum beam scan angle was found to be 67°. Note from Table 6.1 that the difference between the measured coverage and the coverage of the degraded edge sections is

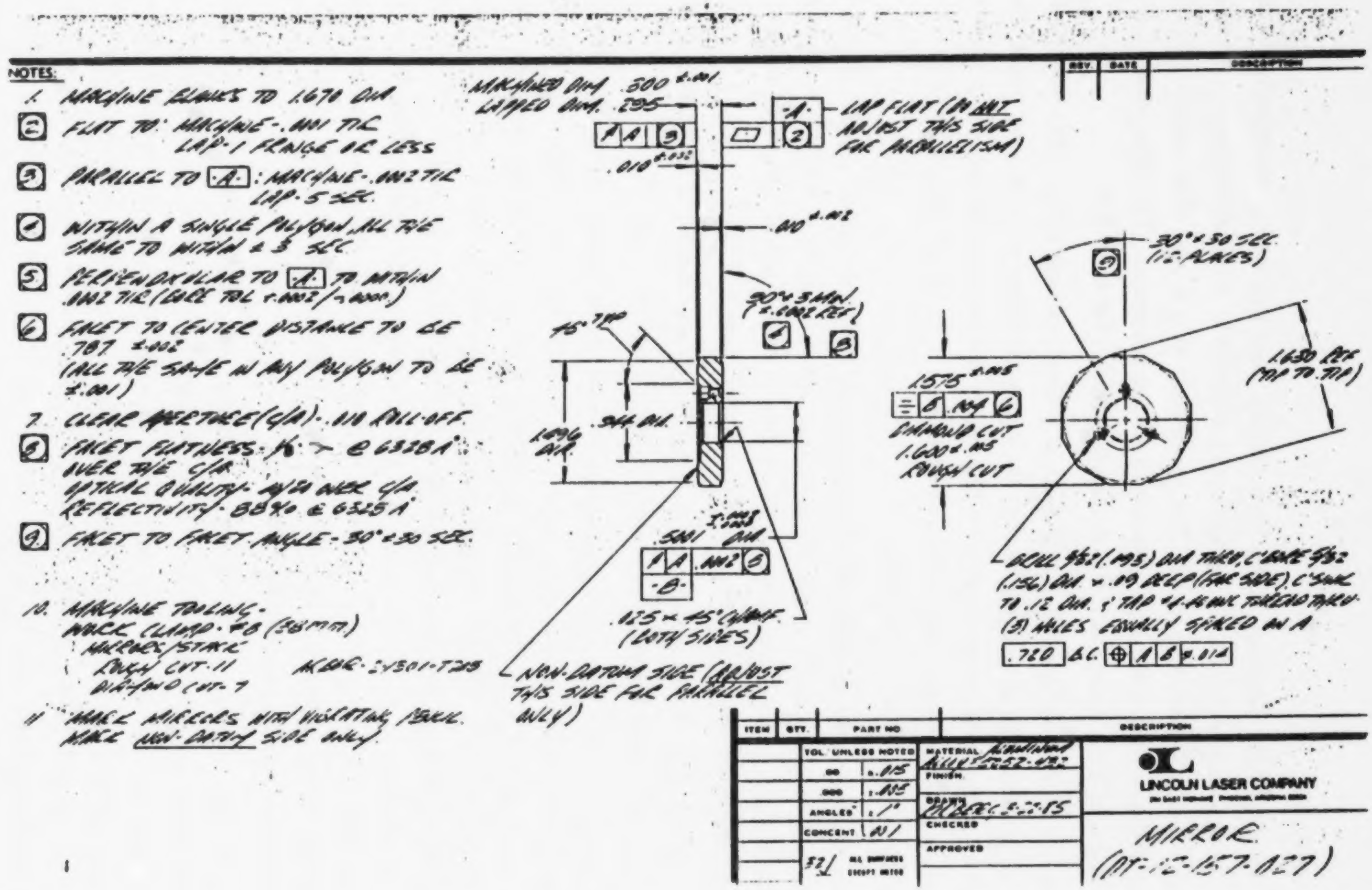
NOTES:
1. MACHINE BLANKS TO 1.670 DIA
2 FLAT TO: MACHINE-.0001 TIR LAP-1 FRINGE OR LESS
3 PARALLEL TO -A-: MACHINE-.0002 TIR LAP-5 SEC.
4 WITHIN A SINGLE POLYGON, ALL THE SAME TO WITHIN ± 3 SEC
5 PERPENDICULAR TO -A- TO WITHIN .0002 TIR (BASE TOL ±.0002/-.0000)
6 FACET TO CENTER DISTANCE TO BE .787 ±.002 (ALL THE SAME IN ANY POLYGON TO BE ±.001)
7. CLEAR APERTURE (C/A)-.010 ROLL-OFF.
8 FACET FLATNESS: 1/6 λ @ 6328 Å OVER THE C/A
OPTICAL QUALITY- 40/20 OVER C/A
REFLECTIVITY- 88% @ 6328 Å
9 FACET TO FACET ANGLE - 30° ± 30 SEC.
10. MACHINE TOOLING-
MACK CLAMP-#8 (38mm)
MIRRORS/STACK
ROUGH CUT-11
DIAMOND CUT-7
MCDR-2Y301-T28
11 MARK MIRRORS WITH VIBRATING PENCIL. MARK NON-DATUM SIDE ONLY
MACHINED DIM .300 ±.001
LAPPED DIM .295
A 3
2
-A-
LAP FLAT (DO NOT ADJUST THIS SIDE FOR PARALLELISM)
.010 ±.002
.010 ±.002
90° ± 3 MIN. (±.0002 REF.)
4
B
45° TYP
1.496 DIA
.344 DIA
.5001 +.0005 -.0000 DIA
A .0002 6
-B-
.125 × 45° CHAMF. (BOTH SIDES)
NON-DATUM SIDE (ADJUST THIS SIDE FOR PARALLEL ONLY)
1.575 ±.005
B .004 6
DIAMOND CUT
1.600 ±.005
ROUGH CUT
30° ± 30 SEC. (12 PLACES)
9
1.650 REF (TIP TO TIP)
DRILL 9/32 (.095) DIA THRU, C'BORE 5/32 (.156) DIA × .09 DEEP (FAR SIDE), C'SINK TO .12 DIA. & TAP #4-40 UNC THREAD THRU (3) HOLES EQUALLY SPACED ON A
.720 B.C. ⊕ A B ±.014
REV
DATE
DESCRIPTION
ITEM
QTY.
PART NO
DESCRIPTION
TOL. UNLESS NOTED
.00 ±.015
.000 ±.005
ANGLES ±1°
CONCENT .001
32 ALL SURFACES EXCEPT NOTED
MATERIAL ALUMINUM ALLOY 5052-H32
FINISH
DRAWN
CHECKED
APPROVED
LINCOLN LASER COMPANY
MIRROR
(07-12-157-027)

Figure 6.6 Polygon specifications.

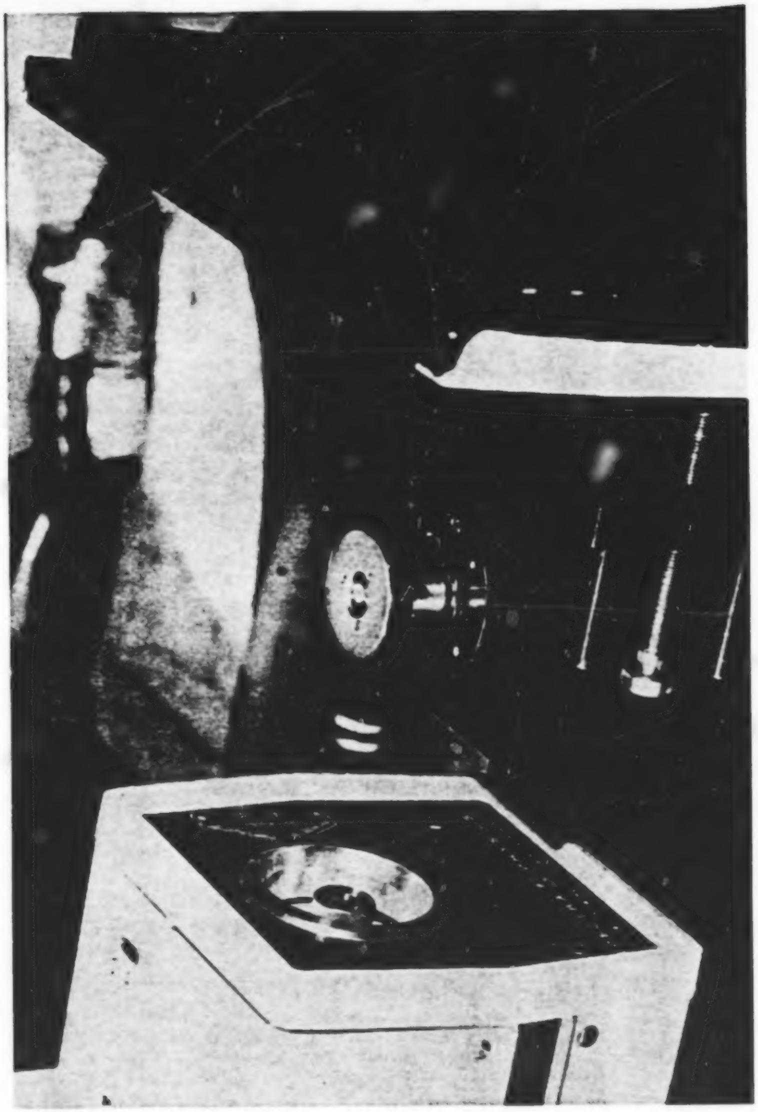

Figure 6.7 Mirrored polygon system.

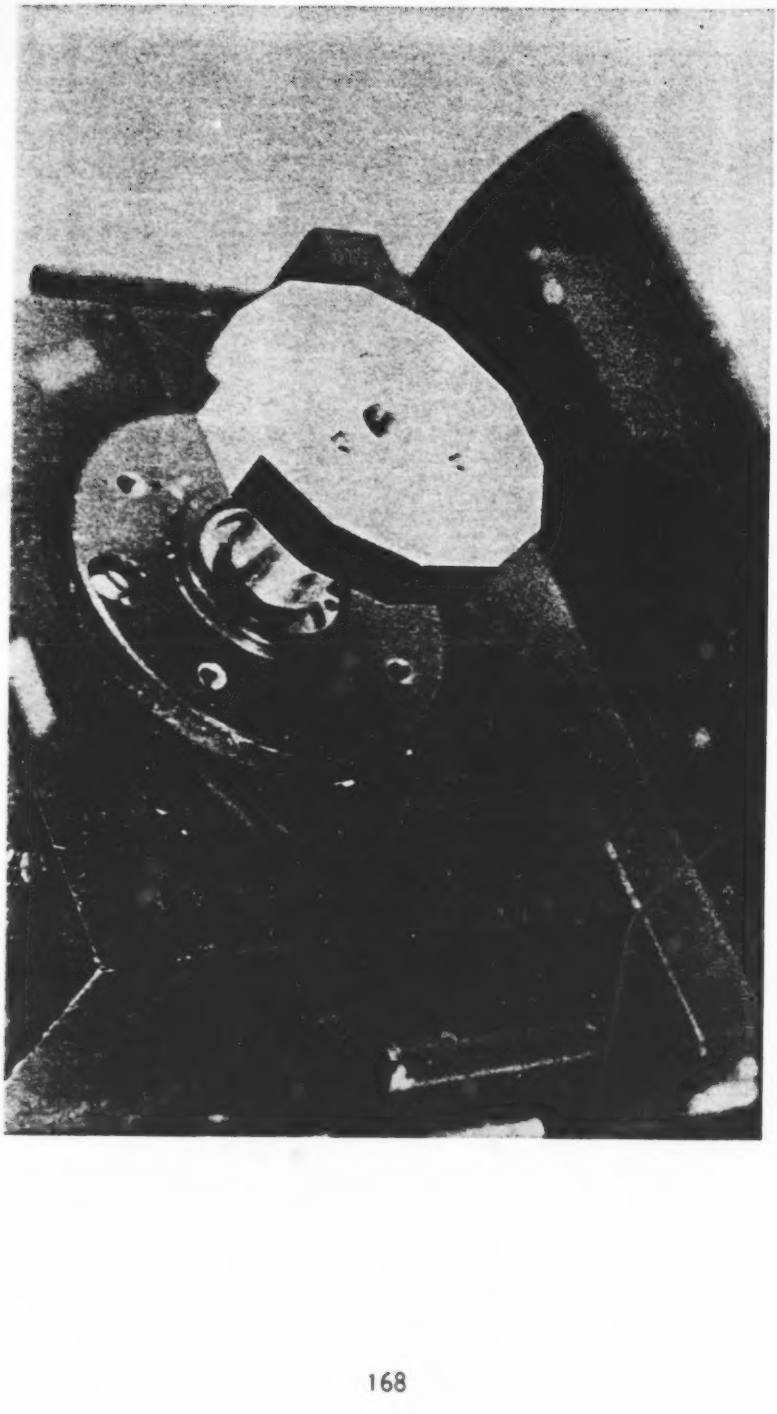

Figure 6.8 Mirrored polygon hardware.

approximately equal to the theoretical coverage. Consequently, the calculations of maximum beam scan angle seem to hold reasonably well. It is very likely that the degraded edge sections are due to the effects of a finite beam width extending over the edges of the polygonal mirror as explained previously.

MEASUREMENTS FOR LIGHT SHEET PRODUCED FROM MIRRORED POLYGON AND .5 mW LASER					
r (cm)	c (cm)	cth (cm)	vleft (cm)	vright (cm)	t (mm)
104	139	120	17	4	9
10	11.5	11.5	0.7	0.3	1.5

r = the distance from the polygon along the light sheet centerline
c = the actual light sheet width at the distance r.
cth = the theoretical light sheet width at the distance r.
vleft = width of the degraded portion of the light sheet at the left edge.
vright = width of the degraded portion of the light sheet at the right edge.
t = the thickness of the light sheet at the distance r.

TABLE 6.1. MEASUREMENTS FOR LIGHT SHEET PRODUCED FROM MIRRORED POLYGON AND .5 mW LASER

The spread of the actual light sheet during the experiment was adequate in covering the area of interest. Illumination of smoke was observed throughout the entire observational area. The exact spread inside the wind tunnel was difficult to determine.

Ideally, the scan frequency of the laser beam should be much larger than the frame rate of the camera. The beam's scan frequency was limited by the speed attainable by the motor. This speed was found to be approximately 2000 RPM. Eq. (6.4) shows that since a speed of 1800 RPM was often used in the experiment, 6 scans per field resulted. A greater number of scans per field was desirable but was not possible with the equipment used. The images obtained using this frequency appeared to have constant illumination, as desired. Analysis of the data will have to be completed in order to determine how constant the illumination actually was.

Using eq. (6.5), it is seen that the motor shaft must rotate at a frequency greater than 300 revolutions per minute for there to be more than 1 beam scan per field. A frequency much smaller than this could result in some frames having sections with no illumination at all. The experiment showed that motor shaft frequencies of less than 300 revolutions per minute did produce many frames without complete illumination. The section of each frame which was illuminated was easily distinguishable from the section which was not illuminated. Inspection of the frames at the normal rate of 30 frames per second gave the illusion of smoke jumping very fast from location to location. This was the result of aliasing.

The thickness of the light sheet was observed to be approximately 1.5 cm in the neighborhood of the building model (223 cm from the polygon mirror). It was also observed to be approximately 3.0 cm at y = 194 cm (417 cm from the polygonal mirror). This gives an approximate thickness spread angle of 0.4°. In addition, the thickness of the light sheet is calculated to vary from 1.2 cm to 2.1 cm within the area of observational interest. This thickness was greater than was hoped for, but it gave images of reasonably good quality. The major factor in having this relatively large thickness was the polygon-to-motor shaft coupling. Adjustments were attempted, but the coupling alignment was not improved; hence, the results remained the same.

Several sequences of images were recorded using the polygonal mirror illumination method. Figure 6.9 shows a sample sequence of images with a time step of 0.1 second. The laser output power was set for 2 W for most of the sequences and 1 W for others. The rotational speed of the polygonal mirror was varied from 200 RPM to 1800 RPM. The tunnel wind speed was varied, but it was primarily set at 2.26 meters per second at a height of 10 cm off of the floor. Several settings of the camera f-stop were tried, ranging from f1.8 to f8.0. The dimensions of the utilized building models were 10cm x10cm x 10cm, 10cm x 10cm x 20cm, 20cm x 20cm x 40cm, and 10cm x 10cm x 40cm. The density of the introduced smoke was held constant throughout most of the experiment, but it was reduced for several sequences of images. Sequences were recorded with the horizontal light sheet at many levels, both below and above the model building height. Some conditions of an earlier study by Huber (1988b, 1989) were repeated for later comparisons.

Generally, the resulting images were quite satisfactory. As the level of the horizontal light sheet was changed, the unique characteristics of the flow at each level were visually apparent.

One very important characteristic of the resulting images was their lack of background illumination outside the region of the smoke flow. Even points close to, but outside of, the smoke envelope had virtually no illumination. Within the visual smoke envelope, very slight patterns in the honeycomb background could be detected. This effect was believed to occur due to the scattering of light from the smoke itself.

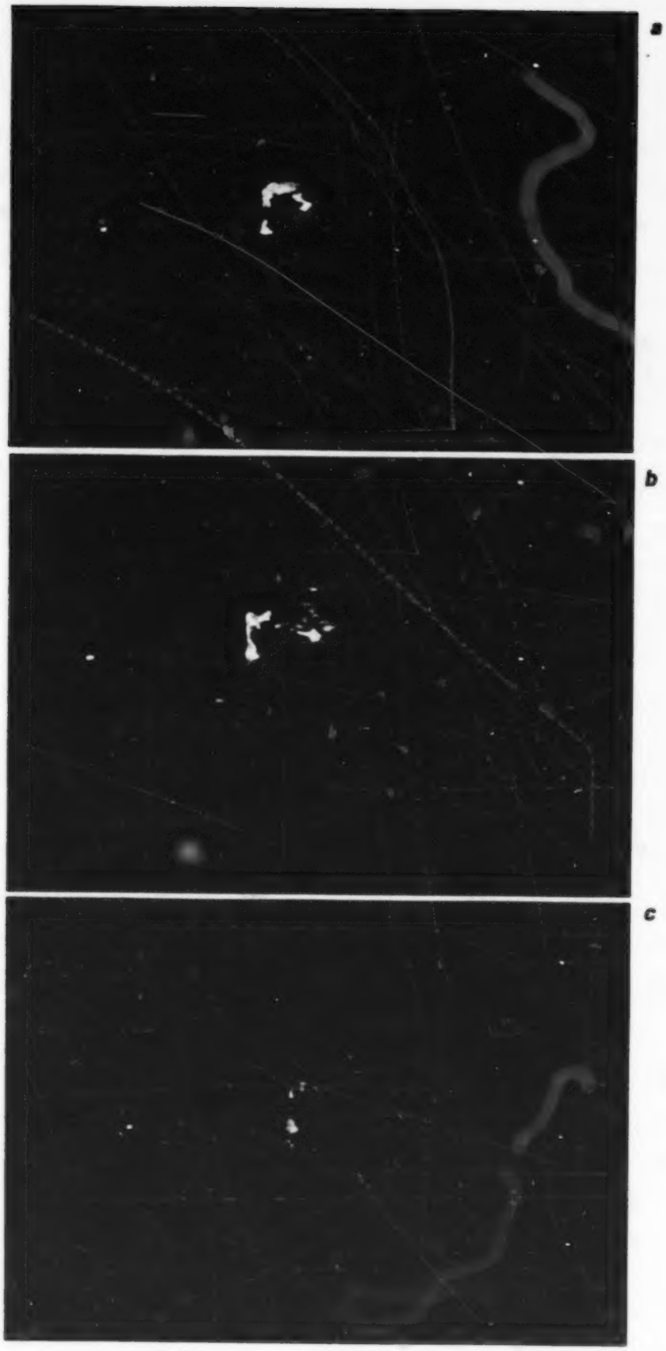

Figure 6.9 Sample sequence of images produced by the polygonal mirror system. Top view. The wind is from the left. Smoke is released from ground level. The flow is illuminated with laser sheet lighting at $z = 1$ cm.
(a) t(0) (b) t(0) + 0.1 sec
(c) t(0) + 0.2 sec.

The lack of background illumination should be very useful for signal processing work which will be carried out on the images. For the analysis of the boundaries of the smoke, removal of background noise by filtering should not be necessary. For the analysis of the entire flow, filtering may not be as vital as when normal flood lamps are used (Forgety, 1989).

6.4 Multiple Lens Method of Producing Light Sheets

Lenses can also be used to produce sheets of laser light. The general configuration which was used is shown in figure 6.10. It consists of lenses, a first-surface mirror, and adjustable mounting hardware. The beam exits the laser and is reflected by the mirror at a 90° angle. The first lens diverges the beam in one plane. The next lens collimates the light. The last lens diverges the beam again in the same plane.

Some advantages of a lens system are:

* It is relatively simple.
* It is relatively inexpensive.
* If it is aligned properly, it always spreads the laser beam before the beam enters the wind tunnel. This reduces the risk of human exposure to light of highly concentrated energy.
* There are no aliasing or timing problems to contend with when cameras are involved.
* Often, the apparatus is easily rotated to produce a sheet of light which is normal to the smoke flow or a sheet which is parallel to the smoke flow.

Some disadvantages of such a system include:

* The intensity distribution of the resulting light sheet is fairly complex.
* Proper alignment of the system can be very difficult if high precision equipment is not used.

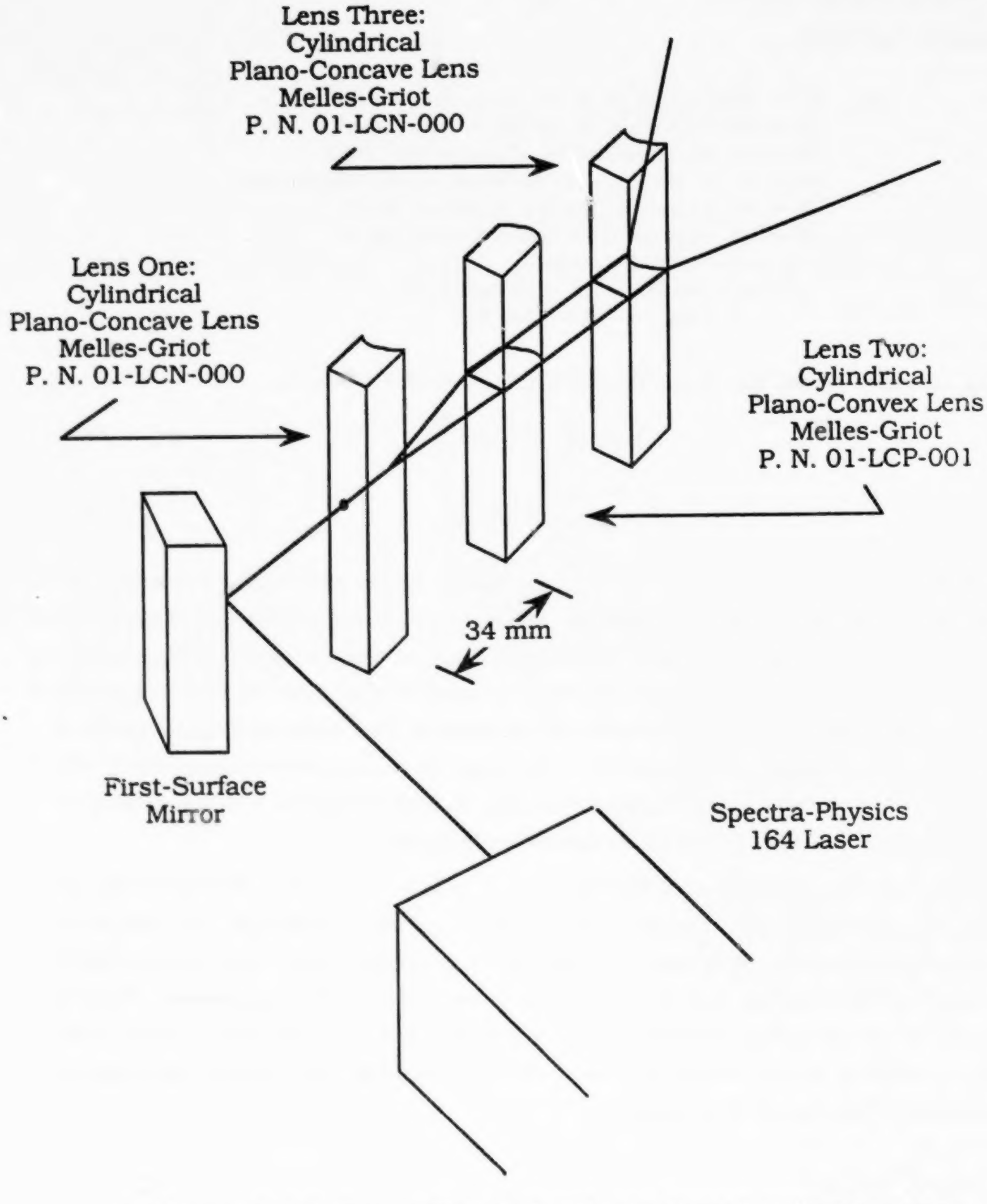
Lens Three:
Cylindrical
Plano-Concave Lens
Melles-Griot
P. N. 01-LCN-000
Lens One:
Cylindrical
Plano-Concave Lens
Melles-Griot
P. N. 01-LCN-000
Lens Two:
Cylindrical
Plano-Convex Lens
Melles-Griot
P. N. 01-LCP-001
34 mm
First-Surface
Mirror
Spectra-Physics
164 Laser

Figure 6.10. Laser light sheet produced using lenses.

6.4.1 Design Considerations

Refer to figure 6.11.

Let: F1 = the focal length of the plano-concave lens 1
F2 = the focal length of the plano-convex lens 2
F3 = the focal length of the plano-concave lens 3
d1 = the diameter of the laser beam, approximately 1mm
d2 = the diameter of the light spread at lens 2
d3 = the diameter of the light spread at lens 3
r = the distance from lens 3
c = the coverage length of the light sheet
at a distance r from lens 3

Treating the lenses as ideal thin lenses, the following relationships are found.

$$\mathrm{d2} = \mathrm{d1}\,\frac{\mathrm{F2}}{\mathrm{F1}} \approx 1\mathrm{mm}\,\frac{\mathrm{F2}}{\mathrm{F1}} \tag{6.7}$$

$$\mathrm{c} = \mathrm{d3}\,\frac{\mathrm{r}}{\mathrm{F3}} \approx \mathrm{d2}\,\frac{\mathrm{r}}{\mathrm{F3}} \tag{6.8}$$

The illumination must be treated as emanating radially from a point source, as was the case with the polygonal mirror method. Unlike the polygonal mirror illumination, the illumination from lenses theoretically has a Gaussian distribution at arcs of constant radius. This is due to the Gaussian intensity distribution across the diameter of the incident laser beam (Young, 1986). In practice, the quality of the lenses can affect the illumination distribution also. Consequently, a suitable calibration function must be applied to the image data to approximate images with uniform illumination throughout the observational area. A final calibration function should, of course, compensate for the nonlinear effects imposed by the camera.

Ideally, each lens transmits all of the light incident upon it without any reflection or loss. In practice, bare glass lenses reflect approximately four percent of the incident light. The amount of reflection can be reduced by using lenses with anti-reflection coatings. Magnesium fluoride, which has a refractive index between that of air and glass, is commonly used for this purpose. There is a reflection at the air-coating interface and also a reflection at the coating-glass interface. Destructive interference occurs between the two reflections, resulting in a reduced reflectance of approximately 1.5 percent (Melles-Griot).

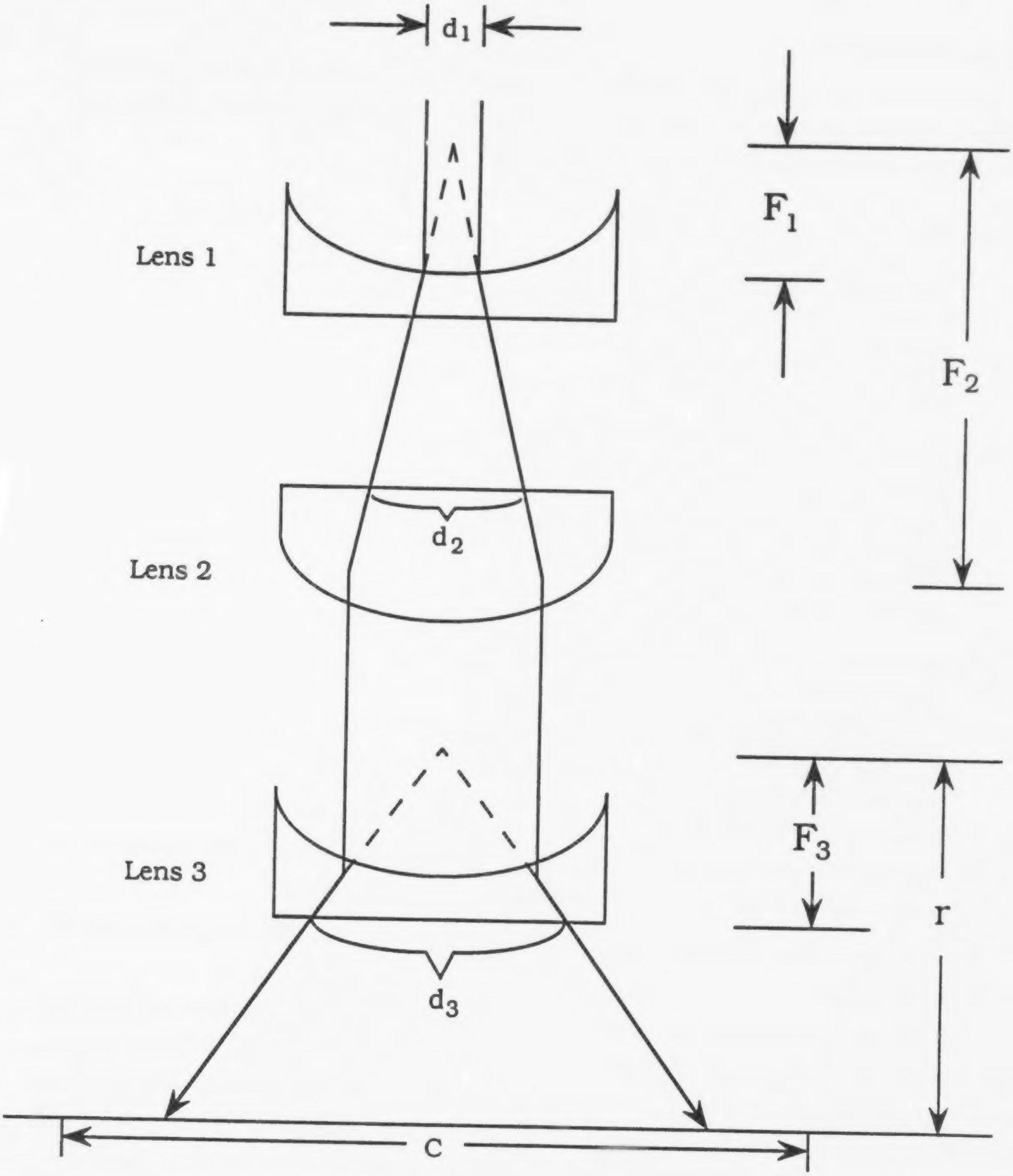
d1
Lens 1
F1
F2
Lens 2
d2
Lens 3
F3
r
d3
C

Figure 6.11. Cylindrical lenses

6.4.2 Implementation

The multiple lens configuration was implemented as shown in Figures 6.12, 6.13, and 6.14. This device could be adjusted to produce either horizontal cr vertical sheets of light. Referring to figure 6.11, the specifications of the lenses were as follows:

Lens 1: cylindrical
plano-concave
focal length: -6.35 mm
physical dimensions: 25mm long x 6.0mm wide
material: glass
manufacturer: Melles-Griot
part number: 01-LCN-000

Lens 2: cylindrical
plano-convex
focal length: 40.0mm
physical dimensions: 60mm long x 15mm wide
material: glass
manufacturer: Melles-Griot
part number: 01-LCP-001

Lens 3: cylindrical
plano-concave
focal length: -6.35mm
physical dimensions: 25mm long x 6mm wide
material: glass
manufacturer: Melles-Griot
part number: 01-LCN-000

These lenses were not purchased with anti-reflective coatings. The loss of a few percent of the available output power of the laser was not considered critical.

Lenses 1 and 3 each required a lens holder type 07-LHC-001 and lens 2 requires a type 07-LHC-003 lens holder.

The near side of the observational area was 143 cm from lens 3. Using eq. (6.7) and (6.8) it is seen that, at this distance, the light sheet's coverage in the x direction is theoretically 142 cm. Since the lenses were positioned at (x =41 cm, y = -199 cm), the light sheet should have been centered at x = 41 cm, with a span from (x = -30 cm, y = -57 cm) to (x = 112 cm, y = -57 cm) along the near side of the observational area. Therefore, the spread of the theoretical light sheet is adequate to cover all but a small upstream portion of the area of observation.

Measurements were made of the power of the actual resulting light sheet in the tunnel using a Scientech 362 power energy meter. The thermopile sensor was cylindrically shaped with a diameter of 3cm; therefore, each reading represents the power of a 3cm section of the sheet at the

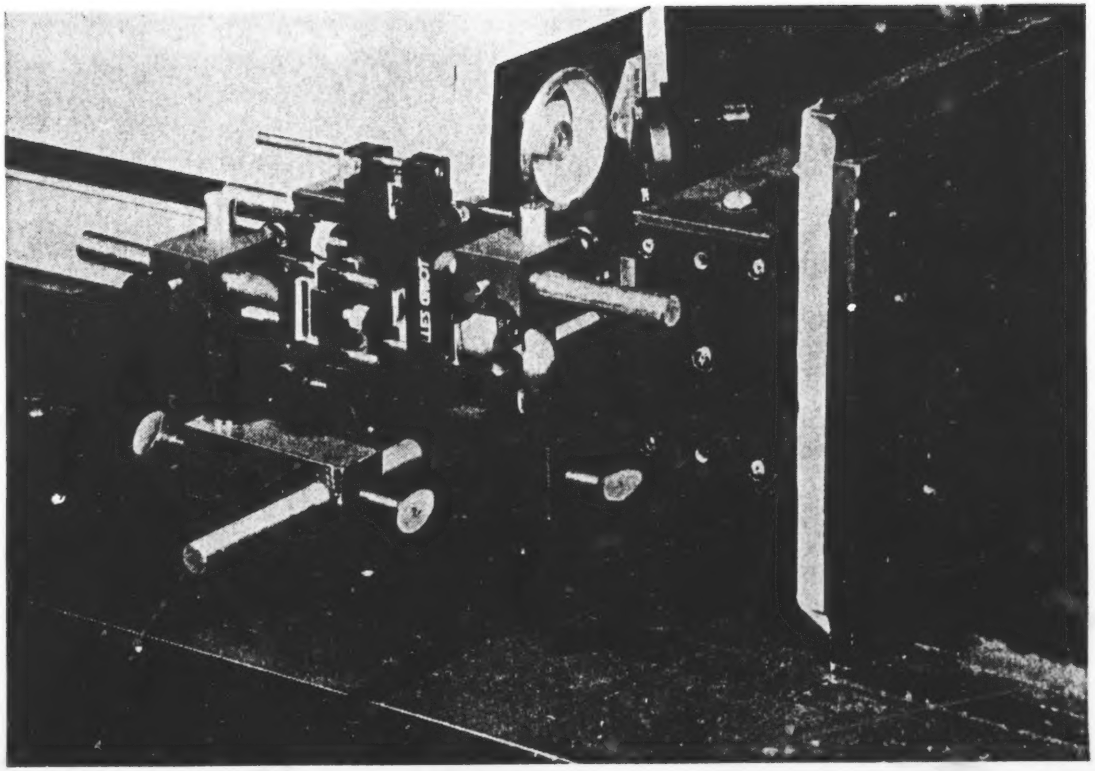

Figure 6.12 Lens system.

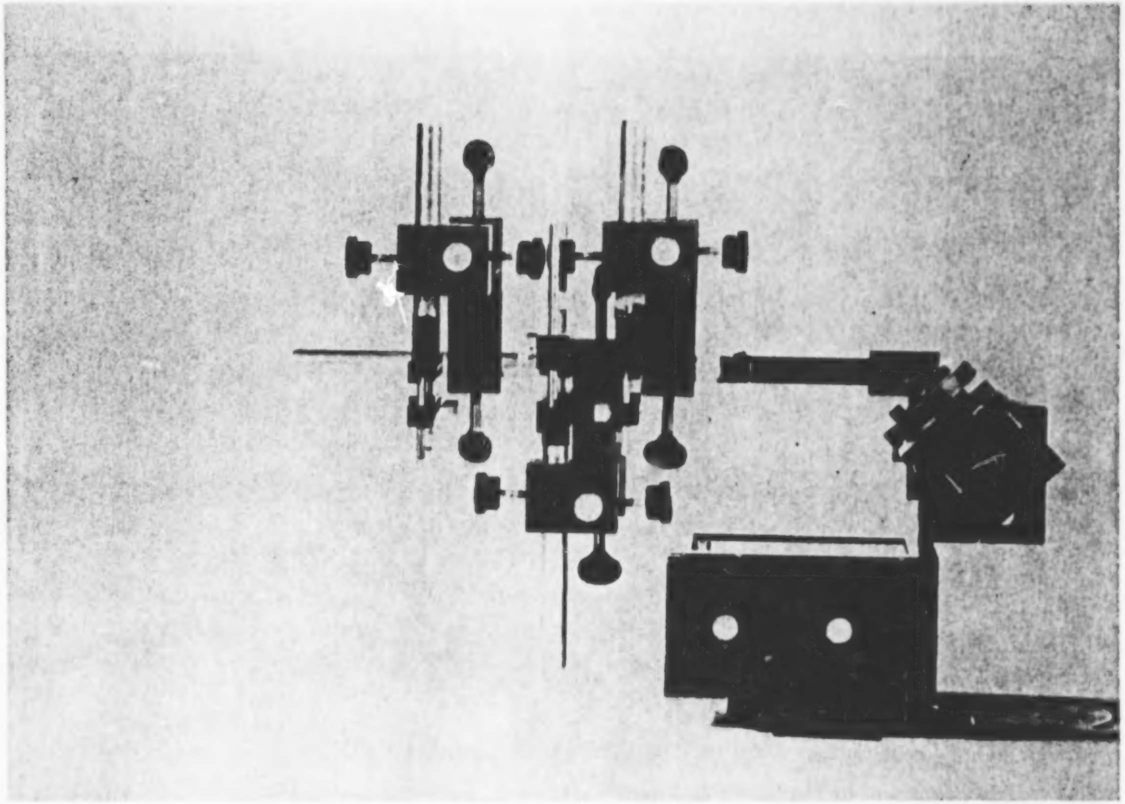

Figure 6.13 Overhead view of lens system.

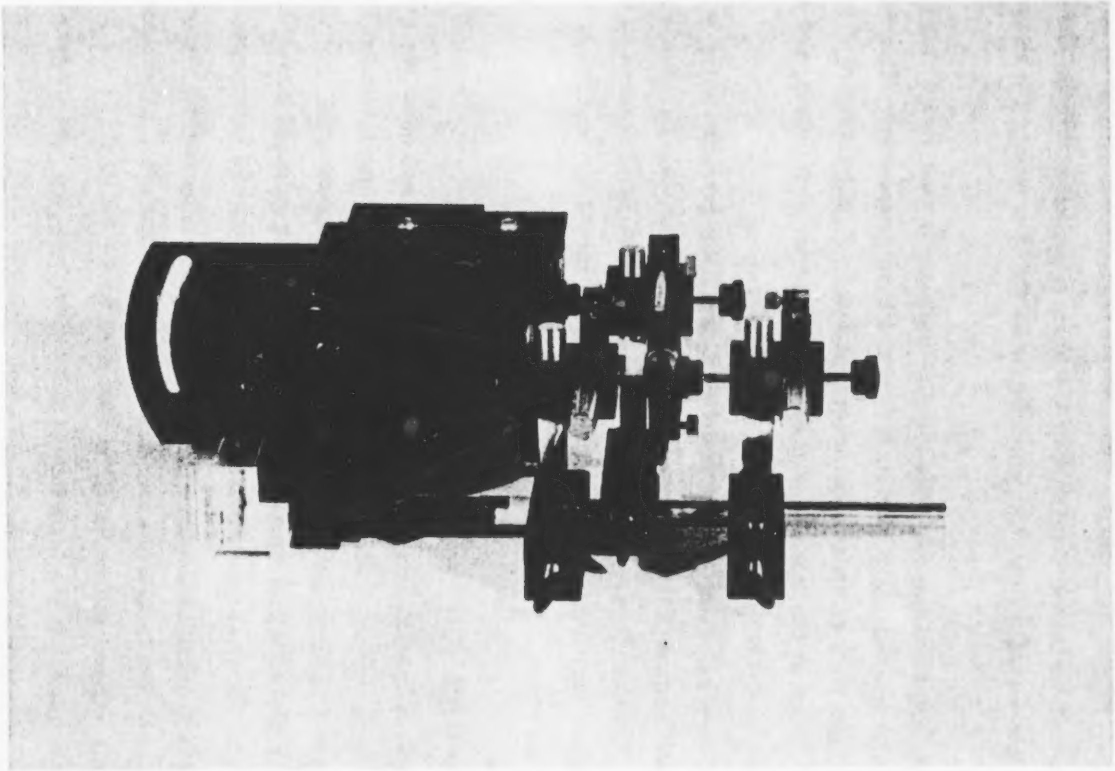

Figure 6.14 Side view of lens system.

given distance. Measurements were made along the straight line from position (x= -55 cm, y= -70 cm) to position (x = 110 cm, y = -70 cm). Measurements were also made along the straight line from position (x = -100 cm, y = 65 cm) to position (x = 160 cm, y = 65 cm). See Tables 6.2 and 6.3 and figures 6.15, 6.16, 6.17 and 6.18. The data clearly show that the illumination was not symmetric; it was skewed upstream. The primary reason for this result is believed to be a slight misalignment of the lenses. Inspection of the lenses after the completion of the experiment showed that the lenses were not exactly perpendicular to the laser beam. No attempt was made to correct this.

The resulting light sheet was relatively thin. At positions (x = 0, y = 0) and (x = 75 cm, y = 194 cm), the thickness was approximately 0.5 cm and 1 cm , respectively. This was determined by observing the light sheet reflection from blocks marked in 1 cm increments. The thickness is calculated to be 0.36 cm at the near side of the observation area (y = -56 cm) and 0.67 cm at the far side of the observation area (y = 65 cm).

Images were recorded using various model sizes, wind speeds, laser output powers, camera f-stop settings, and heights of the light sheet. The recorded images clearly show the characteristics of the flow at different levels. Background noise was essentially eliminated, as it also was for the mirrored polygon experiment. Thus, background noise should not be a major problem when the images are processed.

6.5. Further Analysis

Mathematical calibration functions will be developed which will allow the acquired images to be treated as being uniformly illuminated. In doing this, the illumination from the polygonal mirror will be treated as being inversely proportional to the radial distance. For the illumination from the lenses, a mathematical equation will be fitted to the collected power data. For each method, a correction for non-linear distortion effects of the camera will be incorporated.

Next, image processing techniques will be applied to determine velocity vector projections in the horizontal plane. For instance, a specific section of one frame will be selected. In the next frame, neighboring sections will be tested to determine where the smoke in the first frame traveled. The section which has the highest area correlation with the first frame will be selected. This is a form of template matching. Kimura and Takamori (1985) have demonstrated success with this technique as applied to smoke flow images.

Various search methods for carrying out the template matching technique will be investigated to find a suitable one. For example, a two-dimensional logarithmic search will be tried. Also to be investigated are sequential searches which abort when the cumulative error between the sections exceeds a predetermined threshold (Pratt, 1974).

Table 6.2

Measurements of lens light sheet along the (y = -70cm) line.

x position (cm)	Measurement with laser at 1.0W (W)	Measurement with laser at 2.5W (W)
-55	0	0
-50	0	0.0005
-45	0	0.00025
-40	0.0002	0.0013
-35	0.0004	0.0018
-30	0.0004	0.0017
-25	0.0009	0.0031
-20	0.0017	0.0052
-15	0.0024	0.007
-10	0.0043	0.0095
-5	0.0017	0.0054
0	0.0025	0.007
5	0.0041	0.0085
10	0.0027	0.00785
15	0.0039	0.0085
20	0.00425	0.012
25	0.00425	0.0115
30	0.0055	0.016
35	0.006	0.017
40	0.0065	0.017
45	0.0045	0.01175
50	0.00375	0.009
55	0.0025	0.006
60	0.002	0.0045
65	0.00145	0.00335
70	0.001	0.0022
75	0.0007	0.0015
80	0.00055	0.00135
85	0.0005	0.001
90	0.00025	0.0006
95	0.00085	0.0018
100	0.0001	0.0003
105	0.0001	0
110	0	0.00015

Table 6.3
Measurements of lens light sheet along the (y = 65cm) line.

x position (cm)	Measurement with laser at 1.0W (W)	Measurement with laser at 2.5W (W)
-100	0.0016	0.0035
-90	0.0022	0.0051
-80	0.0024	0.0052
-70	0.0072	0.014
-60	0.0031	0.00475
-50	0.0017	0.0035
-45	0.0031	0.0062
-40	0.0031	0.00695
-30	0.003	0.00615
-20	0.0023	0.00555
-15	0.0025	0.0062
-10	0.0043	0.0094
-5	0.0052	0.0105
0	0.0036	0.0094
5	0.0037	0.0095
10	0.0032	0.0088
15	0.0039	0.0101
20	0.0039	0.0101
25	0.0044	0.0105
30	0.00435	
35	0.0037	0.00975
40	0.00337	0.009175
50	0.00267	0.007825
55	0.0021	0.0061
60	0.00195	0.0058
65	0.00155	0.00445
70	0.0012	0.0037
75	0.00085	0.0028
80	0.00055	0.0019
85	0.00055	0.002
90	0.00045	0.00175
95	0.00025	0.00125
100	0.0005	0.0013
105	0.0002	0.0008
110	0.0002	0.0008
115	0.0004	
120	0	0.00035
130	0.000225	0.00035
140	0.000125	0.00015
150	0	0.00015
160	0	0.000125

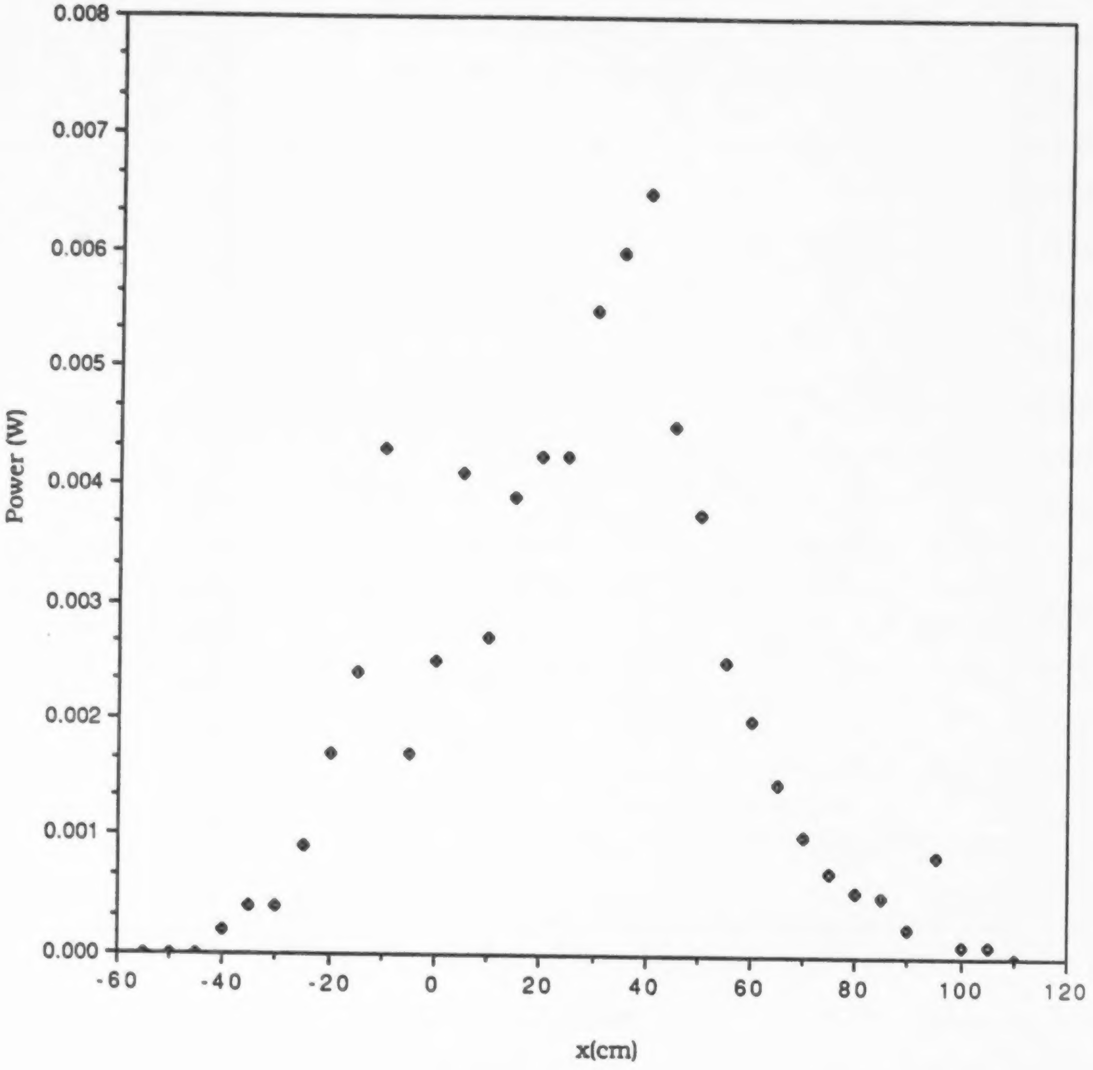

Figure 6.15. Measurements of lens light sheet along (y = -70cm) line; Laser set at 1.0W

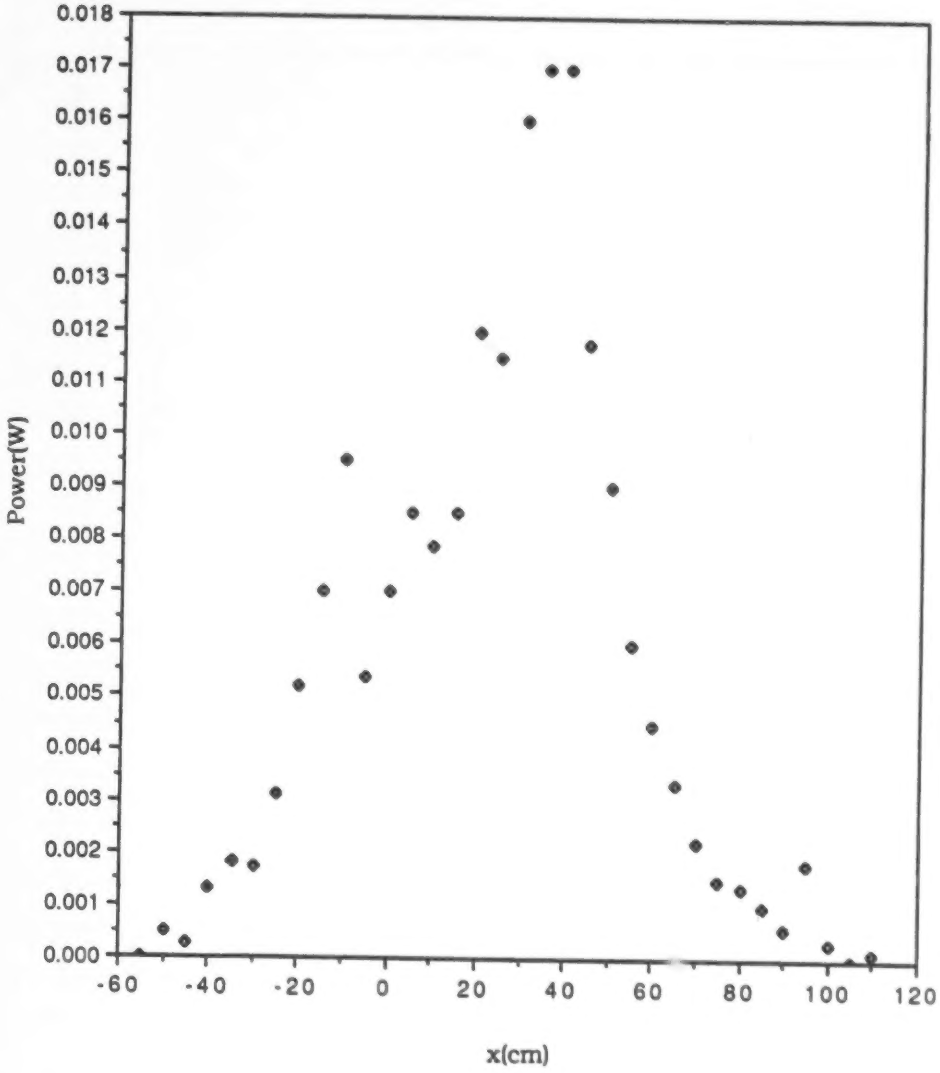

Figure 6.16. Measurements of lens light sheet along (y = -70cm) line;
Laser set at 2.5W

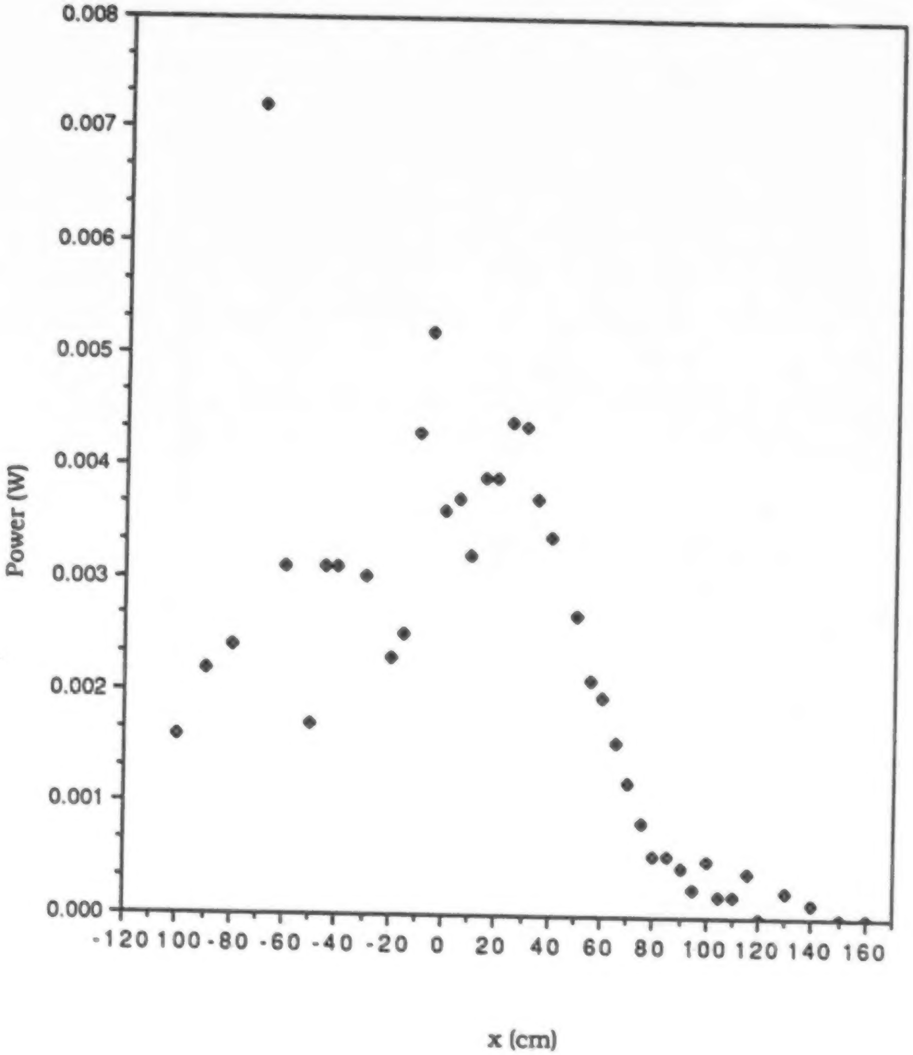

Figure 6.17 Measurements of lens light sheet along (y = 65cm) line; Laser set at 1.0W

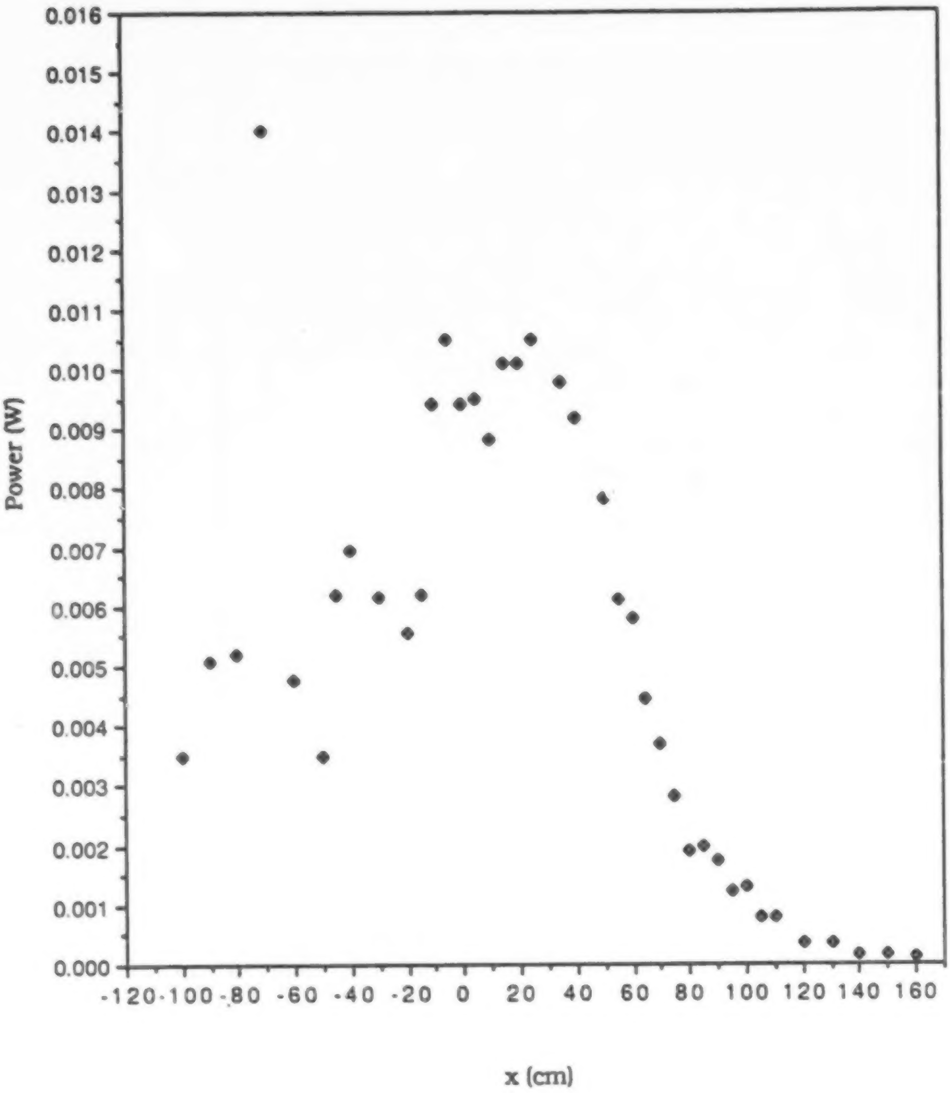

Figure 6.18. Measurements of lens light sheet along (y = 65cm) line; Laser set at 2.5W

The template matching process should first be applied to the original images. Next, it will be applied to the images which have been corrected for non-uniform illumination and camera effects. By comparing the two results, it should be determined if correction functions must be applied to the images in order to determine flow velocity vectors.

Some basic thresholding filters will be used to reduce any noise, but this is not predicted to be necessary. High-pass and edge enhancement filters will be used to produce outlines of the denser sections of the smoke. Combining this process with the template matching technique, determination of velocity vectors may be achievable at a reasonable computation rate.

6.6 Conclusion

Both the mirrored polygon and lens methods of producing laser light sheets for flow illumination are useful. Each produces images which are suitable for qualitative analysis. Also, quantitative analysis may be enhanced via these methods.

The mirrored polygon method is generally more expensive, but it produces images which are easier to analyze quantitatively. To get high quality images, the polygon, motor, and coupling device must be of high precision and quality. Also, the polygon rotational speed must be very high.

The lens method is less expensive, but the resulting illumination is characterized by a fairly complex function. Precision instruments and equipment such as commercially available optical benches are essential for achieving good images.

7 SUMMARY AND CONCLUSIONS

In this report, we presented the results from the cooperative research project, entitled Evaluation of the Wake Effects on Plume Dispersion using Video Image Analysis. The objectives of this research were to evaluate various image processing/analysis techniques for use in analyzing the characteristics of video images of smoke flow dispersion and to propose and implement an alternative approach for recording image flow data. What resulted was three distinct research projects. In the first two projects we evaluated different approaches to analyzing the smoke flow data. The first was based on the more traditional techniques available in image processing and analysis. The second was based on the recent work using fractal theory. The third project addressed the design and implementation of a laser lighting-based system for recording smoke flow data.

One of the characteristics of the image data we were interested in quantifying, was the motion of the smoke, i.e. the time-varying changes in the image intensity values. Because of the nature of the smoke flow data it was difficult or impossible to use existing motion analysis techniques. As a result, we chose to approach the problem using two very different points of view. In the first case, we applied many of the traditional image processing/analysis techniques to assess the contents of the data, to develop a scheme for separating the smoke from the background, and ultimately, to determine the potential for analyzing the motion characteristics of the smoke flow.

The first set of image processing techniques we applied to the data were techniques for determining the signal and noise characteristics of the data. First we displayed the individual bit planes of the digital image data in an attempt to see if the least significant bits contained signal information or noise. Visually it appeared that the least significant bit plane contained only a random distribution of ones and zeros. To confirm this observation, we estimated the autocorrelation, $r(m,n)$, $m,n=-2,\ldots,2$, for the three least significant bit planes. The estimate of the autocorrelation for the least significant bit plane is approximately a unit impulse function . For bit planes 1 and 2 the autocorrelations become less like a unit impulse, there is correlation between adjacent pixel values. Thus what we conclude is that a 7 bit binary representation is adequate to represent the signal information contained in this image data. Alternatively, we can say that for each 8 bit pixel intensity there is approximately 1 bit of random error. Another interpretation is that these data have a signal-to-noise ratio no greater than 42 dB. This is based on the rule-of-thumb that there is approximately a 6 dB increase in signal-to-noise ratio for each additional bit of information. This rule-of-thumb is based on the performance of a pulse code modulation (PCM) system with uniform quantization, (Couch, 1983).

In order to give an assessment of the spatial bandwidth of the image data, to determine whether the image data is likely to have aliasing due to spatial undersampling and to visualize the noise, a discrete Fourier transform (DFT) of the image data was obtained next. The magnitude of the DFT of each image frame was displayed as an image, with the dynamic range of the data rescaled so the largest value is assigned to 255 (white) and the smallest value to 0 (black). It is clear from these images that the image data has a low spatial bandwidth, that is, the data has been spatially oversampled (the highest frequency of the data is much less than the Nyquist frequency), so no aliasing is present. In addition, it was noted that the intraframe noise was not a dominant factor even at the high frequencies.

Next, several linear and nonlinear image domain filtering techniques were applied to the image data to determine the feasibility of reducing what little noise was present. For the set of data we have processed the spatial median filter provided the best technique for reducing unwanted intraframe noise and background artifacts without sacrificing the edge information in the images. In the temporal direction, a temporal low-pass filter yielded more reduction in interframe noise than did a temporal median filter. However, neither seemed warranted for this data.

The next set of image processing techniques that were considered were the edge enhancement techniques. For the low contrast images we have in this data set, edge enhancement does not appear to be extremely beneficial. Initially, it was thought that it might be easier to segment an edge enhanced image than the original data. The difficulty that is encountered is that the edge enhancement process also enhances the background. If the images were higher contrast and there was less reflection of the background, edge enhancement might be more beneficial. It should also be noted that the histograms of the edge enhanced data are different than those of the original data. If one chooses, as we do in section 3, a histogram-based segmentation technique, it would be useful to know if edge enhancement helps or hinders the segmentation process. In this case, it hinders more than helps. We were interested in segmenting the image data into two pieces, smoke and background. To do this, one would like to have bimodal histograms. Edge enhancement on this data tends to make the histograms trimodal. This leads one to believe that the data should be separated into three classes. The question is what three classes? If it were smoke, dark background and grid work this might be useful. However, the range of intensity values for the grid work overlaps with the range of values for the smoke. Thus it did not appear that this would be effective and was not tried. It should be noted, however, the segmentation approach based on optimal thresholding that is described in section 3 could be generalized for trimodal histograms.

Gradient-based edge extraction techniques were evaluated next. Several gradient operators were applied to the smoke image data. The 3 x 3 gradient operators provided edges that were less sensitive to random fluctuations in the image data. Although it is difficult to extract any quantitative information about the motion of the smoke from these images, they have the potential for yielding useful qualitative information about the smoke flow when viewed as a temporal sequence.

Since one of the objectives of this research was to find a way to extract motion characteristics from the data, we evaluated methods for segmenting the image data next. Two approaches were considered, global thresholding and optimal thresholding. From our experiments, we concluded that it is difficult to heuristically find a single global threshold that would segment this image data. However, we found that optimal thresholding provided us with a robust means for segmenting the image data into two regions. We calculated optimal thresholds for nine subimages for each frame of image data and found consistency from frame-to-frame. The segmented image data has the potential for providing useful qualitative insight about the outer boundary of the smoke dispersion when viewed as a sequence and has proven useful for estimating motion parameters.

A very simplistic approach to motion detection involves the subtraction of adjacent frames in a sequence of image data. The idea is that stationary objects will subtract out and leave pixel values of zero, and in areas where motion has occurred, there will be nonzero pixel values. A fundamental assumption of this method is that all the images are spatially registered from frame to frame. We performed first, second, and third-order differencing on the image data. We believe there is potential for obtaining qualitative insight when viewing the first-order difference images as a video sequence. Little insight was gained for this data from second and third-order differencing because of the amplification of interframe noise. Perhaps if a better means for suppressing the interframe noise was found, the second and third-order differencing would be more useful. Alternatively, if cleaner image data is recorded all three difference sequence may prove to be useful both for qualitative and further quantitative assessment of the motion characteristics.

Assuming the boundaries of the regions in the segmented image data reasonably describe regions containing the smoke, they can then be treated as an object with mass and area. The integrated optical density (IOD) is a measure of the mass contained in each thresholded image of smoke. This information was then used to calculate the center of mass for each of the thresholded images. This allowed us to track and estimate the motion of each segment from frame-to-frame. Changes in area and integrated optical density generally reveal the stages of smoke accumulation observed by Huber. An increase in area and optical density would imply the end of the cycle of smoke accumulation, and a decrease in area would be expected to follow. An increase in optical density and a decrease in area might imply that the smoke is beginning its cycle of accumulating.

The last image processing operation that was performed was an attempt to visualize the boundary deformation of the segmented image data from frame-to-frame. Using the thresholded images, the boundary of each image was extracted in a binary image. Only the points on the boundary contour have a nonzero pixel value. By overlaying these binary images, a comparison of the deformation of the boundaries over time may be made. At this time only a qualitative comparison has been made, but future work could consider the boundary deformation more quantitatively. Attributes of shape and size could be computed and compared. This same process could be performed inside the smoke to characterize the boundary between diffuse and more concentrated smoke. Further work in this area would possibly derive significant information about changes in concentration of the smoke.

In summary, we were able to estimate basic motion characteristics of the centroid of the segmented image data. The advantage of these approaches is there simplicity and no constraints had to be employed regarding the linearity of the motion. One disadvantage is that the image data files analyzed in the major portion of this research were collected using flood illumination. Hence, the motion information extracted was for 3-D smoke flow data projected onto a 2-D image plane. There is a loss of information in this projection that cannot be recovered. Future work should include extending the motion estimation technique to include higher order moments of the segmented image data and to applying this approach to the image data recently collected in project three using the laser sheet lighting. In addition, other features of the image, such as correlations of the original image data, boundaries of segmented data, and intensity contours should be analyzed as a function of time. Preliminary results of this research were described in (Huber, 1988c), a copy of which is contained in Appendix A. A more in-depth paper describing the study is in preparation.

In the second project, we used the theory of fractals for extracting information from the smoke dispersion. A new model based on fractal concepts is developed and applied to a sequence of video images of smoke plume dispersion. The new model provides some qualitative and quantitative interpretations of transient flows by utilizing several fractal parameters were measured to determine the flow activity. The parameters that were used in this study were the horizontal fractal parameter, the vertical fractal parameter, and two higher-order fractal dimensions, the correlation and information dimensions. The results were related to the motion characteristics and plume concentration. The computed fractal parameters were tested for various sized windows and provided us with information about the spatial-temporal behavior of the smoke flow. The initial results appear to be promising, but further research is needed to collect and analyze a set of data that includes video imagery as well as output from other measurement systems, e.g., hot-wire anemometry or hydrocarbon tracer. As a part of this research project, a review of dimensionality measurements for chaotic dynamical systems was prepared, which is contained in

Appendix B. In addition, two conference papers have been written (Ait-Kheddache, 1987) and (Ait-Kheddache, 1988).

In the third project we designed and implemented an alternative approach for capturing the smoke flow image data. The image data that was recorded previously was captured under flood lighting conditions. As a result, the two-dimensional image data was a projection of the three-dimensional volume of smoke flow onto a two-dimensional image plane. In the new system, laser-sheet lighting was used to generate a plane of illumination. Hence, we could selectively illuminate planar surfaces in the three-dimensional volume of smoke flow. Data was collected for various planar sheets of light generated by both a rotating polygonal mirror and a fixed lens configuration. As part of this research, a user's guide for the Spectra-Physics Model 164 laser was prepared. It is provided in Appendix C. This data was collected in the last six months of the research agreement, so only preliminary evaluations on the usability of the data have been performed (see Appendix D). The preliminary analysis of the data from the laser-sheet lighting experiments found the images to give clearer more detailed data for analysis. The next step should be to apply techniques tested in Projects 1 and 2 using the new data. It appears that this data will provide the researchers at the EPA and the University with a wealth of new information with which to work.

Appendix B. In addition, two conference papers have been written (Ait-Kheddache, 1987) and (Ait-Kheddache, 1988).

In the third project we designed and implemented an alternative approach for capturing the smoke flow image data. The image data that was recorded previously was captured under flood lighting conditions. As a result, the two-dimensional image data was a projection of the three-dimensional volume of smoke flow onto a two-dimensional image plane. In the new system, laser-sheet lighting was used to generate a plane of illumination. Hence, we could selectively illuminate planar surfaces in the three-dimensional volume of smoke flow. Data was collected for various planar sheets of light generated by both a rotating polygonal mirror and a fixed lens configuration. As part of this research, a user's guide for the Spectra-Physics Model 164 laser was prepared. It is provided in Appendix C. This data was collected in the last six months of the research agreement, so only preliminary evaluations on the usability of the data have been performed (see Appendix D). The preliminary analysis of the data from the laser-sheet lighting experiments found the images to give clearer more detailed data for analysis. The next step should be to apply techniques tested in Projects 1 and 2 using the new data. It appears that this data will provide the researchers at the EPA and the University with a wealth of new information with which to work.

8 REFERENCES

A. Ait-Kheddache and S.A. Rajala, "Use of Fractal Parameters to Determine Local Spatio-Temporal Characteristics of a Turbulent Pollutant from Video Images," *Proceedings of the 25th Allerton Conference*, Vol. 1, pp. 473-482, 1987.

A. Ait-Kheddache and S.A. Rajala, "Texture Classification based on Higher Order Fractals," *IEEE Int'l. Conf. on Acoustics, Speech, and Signal Processing*, April 1988.

H. Arnold, K. Hinsch, and W. Platen, "Analysis of Non-Stationary Flows by Evaluating the Fringe Visibility in Speckle Velocimetry," *Flow Visualization IV*, Hemisphere Publishing Corp., pp. 127-132, 1987.

A. Babloyantz, "Evidence of Chaotic Dynamics of Brain Activity during the Sleep Cycle," in *Dimensions and Entropies in Chaotic Systems*, G. Mayer-Krress, ed., Berlin:Springer-Verlag, pp. 241-245, 1986.

J. Balatoni and A. Renyi, "On the Notion of Entropy," in *Selected Papers of A. Renyi*, Vol. 1, Akademia Budapest, pp. 558-586, 1976.

J.C. Balint, M. Ayrault, and J.P. Schon, "Quantitative Investigation of the Velocity and Concentration Fields of Turbulent Flows Combining Visualization and Image Processing," *Flow Visualization III*, Hemisphere Publishing Corp., pp. 254-258, 1985.

D.H. Ballard and C.M. Brown, *Computer Vision*, Englewood Cliffs, NJ:Prentice-Hall, 1982.

L. Beiser, "Laser Scanning Systems," included in *Laser Applications*, New York:Academic Press, 1974, edited by Monte Ross, pp. 53-159.

A. Brandt, "Hydrodynamic Flowfield Imaging," *Flow Visualization III*, Hemisphere Publishing Corp., pp. 279-284, 1985.

J.G. Caputo, B. Malraison, and P. Atten, "Determination of Fractal Dimensions and Entropy for Various Flows: An Experimentalist's Viewpoint," in *Dimensions and Entropies in Chaotic Systems*, G. Mayer-Kress, ed., Berlin:Springer-Verlag, 1986.

K.R. Castleman, *Digital Image Processing*, Englewood Cliffs, NJ:Prentice Hall, Inc., 1987.

W.E. Castwell and J.A. Yorker, "Invisible Errors in Dimension Calculations: Geometric and Systematic Effects," in *Dimensions and Entropies in Chaotic Systems*, G. Mayer-Kress, ed., Berlin:Springer-Verlag, 1986.

P.C. Chatwin and P.J. Sullivan, "The Basic Structure of Clouds of Diffusing Contaminant," in *Mathematical Modeling of Turbulent Diffusion in the Environment*, C.J. Harris, ed., New York:Academic Press, pp. 3-31, 1979.

C.K. Chow and T. Kaneko, "Boundary Detection of Radiographic Images by a Threshold Method," in *Frontiers of Pattern Recognition*, New York:Academic Press, 1972.

L.W. Couch, *Digital and Analog Communication Systems*, New York:Macmillan Publishing Co., 1983.

A.E. Cowart, *The Detection of Unresolved Targets in Sequential Imagery Using the Hough Transform*, PhD dissertation, North Carolina State University, 1986.

A. Forgety, "Applying Image Processing to Flow Analysis of an Aerosol Pollutant," Master's thesis, North Carolina State University, 1989.

S.K. Friedlander, *Smoke, Dust, and Haze: Fundamentals of Aerosol Behavior*, New York:John Wiley, 1977.

N.C. Gallagher, G.R. Arce, and T.A. Nodes, "Median Filters," in *Advances in Computer Vision and Image Processing," New York:JAI Press Inc., 1986.*

R.C. Gonzales and P. Wints, *Digital Image Processing*, Reading, MA:Addison-Wesley, 1987.

P. Grassberger and I. Procaccia, *Physica*, Vol. 13D, pp. 34-40, 1984.

T.C. Halsey, M.H. Jensen, L.P. Kadanoff, I. Procaccia, and B.I. Shraiman, "Fractal Measures and their Singularities: The Characterisation of Strange Sets," *Phys. Review A*, Vol. 33, No. 2, pp. 1141-1151, 1986.

S.R. Hanna, "Concentration Fluctuations in a Smoke Plume," *Atmospheric Environment*, Vol. 18, No. 6, pp. 1091-1106, 1984.

R.M. Haralick and L.G. Shapiro, "Image Segmentation Techniques," *Computer Vision, Graphics, and Image Processing*, Vol. 29, pp. 100-132, 1985.

T.D. Hayosh, "Technical Considerations of Rotating Mirror Deflectors, Simple and Sophisticated," SPIE, Vol. 84, *Laser Scanning Components & Techniques*, pp. 123-131, 1976.

H.G.E. Hentschel and I. Procaccia, "The Infinite Number of Generalised Dimensions of Fractals and Strange Attractors," *Physica*, Vol. 8D, pp. 435-444, 1983.

L. Hesselink, "Digital Image Processing in Flow Visualisation," *Ann. Rev. Fluid Mech.*, Vol. 20, pp. 421-485, 1988.

A.H. Huber and S.P.S. Arya, "An Investigation of Transient Aspects of Atmospheric Dispersion Processes in the Wake of a Building through Video Image Analysis," Seventh Symposium on Turbulence an Diffusion Preprints, American Meteorological Society, November 1985.

A.H. Huber, *Distribution of Pollutant Concentrations Downwind of a Point-Source in the Near Wake of a Building*, Ph.D. Thesis, North Carolina State University, 1988a.

A.H. Huber, "Video Images of Smoke Dispersion in the Near Wake of a Model Building. Part 1. Temporal and Spatial Scales of Vortex Shedding," *Journal of Wind Engineering and Industrial Aerodynamics*, Vol. 31, pp. 189-223, 1988b.

A.H. Huber, S.P. Arya, S.A. Rajala, J.W. Borek, "Applications for Video Image Analysis of Smoke Dispersion in the Near Wake of a Model Building," *Proc. of the Fourth International Workshop on Wind and Water Tunnel Modelling of Atomospheric Flow and Dispersion*, 1988.

A.H. Huber, "Video Images of Smoke Dispersion in the Near Wake of a Model Building. Part 2. Cross-Stream Distribution," *Journal of Wind Engineering and Industrial Aerodynamics*, Vol. 32, pp. 263-284, 1989.

A.K. Jain, *Fundamentals of Digital Image Processing*, Englewood Cliffs, NJ:Prentice Hall, 1989

K. Kanatani, "Detecting the Motion of a Planar Surface by Line and Surface Integrals," *Computer Vision, Graphics, and Image Processing," 1984.*

I. Kimura and T. Takamori, " Image Processing of Flow Around a Circular Cylinder by Using Correlation Techniques," *Flow Visualization III*, Hemisphere Publishing Corp., pp. 221-226, 1985.

J.T. Lee, D.L. Call, R.E. Lawson, W.E. Clements, and D.E. Hoard, "A Video Image Analysis System for Concentration Measurements and Flow Visualisation in Building Wakes," Los Alamos National Laboratory, Report No. LA-UR-88-4014, 1989.

J.O. Limb and J.A. Murphy, "Estimating the Velocity of Moving Images in Television Signals," *Computer Graphics and Image Processing*, Vol. 4, pp. 311-327, 1975.

S. Lovejoy and B.B. Mandelbrot, "Fractal Properties of Rain, and a Fractal Model," *Tellus*, Vol. 37, pp. 209-232, 1985.

S. Lovejoy and D. Schertser, "Scales, Symmetries, Fractals, and Stochastic Simulations of Atmospheric Phenomena," *Bull. Ame. Meteorol. Soc.*, Vol. 67, pp. 21-32, 1986.

B.B. Mandelbrot, *Fractals: Form, Chance and Dimension*, San Francisco, CA:Freeman and Co., 1977.

B.B. Mandelbrot, *The Fractal Geometry of Nature*, San Francisco, CA:Freeman and Co., 1983.

B.B. Mandelbrot, "Fractal Measures (Their Infinite Moment Sequences and Dimensions) and Multiplicative Chaos: Early Works and Open Problems," in *Dimensions and Entropies in Chaotic Systems*, G. Mayer-Kress, ed., Berlin:Springer-Verlag, pp. 19-27, 1986.

W.N. Martin, S. Yalamanchili, and J.K. Aggarwal, "Extraction of Moving Object Descriptions via Differencing, *Computer Graphics and Image Processing," 1982.*

G.G. Medioni and Y.Yasumoto, "A Note on Using the Fractal Dimension for Segmentation," *IEEE Computer Vision Workshop*, Annapolis, MD, ppl 25-30, 1984.

C.L. Medler, L.M. Gelberg, and R.P. Burkhart, "Graphical Realisation of Turbulent Smoke Plumes on the Pixar," *Proc. Smoke/Obscurants Symposium X*, Harry Diamond Laboratories, Adelphi, MD, pp. 235-247, 1986.

The Melles-Griot Corp., *Optics Guide 3.*

W. Merzkirch, *Flow Visualization*, First Edition, New York:Academic Press, 1974.

T.J. Mueller, " Recent Developments in Smoke Flow Visualisation, " *Flow Visualization III*, Hemisphere Publishing Corp., pp. 30-40, 1985.

A.N. Netravali and J.D. Robbins, "Motion Compensated Television Coding - Part I," *Bell System Technical Journal*, Vol. 58, pp. 631-670, 1979

A.N. Netravali, J.A. Stuller, and J.D. Robbins, "Interframe Television Coding using Gain and Displacement Compensation," *Bell System Technical Journal*, Vol. 59, pp. 1227-1240, 1980.

H.-O. Peitgen and P.H. Richter, *The Beauty of Fractals*, Springer-Verlag:Berlin, 1986.

A.P. Pentland, "Fractal-based Description of Natural Scenes," *IEEE Trans. on Pattern Analysis and Machine Intelligence*, Vol. PAMI-6, pp. 661-674, Nov. 1984.

R. Porcar and J.P. Prenel, "Visualisation by Means of Coherent Light Sheets: Applications to Different Flows," *Optics and Laser Technology*, Vol. 14, No. 5, pp. 261-268, October, 1982.

R. Porcar, J.P. Prenel, and G. Diemunsch, and P. Hamelin, " Visualisations by Means of Coherent Light Sheets; Applications to Various Flows," *Flow Visualization III*, Hemisphere Publishing Corp., pp. 123-127, 1985.

W.K. Pratt, "Correlation Techniques of Image Registration," *IEEE Transactions on Aerospace and Electronic Systems*, Vol. AES-10, No. 3, May 1974, pp. 353-358.

W.K. Pratt, *Digital Image Processing*, New York:John Wiley & Sons, 1978.

J.P. Prenel, R. Porcar, and G. Diemunsch, " 3D Flow Visualisations by Means of Laser Beam Sweeps," *Flow Visualization IV*, Hemisphere Publishing Corp., pp. 99-103, 1987.

I. Procaccia, "The Static and Dynamic Invariants that Characterise Chaos and the Relations between them in Theory and Experiments," *Physica Scripta*, Vol. T9, pp. 40-46, 1985.

I. Procaccia, "The Characterisation of Fractal Measures as Interwoven Sets of Singularities: Global Universality at the Transition to Chaos," *Dimensions and Entropies in Chaotic Systems*, G. Mayer-Kress, ed., Berlin:Springer-Verlag, pp. 8-18, 1986.

A. Rosenfeld and A.C. Kak, *Digital Picture Processing*, Second Edition, Vol. 2, New York: Academic Press, 1982.

I.K. Sethi and R.J. Jain, "Finding Trajectories of Feature Points in a Monocular Image Sequence," *IEEE Trans. on Pattern Analysis and Machine Intelligence*, Vol. PAMI-9, pp. 56-73, 1987.

Speedring Division of the Schiller Corp., *Rotating Mirror Scanners, Substrates and Coatings,* Technical Bulletin 101-3, a technical bulletin from Speedring Division of Schiller Corp.

M. Stanlisas, " Ultra High Speed Visualisation of Unsteady Flows using a Pulsed Ruby Laser," *Flow Visualization III*, Hemisphere Publishing Corp., pp. 41-44, 1985.

H. Stapountzis, D.D. Stretch, and R.E. Britter, "Diffusion of Smoke Behind a Line Source in Grid Turbulence," *Flow Visualization IV*, Hemisphere Publishing Corp., pp. 210-214, 1987.

C. Veret, "Flow Visualisation by Light Sheet," *Flow Visualization III*, Hemisphere Publishing Corp., pp. 106-112, 1985.

Von Karman Institute, "Digital Image Processing in Fluid Dynamics," Lecture Series 1984-03, Von Karman Institute for Fluid Dynamics, Belgium, 1984.

M. Young, *Optics and Lasers*, New York:Springer-Verlag, 1986.

APPENDIX A

Applications for Video Image Analysis of Smoke Dispersion in the Near Wake of a Model Building

APPLICATIONS FOR VIDEO IMAGE ANALYSIS OF SMOKE DISPERSION IN THE NEAR WAKE OF A MODEL BUILDING

Alan H. Huber*
Atmospheric Research and Exposure Assessment Laboratory
U. S. Environmental Protection Agency
Research Triangle Park, NC 27711 U.S.A.

S. Pal Arya
Department of Marine, Earth and Atmospheric Sciences
North Carolina State University
Raleigh, NC 27695 U.S.A.

Sarah A. Rajala
Department of Electrical and Computer Engineering
North Carolina State University
Raleigh, NC 27695 U.S.A.

James W. Borek
Computer Sciences Corporation
Research Triangle Park, NC 27709 U.S.A.

Paper presented at the
Fourth International Workshop on Wind and Water
Tunnel Modelling of Atmospheric Flow and Dispersion
October 3-6 1988, Karlsruhe, Germany
and
Manuscript submitted to
Atmospheric Environment

ABSTRACT

A summary of analyses of video images of smoke in a wind tunnel study of dispersion in the near wake of a model building is presented. The analyses provide information on both the instantaneous and time-average patterns of dispersion. Since the images represent vertically-integrated or crosswind-integrated smoke concentration, only the primary spatial and temporal scales of pollutant dispersion can be examined. Special graphic displays of the results are presented to assist in the data interpretation. The video image format is shown to have great potential as an easily quantifiable electronic medium for studying the dispersion of smoke.

---

* On Assignment from the National Oceanic and Atmospheric Administration, U.S. Department of Commerce

1. INTRODUCTION

We have been investigating the application of analyses of video images of smoke flow in the wake of a model building in a meteorological wind tunnel. Analyses of video recorded images of smoke can provide important temporal and spatial resolution, which can more easily provide a better understanding of the dispersion processes than is possible from traditional point-sampling techniques. Wind tunnel modeling provides a practical method for evaluating the aerodynamic building wake influences on plume dispersion without the variability in atmospheric conditions. Also, more detailed measurements are possible in the controlled environment of the wind tunnel.

Photographs of smoke have been used for many years in studies to provide a visualization of dispersion patterns. Photographs are usually viewed qualitatively, because of the time and difficulties involved in quantifying their images. A detailed quantitative analysis of photographs (or their negatives) is possible by using a microdensitimeter to quantify the variation of brightness over the picture (e.g. Nappo, 1984).

The video image format has great potential as an easily quantifiable electronic medium. The quantized video picture elements (pixels) may be analyzed using digital image processing methods. Digital image processing is rapidly becoming an important element in fluid dynamics research. We will not provide a review of methods here; see, for example, the Von Karman Institute (1984) and Hesselink (1988).

This paper presents a summary of our experience with analyses of video images of smoke. We began in 1984 to evaluate the applicability of video images to study the transient flow and dispersion characteristics in the wake of a building. The digitization of video images was not found to be a difficult problem. The management of all the data that can be generated was found to be a greater problem. There is a need for the determination of efficient digital image analysis techniques that are most applicable to the problem being studied. The rapid advancements in microelectronics continue to increase the power of video image analysis systems at a reduced cost. The use of new analysis systems that can perform image processing directly from the original video format should eliminate some of the data management problems. The growth in both the quality and the availability of video image analysis systems over the past few years has been startling. We expect this growth to continue.

A brief description of our experimental design and equipment is given in Section 2. A detailed description is presented by Huber (1988). Temporal and spatial scales of vortex-shedding of smoke puffs have been estimated through the calculations of spectral densities and autocorrelations (Huber, 1988). The temporal-spatial distributions of cross-stream profiles have been analyzed as functions of coordinates in time and space (Huber and Arya, 1989). Several image analysis techniques that modify the original pictures to provide enhanced features within the pictures and motion estimation are being evaluated. A report on these techniques is being prepared. A summary of our progress on this research project is presented in Section 3. Special graphic displays of results are presented to assist in the data interpretation.

2. EXPERIMENTAL DESIGN

The experiments were conducted in the Meteorological Wind Tunnel at the U.S. Environmental Protection Agency's Fluid Modeling Facility. It is an open-return wind tunnel with a test section 2.1 m high, 3.7 m wide, and 18.3 m long (Snyder, 1979). Flow downstream of a 0.1 m and a 0.2 m high (H) rectangular-shaped block was studied. The along-stream building length was equal to the building height. The cross-stream building length was twice the building height and was oriented perpendicular to and at a 45 degree angle to the freestream flow. The neutrally stratified boundary layer was 1 m deep. The mean velocity upstream of the building at an elevation $z=0.5H$ was used to categorize the flow; it was set at a nominal value $U_n = 1$, 2, or 4 m/s. The longitudinal turbulence intensity was 10-20 percent upstream of the building.

An oil-fog smoke was generated and emitted into the wind tunnel through a pipe, with the outflow pointed downstream. The stream of smoke simulated point-source emissions at ground level, midway along the leeward side of the building. The origin of the x,y,z coordinate system (along-stream, cross-stream, and elevation) was set at this same point. Since the smoke was emitted with excess momentum, a precise alignment of the jetting smoke was difficult. This added some unwanted asymmetry to the distribution of smoke. A 600-W flood light was placed 3 m downstream from the leeward building edge. The light was mounted in the center of the tunnel and elevated approximately 0.3 m. The light was aimed horizontally upstream toward the building. The resulting light, in the absence of the smoke, reflected off the floor, and was observed to be nearly uniform over the cross-stream profile of interest. The illumination levels and the attenuation of light in the smoke cloud were not directly measured. Black-and-white images of smoke were recorded at a rate of 30 pictures per second (U. S. standard NTSC RS170 format) with the camera connected to a standard VHS recorder. The camera was mounted outside the wind tunnel either looking down through a ceiling window (top view) or looking through a side window (side view). Selected sequences of video pictures were both visually and digitally studied.

Each smoke picture represents a two-dimensional view of the smoke-scattered light integrated through the third dimension. The digitized luminance value (called image intensity) represents an indirect measure of the smoke particle concentration through the field of view. This is valid for light scattered by either monodispersed or polydispersed particles, provided the overall transmissivity is sufficiently large (i.e., secondary scattering and fluctuations in the attenuation of light are insignificant). This condition is believed to have been met in this study. However, no special measurements were made to verify this presumption. We may pursue these measurements when the needed instumentation is obtained.

The video luminance analog signal was digitized by a video sequence processor at the North Carolina State University's Image Processing Laboratory. The digitized luminance signal is on a unitless gray scale from 0 to 255 (an 8 bit binary representation). A value of zero would result for zero luminance and a value of 255 would result for full-scale saturation in the luminance signal. However, the video sequence processor has a guard-band protection which was designed to limit the signal extremes. These limited digitized values fall between 16 and 240 (i.e., between 6 and 94 percent of the full scale). The guard band has been observed to shift on occasions.

Table 1 presents a histogram for a 15-second sample of digitizer output across ($-3<y/H<3$) the plume at $x/H=3$ (note; the total number of values is 248,850 , i.e. 553 pixels for each of 450 frames). The downstream position for these data is just downstream of the recirculating cavity flow near the building. This position provides the best opportunity to measure the shedding vortices without complications due to significant recirulating flow in the cavity. The lowest observed intensity (approximately 25) corresponds to the expected reference black level. The intensity level of 50 was found to correspond to the mean background intensity in the absence of smoke. The variation around the background mean of 50 (25 to 75) corresponds to fluctuations due to a noise level that is approximately 10 percent of the full scale. The gap in the histogram separates the band of low intensity values (for pixel locations near the tail of the plume) from the band of higher intensity values (for intense smoke puffs across the plume) which have peak probability at the 155-160 level. The highest observed intensity (approximately 240) corresponds to the expected upper limit for the digitizer. Histogram contours with intensity intervals of 5 over the 0 to 255 range were found to be generally smooth as observed here. A look at the observed probability for each integer intensity revealed that the digitizer quantization is limited to 64 levels (values of the upper 6 bit binary representation) each with 4 units of random error (values of the lowest 2 bit binary representation).

The original intensity was corrected for estimated background by subtracting 50 and then normalized to give a range of 0-100 percent. The background intensity was found to be slightly variable over the image due to reflections and was slightly contaminated along the plume edge by scattered light from the plume core. The estimated background at 50 was found to be good enough for our study. The few original values that were less than 50 were set to a normalized value of 0 percent. The normalized scale range should correspond to a unitless scale that is an indirect measure of the vertically-integrated smoke concentration, up to full-scale saturation. Table 2 presents histograms of normalized intensity for pixels positioned at y/H=0 and y/H=-1.5H. The distributions were observed to be symmetric near the center of the plume and to be increasingly skewed away from the plume center. All distributions for intensity values at one pixel position were found to be unimodal in comparision to the bimodal character of the distributions for intensity values across the picture (Table 1).

3. RESULTS

3.1. Profiles

The distributions of intensity in a series of profiles at x/H=3 were analyzed as functions of coordinates in time and space. The downstream position at x/H=3 was observed to be slightly downstream of the recirulating "cavity" flow adjacent to the building. Figure 1 presents a contour plot for three ranges of normalized intensity standardized by the mean intensity at the plume centerline. These normalized intensities are a standardization (relative to the mean centerline value) of normalized intensity as defined in Section 2. The minimum intensity level of 0.1 was chosen to represent the areas of minimum smoke intrusion above background noise. The contour level above 1 was chosen to represent the high-concentration areas around the smoke plume centerline. This type of plot depicts the large scale structure of the smoke flow.

The contour patterns were found to be quite sensitive to the selected intensity ranges. More detail can be observed by including many contour intervals in this type of plot. However 3 to 4 intervals were found to provide the clearest depiction of the transport of smoke from the cavity zone into the flow downstream of the building. The differences between the two cases with 0 degree building orientation appeared to be purely time scaled. The size and frequency of the high-concentration intervals were found to be inversely proportional to the flow velocity. The 45-degree case appeared to have a narrower region of high concentration and its centerline was shifted to $y/H=-1$. The flow streamlines over the building converged toward the ground around the edge of the building that had been rotated in the downstream direction. The location of the peak intensity was observed to be increasingly skewed in alignment with the side edge that had been rotated in the downwind direction.

Temporal plots of intensity for selected pixels were examined to provide a more detailed look at the pattern of smoke over temporal-spatial coordinates. Figure 2 presents the pixel signals at two postions using the same intensity values that were contoured in Figure 1. These plots display the smaller scale structure. The fluctuations were larger away from the plume centerline. The patterns of maximum and minimum intensities away from the plume centerline were comparable but more peaked and slightly out of phase with those of the central core of the plume. The variations of intensity for the 45-degree cases were less than for the 0-degree cases because the flow of smoke downstream from the rotated building was more concentrated and meandered less.

Figure 3 compares profiles of the means and the standard deviations of the same intensity values for the 0-degree case and the 45-degree case that were contoured in Figure 1. The distribution of the means was symmetric about source position ($y/H=0$) for the 0 degree case. The distribution of the means was skewed across the rotated building with the highest values in alignment with the edge of the building that was rotated downstream. The larger standard deviations were located in a region 0.5H away from building edge for both the lateral and vertical views. This was the outer region of the plume into where the concentrated smoke meandered intermittently.

Additional spatial and temporal statistics for the cross-stream distribution of smoke are evaluated and reported by Huber and Arya, 1989. That paper also also reports statistics for the distributions of conditionally-sampled intensity. Plume meander is less significant to the overall distribution than is the instantaneous plume spread across the downstream projection of the width of the building. The periodicity in the smoke dispersal is observed in the calculated statistics. The time-averaged profiles of smoke are comparable with tracer concentration measurements in the building wake.

Temporal and spatial scales of vortex-shedding of smoke puffs have been estimated through calculations of spectral densities and autocorrelations for values among individual picture elements and are reported by Huber, 1988. The dominant frequencies (Hz) near the center of the wake are 0.1-0.3 times the ratio of the velocity to building height. Estimated integral length scales near the center of the wake flow are 1-2 times the building height. The temporal and spatial scales are smaller away from the building center. These results are consistent with the depiction provided in Figure 1 and 2.

The time series analyses are being expanded to include cross-correlatations and cross-spectra. For example, Figure 4 compares the correlation coefficients of the plume center ($y=0$ or $z=0.5H$) with other positions across the plume. Correlation analyses provide a good measure for estimating the spatial spread of the smoke puffs. Cases differing only in mean velocity were found to have the same pattern of correlation with time lag being inversely proportional to the mean velocity. Correlations ranging over significant time lag were found to be symmetric about its peak value. Peak cross-correlations in the top view occured at zero lag time and were significant at separation distances less than H. Peak cross-correlations in the side view occured at lag times which indicated that rising intensity lagged at the higher elevation. As for the top view, cross-correlations were significant at separation distances less than H. These results indicate that coherent puffs of smoke less than H in size were periodically swept from the ground and transported downstream.

3.2. Full Picture

The full picture frames are also being evaluated. Figure 5 presents a contour plot of a 4-s averaged full picture of normalized intensity. The normalized intensities were calculated in the same way as discussed in Section 2 and then all values were standardized by the observed maximum mean intensity. The building edges are outlined in each picture. The source was located near $x/H=0$, $y/H=0$, $z/H=0$; however, the source momentum resulted in some jetting of the smoke downstream.

We expect that secondary scattering and fluctuations in attenuation of the light are significant very near the source, prior to being mixed within the building wake (i.e., $x/H<0.5$, $z/H<0.5$). Thus, the observed maximum value occurred near the center of the wake-cavity region where the mean velocity is expected to be a minimum. Considering that the intensity represents the vertically-integrated or crosswind integrated smoke concentration, the depiction appears to be qualitatively correct.

The general features of the highly intense "cavity" region are clearly depicted in Figure 5. In the top view, parts of the painted white lines along the 10-cm (0.5H) grid are evident. In the side view some of the beads strung 5-cm apart as vertical markers are evident. Except for $x/H<0.5$, $z/H<0.5$ the full picture does not appear to be distorted by light attenuation in either the downstream or cross-stream directions. However, additional research is needed to quantitatively evaluate these full pictures.

A number of image analysis techniques have been applied to these full-picture data . A complete report of this work will be presented in due course. A brief discusion of the application of frame differencing, spatial filtering, and image segmentation follows here.

Frame Differencing

A difference operator applied over a sequence of images provides us with information about the changes that occur in intensity with respect to time. If the background lighting conditions do not change from frame to frame and there is not a significant amount of noise, nonzero values at the output of the difference operation can be attributed to the temporal changes in the smoke. An nth-order difference applied over a the x,y space is given as follows:

$$d_k^n(x,y) = d_k^{n-1}(x,y) - d_{k-1}^{n-1}(x,y)$$

where d_k^n is the nth-order difference at frame k (e.g., the 1st-order difference at frame 2, d_2^1, is the difference between frame 2 and frame 1; the higher order differences follow similarly while cascading to the 1st-order difference).

The advantage of an nth-order difference over a simple 1st-order difference is its decreased sensitivity to low frequency time-correlated noise. On the other hand, the nth-order difference is more sensitive to temporally uncorrelated white noise. In our application, it was found that any difference operator applied directly to the image data with order greater than two was saturated by the noise in the recorded data. However, the sequences generated at the output of either the first or second difference yielded usable data. We have found the video display of a sequence of 1st-order frame differences to provide an enlightened look into the 3-dimensional motion of smoke near the building. At present, we are investigating the feasibility of using a noise cleaning procedure prior to the difference operation.

Spatial Filtering for Edge Enhancement

Several spatial high-pass filters were applied to the image data to evaluate the effectiveness of enhancing the "edges" in this type of data. The simplest of these two-dimensional filter structures is based on calculation of the spatial gradient. They are generally implemented as non-recursive, finite-impulse-response filters. An example filter that we have examined is given by:

$$\begin{bmatrix} 0 & -1 & 0 \\ -1 & 5 & -1 \\ 0 & -1 & 0 \end{bmatrix}$$

where the center of this 3 by 3 "mask" is applied over the whole image (i.e. the value from the filter is an average composed of 5 times the original value and -1 times each value for its adjacent pixels). This filter should clearly enhance regions having a large spatial gradient.

As is the case with temporal differencing, we again must be concerned about the effect of noise on the results. Spatial high-pass filtering amplifies the image information in regions where the spatial gradient is high and de-emphasizes the information where the gradient is low. However, a white noise contaminated image will have high values of the spatial gradient spread uniformly over the image. The result is that the noise can mask other potentially useful edge-type information in the image.

For our sequences, the spatial filter listed above worked well. Figure 6b presents an example for one filtered frame. The plume edges were enchanced in comparison with the original frame (Figure 6a). In these pictures the building lies in the bottom and the top of the picture is cut at x/H=2. The 10-cm grid markings are seen in both pictures.

Image Segmentation

Image segmentation is defined as the process of partitioning an image into disjoint regions which are uniform and homogeneous with respect to some characteristic. Image characteristics which have been shown to be useful include gray-level intensity, texture and motion. Although a large number of segmentation algorithms have been developed, many of those are restricted in their applications because of various constraints. The most common of the constraints is the need for well defined boundaries between the disjoint regions. Because of the nature of the image data we are analyzing, it was not clear that image segmentation in any form would provide useful results. However, we were interested in finding out what the limitations were.

At this stage in the research, we have concentrated on the most straight-forward of the image segmentation algorithms, i.e., gray-level thresholding. Gray-level thresholding starts by calculating the histogram of the image or a portion of the image. A threshold(s) is then chosen from the histogram that will allow us to separate the objects of interest from the background information. If there is a sufficient difference in the intensity values of the background and the objects of interest, this type of segmentation technique will be successful. The histogram thresholding techique has been applied to the original image data, a mean image, and a difference sequence created by subtracting the mean image from each frame of the original data. In each case, we were able to segment out some of the interesting features of the image sequence for visualization. Figure 6c presents an example for one frame. At present, we are evaluating the impact of performing spatial filtering prior to the segmentation process and investigating alternative methods for segmentation.

4. CONCLUSIONS

Analyses of digitized video recorded images of smoke provide practical information for quantifying the primary spatial and temporal scales of pollutant dispersion in the wake of a building. This technique provides spatial details over the full picture and temporal fluctuations not as easily obtainable from a traditional point concentration mapping.

We believe there are a number of image analysis techniques that can be used to aid in improving the visualization of this type of image data. In the continuation of this research, we will be investigating the use of motion-estimation techniques for extracting both qualitative and quantitative information from the image data.

Acknowledgements

This research was supported by the United States Environmental Protection Agency. Support to North Carolina State Univerisy was provided through Cooperative Agreement CR813368. We are grateful to the staff of the U.S. Environmental Protection Agency Fluid Modeling Facility for assistence with the wind tunnel study and to several people in the Image Processing Laboratory at North Carolina State University for assistence with the video image analyses (particularly Adnan Alattar and Alice Forgety).

REFERENCES

Hesselink, L. (1988) Digital image processing in flow visualization. *Ann. Rev. Fluid Mech. 1988 20:421-85.*

Huber, A. H. (1988) Video images of smoke dispersion in the near wake of a model building. Part I. Temporal and spatial scales of vortex shedding. *J. Wind Engr. Ind Aerodyn., 31 (1988) 189-223.*

Huber, A. H. and S. P. S Arya (1989) Video images of smoke dispersion in the near wake of a model building. Part II. Cross-stream distribution. *J. Wind Engr. Ind Aerodyn., 32 (1989) 263-284.*

Nappo, C. J. (1984) Turbulence and dispersion parameters derived from smoke-plume photoanalysis. *Atmos. Environ., 18, 299-306.*

Snyder, W. H. (1979) The EPA meteorological wind tunnel: Its design, construction, and operating characteristics, U.S. Environmental Proctection Agency Report NO. EPA-600/4-79-051, Research Triangle Park, N.C., 1979.

Von Karman Institute (1984) Digital image processing in fluid dynamics. Lecture Series 1984-03, Von Karman Institute for Fluid Dynamics, Belgium.

TABLE 1. Histogram of intensity values across -3<y/H<3 for 15-s series; U_n = 2 m/s, H = 0.2 m, x/H = 3.

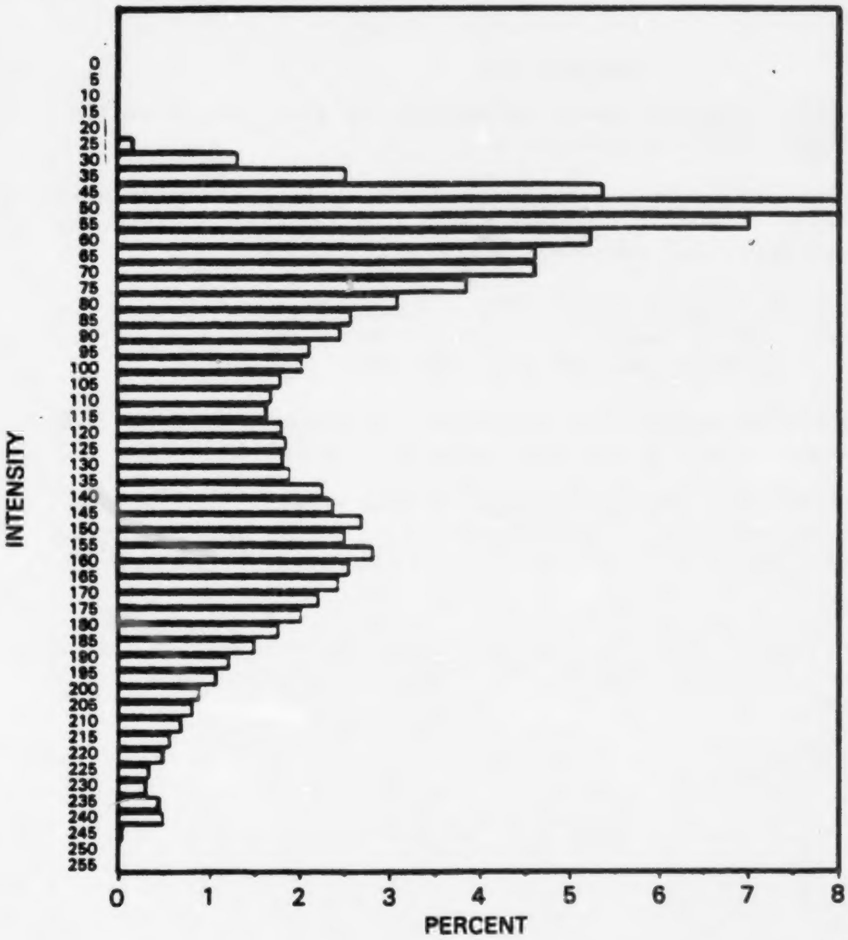

INTENSITY	PERCENT	CUM.PERCENT
0	0.00	0
5	0.00	0
10	0.00	0
15	0.00	0
20	0.01	0
25	16	0
30	1.31	1
35	2.50	4
45	8.40	18
50	6.99	25
55	5.21	30
60	4.60	35
65	4.58	39
70	3.85	43
75	3.08	46
80	2.57	49
85	2.45	51
90	2.11	53
95	2.03	55
100	1.79	57
105	1.68	59
110	1.64	60
115	1.80	62
120	1.85	64
125	1.81	66
130	1.88	60
135	2.25	70
140	2.37	72
145	2.69	75
150	2.49	77
155	2.81	80
160	2.54	83
165	2.42	85
170	2.21	87
175	2.01	89
180	1.75	91
185	1.49	93
190	1.21	94
195	1.07	95
200	0.89	96
205	0.81	97
210	0.69	97
215	0.57	98
220	0.50	98
225	0.34	99
230	0.31	99
235	0.43	99
240	0.49	100
245	0.04	100
250	0.00	100
255	0.00	100

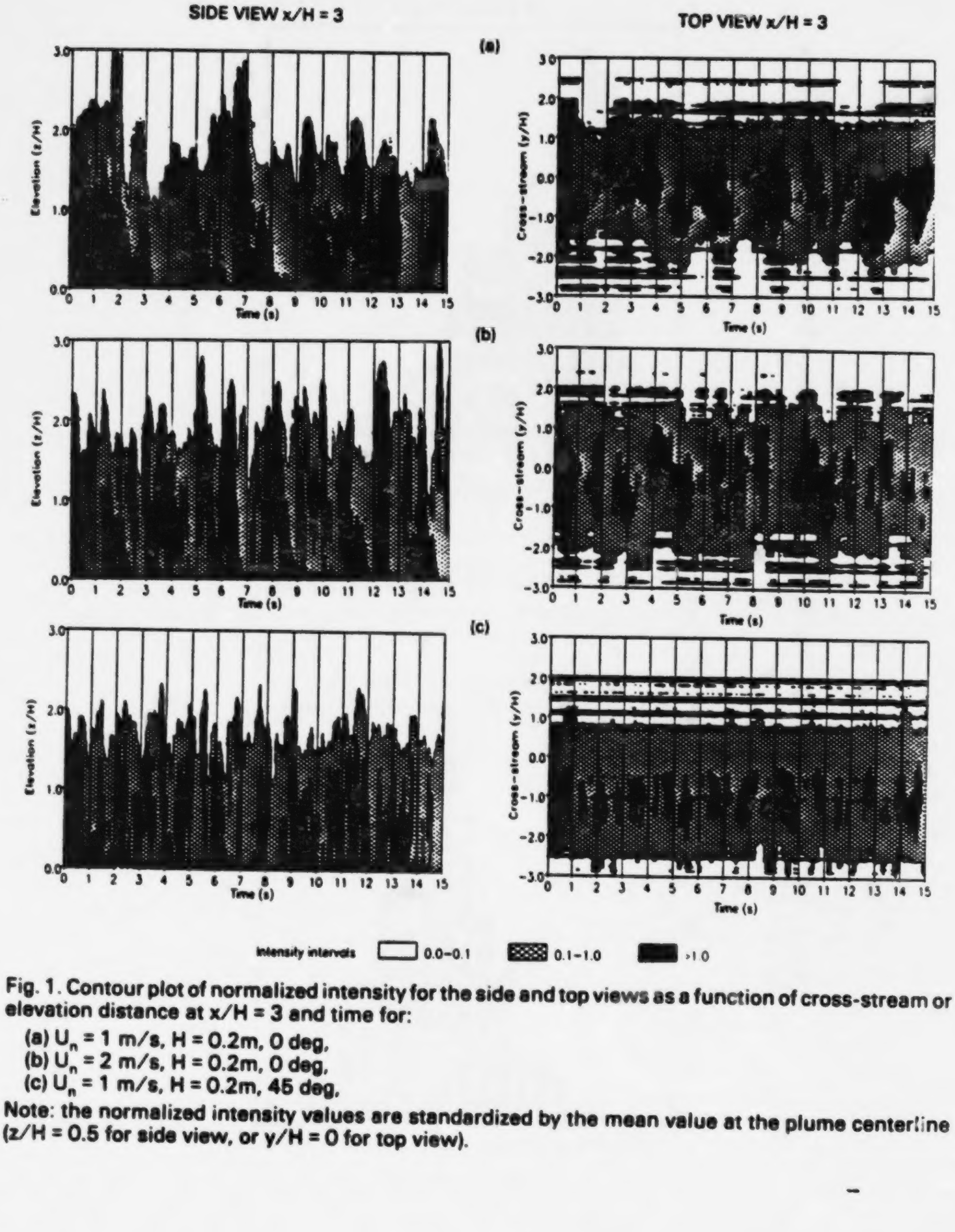

Fig. 1. Contour plot of normalized intensity for the side and top views as a function of cross-stream or elevation distance at x/H = 3 and time for:

(a) U_n = 1 m/s, H = 0.2m, 0 deg,
(b) U_n = 2 m/s, H = 0.2m, 0 deg,
(c) U_n = 1 m/s, H = 0.2m, 45 deg,

Note: the normalized intensity values are standardized by the mean value at the plume centerline (z/H = 0.5 for side view, or y/H = 0 for top view).

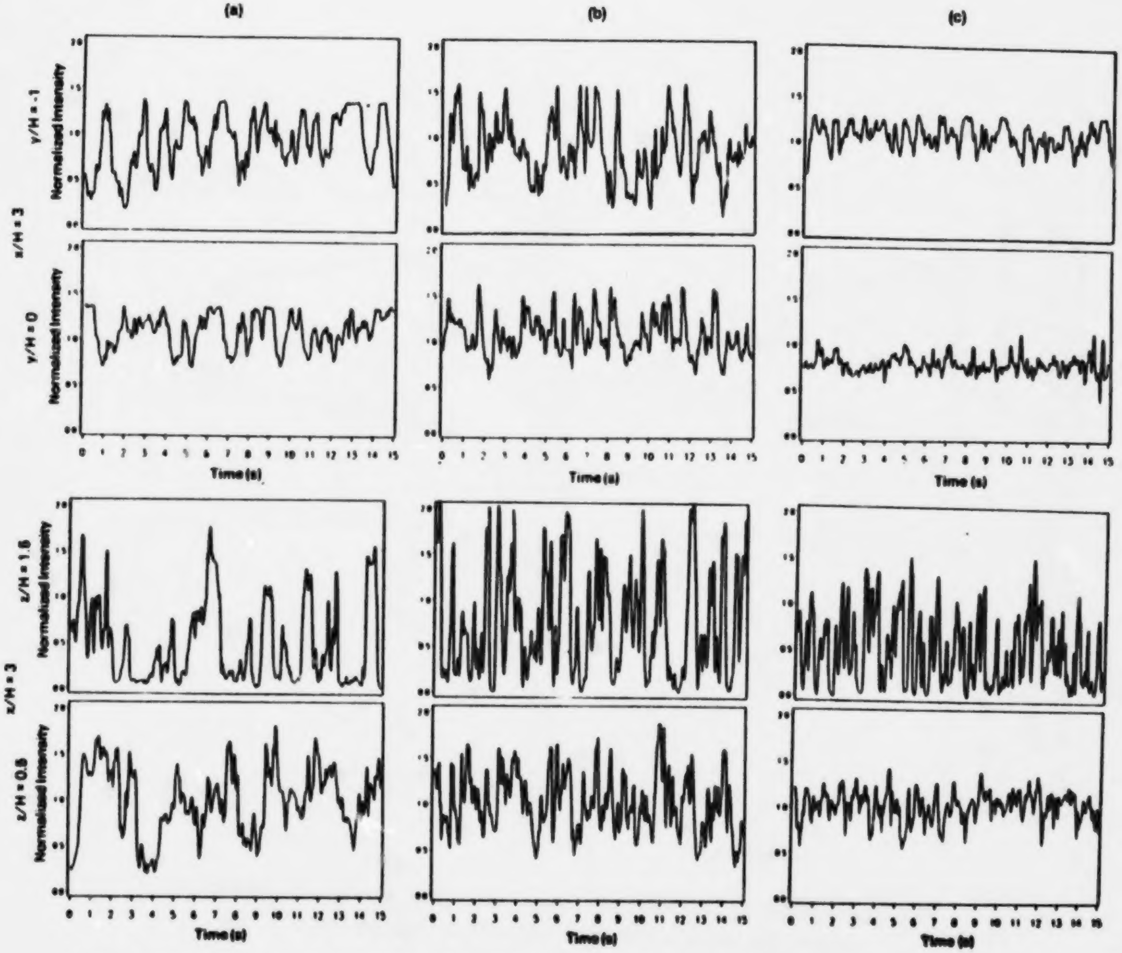

Fig. 2. Temporal variations of normalized intensity (relative to the mean centerline value) at x/H = 3 for (a) U_n = 1 m/s, H = 0.2 m, 0 deg (b) U_n = 2 m/s, H = 0.2 m, 0 deg. (c) U_n = 2 m/s, H = 0.2 m, 45 deg.

Note: the solid line is for $U_n = 2$ m/s, H = 0.2 m, 0 deg,
the dashed line is for $U_n = 2$ m/s, H = 0.2 m, 45 deg

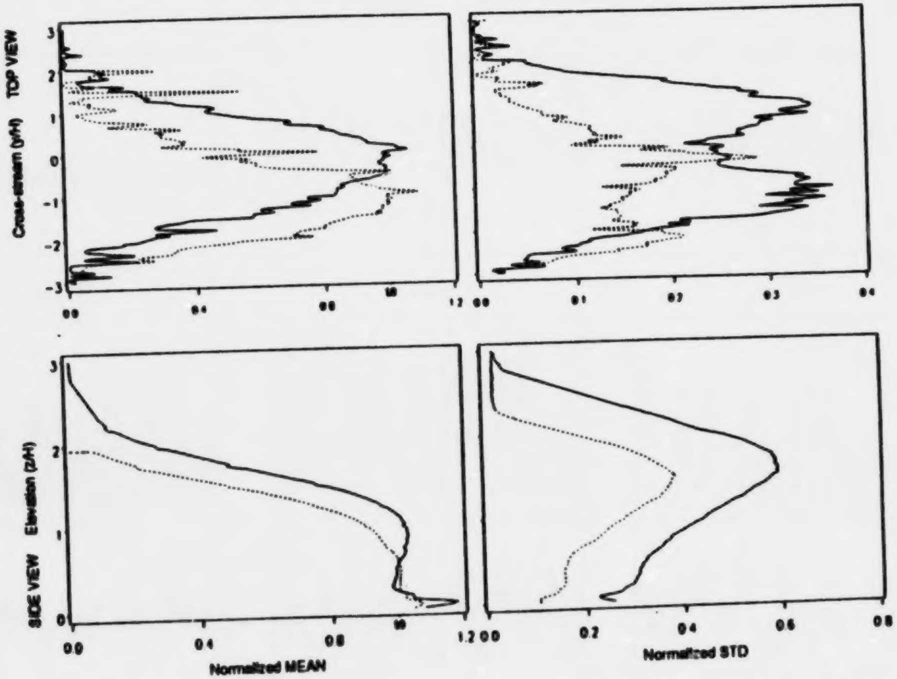

Fig. 3. Profiles of the normalized mean and standard deviation of intensity (relative to the centerline mean value).

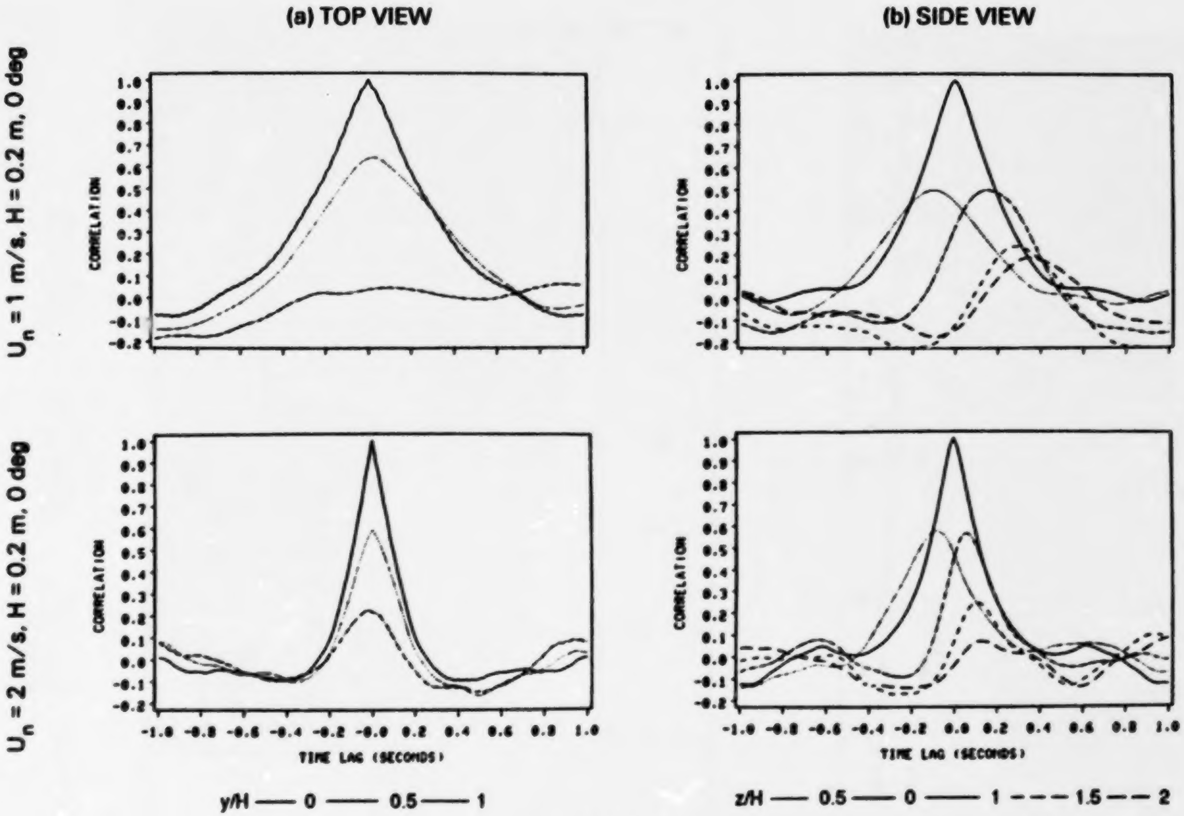

Fig. 4. Correlation coefficients between values at :
(a) y/H = 0 and indicated position
(b) z/H = 0.5 and indicated position

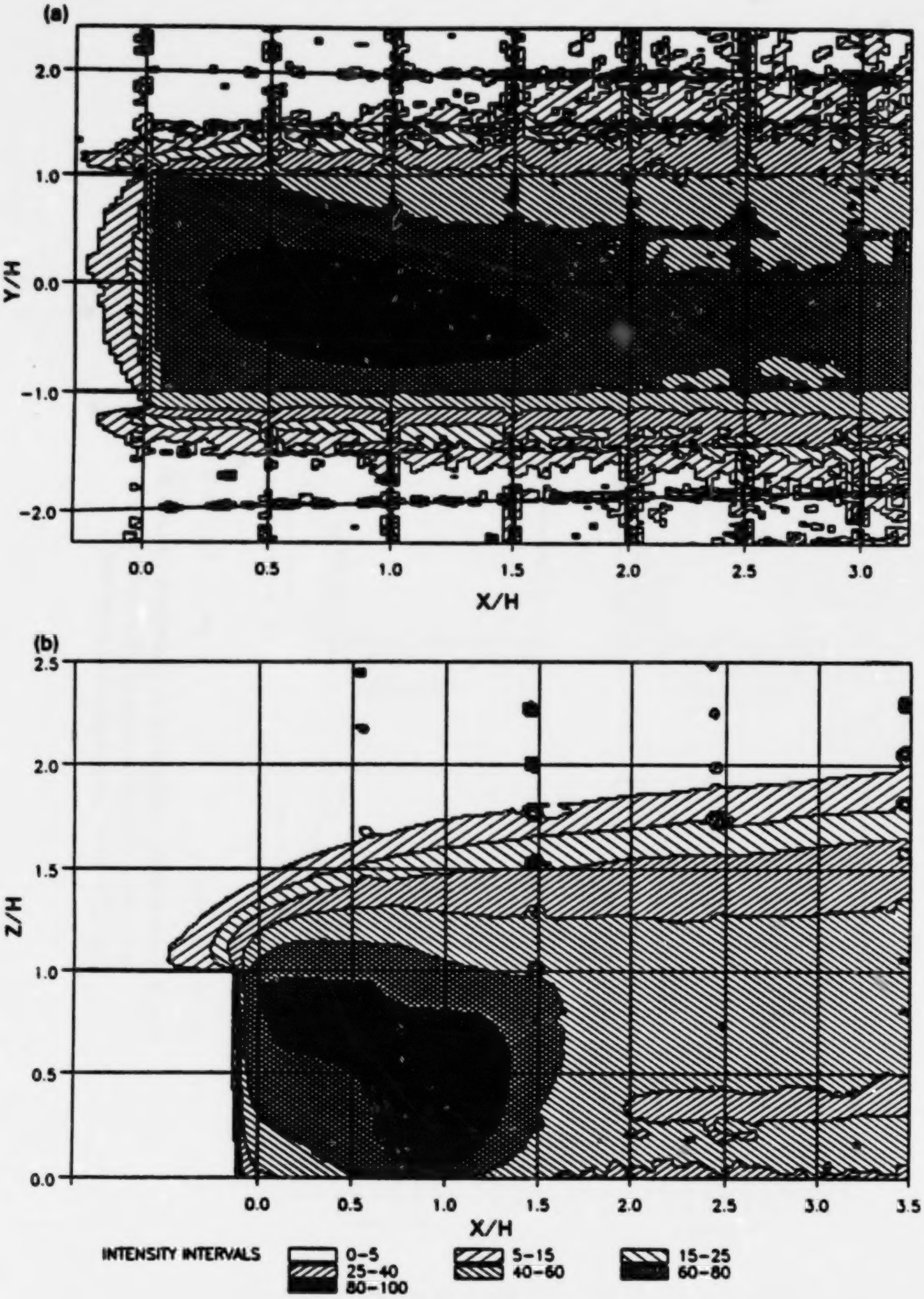

Fig. 5. Contour plot of 4-s-averaged full picture for normalized intensity (relative to the maximum mean intensity) for $U_n = 2$ m/s, H = 0.2 m, 0 deg: (a) top view, and (b) side view.

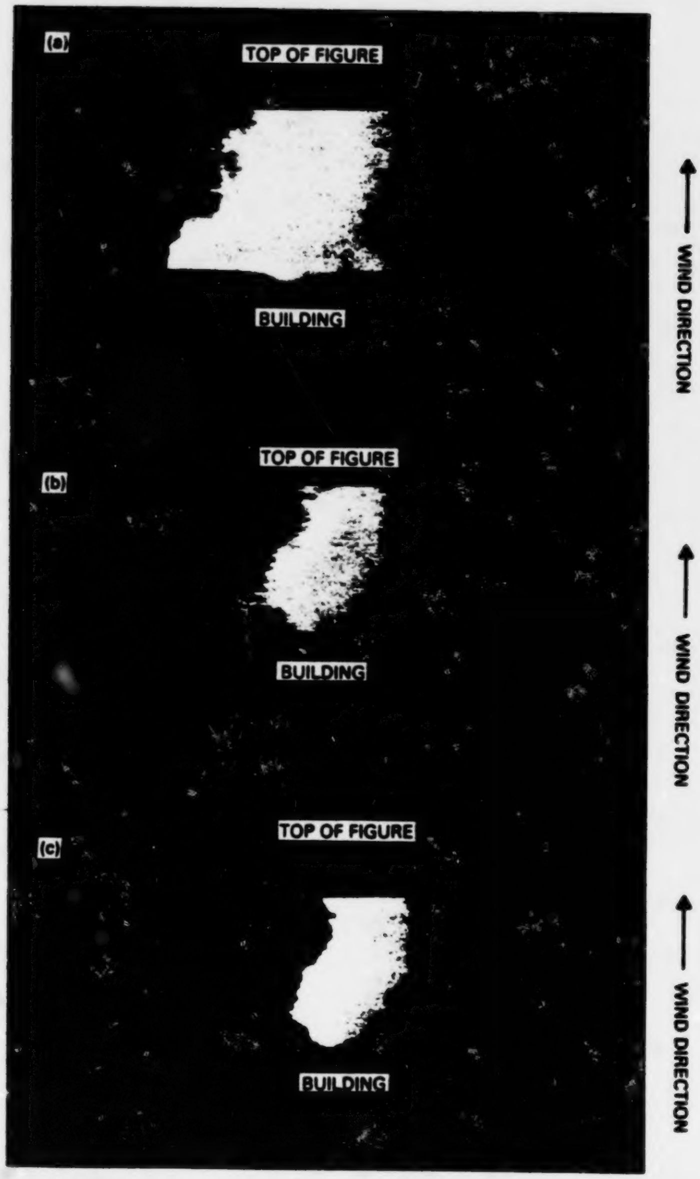
(a)
TOP OF FIGURE
BUILDING
WIND DIRECTION
(b)
TOP OF FIGURE
BUILDING
WIND DIRECTION
(c)
TOP OF FIGURE
BUILDING
WIND DIRECTION

Fig. 6. Photograph of one full frame (within x/H<2) from the top view sequence: (a) original image, (b) spatial filtered image (c) segmented image

APPENDIX B

DIMENSIONALITY MEASUREMENTS FOR CHAOTIC DYNAMICAL SYTEMS

Sarah A. Rajala
and
Amar Ait-Kheddache

North Carolina State University
Electrical and Computer Engineering
Campus Box 7911
Raleigh, NC 27695-7911

ABSTRACT

In this paper we present a review of the current status of research on the dimension of strange attractors and the connection to the concept of a fractal dimension. Dimension is an important measure of dynamical systems because it gives us a way to find their number of degrees of freedom or to characterize their attractors. Unfortunately, for chaotic dynamical systems whose structure is not regular or smooth, defining and/or estimating the dimension is nontrivial. The fractal dimension can be used as a measure for describing these chaotic dynamical systems and their strange attractors.

The concepts of strange attractors, dimensionality and their relationship to fractals are presented. In addition, methods for estimating the dimension, techniques for reducing the dimension and several applications will be discussed.

1. INTRODUCTION

In *The Elements,* Euclid compressed the whole of geometric science to an axiomatic configuration in which all the propositions and theorems were inferred from a small number of axioms and postulates. Geometry, which furnishes us with information about the structure of the space in which we exist and of the spatial relationship between the objects and phenomena we encounter in life, was placed in a unique position and was regarded as the completely developed and perfected science. Shortly before the time of Euclid, Plato established his Academy and over the door placed the sign, "Let no one enter unless he knows geometry." After Euclid wrote *the Elements,* Plato's successors at the Academy changed the sign to read, "Let no one enter here unless he knows Euclid."

Is it possible that a time will come in the future to once again change Plato's sign? This time to read, "Let no one enter here unless he knows fractals". The answer remains open, but Mandelbrot [1] said: "Why is geometry often described as cold and dry? One reason lies in its inability to describe the shape of a cloud, a mountain, a coastline, or a tree." The physicist J.A. Wheeler [2] said: "No one is considered scientifically literate today who does not know what a Gaussian distribution is, or the meaning and scope of the concept of entropy. It is possible to believe that no one will be considered scientifically literate tomorrow who is not equally familiar with fractals." "Why all the fuss about fractals?", asked Leo Kadanoff in *Fractals: Where's the Physics?* [3]. Jaggard, et al. [4] replied, "We are concerned not only with the beauty and elegance of fractal geometry but also with its application to viewing and solving problems of engineering analysis and synthesis in new ways." This appears to be a reasonable answer since the theory of fractal concepts provides a wealth of ideas for scientists with different backgrounds.

Fractal set theory was first mentioned a century ago in correspondence between Cantor and Dedekind who discovered mathematical structures that were not adaptable to Euclid's or Newton's models. However, for almost three centuries the predominant mathematical method for building models has been differential calculus, in which Newton stated his laws of gravitation and motion in term of differential equations. However, these differential equations, as powerful as they are, have limitations since they describe only phenomena where change is continuous and smooth. A new concept was needful to overcome these limitations. Two decades ago, Benôit Mandelbrot pioneered the use of fractal models [1,5] and opened an unlimited number of doors to solve some "unsolvable" problems in economics and the hard sciences.

The word "fractal" was derived from the Latin adjective *fractus,* meaning irregular or fragmented. Mandelbrot [1] defined of a fractal as a set (subset of R^n) with its Hausdorff dimension strictly greater than its topological dimensions. However, Mandelbrot pointed out that the definition was incomplete because of the exclusion of a number of irregular sets which should also be categorised as fractals. An example of such an irregular set is a turbulent flow (unconstrained flow), which is an ensemble of a hierarchy of scales. Furthermore, fractals refer to a great number of complicated objects which are statistically self-similar. For example, two photographs of the same medium taken with two different frame sizes that are impossible to discriminate. Technically, the self-similarity property may be applied to either bounded or unbounded sets, as long as each piece of a shape is geometrically similar to the whole.

The intent of this paper is to present a review of the current status of research on the dimension of strange attractors and to provide a connection between the concepts of fractal dimension and strange attractors. It is already accepted in the dynamical systems literature that the calculation of the fractal dimension of strange attractors is an improvement over conventional statistical measures. These concepts are regarded as mathematical tools which circumvent the fuzziness and obscurity of dynamical systems. In fact, the fractal dimension provides a measure of the degree to which the phase space is filled by the solutions. It is this fact that has provided one of the primary motivations for utilizing this theory to study complex dynamical systems.

In [1] Mandelbrot stated that an attractor is strange when it is fractal. Putting it in another way, an attractor is strange if it possesses a non-integer fractal dimension. In general terms, the liaison between strange attractors and fractals takes place in phase space. Alternatively, an attractor is said to be chaotic if nearby orbits diverge exponentially from one another through time. Historically, chaos has meant irregular, disordered, erratic. Hence, the characterization chaotic refers to the dynamics of the attractor, while strangeness refers to the topology of the attractor.

The condition for attraction for a given ordinary first-order nonlinear differential equation, e.g., $\frac{dx(t)}{dt} = f(x(t))$ is given by the following:

$$\nabla \cdot f < 0 \tag{1}$$

The dimension of the attractor is regarded as a fundamental measure for describing its compressibility properties. Said differently, the dimension of the attractor provides the amount of information requisite to specify the location of a point on the attractor to within a given accuracy. Another property of interest is the information dimensionality. It can be regarded as the number of bits which can dynamically be stored on the attractor. For trajectories on the attractor, the dimensionality reduction initiates a reduction in the information necessary to state explicitly an initial condition. Knowing the information dimension of an attractor permits one to calculate the information acquired when an individual, separate measurement is made to within a given accuracy.

This paper is composed of nine sections. In the first is an introduction and motivation for the fractal concepts and strange attractors. Section two gives some definitions of dynamical systems, strange attractors and the importance of the dimensionality concept. The third section presents the definitions and methods for estimating the parameters characterizing the behavior of chaotic strange attractors, that is, Hausdorff (fractal) dimension, capacity and information dimensions, and the Lyapunov exponents. The fourth section gives some examples of dynamical systems with strange attractors. Section five introduces the dimensionality reduction techniques and estimation of intrinsic dimension. Section six describes recent techniques for estimating the dimension of attractors. Section seven states new techniques to estimate the fractal dimension using image processing tools while section eight discusses the importance and applications of strange attractors. Section nine is the summary and indicates the prognosis for the future.

2. CONCEPT OF ATTRACTORS

2.1 Dynamical systems and topological definition of attractors

In this paper, a dynamical system will be defined to be anything with at least a couple of parts which change with the passage of time. To understand a dynamical system is to know how its states (the relationships existing between the parts of the system) vary with respect to time. Alternatively, a simple definition says that a dynamical system is an ensemble of time trajectories representing its behavior. The following is an example of a discrete dynamical system that maps a metric space (usually a subset $\mathbb{R}^n$, $n \geq 1$) onto itself.

$$x_{n+1} = T(x_n) \tag{2}$$

where x is a vector.

Our interest will be in the behavior of the attractors for the system defined in (2), i.e., the sequence of points or orbits $(x_1, x_2, \ldots, x_n, \ldots)$. Assume an initial state for the system at $n=0$. The trajectories converging to a limit set, once the transients for the system have disappeared (equilibrium state) are known as an attractor. Topologically, an attractor A is a nonempty compact set having a neighborhood N in S (where S is an open set in some real Banach space B) such that every trajectory beginning in the neighborhood N has both compact closure in S and its limit point in A. The basin (realm or set of initial conditions) of A is the compact closure of the trajectories that approach A. In more general terms, nonperiodic (disordered) states of deterministic systems are called chaotic and they are portrayed by complicated attractors that have been named strange [6,7] or even strange-strange [8]. Furthermore, a strange attractor is sensitive to its initial conditions and very often has a complicated, highly fractured structure.

2.2 Why is there an interest in dimension?

Several answers may be given to this question. First, it is useful to have a measure to characterize or classify attractors. The measure may be nothing more than a probability used to describe the structure of each region of the attractor. Second, dimension can be used to describe the degree of strangeness of strange attractors. Specifically, dimension can represent the amount of information required to situate a point on the attractors with a certain accuracy, thus providing the number of relevant degrees of freedom for a dynamical system.

The concept of dimension has evolved over the years from a basic definition given by Henri Poincaré [9]. The practicability of these dimension measurements, however, has increased recently with the advancement of computing systems. Shepard [10] was the first who addressed the notion of dimension associated with a given data set for the purpose of accounting for the number of relevant parameters in psychology studies. Fukunaga [11] refined these ideas to measure the intrinsic dimension of data in a wide range of disciplines (e.g., taxonomy, artificial intelligence, signal analysis, and pattern recognition). This prompted scientists to extend the aforementioned ideas to the context of dynamical systems. Several techniques for estimating the fractal dimension of attractors were proposed by Packard et al. [12].

Defining and estimating the dimension of simple attractors is not difficult. For instance, employing any appropriate definition of measure (dimension), a fixed point has dimension zero, a stable cyclic oscillation has dimension one, a doubly periodic attractor (2-torus) has dimension two. Notice that their degree is integer-valued. For the case of strange attractors, however, the structure is no longer regular and smooth, but complex and fractured. Because of the two reasons, their dimension takes a non integer value.

Before closing this subsection, it is of interest to envisage a two dimensional map.

$$x_{n+1} = x_n + y_n + \delta\cos 2\pi y_n \tag{3.a}$$

$$y_{n+1} = x_n + 2y_n \tag{3.b}$$

According to Sinai [13], for small values of δ, the attractor of the above-mentioned map is the entire square, thus, a topology of dimension two. For almost every initial condition (basin), there is a trajectory that approaches to every point on the square. According to Farmer, et al. [14], although there exist a great number of distinct definitions of dimension, the relevant definitions may be divided into two categories, those which only depend on metric properties and those which are based on metric and probability properties. The latter includes the natural measure of an attractor which can be found from a knowledge of the stability properties of the orbit on the attractor. The stability properties are nothing more than the knowledge of the Lyapunov numbers or Lyapunov dimension. The Lyapunov dimension is regarded as another category of measurement since it is defined in terms of dynamical characteristic of an attractor rather than the previous mentioned categories.

3. DIMENSIONALITY CONCEPT

3.1 Hausdorff dimension

The Hausdorff dimension was originally introduced by Felix Hausdorff [15] in 1918.

To aid in defining the Hausdorff dimension of a subset E contained in a ρ-dimensional Euclidean space, envisage a covering of it with ρ-dimensional cubes of variable edge length ϵ_i. Then define the expression $H_d(\epsilon)$ as

$$H_d(\epsilon) = inf \left\{ \sum_i (\text{edge length } \epsilon_i)^d \right\} \tag{4}$$

where the infimum is taken over all possible coverings such that $\epsilon_i \leq \epsilon$.

Let $H_d = \lim_{\epsilon \to 0} H_d(\epsilon)$, we obtain the d-dimensional Hausdorff measure.

According to Hausdorff, there is a critical value of d above which $H_d = 0$ and below which $H_d = \infty$. The aforementioned critical value $d = d_H$ is the Hausdorff dimension. To obtain an accurate estimate of d_H, it is advisable to first optimize the regular grid of cubes, i.e., find the number of covering needed to fill the subset E. If it is not done estimates may be erroneous.

3.2 Capacity dimension

The capacity is nothing more than a simplified form of the Hausdorff dimension. It was first defined by Kolmogorov [16] for use in solving electrostatic problems, and then it was extended to the domain of attraction (potential theory). Capacity is given by:

$$d_c = \lim_{\epsilon \to 0} \frac{\log N(\epsilon)}{\log(1/\epsilon)} \tag{5}$$

where $N(\epsilon)$ is the smallest number of ρ-dimensional cubes of length ϵ needed to cover the subset E. For simple subsets such as a point $(N(\epsilon)=1)$, line $(N(\epsilon) \sim \epsilon^{-1})$ and an area $(N(\epsilon) \sim \epsilon^{-2})$, the capacity dimension is an integer. However, for highly fractured and complex sets such as strange attractors, d_c is no longer an integer. This can be illustrated by considering an example using fractal trajectories [1].

3.3 Fractal trajectories

Let us start with a simple geometric form such as a straight line or a circle, we then construct a pattern portraying a very irregular envelope curve or a complex trajectory of a dynamical system. Such a trajectory may be restricted to an irregular segment of a curve. The segment may be aperiodic and the curve will be non-differentiable at an infinite number of points (for example, the trajectory described by the Brownian motion of a particle in a liquid). Now we want to estimate the length of the segment between its two extreme points A and B, as well as its dimensionality.

First, we start by selecting a yard stick of length y and then attempt to count the number of equal sides of length y of the aperiodic segment under consideration. Thus, we obtain an estimate of the length $L(y)$ by multiplying the length yardstick y by the number of equal sides. $L(y)$ depends on the length y thus it is useful to find $L(y)$ for different values of y. An analytic formula for the function $L(y)$ is given by

$$L(y) = Cy^{1-d} \tag{6}$$

C is a constant and d is a value equal to or greater than unity. The constant d is named the fractal dimensionality of the curve and it is commonly a noninteger value.

To understand the nature of fractal dimensionality we begin with a straight line in a one-dimensional Euclidean space. Therefore, for every positive integer M, the segment $0 \leq s < S$ can be divided into M non-overlapping segments of the form

$$\frac{(m-1)S}{M} \leq s < \frac{mS}{M} \tag{7}$$

where $m \epsilon [1, M]$. Each of these segments is obtained from the entire original segment by a similarity of ratio $r(M) = \frac{1}{M}$.

Using this same logic, consider a plane in a two-dimensional Euclidean space. For every square number M, the rectangle $0 \leq u < U$, $0 \leq v < V$ can be divided exactly into M non-overlapping small rectangles of the form

$$\frac{(p-1)U}{\sqrt{M}} \leq u < \frac{pU}{\sqrt{M}} \tag{8}$$

$$\frac{(q-1)V}{\sqrt{M}} \leq v < \frac{qV}{\sqrt{M}} \tag{9}$$

where $p \epsilon \left[1, \sqrt{M}\right]$, $q \epsilon \left[1, \sqrt{M}\right]$. As before, each small rectangle is obtained from the original configuration by a similarity of ratio $r(m) = \frac{1}{\sqrt{M}}$.

In general, whenever $M^{1/d}$ is a positive integer, a d-dimensional rectangular parallelepiped can be divided into M small similar parallelepiped configurations obtained from the original configuration by a similarity ratio $r(M) = \frac{1}{M^{1/d}}$. Therefore the dimension d is described by the following relation:

$$d = \frac{lnM}{\ln(1/r(M))} \tag{10}$$

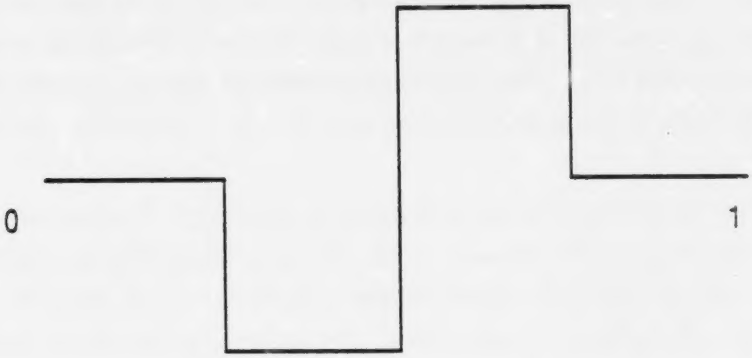

Figure 1: Use of self-similar scaling to create a fractal curve

As an example, consider the cube given in figure 1 in the interval [0,1]. It is composed of $M=8$ segments. We then replace each small segment with a configuration similar to the original with a similarity ratio $r(M)=\frac{1}{4}$. The new configuration is composed of $M \times M$ smaller segments of length $\left(\frac{1}{4}\right)^2$. The desired self-similar configuration is obtained by an infinite sequence of such steps. It is clear that the total length of such a configuration in the unit interval tends to infinity and its fractal dimension is given by:

$$d = \frac{lnM}{ln(1/r(M))} = \frac{ln8}{ln4} = 1.5 \tag{11}$$

3.4 Information dimension

The information dimension [17] can be motivated by the desire to know how much information is contained in a measurement of an initial condition. A measurement is a summary of the value of a variable in terms of a finite number of digits. In a chaotic dynamical system, most of the information about an initial condition is lost after a finite amount of time except for the statistical information. In other words, the information dimension will contain a measurement of how much information exists in an initial condition after the transients have died away.

Consider a measuring device with a uniform scale of resolution ϵ, then the measurement of any of the M state variables, as defined in the previous section, furnishes one of ϵ^{-1} possible numbers. Assume now that such a device is assigned to each of the M state variables of a physical system. The discretization of the scales of those devices then produces a set of non-empty mutually exclusive hypercubes. The domain comprising the strange (chaotic) attractor is thus sectioned into ϵ^{-M} cubes (boxes, each of dimension M). Each measurable state coincides with a cube.

Let $m(\epsilon)$ be the number of cubes with non-zero probability. Furthermore, let $P_i(\epsilon)$ be the probability of occurrence of the attractor in the ith cube, there exists at least one point of the attractor the cube. Farmer [18] referred to the collection of probabilities $\{P_i(\epsilon)\}$ as a coarse grained probability distribution of resolution ϵ. The information obtained in making a measurement at resolution ϵ is, then,

$$I(\epsilon) = \sum_{i=1}^{m(\epsilon)} P_i(\epsilon) \log P_i(\epsilon) \quad \text{bits} \tag{12}$$

As the scale of resolution ϵ increases, the number of cubes diminishes and a sequence of successively more refined, less coarsely grained probability distributions is obtained. The information dimension is related to the average amount of information $I(\epsilon)$ by

$$d_I = \lim_{\epsilon \to 0} \left(\frac{I(\epsilon)}{\log (1/\epsilon)} \right) \quad . \tag{13}$$

Physically speaking, the information dimension d_I represents the rate at which the information increases as the precision of the measurements, ϵ, is decreased.

The asymptotic value of the slope of the plot $I(\epsilon)$ versus $\log(\epsilon)$ gives a measure of the information dimension d_I. The knowledge of the information dimension of an attractor permits us to deduce the information $I(\epsilon)$ obtained in making a measurement of a state of resolution ϵ from the following:

$$I(\epsilon) = d_I \left|\log(\frac{1}{\epsilon})\right| \tag{14}$$

In particular, if all cubes have equal probability then (14) becomes

$$I(\epsilon) = \log \ m(\epsilon) \tag{15}$$

and the information dimension attains its maximum value and reduces to the fractal dimension

$$d_F = \lim_{\epsilon \to 0} \frac{\log m(\epsilon)}{\log(1/\epsilon)} \tag{16}$$

The fractal dimension d_F is therefore regarded as an upper bound to the information dimension d_I.

3.5 Characteristic Lyapunov exponents and Lyapunov dimension

A major problem in the analysis of dynamical systems is the estimation of the Lyapunov exponents of strange attractors reconstructed from time series data. The techniques which have been developed to date for extracting the Lyapunov exponents are found in [19-22]. The Lyapunov exponents quantify the local dynamical behavior of the attractor, measuring the sensitivity of trajectories to small changes in initial conditions. More importantly, the dimension of the chaotic attractors can be obtained from the dynamics of the system or in terms of the spectrum of Lyapunov exponents of the attractor. The Lyapunov exponents are simply the logarithm of the absolute values of the eigenvalues of the Jacobian matrix computed at the fixed point and gives us a qualitative assessment of the local stability properties of an attractor. To see this, start with an infinitesimal ball with a radius $\delta(0)$ at time $t=0$. As the ball evolves under the effect of a non-uniform flow, it's shape will deform. However, the assumption of an infinitesimal state-space element ensures us that the change in shape will be caused only by the linear portion of the flow, hence the "ball" keeps an ellipsoidal configuration as it develops.

Let $\delta_k(t)$ be the kth constituent of the set of principal axes of the ellipsoidal configuration at time t. The kth Lyapunov exponent λ_k is then given by:

$$\lambda_k = \lim_{t \to \infty} \frac{1}{t} \lim_{\delta(0) \to 0} \log_2 \left[\frac{\delta_k(t)}{\delta(0)}\right] \tag{17}$$

For an M-dimensional dynamical system, there exist M Lyapunov exponents in the spectrum of the attractor. The positive exponents measure the long-term average exponential stretching of close trajectories whereas the negative ones measure the long-term average exponential contraction (convergence) of trajectories onto the attractor. The sum of the exponents constitute the average divergence, which for a dissipative system having an attractor ought to be negative.

The arrangement of the Lyapunov exponents in nonincreasing order is common among physicists. Hence, for example, the symbol set {+,0,-} specifies an attractor in a three-dimensional space with exponential spreading along one dimension, (e.g., the x-direction), neutral stability along the flow, (i.e., the y-direction) and exponential contraction of trajectories in the third dimension (i.e., z-direction). It should be noted that attractors other than stable steady states always possess at least one null exponent. This occurs because, on the average point elements belonging to a trajectory restricted to a compact set can neither diverge nor combine. Furthermore, a dissipative system satisfies the inequality $|\lambda(-)| > \lambda(+)$. In the following, we will attempt to further motivate the reader by presenting the technique for determining the Lyapunov numbers. Note, the Lyapunov exponents are the logarithms of the Lyapunov numbers.

Consider a ρ-dimensional map of an attractor

$$x_{n+1} = T(x_n), \tag{18}$$

where x is a ρ-dimensional vector. Recall, the Lyapunov numbers are the absolute values of the Jacobian matrix of the map evaluated at the fixed point. To define the Lyapunov numbers, let

$$J_n = [J(x_n) \cdot J(x_{n-1}) \cdots J(x_1)] \tag{19}$$

where $J(x)$ is the Jacobian matrix defined at the fixed point, that is:

$$\begin{aligned} J(x_n) &= \frac{\partial T}{\partial x}\bigg|_{x_n} \\ J(x_{n-1}) &= \frac{\partial T}{\partial x}\bigg|_{x_{n-1}} \\ &\cdots \\ J(x_1) &= \frac{\partial T}{\partial x}\bigg|_{x_1} \end{aligned} \tag{20}$$

Then

$$J_n = \left[\frac{\partial T}{\partial x}\bigg|_{x_n} \cdot \frac{\partial T}{\partial x}\bigg|_{x_{n-1}} \cdots \cdot \frac{\partial T}{\partial x}\bigg|_{x_1} \right] = \frac{\partial T^{(n)}}{\partial x}\bigg|_{x_0} \tag{21}$$

The above is valid because of the fact that the slope of the nth iterated map at some point x_0 equals the product of the slopes of the initial map at the points x_n, $x_{n-1}, \ldots, x_1$, respectively. If we let $j_1(n) \geq j_2(n) \geq \ldots \geq j_\rho(n)$ be the magnitudes of the eigenvalues of J_n, the Lyapunov numbers are then given by:

$$\lambda_i = \lim_{n\to\infty}[j_i(n)]^{1/n} \quad i = 1,\ 2,\ldots,p \tag{22}$$

where the positive real nth root is chosen.

Consider the following example using a two-dimensional map. The goal of the example is to present an argument that motivates the relationship between the spectrum of Lyapunov exponents and the information dimension. For a two-dimensional map, define λ_1, λ_2 to be average spreading coefficients of an infinitesimal circular disc of radius ϵ. This is illustrated in figure 2.

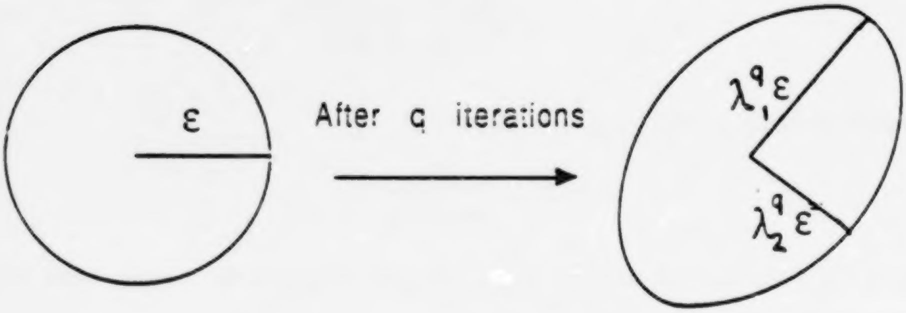

Figure 2: An infinitesimal circular disc after q iterations. Used to understand the effect of Lyapunov exponents on a 2-D system.

As discussed previously, the Lyapunov exponent for which divergence occurs coincides with $\lambda_1 > 1$, whereas the Lyapunov exponent for which contraction occurs coincides with $\lambda_2 < 1$. For a chaotic attractor, this is logical since on the average nearby points initially diverge at an exponential rate, and therefore at least one of the Lyapunov exponents must be larger than one. As shown in figure 2, after q iterations of the two-dimensional map, the original small circular disc will be approximately mapped into an ellipsoidal configuration with major and minor half-axes $(\lambda_1)^q\epsilon$ and $(\lambda_l)^q\epsilon$, respectively.

As cited before, the goal of this simple example is to find a relationship between the spectrum of Lyapunov exponents and the information dimension of the map. To achieve this goal, we will follow the previous work by Farmer et al. [14]. Begin by covering the two-dimensional attractor with $N(\epsilon)$ squares of side length ϵ and then iterate the map q times. For ϵ small and q fixed, the action of the mapping is approximately linear over the square and each square will be stretched into a long parallelogram. Using the fact that $\lambda_1 > 1 > \lambda_2$, the average dimension of the new configurations will be $(\lambda_1)^q\epsilon$ and $(\lambda_2)^q\epsilon$, respectively. $(\lambda_1)^q\epsilon$ represents the length of the parallelogram and $(\lambda_2)^q\epsilon$ represents its width. Assume now that a finer covering of squares is chosen with sides of length $(\lambda_2)^q\epsilon$. About $(\lambda_1/\lambda_2)^q$ smaller squares are required to cover each parallelogram. The number of elements in the new partition may be estimated by using:

$$N((\lambda_2)^q\epsilon) = N(\epsilon)\ \left(\frac{\lambda_1}{\lambda_2}\right)^q \tag{23}$$

Further, by using the fact that $N(\epsilon) \approx k(\frac{1}{\epsilon})^d$, (23) may be rewritten as:

$$k\left(\frac{1}{\lambda_2{}^q}\epsilon\right)^d = k\left(\frac{1}{\epsilon}\right)^d\ \left(\frac{\lambda_1}{\lambda_2}\right)^q \tag{24}$$

Taking the logarithm of (24) and solving for d gives

$$d = 1 + \frac{\log\lambda_1}{\log(1/\lambda_2)} \tag{25}$$

This formula is valid for two-dimensional maps. Its generalization to ρ-dimensional maps is straightforward and is given by [13]:

$$d = k + \frac{\log(\prod_{i=1}^{k}\lambda_i)}{\log(1/Lambda_{k+1})} \tag{26}$$

where k is the greatest value for which $\prod_{i=1}^{k}\lambda_i \geq 1$. If $\lambda_1 < 1$, define $d=0$; but if $\prod_{i=1}^{\rho}\lambda_i \geq 1$, define $d=\rho$. The quantity d is referred to as the Lyapunov dimension and under some conditions, the Lyapunov dimension coincides with the information dimension.

4. EXAMPLES OF DYNAMICAL SYSTEMS WITH STRANGE ATTRACTORS

In order to further motivate this review, we will provide the reader with a list of many examples of strange attractors. More importantly a typical three-dimensional strange attractor is investigated in detail. The strange attractors found in the literature include: the dissipative Hénon-Heiles model [23], the Brussel model for a chemical system [24], the Shilnikov attractors [25], the Volterra attractors [26], the Rössler attractors [27], the Duffing attractors [28], the Josephson junctions [29], the Robbins dynamo [30], the Rikitake dynamo [31], the model of the Belousov-Zhabotinskii [32], the Glass-Mackey model [18], the model of a baleen whales population [33], the model for the interaction of perturbations [33], the Goldbeter-Lefever model and the Sel'kov-Higgins model [34], the five-mode truncated Navier-Stokes equations [36], the quadratic model fo chemical kinetics [36], the forced nonlinear oscillator [29], the forced negative-resistance oscillator [37], the nonlinear oscillator with dissipative and forcing term [38], the parameter driven pendulum [39], the particle under the action of a potential and electric field [40], the Feigenbaum attractors [41-42], the double scroll [43-44], the electroencephalogram (EEG) attractors [45], the solenoid and the Plykin attractor (hyperbolic attractor) [46].

We now turn to a more detailed example of a typical three-dimensional strange attractor: the Lorenz model [47]. As is well known, the atmosphere is regarded as one of the most sensitive systems, in particular, the dynamics of the atmosphere are extremely sensitive to initial conditions. The result is a system for which it is very difficult or impossible to predict its future status. This is often the case in weather prediction, even with the impressive improvements in modeling and data collection.

Before illustrating Lorenz's model (wings of a butterfly), consider his comments in [47].

> "Certain hydrodynamical systems exhibit steady state flow patterns, while other oscillate in a regular periodic fashion. Still others vary in an irregular, seemingly haphazard manner, and, even when observed for long periods of time do not appear to repeat their previous history.... Lack of periodicity is very common in natural systems and is one of the distinguishing features of turbulent flow."

In fact, the equations that he proposed are perhaps regarded as the most fundamental in the search for strange attractors.

Lorenz's model is based on a simple set of equations describing the Consider the system.

$$\dot{X} = -\sigma X + \sigma Y \tag{27.a}$$

$$\dot{Y} = -Y + rX - XZ \tag{27.b}$$

$$\dot{Z} = XY - bZ \tag{27.c}$$

where, "˙" represents a rate of change with respect to time. X, Y and Z are locations and σ,r, and b are constants. These equations represents the "Lorenz attractor." Under certain choices of constant values and initial conditions, the system leads to steady-state or periodic trajectories. However, the most fascinating situations are those that are either non-periodic or non-stationary, that is, there is no regularity and no predictability in the process. The latter situations were analyzed numerically [47] and Lorenz found that the trajectories became restricted to a convoluted surface that possesses zero volume. If the trajectories were periodic, then the solutions would be restricted to a closed, deformed configuration that had neither area nor volume. Most of the time, the Lorenz trajectories converge to a limited number of points, called attractors.

For several iterations, the trajectory may stay in the neighborhood of one of the attractors and then suddenly leave this mode and go monotonically toward another available attractor, stay there for awhile and then return to the vicinity of the previous attractor. The type of trajectory and the parameters that control displacements from one attractor to another are of immense importance because of their relevance to our understanding of the solutions to these dynamical systems.

In an attempt to further understand the work of Lorenz, Takeyama [48] demonstrated that the Lorenz model of convective instabilities can be transformed to one-dimensional dynamics of an overdamped non-periodic oscillator with memory in a potential well. Eliminating Y and solving for Z in terms of X^2 in the Lorenz model, Takeyama arrived at the following equation for $X(t)$:

$$\begin{aligned}&\ddot{X}(t) + (1+\sigma)\dot{X}(t)\\ &\quad + \sigma\left[1 - r + \frac{1}{2\sigma}X^2(t) + \left(1 - \frac{b}{2\sigma}\right)\int_0^\infty [X(t-\tau)]^2 \exp(-b\tau)\,d\tau\right]X(t) = 0\end{aligned} \tag{28}$$

Assuming $b > 0$ and that the motion of the particle began at $-\infty$, $\exp(-b\tau)$ can be expressed by a δ function yielding:

$$\begin{aligned}&\ddot{X}(t) + (1+\sigma)\dot{X}(t) + \frac{dU}{dX}\\ &\quad + \left[\left(\sigma - \frac{b}{2}\right)\int_0^\infty [X^2(t-\tau) - X^2(t)\exp(-b\tau)]\,d\tau\right]X(t) = 0\end{aligned} \tag{29}$$

where U is given by:

$$U(X) = \sigma\left(\frac{1-r}{2}X^2 + \frac{1}{4b}X^4\right) \tag{30}$$

This equation models the motion of an overdamped particle in a potential well $U(X)$ under the effect of an extra force which depends on the history of motion. In fact, this force establishes the occurrence of motion.

A complete account of attractors and bifurcations of the Lorenz equations can be found in [49].

5. DIMENSION REDUCTION TECHNIQUES AND ESTIMATION OF INTRINSIC DIMENSIONS

Because of the large dimension of some patterns and the resulting complexity of analyzing such patterns, dimension reduction techniques are important. Information compression (dimension reduction) is achieved by a mapping process. The aim of which is to transform the useful data contained in the original pattern into a new pattern whose dimension is much lower. This is achieved by ignoring redundant and irrelevant information. The new lower dimension is called the intrinsic dimension of the pattern.

The aim of this section is to review some of the interesting methods used for extraction the intrinsic dimension of high-dimensional sets. Among the methods are the Karhunen-Loève (K-L) expansion, the k-nearest-neighbor (kNN) method, multidimensional scaling and projection pursuit. We shall discuss briefly the ramifications of using these techniques with strange attractors and chaotic dynamical systems. It turns out that most of the techniques for estimating the dimension in the dynamical chaos-strange attractor field are variants of kNN multivariate density estimators.

Physically speaking, strange attractors and other chaotic dynamical systems have four distinguishing features:

a) The existence of a causal connection among points of a set.
b) The intrinsic dimension is often noninteger.
c) The low-dimensionality property of the embedding space.
d) A discretized trajectory comprised of a large set of points.

5.1 Nearest-neighbor Technique

The distinguishing characteristic of the k-nearest-neighbor method (kNN) is the fact that it is a nonparametric estimator of density functions (in general, multivariate probability densities). The algorithm provides a simple estimate of a probability density function. In the following, we shall describe how the method works.

Start with a set of sample points $\{x_i\}$, $i=1,2...,n$, embedded in a d_1-dimensional Euclidean space. The sample points $\{x_i\}$ belong to an unknown distribution with probability density function $p(x)$. To estimate $p(x)$, one centers a hypervolume $S(x)$ about x and then lets $S(x)$ grow until it encloses k samples. These samples are the k nearest neighbors of x. The estimate of the density function is given by:

$$\hat{p}(x) = \frac{k}{nV} \quad , \tag{31}$$

where n is the total number of sample points and V is the hypervolume of $S(x)$ containing the k sample points whose distance from x is less than r_{kNN} (r_{kNN} is the distance from x to its k^{th} NN). The estimate $\hat{p}(x)$ in (30) is asymptotically unbiased and consistent [50].

In general, k will depend on n and it can be shown [50-51] that the aforementioned asymptotic unbiasedness and consistency of $\hat{p}(x)$ are guaranteed under the following two conditions.

$$\lim_{n \to \infty} k(n) = \infty \tag{32}$$

$$\lim_{n \to \infty} k(n)/n = 0 \tag{33}$$

Duda and Hart [52] found that $k = h_1\sqrt{n}$ works well; where h_1 is a constant of proportionality. Furthermore, the above two conditions are necessary and sufficient to ensure the convergence of the estimate $\hat{p}(x)$ to $p(x)$ in probability at all sample points.

Assuming an Euclidean distance, the volume V becomes a hypersphere and is given by:

$$V = V_{d1}(r_{kNN})^{d1} \quad , \tag{34}$$

where V_{d1} is a volume of a unit d_1-dimension and is given by

$$V_{d1} = \frac{\Pi^{(\frac{d_1}{2})}}{\Gamma(1+\frac{d_1}{2})} \tag{35}$$

Using (34) and (35) and taking the logarithm of both sides, (31) can be rewritten as:

$$d_1 \log r_{kNN} = \log(\frac{k}{n}) - \log[V_{d_1}\hat{p}(x)] \tag{36}$$

Since $\hat{p}(x)$ depends on the number of samples k, it is fruitless to use equation (36) for estimating the dimension d_1.

To circumvent the problem in (36), assume that $p(x)$ is continuous and nonzero at x, then the density function for $r_{kNN}(x)$ for small $r > 0$ and sufficiently large n is given in [53] by:

$$R_{7NN}(r) = \left(\frac{d_1}{r\Gamma(k)}\right)\left(np(x)r^{d_1}V_{d_1}\right)^k \ \exp\left[-np(x)r^{d_1}V_{d_1}\right] \tag{37}$$

The first order moment of the distance $r_{kNN}(x)$ is given by:

$$E\{r_{kNN}(x)\} = \frac{\Gamma(k+\frac{1}{d_1})}{\Gamma(k)[r(np(x)V_{d_1})^{1/d_1}]} \tag{38}$$

By the same logic, the first order moment of the sample averaged distance $\bar{r}_{kNN}(x)$ to the k^{th} NN over the set of points n is given by:

$$E\{\bar{r}_{kNN}(x)\} = \frac{k^{1/d_1}W_n}{H} \tag{39}$$

where $H = \dfrac{\Gamma(k)k^{1/d_1}}{\Gamma(k+\frac{1}{d_1})}$ and W_n is independent of k and is given by

$$W_n = \frac{1}{n} \sum_i [np(x_i)V_{d_1}]^{-\frac{1}{d_1}} . \tag{40}$$

Using the approximation $E\{\bar{r}_{kNN}(x)\} \approx \bar{r}_{kNN}$, an estimator $\hat{d}_1$ of d_1 may be found and is given by

$$\log H = \frac{1}{\hat{d}_1}\log k + \log W_n - \log \bar{r}_{kNN} \tag{41}$$

From (41), a plot of $\log \bar{r}_{kNN}$ versus $\log k$ for $k=1,2,\ldots,k_{\max}$ can be generated and a least-square fit of a straight line can be passed through the points. The slope of the line is $\frac{1}{\hat{d}_1}$ and $\hat{d}_1$ is solved for iteratively to obtain the estimate of d_1. Pettis et. al. [53] found that the term $\log H$ is in the range of $0 \leq \log H \leq 0.12 \ \forall\ k,\ \forall\ d_1$ and the maximum value occurs when $k=1$ and $d=2.17$. They started their iteration by letting $\log H$ be zero.

It has been shown in [54] that the ratio of two consecutive first order moments of the distance to the kNN is independent of the total number of sample points n and the nature of the distribution $p(x)$ but depends only on k and the dimensionality d_1. That is,

$$\frac{E\{r_{(k+1)NN}\}}{E\{r_{kNN}\}} = 1 + \frac{1}{kd_2} \tag{42}$$

where d_2 depends only on neighboring information and therefore expresses the intrinsic dimensionality. It should also be noted that equations (37) and (38) can be extended to higher-order moments of the distance to the kNN, that is, compute $E\{r_{KN}^{m}\}$ and $E\{\bar{r}_{kNN}^{m}\}$ where m is the m-

order moments. Details of derivations are to be found in [54].

5.2 Multidimensional scaling

Multidimensional scaling [55] is a method based on a set of proximity measures. A proximity measure is a number which expresses a degree of similarity or dissimilarity between two objects. Given some proximity measure, the multidimensional scaling technique creates a spatial representation composed of a geometrical form of points. In general the number of points corresponds to the number of objects (one-to-one mapping or bijective transformation). It is interesting to note that the smaller the degree of similarity (or the larger the degree of dissimilarity) between two objects, the more distant they are in the spatial representation. This aforementioned comparison ensures an adequate multidimensional scaling.

Assume the proximity matrix $\{p_{ij}\}$ is known. Three things must be selected to define multidimensional scaling: the dimensionality d_1 of the embedding space, an initial configuration, and the metric of the space. The major idea behind multidimensional scaling is to relate the proximity matrix elements p_{ij} monotonically to the distances $\delta_{ij} = ||x_i - x_j||$ in the selected d_1-dimensional space. That is, find a best monotonic function such that $g(p) = \delta$.

To ensure the monotonicity of the function g, a least squares criterion is used to minimize the following expression:

$$G = \min_{x_i} \left[\frac{\sum_i \sum_j [g(p_{ij}) - ||x_i - x_j||]^2}{\gamma} \right]^{1/2} \tag{43}$$

where γ is a scale factor. In general, a regular d_1-simplex is used to start the minimization in the highest dimensional space, say, $d_1 = n-1$, where n represents the total number of objects (the total number of points in the geometrical configuration). Once the minimum in G is obtained, the embedding dimension is reduced and the process of minimization is repeated.

An alternative technique for multidimensional scaling is the nonlinear transformation based on Sammon's ideas [56]. The nonlinear mapping begins with n points in d_1-dimensional space and reduces them into a two-dimensional (2-D) space by minimizing the accumulated error with a normalized factor as given by

$$\left[\sum_{i<j}^{n} (\delta_{ij}) \right]^{-1} \sum_{i<j}^{n} \left[\frac{(\delta_{ij} - r_{ij})^2}{\delta_{ij}} \right] \tag{44}$$

where δ_{ij} is defined as $||x_i - x_j||$ in d_1-dimensional space whereas r_{ij} in 2-D space.

5.3 Karhunen-Loève Expansion

The Karhunen-Loève expansion (K-L) [57] is a method for projecting a pattern vector into a new coordinate system, where the new coordinate system has a lower dimensionality than the original. Furthermore, the components of the transformed pattern vector are uncorrelated. The compression process is accomplished using a linear or a nonlinear mapping which projects the unique information contained in the original pattern onto a small number of feature variables, while attempting to diminish the irrelevant and redundant information.

In general, the transformation (for simplicity purposes, assumed to be linear) used to achieve the aforementioned goals is given by:

$$\mathbf{x} = \sum_{i=1}^{d_1} \mathbf{y}_i \mathbf{b}_i \tag{45}$$

where $\mathbf{x}$ is a d_1-dimensional random vector (original pattern) described in terms of a set of basis vectors. The $\mathbf{b}_i$ vectors are linearly independent, orthonormal and deterministic (and in general, may be specified in advance). Under these conditions, the $\mathbf{y}_i$ may be found using the projection operation.

$$\mathbf{y}_i = \mathbf{b}_i^T \mathbf{x} \qquad (i=1,2,\ldots,n) \tag{46}$$

where n is the total number of sample points and T stands for transpose.

Let $\mathbf{y}$ be defined by:

$$\mathbf{y} = [y_2, y_2, \ldots, y_{d_1}]^T \tag{47}$$

Now, suppose we wish to ignore all but $d_2 (d_2 << d_1)$ components of $\mathbf{y}$ and still represent $\mathbf{x}$ with some minimum error. We will therefore compute the first d_2 elements of $\mathbf{y}$ and replace the others with constants (constants are chosen to be zero, in general). The error is guaranteed to be minimum if the basis vectors $\mathbf{b}_i$ are chosen to be the eigenvectors corresponding to the d_2 largest eigenvalues of the covariance matrix C_x (from the the n d_1-dimensional sample points). These d_2 eigenvectors define the linear mapping required to achieve the information compression from high-dimensional space d_1 to low-dimensional space d_2.

The fraction of the total variance (in d_1-space) that is kept in d_2-space is given by the following ratio

$$r = \frac{\sum_{i=1}^{d_2} \lambda_i}{\sum_{j=1}^{d_1} \lambda_j} \quad . \tag{48}$$

In general, when the ratio r is greater or equal to 0.9 ($r \geq 0.9$), the dimension d_2 is called the intrinsic linear dimension of the data set. Note that the above discussion is limited to linear transformations. Alternative techniques based on local K-L expansions are needed to extend the dimension reduction techniques to nonlinear mappings. One method consists in investigating local subsets of the whole data set. The subsets are located in topological hyperspherical regions whose size has been specified according to some criterion. Once the local intrinsic dimensions are obtained, the global intrinsic dimension then follow [58-59].

5.4 Projection Pursuit Techniques

The projection pursuit (PP) techniques are regarded as means for obtaining adequate low-dimensional projections of a high-dimensional point set by satisfying some criterion. The chief role of the criterion is to maximize a projection index or objective function. The principal goal of the technique is to select a number of distinct projection indices from which distinct characterizations of the high-dimensional set can be obtained. Friedman et al. [60] were the first authors who implemented the projection pursuit techniques. Friedman et al. [61-62] extended their original finding to projection pursuit regression (PP-regression) and projection pursuit density estimation.

Following reference [62], the projection pursuit estimation method builds estimates of the unknown density function $p(x)$ recursively.

$$p(x) \sim P_I(x) = P_{init}(x) \prod_{i=1}^{I} h_i(u_i \cdot x) \tag{49}$$

where $P_I(x)$ is the estimate after I iterations of the algorithm, $P_{init}(x)$ is a specified initial multivariate density function, $h_i(\cdot)$ is a univariate function, and u_i is a unit vector indicating a direction in the d_1-dimensional embedding space, such that

$$u_i \cdot x = \sum_{j=1}^{d_1} u_{ij} \; x_j \quad ; \tag{50}$$

A recursive expression may be obtained from (55),

$$P_i(x) = P_{i-1}(x) h_i(u_i \cdot x). \tag{51}$$

The algorithm selects the directions u_i and builds the corresponding functions $h_i(u_i \cdot x)$. Details of the projection index criterion and the optimal value of the directions $u sub i$ are given in [62].

6. METHODS FOR ESTIMATING THE DIMENSION OF AN ATTRACTOR

A time evolution of a physical system can be described by a trajectory in an n-dimensional phase space. The estimation of the dimension of an attractor from a time series is important because it represents a measure of the complexity of the physical system. Several techniques exist for estimating the dimension of an attractor including: the technique of averaging over a number of variables (number of nearest neighbors) and the technique of pointwise dimensions. [63-67] In general, these measurements to describe the state of the physical process are made over a long duration of time at a small number of positions.

In what follows, we use a time series $Z(t)$ to represent a sequential measurement performed on a state variable of a dynamical phenomenon. Knowing this time series permits us to investigate the type of dynamical phenomenon we are dealing with, i.e., whether it is an attractor or random noise. Furthermore, it is possible to estimate the minimum number of independent variables whose interplay in time would account for the multi-dimensional dynamical phenomenon at hand.

Following the procedure proposed in [64], we define $\dot{Z}(t) = f(Z;\mu)$ to be a system of M coupled nonlinear ordinary differential equations representing the model of the physical system of interest. The trajectory of the system is governed in a state space of dimension M with coordinates $Z_i(i=1,...,M)$. Note that the dimension M of the state space is still unknown and the form of the state space with coordinates $Z(t)$, $\dot{Z}(t),...,Z(t)^{(M-1)}$ is topologically equivalent to the original state space and so is the configuration with coordinates $Z(t)$, $Z(t + \tau)$, $Z(t + 2\tau),...,Z(t + (M-1)\tau)$, for every fixed time delay τ (chosen to be not too small). Thus, a trajectory of a dynamical phenomenon may be constructed from knowledge of a sequential measurement (time series $Z(t)$).

In the following, we describe how a dimension of an attractor is developed from a time series. We also recall several alternative techniques for estimating the dimension.

6.1 Correlation Dimension

Grassberger and Procaccia [57] suggest a new measure for the strangeness of attractors, a measure that can be obtained from any long-time series bypassing the use of Poincaré maps [68]. This measurement is closely related to the fractal dimension and is referred to as the correlation dimension. In a dynamic system which exhibits chaotic behavior and has a strange attractor, the locations of pairs of points (Z_i, Z_j) on the trajectory (assumed adequately separated in time) are uncorrelated. However once we are positioned on the attractor there is some degree of spatial correlation between the points Z_i and Z_j. The distances between the points is $|Z_i - Z_j|$ for all $i,j \in [1, N]$, where N represents the number of pairs of points $Z_{i,}$ Z_j such that M equals mN. Select an arbitrary distance R and examine the difference measure $|Z_i - Z_j| - R$. If the difference measure is negative, we assign the value 0, otherwise we assign the value 1. Applying this approach to all pairs of points, the correlation measure is defined as:

$$C(R) = \lim_{N\to\infty}\frac{1}{N^2}\sum_{i=1}^{N}\sum_{j=1}^{N}\theta(R - |Z_i - Z_j|) \tag{52}$$

where $\Theta(\cdot)$ is the Heaviside function. Mathematically, $C(R)$ counts the number of points $\sum^{N}\theta(R - |Z_i - Z_j|)$ contained in a cube of specified side length R, averages over all the cubes that are located at distinct target points Z_j and then normalizes. Furthermore, for small R $C(R)$ behaves as a power of R.

$$C(R) \sim R^{d} \tag{53}$$

The value of the exponent d can be obtained from a time series of one or more variables.

6.2 Pointwise Dimension

The pointwise dimension or mass dimension [1,65] consists of counting the number of data points $\sum^{N}\theta(R - |Z_i - Z_j|)$ contained in a cube of side length R centered at a point Z_0 on the attractor. It is given by the following formula:

$$D_z = \lim_{M\to\infty}\ \lim_{R\to 0}\ \frac{\log\frac{1}{M}\sum^{N}\Theta(R - |Z_i - Z_j|)}{\log R} \tag{54}$$

The definition requires an infinite number of data points and an infinite precision. Neither can be satisfied so an average is taken over several target points Z_0. The values of the pointwise dimension D_z result from computing the slope of a straight line fit to each curve in the $\frac{\log R}{\log M}$ plot using least squares fit.

If the dimension D_z is linearly increasing with M then the phenomenon is stochastic with a large number of degrees of freedom. If it is not the case, that is the plot of D_z versus M levels off and saturates above a critical value $D_p = M_p$, this is a sign that we have a strange attractor with a minimum number of degrees of freedom D_c (degree of complexity of the phenomenon).

6.3 Averaging Method (Number of Nearest Neighbors)

The averaging method was presented in [56]. It is based on averaging a specified number of data points contained in cubes of different radii. The investigations inferred that the number of nearest neighbors, N, is related to the fractal dimension D_f of the attractor and to the average radius $\bar{R}(N)$ of the cubes having N data points. N is given by:

$$N \sim \bar{R}(N)^{D_f} \tag{55}$$

6.4 Use of the kth Nearest Neighbor Algorithm

Brandstater et al. [69] attempted to compute the attractor dimension from the time series of all elements in a defined surface plane. Their calculation is based on the kth nearest neighbor algorithm (k-NN). By scaling the average distance of the k-NN on the attractor $<r_k>$ an estimate of the dimension was attempted. Assuming that $r_k(z_i)$ is the distance between point z_i and its k-NN and

$$<r_k> = \sum_i r_k(z_i) \tag{56}$$

Then,

$$<r_k> \sim G(d', k) k^{1/d'} \tag{57}$$

and

$$G(d', k) = \frac{[k^{1/d'}\ \Gamma(k)]}{\Gamma(k + \frac{1}{d'})} \tag{58}$$

d' can be estimated using an iterative technique.

7. APPLICATIONS OF STRANGE ATTRACTORS

One of the motivations for this section is to present the possible answers for the following question. What are the practical techniques for creating a Markov chain out of continuous nonlinear dynamics?

First, consider a strange attractor in state space. Perform an arbitrary analog-to-digital transformation using a Poincaré mapping (return mapping). This implies cutting the trajectory with a hyperplane, registering the isophasic crossings and obtaining a set of discrete coupled difference equations. Second, select an arbitrary partition of the discrete map and then derive a Markov chain whose number of states coincides with the partition number and whose transitional probabilities are established by the local slope of the map. The conditional probability of transiting from the kth partition element to the lth one in j iterations is given by

$$P_j(l|k) = \frac{\mathbf{A}T^{-1}(l)\cap(k)]}{\mathbf{A}(k)} \tag{59}$$

where **A** is the invariant measure of the map T and "$\cap$" stands for the intersection between elements.

An alternative to the above is to regard the case of more than one coexisting attractor. In this case, external noise can make available a sequential route from one attractor to another. The result is a Markov chain whose number of states coincides with the number of coexisting attractors and transitional probabilities are established by the nature of superimposed noise and the distribution of residence times. In the remainder of the section, we detail this alternative and give an application for multi-attractor systems.

8. COMPLEXITY OF BASINS

Consider a system composed of A attractors denoted by $\{a_i\}$ $(i-1,2,\ldots,A)$. For each attractor, define the ratio of the volume of the basin of attraction in a given bounded phase space by b_i $\left(\sum_{i=1}^{A} b_i = 1\right)$. The complexity for basins is then defined by

$$C_B = -\sum_{i=1}^{A} b_i \ln b_i \tag{60}$$

This complexity characterizes the information in the initial state requisite to foretell the final state. Examples of complex basin structure are the fractal basin boundary [65] and the fractal basin structure [70]. For these examples, it is of to define the complexity for basins C_B in a small ball with radius ϵ and examine how $C_B(\epsilon)$ scales as ϵ tends towards zero.

8.1 Transiting (Jumping) among Attractors by Noise

As noted earlier, if a dynamical system possesses more than one attractor, then a unique invariant measure will not be reached. Such a system may be regarded as a two-phase process. In the first phase, the trajectory (state) spends most of its time in the neighborhood of the original attractor (residence without noise). In the second phase, the trajectory transits to some other attractor because of the noise effect (jumping among attractors by noise). In general, the process time of the second phase is much shorter than the first phase.

Define a transition matrix between attractors as follows. Assume that a small noise is superimposed the attractor a_k , a jump from the attractor a_k to another attractor, say, a_l occurs with some probability. This probability is named transition probability $P(l/k)$ and is defined as the ratio of the transition from a_k to a_l . The jumping process usually depends on the state of the system when the noise is applied, the location at which the noise occurs and finally on the power of the noise. It is worthwhile to note that the above ratio of transition is a measure computed for all states when a noise is applied.

The probability that a system is at the neighborhood of the attractor a_k for a weak noise is given by $q_k =$ the kth component of the eigenvector for P_{lk} corresponding to the eigenvalue i. If the eigenvalue i is degenerate with the multiplicity m_p, there are m_p invariant measures within the above weak-noise limit approximation. Note that some attractor a_k may be so weak that P_{ki} is null $\forall_i$. If q_k is zero, the probability at the attractor a_k is also zero.

8.2 Complexity of the Jumping Process among Attractors

Assume that the probability measure q_k is reached by noise, then the complexity for the probability distribution for the attractors is defined by

$$C_M = -\sum_k q_k \ln q_k \tag{61}$$

for a given invariant measure. C_M represents the gain in information resulting from the measurement to determine at which attractor the system stays at once all the transients have decayed. Another measure of interest is the dynamical information. This quantity determines how much information is produced during the transition of the state of the system from attractor a_k to attractor a_l when noise is applied. This dynamical information gain is defined as:

$$C_D = -\sum q_k P_{lk} \ln P_{lk} \tag{62}$$

using the fact that the ratio for the transition from a_k to a_l is $q_k P_{lk}$.

Suppose that C_D is large, then the information gained after the noise is also large. In other words, there is a large uncertainty about which attractor the dynamical systems settles down upon once noise is added. The difference between the information gain C_M and the dynamical information gain C_D is called a mutual information, that is, $C_T = C_M - C_D$.

8.3 Complexity in a Cognitive Channel with Multi-attractors

As an example for the complexity theory for multi-attractor systems, a cognitive channel is investigated. First, recall that the human mind has the capacity of mapping the external world. In other words, the human mind compresses large, complicated strings of overlapping environmental stimuli (external observations) and then utilises the compressed outputs for simulating physical phenomena. One could theorize that this process of self-organization and categorization could be fulfilled by an intermediary, an ensemble of coexisting strange attractors in the cognizant apparatus. Each attractor "attracts", and hence, compresses entire subsets of initial conditions which, in total, designate the set of external stimuli. This mechanism is illustrated in figure 3.

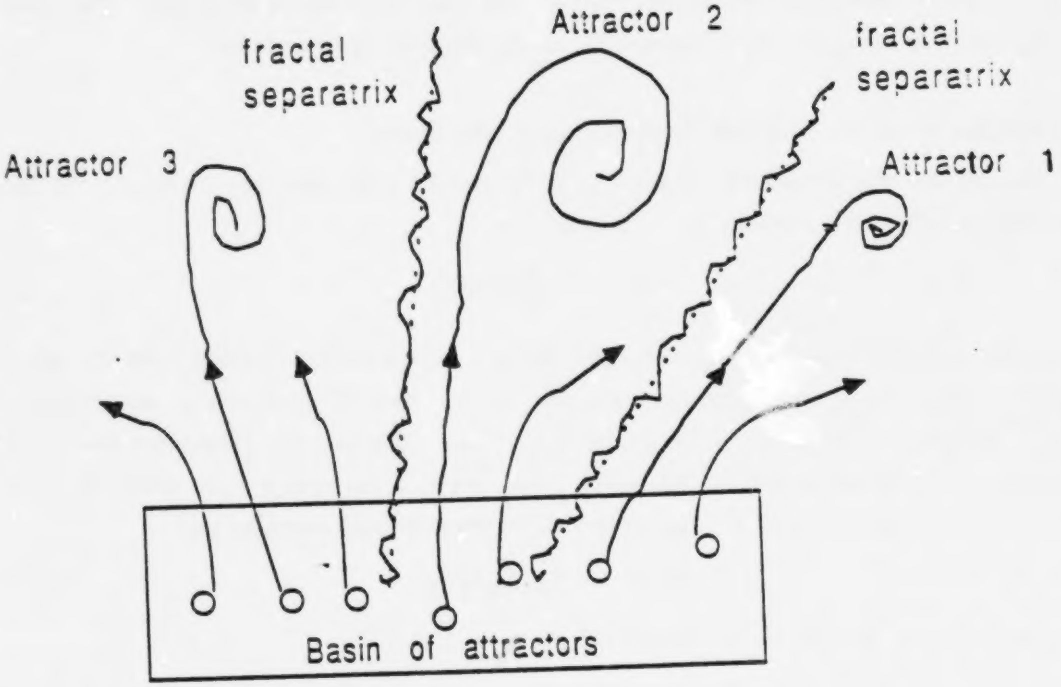

Figure 3: A simplified drawing of a cognitive channel.

The set of initial conditions can be thought of as constituting the basin of the attractors. The process of partitioning and category formation in the brain include the topology of the separatrices (fractal basin boundaries) among the single subset of the basin. In what follows, we attempt to envision the dynamical equivalent of an information channel relating a mapping between an ensemble of messages at the transmitter and an ensemble of outputs at the receiver. Before doing so, it would be highly desirable to recall that an information channel according to Shannon's theory supplies a one-to-one mapping (bijective transformation) between the transmitter and the receiver and in all likelihood, is not connected with the process of cognition.

The only function of the classical information channel is for duplication of the transmitted information, as it is, at the receiving end with minimum error and high speed. To attain our goal, the set of messages should be classified as an ensemble of initial conditions on the basin of the multi-attractor set in an M-dimensional state space where M represents the number of variables relating the dynamical phenomenon under study. However, the receiver is classified as an ensemble of attractors of lower dimensionality embedded as invariant compact subsets in the mentioned M-dimensional state space. Converging to the attractor by the intermediary of short or long transients in state space corresponds to the process of advancing signal abstraction or compression.

At this stage several questions arise from figure 3. How is the ensemble of initial conditions (messages) divided among the multi-attractor set. One has to bear in mind that the mapping between messages and attractors is not bijective: entire subsets of the basin converge to only one attractor. Also some points of the basin may undergo a transient trajectory without converging anywhere. Furthermore, how can one tell which subset of the basin will map into which attractor? To answer the above questions is not easy. Nevertheless, Grebogi et al. [71] have addressed a simple case. This case is composed by two simple attractors, namely two steady states. One envisages a two-dimensional non-invertible map (the channel) and then looks for a fractal basin boundary (fractal separatrix) between the two subsets of the initial conditions (basin).

Accuracy is sometimes indispensable in collecting measurements (initial conditions) for reliable prediction of the relevant attractor into which the observed phenomenon will be classified. If this can be accomplishment, the set of attractors in the model represent dynamically stored patterns in the brain against which entire ensemble of externally colliding stimuli is convoluted. Knowledge of the state-space dimensionality of the colliding messages and the fractal dimensionality of the corresponding attractors allows one to estimate in each situation the degree of average compressibility to which a given M-dimensional stimulus is subjugated. Moreover, examination of the topology of the fractal separatrices of the basin permits one to evaluate the uncertainty associated with the type to which the given stimulus belongs. The degree of compressibility and the entropy partitioning are the two chief macroparameters describing the cognizant apparatus at a given hierarchical level. These parameters can be computed once the mapping is known.

8.4 Example of a Fractal Basin Boundary

Following Grebogi et al. [71], we consider an example of a fractal separatrix. Envisage the following two-dimensional non-invertible map:

$$u_{n+1} = 2u_n \qquad (mod 2\pi) \qquad 0 \le u_n \le 2\pi \tag{63.a}$$

$$v_{n+1} = \gamma v_n + \cos u_n \qquad 1<\gamma<2 \tag{63.b}$$

The Jacobian matrix of this map has 2 and γ for eigenvalues. Both eigenvalues exceed 1, hence there are no attractors for finite v. The initial conditions produce orbits which will asymptotically diverge to either $v = +\infty$ or $v = -\infty$ as n tends to infinity.

The two limits, that is, $v = +\infty$ and $v = -\infty$ may be viewed as two coexisting attractors. The aim of the problem is to find the basin boundary of the two attractors. That is, find $f(u)$ such that the initial conditions in $v > f(u)$ asymptotically directs the orbits to $v = +\infty$ whereas those in $v < f(u)$ directs the orbits to $v = -\infty$. According to [71], the expression for $f(u)$ is given by

$$v = f(u) = -\sum_{k=1}^{\infty} \gamma^{-(k+1)} \cos(2^k u) \tag{64}$$

The convergence of (64) is guaranteed since $\gamma > 1$.

$$\frac{df(u)}{du} = \frac{1}{2}\sum_{k=1}^{\infty}\left(\frac{2}{\gamma}\right)^{(k+1)} \sin(2^k u) \tag{65}$$

Since $\gamma < 2$, the equation (64) diverges, therefore $f(u)$ is not differentiable. The separatrix $v = f(u)$ was found to have an infinite length and a fractal dimensionality d given by

$$d = 2 - \left(\frac{\ln\gamma}{\ln 2}\right) = 2 - \log_2\gamma \tag{65}$$

9. CONCLUSIONS

In summary, the phenomenon of strange attractors has captured an immense amount of attention over the years. Extensive research has been directed toward the chaotic, unpredictable motions of nonlinear systems with comprehensively resolute parameters. The results of the research have been important not only from a physical and mathematical point of view, but also to many diverse fields of engineering. Considerable progress has been made in developing a theory of strange attractors. In recent years, however, abstract mathematical objects have been viewed in a new light with the introduction of fractals.

Strange attractors can be created by merely solving differential equations. The chaotic solutions of these equations have been introduced as models for a number of physical phenomena in which the underlying physical operation is statistical and intermittent, i.e clustered in space and/or in time. One of the fundamental problems has been to measure the statistical properties of a strange attractor. One of the measures that has become popular is the fractal dimension. In this paper we have described the importance of fractals and their use with strange attractors.

In the remainder of this concluding section, we discuss some of the existing handicaps of the various measures and attempt to indicate a prognosis for future directions.

The computation of fractal dimensions is not easily accomplished for attractors of dimension greater than three. In effect the number of data points, the burden of computation, and the accuracy requirements make it virtually insoluble [72]. The primary problem results from the existence of many cells are visited infrequently causing the amount of computation to be unacceptable.

Another difficulty arises when addressing the issue of the information dimensionality of multiple attractors. The problem is that we may not know whether the degree of abstraction or compressibility of the basin of initial conditions holds everywhere. Ott et al. [73] examined the feasibility of invariance for a number of dimensions of strange attractors and discovered some well-defined coordinate transformations for securing the invariance of the transformation dimensionality. However, further investigations are needed in this direction.

A complete understanding of strange attractors will require a continued research effort to explicate some facts that are still fuzzy to scientists. In addition, further work is needed in applying the existing mathematical theory to the many scientific and engineering problems. The understanding of strange attractors will play an important role in describing turbulence and calculating or manipulating its motion, which as yet has been unsolved. To do so, for example, one might consider experimental data and the output from numerical simulations on turbulence and then compute the Lyapunov exponents and dimensions and/or fractal dimension of the attractors as a function of the Reynolds number.

APPENDIX C

User's Guide: Spectra-Physics Model 164 Laser

USER'S GUIDE: SPECTRA-PHYSICS MODEL 164 LASER

David S. Trotter

Electrical & Computer Engineering Department
North Carolina State University

USER'S GUIDE: SPECTRA-PHYSICS MODEL 164 LASER

The Spectra–Physics Model 164 laser can be used as an illumination tool for the F.M.F. wind tunnel. To date, it has been used to produce "sheets" of light for analyzing well–defined layers within smoke flows. It is a five watt, continuous wave, argon ion laser which emits light with wavelengths from 488 nm to 514 nm (visible blue region). The instrument consists of the laser head (containing the plasma tube and optics) and the power supply (containing the high–power electronic controls). See Figure 1. The laser requires an electrical power input of 208 volts, three–phase, at a current rating of 40 amps (220 volts, three–phase, is acceptable). Water for its cooling system must be provided at a flow rate of at least 2.2 gallons per minute and at a pressure between 25 and 50 p.s.i.. For detailed specifications and operating procedures, refer to the Spectra–Physics Model 164 Instruction Manual.

Why Use a Laser ?

The light emitted by a laser is different from that produced by other light sources. It is monochromatic; i.e., it consists of only a small band of wavelengths. The light is also coherent; i.e. it consists of waves which are in–phase. In addition, the beam does not diverge or spread much.

Two optical systems have been developed which produce two–dimensional sheets of laser light. Because laser light diverges very little through free space, these thin sheets of laser light have constant thicknesses over long distances. Consequently, these two systems can illuminate smoke flows in "layers" or "planes" which are well–suited for image analysis.

A. Laser safety

DANGER !!!!! This laser can be very dangerous if the proper precautions and procedures are not followed. The laser beam is capable of producing serious and permanent eye damage (including blindness) and serious burns to the skin. The damage threshold for a person's eye is only 10 milliwatts per square centimeter at the wavelength that this laser emits. This laser is capable of emitting 50,000 times that intensity. In addition, the power supply's extremely high voltage can be a deadly shock hazard if the power supply is taken apart. Finally, the plasma tube becomes very hazardous if it is broken because the Beryllium Oxide from its bore is harmful if inhaled.

Always follow these safety precautions and procedures:

1. Use the laser only if you are authorized and knowledgeable in its operation.

2. ALWAYS wear the W2204A LaserGard protective goggles when operating the laser. Note: These goggles are intended to provide protection from indirect and reflected laser beams; they are NOT intended for viewing the beam directly. If the beam strikes the goggle, the lens will darken at the point of impact and the darkening will spread from that point. When this happens, protection to the eyes is provided for less than 30 seconds. Close your eyes and leave the area immediately.

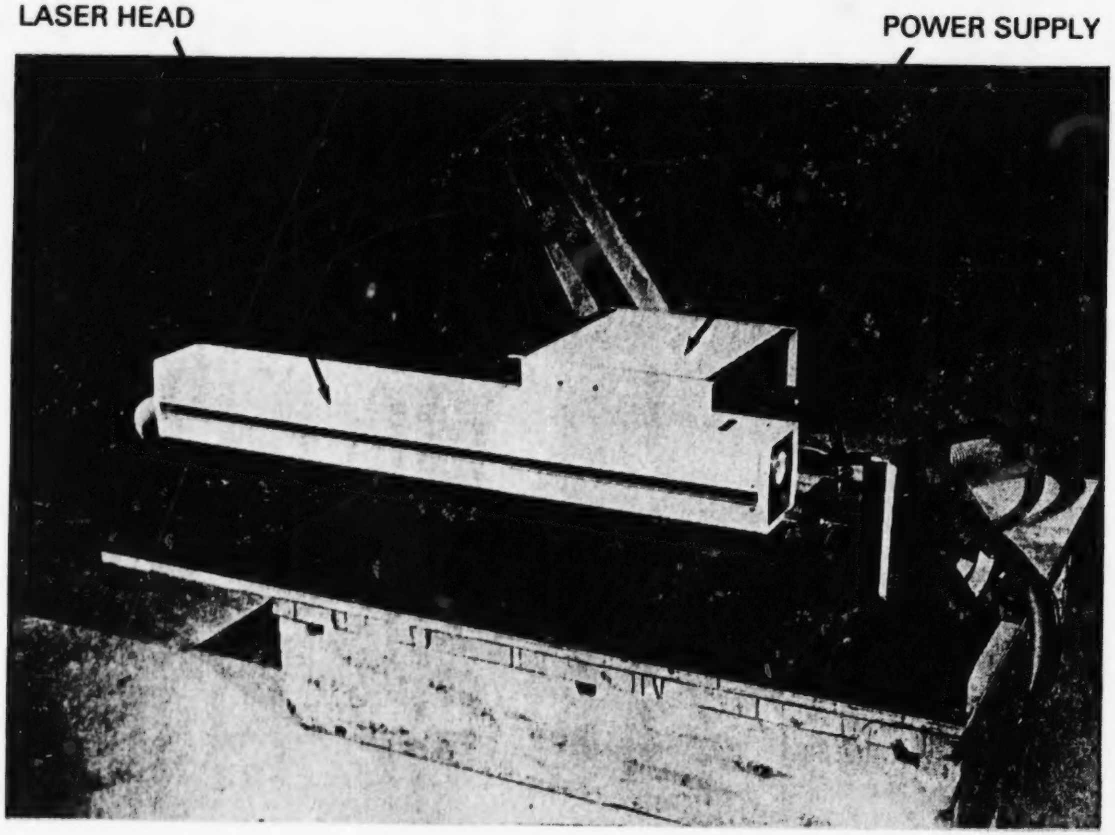
LASER HEAD
POWER SUPPLY

Figure 1. Laser system.

a. Remember that the protective goggles filter out most of the illumination at the laser's wavelength. Even if you do not see any evidence of the beam through the goggles, the laser may be on. In fact, you will not be able to see the reflection of the beam through the goggles until the laser output approaches 1 watt. So, do not take your goggles off until you are sure that the laser is off. To safely view the effects of the laser at any power, you can use a video camera and a remote monitor.

3. NEVER operate the laser when other people are in the facility unless they are wearing the W2204A LaserGard goggles and are actively participating in the laser exercise. This requirement may be relaxed if a cover is used over the laser which totally encloses the laser, leaving no possibility of the beam escaping the cover. Always place warning signs on the entrance doors to the lab area when operating the laser. These signs should include a phone number where someone can call you for permission to enter when it is safe. (The number for the phone beside the wind tunnel is often a convenient one.)

4. NEVER, NEVER, NEVER look directly into the laser beam, even if you have the protective goggles on.

5. Avoid standing in front of the laser.

6. Remove all unnecessary shiny objects from the work area. Remember, a reflection from a highly reflective surface can be just as dangerous as the original laser beam.

7. Always have a flat-black target for the beam or light sheet to hit. If the laser is to be operated without the optics for spreading the beam, you may want to use the flat black metal target bent at a sharp angle. You may want to fabricate a flat-black cone shaped target for "trapping" the laser beam.

8. Whenever possible, paint each piece of apparatus to be used in the work area flat-black.

9. Do not place the laser near eye level, if possible. When using the laser at the wind tunnel, the laser will have to be at eye level at times. When this is necessary, place the power supply (control unit) on the floor. This allows the operator to be at a level different than that of the beam during start-up.

10. It is a good idea to establish a work area behind a set of curtains which shield the area from all laser light and reflections. The laser illumination can be seen with a tripod-mounted video camera and observed on a remote monitor from behind the curtains. This work area is also useful for doing computer work.

11. Immediately before starting the laser, always inform others working with you that you are about to do so. Wait for an acknowledging response before actually starting the laser; never just

assume that your co-workers heard you.

12. After mounting fixtures or optical parts, set the laser at minimum power before restarting it. As a result, any stray reflections which misalignment cause will have a smaller potential for danger.

13. When using the rotating polygonal mirror to produce light sheets, always start the rotation of the polygon before starting the laser. This ensures that the laser beam is always rotating, producing less average power per unit area. In turn, this reduces the safety hazard.

14. Whenever possible, operate the laser under normal facility overhead lighting. This constricts the pupil of the eye, limiting the probability of retinal damage. This precaution is often not practical when recording smoke flows in the wind tunnel.

15. When using the laser at the wind tunnel, use the laser cover and a hood between the laser and the wind tunnel window. This will block reflections that bounce off of the window.

16. Remember that glass and acrylic plastic reflect light in addition to transmitting it. Consequently, one should be cautious of reflections off of lenses and the wind tunnel window.

17. Never enter the power supply unit while it is connected to the F.M.F. 220 volt outlet. DEADLY voltages are present. Even when the power supply unit is not plugged in, be cautious of capacitors which may remain charged at high potential.

18. Run a short hose from the water over-pressure drain on the power supply away from the power supply unit. Thus, if overflow water is emitted, it will not flow into the high voltage power supply. Also ensure that there are no leaks at the pipe fittings at the rear of the power supply.

19. Never place any part of your body in the beam.

20. The key may be removed from the master control key-switch on the power supply to ensure that unauthorized persons do not start the laser.

B. Laser operation

1. Connect one end of the 3/4 inch diameter garden hose to the spigot at the northwest corner of the facility. If necessary, connect two hoses together to reach the location where the laser will be operated. Connect the other end of the hoses to the inlet of the Teel 1P879A pump. The outlet of the Teel pump should be connected to a valve and in-line filter. From here, a short hose should run to the water inlet at the rear of the laser power supply. See Figures 2 and 3. Note: Hoses with diameters of less than 3/4 inch should not be used. They will restrict the water flow too much. Additional Note: Always use rubber washers or pipe thread tape on connections where applicable.

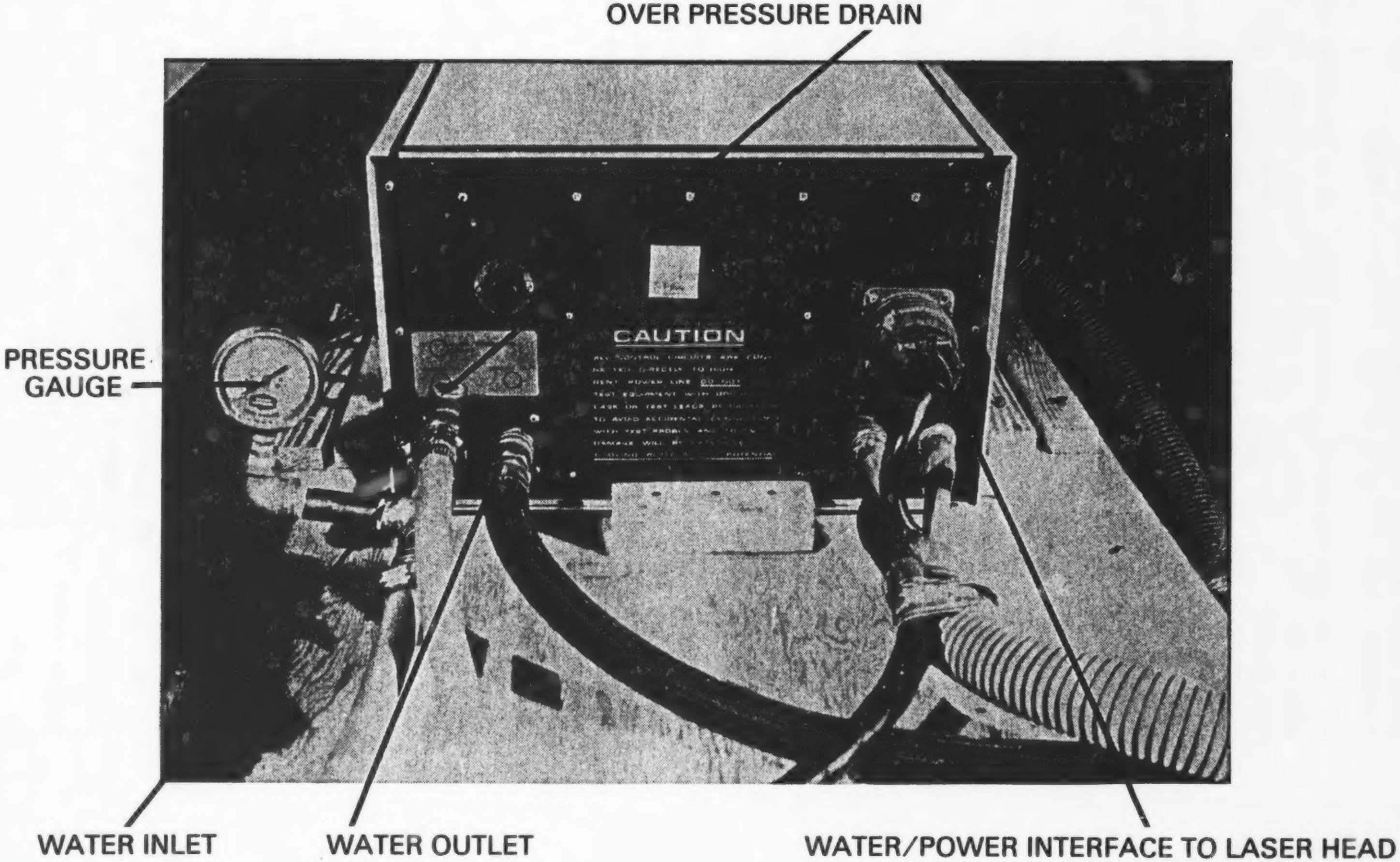
OVER PRESSURE DRAIN
PRESSURE GAUGE
CAUTION
WATER INLET
WATER OUTLET
WATER/POWER INTERFACE TO LASER HEAD

Figure 2. Rear panel of laser power supply.

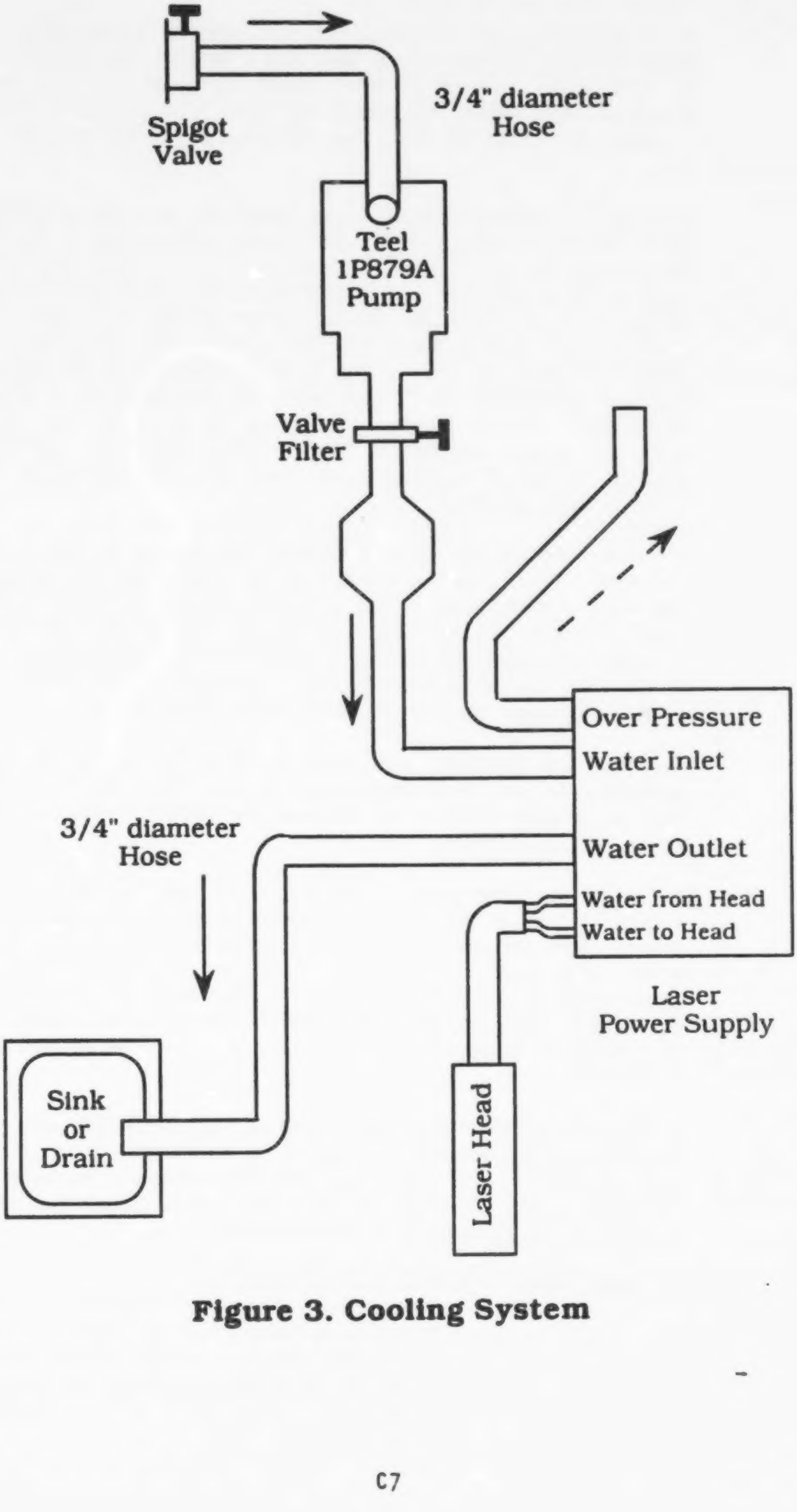
Spigot Valve
3/4" diameter Hose
Teel 1P879A Pump
Valve Filter
Over Pressure
Water Inlet
3/4" diameter Hose
Water Outlet
Water from Head
Water to Head
Laser Power Supply
Sink or Drain
Laser Head

Figure 3. Cooling System

2. Connect one end of another 3/4 inch diameter garden hose to the water outlet at the rear of the laser power supply. See Figures 2 and 3. If necessary, connect two hoses together to reach from the laser to a sink or drain. Place the other end of the hose securely in the sink or drain. Note: Use only hoses with diameters of 3/4 inch or greater.

3. Open completely the valve on the spigot to which you connected the hose. Wait approximately one minute for the water to flow to the pump. Next, insert the pump's power plug into a 120 volt outlet, and turn the pump on. Remember, the pump should only be turned on AFTER water is flowing to it. Check the pressure gauge at the water inlet to the power supply. Adjust the in-line valve so that the gauge indicates a pressure of about 40 p.s.i. Never allow the pressure to fall below the minimum specification of 25 p.s.i. or above the maximum specification of 50 p.s.i. If the pressure rises above 50 p.s.i., the over-pressure drain will actuate and release water. Once you have adjusted the pressure, inspect all connections for leaks and take appropriate action to fix any that are found.

4. Make sure that the water is flowing freely out of the hose and into the drain. Next, obtain a 3 gallon bucket which has been marked for measuring water volume. Using a watch, let the water flow from the hose into the bucket for exactly one minute. Ensure that the flow rate is at least 2.2 gallons per minute, as specified by the manufacturer.
If the flow rate is inadequate, small adjustments in the pressure may help. (Remember that the maximum allowed pressure is 50 p.s.i.)

The laser has interlocks which turn it off if the water flow rate is inadequate or the water temperature is above that specified (35^0 C). Still, it is good practice to maintain the proper conditions without relying on the interlocks.

5. Insert the three-phase (three-pronged) plug of the laser power supply into the in-line female connector on the three-phase extension cord. Twist the connectors in a clockwise fashion to lock them in place. Now, insert the plug of the extension cord into the three-phase power outlet dedicated for the laser. (This outlet is the only one in the facility which provides the necessary 208 volt, three-phase power at a rating of 40 amps.) Twist the plug in a clockwise manner to lock it in place.

6. Put your W2204A LaserGard goggles on. The three lamp indicators on the power supply marked "line" should be on indicating that power has been connected. Also, the " water on" lamp indicator should be lit on the power supply, showing that the water flow is sufficient. Referring to Figure 4, set the controls at these positions:

meter switch: 5 W (5 watt) position
current control: minimum position (counter-clockwise). (After it has been verified that the beam is following a safe path, the current control should be set at about the 4 position for starting the laser.)

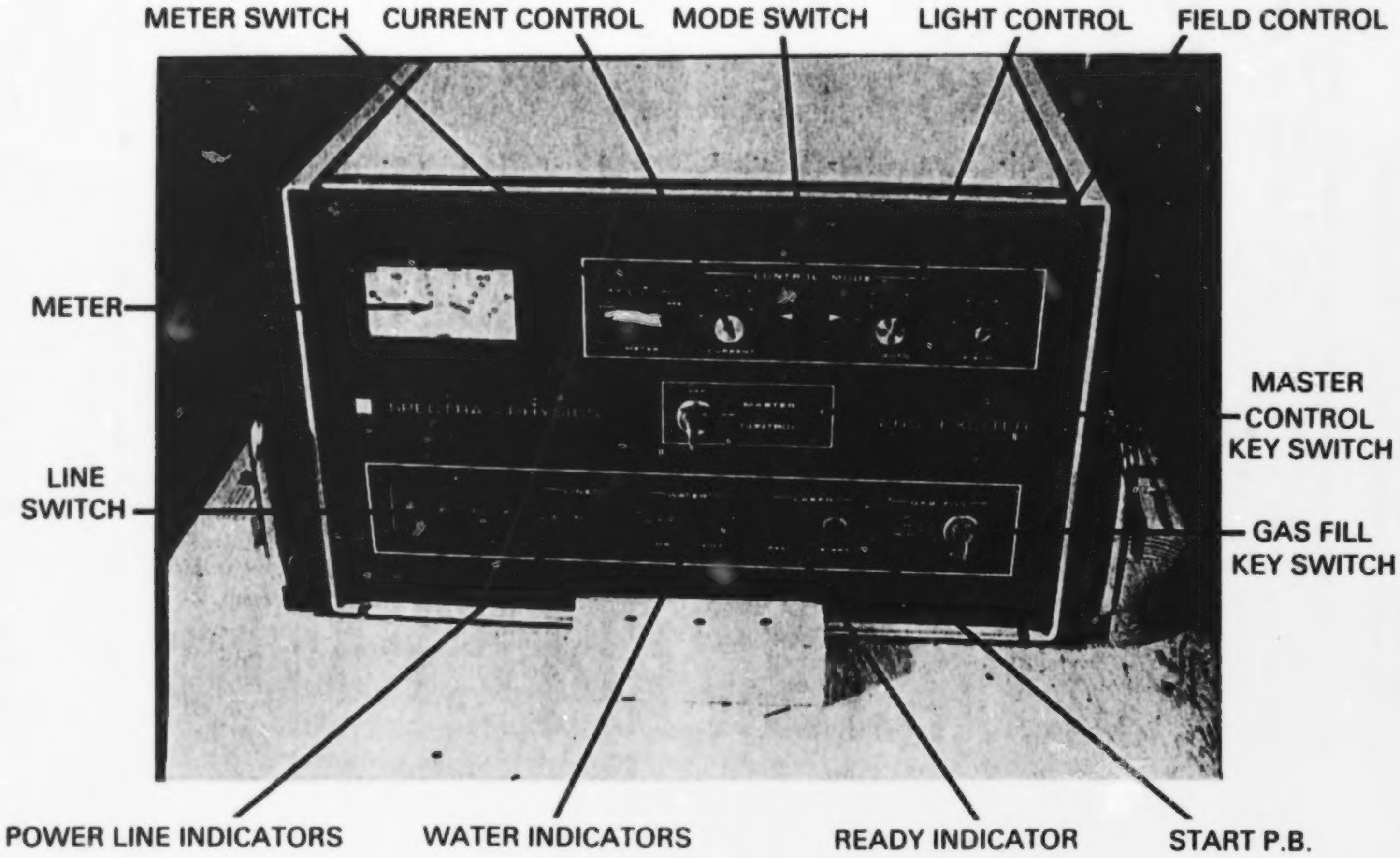
METER SWITCH
CURRENT CONTROL
MODE SWITCH
LIGHT CONTROL
FIELD CONTROL
METER
MASTER CONTROL KEY SWITCH
LINE SWITCH
GAS FILL KEY SWITCH
POWER LINE INDICATORS
WATER INDICATORS
READY INDICATOR
START P.B.

Figure 4. Laser power supply.

mode switch: left position, selecting the current mode instead of the light control mode.
light control: minimum position (counter-clockwise)
field control: maximum position (fully clockwise)

7. Insert the master control key and turn it clockwise. Pull the line switch up to the on position. After about 30 seconds, the "ready" lamp will light. Press the "start" button and the laser will produce an output beam. The "ready" light will go out.

8. The laser is now operating in the current control mode. This means that the plasma current in the tube is regulated to a constant value. Due to imperfections in the laser system, the power in the output beam may fluctuate in this mode. The laser should be started in this mode and operated in this mode for general purpose use.

The light stabilized mode can be selected by moving the mode switch to the right hand position. This mode stabilizes the output beam, compensating for disturbances in the system. It does this by monitoring the beam's power and incorporating a feedback control loop. This mode should be used only at powers between 100 mW and 2 watts. The light stabilized mode is suggested for illuminating the wind tunnel since stability of the illumination is critical.

When switching from the current mode to the light mode or vice-versa, you should set the current control and light control knobs at approximately the same setting. This eliminates large unexpected changes in the beam power.

The output power of the laser can be adjusted by rotating the current control or light control knob. The value of the power can be observed on the meter by selecting "5W" or "1W" on the meter switch.

The following meter switch selections are possible:

50 Amps: The meter indicates the tube current. The full-scale reading is 50 Amps.

5W: The meter indicates the power of the laser beam. The full-scale reading is 5 watts.

1W: The meter indicates the power of the laser beam. The full-scale reading is 1 watt.

Fill: This mode is used to detect if the tube has low pressure and needs a gas fill. The validity of the meter indication in this mode is uncertain on the F.M.F. laser. See the operator's manual under "Gas Fill".

Reg: The meter indicates the voltage drop across the regulator in the power supply.

The field control should always be turned to the maximum (fully clockwise) position.

When the laser is initially started, a low-pressure alarm may sound. This should be ignored until the laser has operated for about 30 minutes. If the alarm sounds after this 30 minute warm-up period, the gas pressure in the tube may be low. See the " Gas Fill" section in the instruction manual (p. 6.7). Note: The laser has periodically sounded this alarm after the designated warm-up period, and the gas fill procedure has been carried out, but it remains unclear if there really is a low-pressure problem.

9. To turn the laser off, rotate the master control key-switch counterclockwise. The line-switch should disengage at the same time. It is a good idea to reduce the current control and light control settings to minimum power when turning the laser off. This ensures that the output power level will be at a minimum when it is started again unless the next operator consciously increases the power output setting.

The following maintenance procedures should be followed in order to keep the laser operating correctly:

1. Operate the laser once a week for at least an hour.

2. Low output beam power is sometimes caused by misalignment of the rear optics. To re-align them, follow these procedures:

    a. With the laser off, face the rear of the laser head. Locate the holes at the upper right and lower left corners. Inside these holes are screws for the horizontal and vertical adjustment of the rear optics.

    b. Start the laser and select the current mode. Set the power at 1/2 watt.

    c. Insert a thin screwdriver in the upper right hole until you feel the adjustment screw. Turn the screw very slowly counterclockwise. If the meter indicates that the power is increasing, continue turning counterclockwise until the meter shows a decrease in power. Otherwise, turn clockwise until the meter shows a decrease in power. Repeat this step until a peak power is achieved.

    d. Repeat the procedures of step "c" with the lower left hole.

    e. Repeat steps "c" and "d" until the output power has been maximized.

Very slight movement of these adjustment screws can cause considerable changes in beam output power. Due to this sensitivity, any vibration of the laser head may cause a reduction in peak power.

3. If the low-pressure buzzer sounds continuously after the laser has

warmed up for more than 30 minutes, a gas fill may be needed. Carry out these procedures:

a. Using the usual safety precautions, set the mode switch to current control (left position). Set the current control and the field control to maximum.

b. Turn the meter switch to "fill". The meter reading should be in the white zone.

c. Turn the "Gas Fill" key-switch clockwise, and release it immediately.

d. The fill valve should click, the meter indicator should slowly point toward the green zone, and the buzzer should stop. This could take several minutes.

e. If the meter does not move to the green region and the buzzer does not stop buzzing within 15 minutes, repeat the process.

Note: This procedure has been carried out in the past, but it was unclear if there was actually any gas fill action taking place.

C. Lenses and associated hardware

One set of hardware which was developed for producing sheets of laser light consists of lenses, a first-surface mirror, and adjustable mounting hardware. See Fig. 5. The beam exits the laser and is reflected by the mirror at a 90^0 angle. The first lens (cylindrical, plano-concave, Melles-Griot p.n. 01-LCN-000) diverges the beam in one plane. The next lens (cylindrical, plano-convex, Melles-Griot p.n. 01-LCP-001) collimates the light. The last lens (cylindrical, plano-concave, Melles-Griot p.n. 01-LCN-000) diverges the beam again in the same plane. The hardware can be arranged to produce either horizontal or vertical light sheets with significant intensities within a spread angle of approximately 52^0. Unfortunately, the intensities are not uniform across the sheets. Follow these procedures for aligning the lenses and associated hardware:

1. Mount the hardware as in Figures 6,7, and 8 to produce horizontal light sheets. To produce vertical light sheets, mount the lens holders upright with the blocks designed for this purpose.

2. Note that the hardware is designed so that the fixture can be rotated about a central pivot point on the mounting block. For horizontal sheets, adjust the fixture so that the main steel rod is at a horizontal position. For vertical sheets, adjust so that the main steel rod is 26^0 from horizontal. A large protractor should be used to do this. This 26^0 angle eliminates most of the reflection of the light off of the tunnel floor and allows a wide angle of coverage within the tunnel.

3. Adjust the lens holder closest to the mirror and the lens holder in the middle so that they are 34 mm apart. This distance largely determines the angle at which the resulting sheet will spread. The

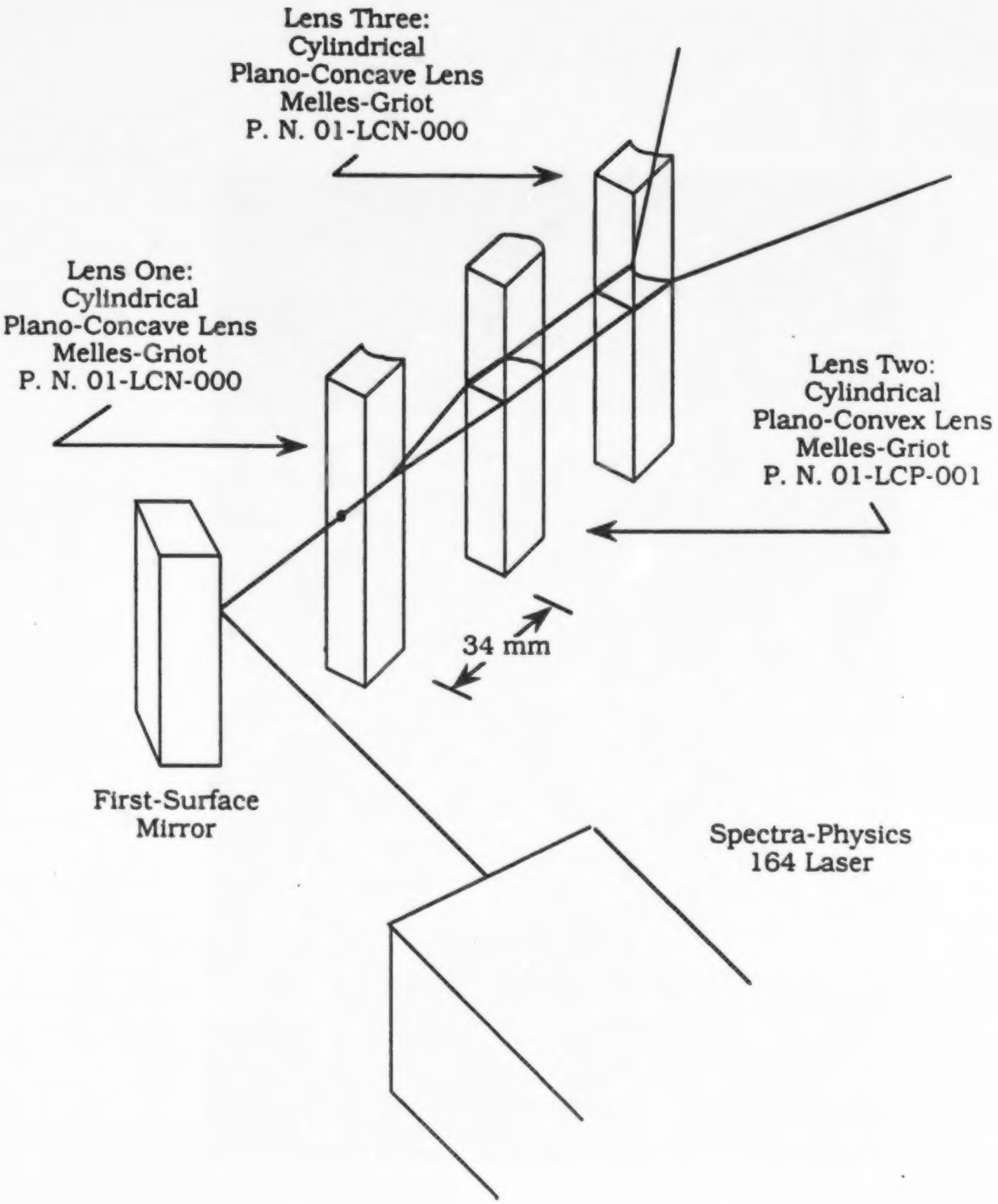
Lens Three:
Cylindrical
Plano-Concave Lens
Melles-Griot
P. N. 01-LCN-000
Lens One:
Cylindrical
Plano-Concave Lens
Melles-Griot
P. N. 01-LCN-000
Lens Two:
Cylindrical
Plano-Convex Lens
Melles-Griot
P. N. 01-LCP-001
34 mm
First-Surface
Mirror
Spectra-Physics
164 Laser

Figure 5. Laser light sheet produced using lenses.

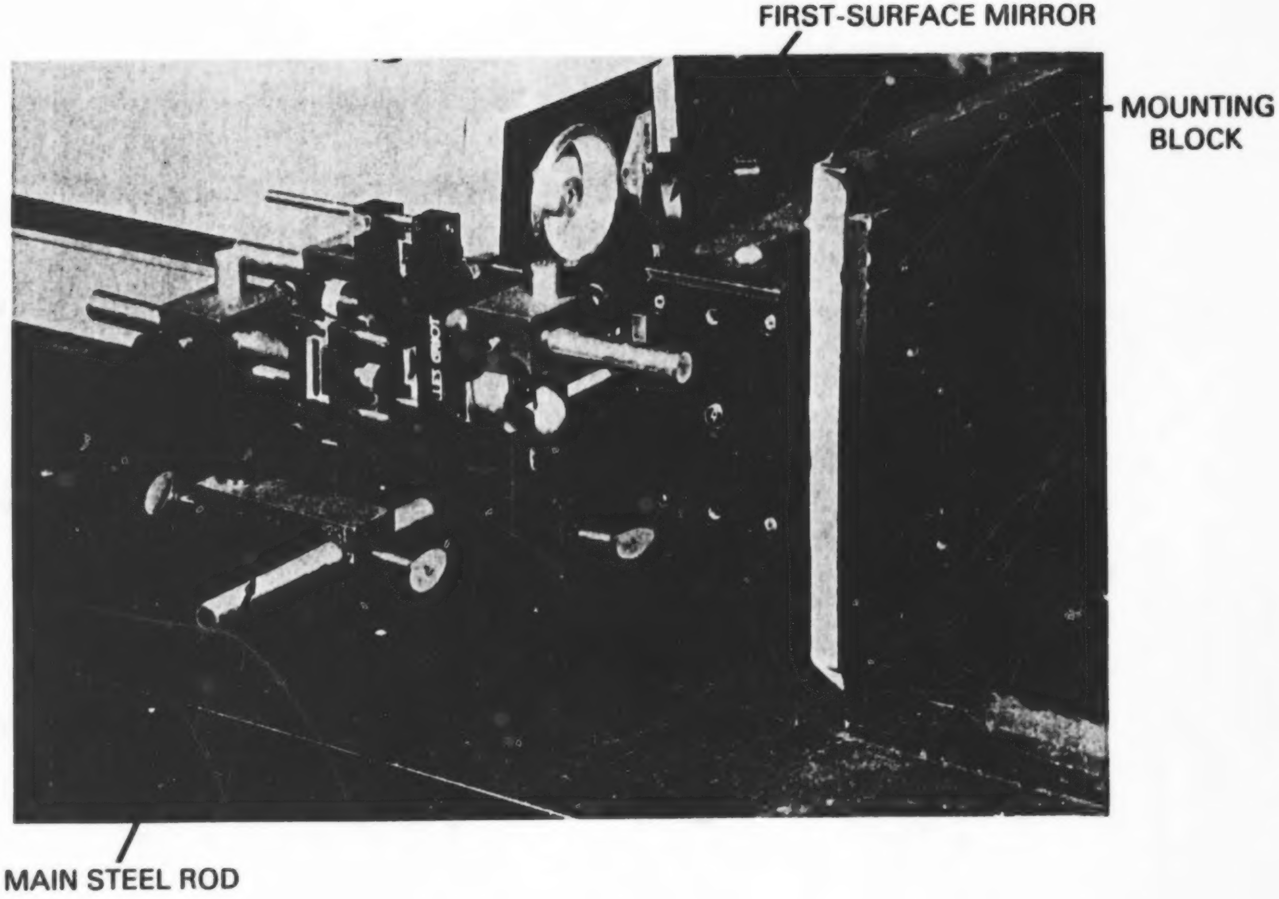
FIRST-SURFACE MIRROR
MOUNTING BLOCK
MAIN STEEL ROD

Figure 6. Lens system.

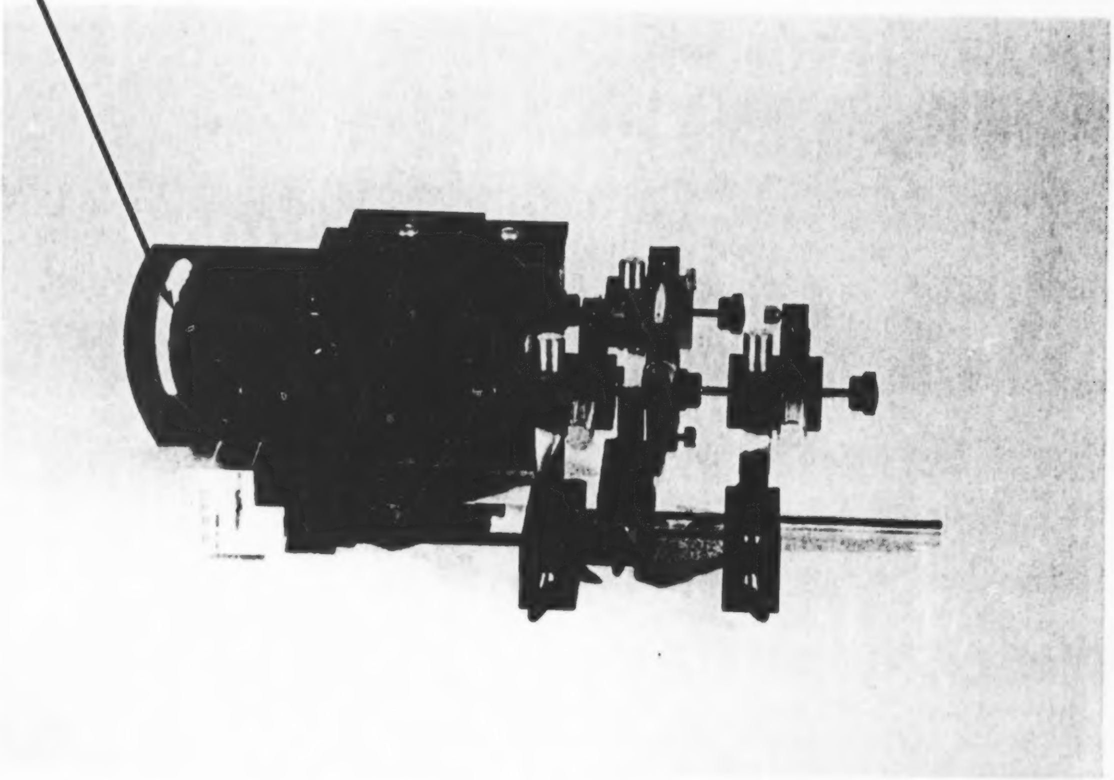
ROTATION ADJUSTMENT SLOT

Figure 7. Lens system, side view.

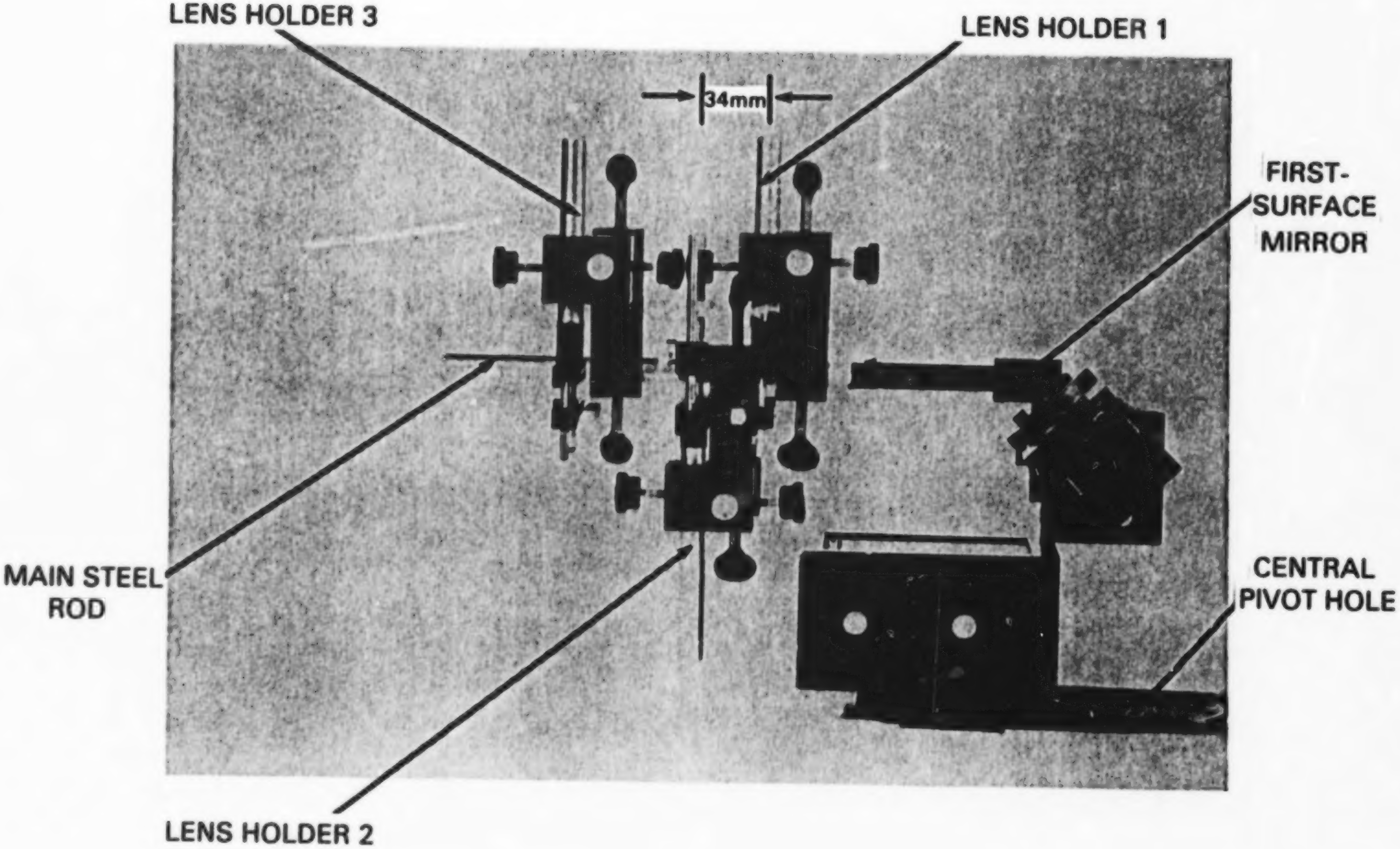
LENS HOLDER 3
LENS HOLDER 1
34mm
FIRST-SURFACE MIRROR
MAIN STEEL ROD
CENTRAL PIVOT HOLE
LENS HOLDER 2

Figure 8. Lens system, top view.

distance between the middle lens holder and the one farthest from the mirror is not critical but should be kept at a minimum.

Adjust the fixture and lens holders so that they look approximately lined up, and leave some room for adjustment in each direction.

4. Now, cut two pieces of acrylic plastic to lengths of 25 mm and heights of 6 mm. Cut one piece of acrylic plastic to a length of 60 mm and a height of 15 mm. Remove the lenses from the fixture. Replace the lenses with the plastic pieces. Place the 25mm x 6 mm plastic pieces in the first and last lens holders, in place of the concave lenses. Place the 60 mm x 15 mm plastic piece in the middle lens holder, in place of the convex lens. Important: These pieces should be mounted in the lens holders in the following manner:

a. The lens holder closest to the mirror should hold the piece by the wider flat surfaces adjacent to the grooves. The flat surfaces are designed to hold concave lenses.
b. The middle lens holder should hold its plastic piece with its grooves, which are designed to hold convex lenses.
c. The lens holder farthest from the mirror should hold its piece by the flat surfaces adjacent to the grooves. In addition, it is very important that the plastic piece be held on the side of the holder at which the light will exit. If this is not done, a large portion of the light sheet will be blocked.

Make absolutely sure that the laser is OFF; i.e., PLACE THE LINE SWITCH IN THE OFF POSITION, TURN THE MASTER CONTROL KEY-SWITCH TO THE OFF POSITION, REMOVE THE KEY, AND UNPLUG THE POWER PLUG FROM THE WALL OUTLET. Now, looking through the acrylic plastic pieces with one eye, try to align your line of sight with the fixture mirror. If everything is aligned perfectly, you will be able to see your own eyeball centered in the mirror. This is a result of overhead light reflecting off of your eyeball, through the plastic pieces, reflecting off the fixture mirror, into the laser aperture, to the laser optics, and reflecting back along the same path. Make any adjustments necessary to align the apparatus as perfectly as possible. Unfortunately, the alignment is very critical in producing reasonable results.

5. Using a high quality lens tissue, clean the lenses. To do this, hold the lenses by the non-polished ends. Breathe on the lenses to produce moisture on their surfaces. Then, lightly wipe the surfaces with the lens tissue, using a very confined circular motion. Remove any oily spots since they tend to heat up when exposed to the high power laser beam.

6. Replace the acrylic plastic pieces with the lenses, placing them in the exact same locations. Remember that the outermost lens must be placed on the side of the holder from which the light exits.

7. Set up a tripod mounted camera and monitor for the purpose of viewing the laser sheet. Place the monitor behind a barrier for

protected viewing.

8. Put your LaserGard protective goggles on. Set the laser at MINIMUM power, and start it. Be cautious of stray reflections. Remember, the lenses will always produce some reflections. By viewing the monitor, determine if a light sheet has been produced. If a sheet is present but has an unacceptable spread, try adjusting the distance between the two lenses closest to the mirror. If the resulting light sheet is unsatisfactory, repeat the preceding steps.

9. If no light sheet is evident, you may want to determine if the beam is hitting the first lens at least. Turn the laser off. Tape a small piece of flat-black paper to the front of the first lens holder directly in front of the lens. With your LaserGard goggles on, start the laser and increase power to about 3 watts for about 30 seconds. Now, turn the laser off. The laser should have burned a hole through the paper where it struck it. Consequently, you can inspect the location of such a hole to determine if the beam was striking the first lens.

D. Rotating Polygonal Mirror and Associated Hardware

Another set of hardware developed for producing laser light sheets uses a twelve-sided, polygonal mirror. A d.c. motor rotates this polygonal mirror at high speed, which in turn reflects the laser beam and scans it in a single plane. This effectively produces a sheet of laser light. See Figure 9.

The beam sweeps through an angle of 60^0. At this time, only horizontally scanned sheets are possible. The thickness of the light sheet depends on the precision of the polygon, the coupling between the polygon and the motor shaft, and the motor itself. The imperfections in the motor and the shaft coupling have been observed to produce some error in the F.M.F. fixture. The thickness of the sheet is approximately 1.5 cm after it has crossed half of the tunnel width (1.85 m) and approximately 3 cm after it has crossed the entire tunnel width (3.7 m).

The rotational speed of the polygon has been roughly calibrated with the VIZ WP-707 power supply providing power to the d.c. motor. This was accomplished using a Model 510-AL stroboscope (manufactured by Electronic Brazing Co.). The results are shown in Table 1.

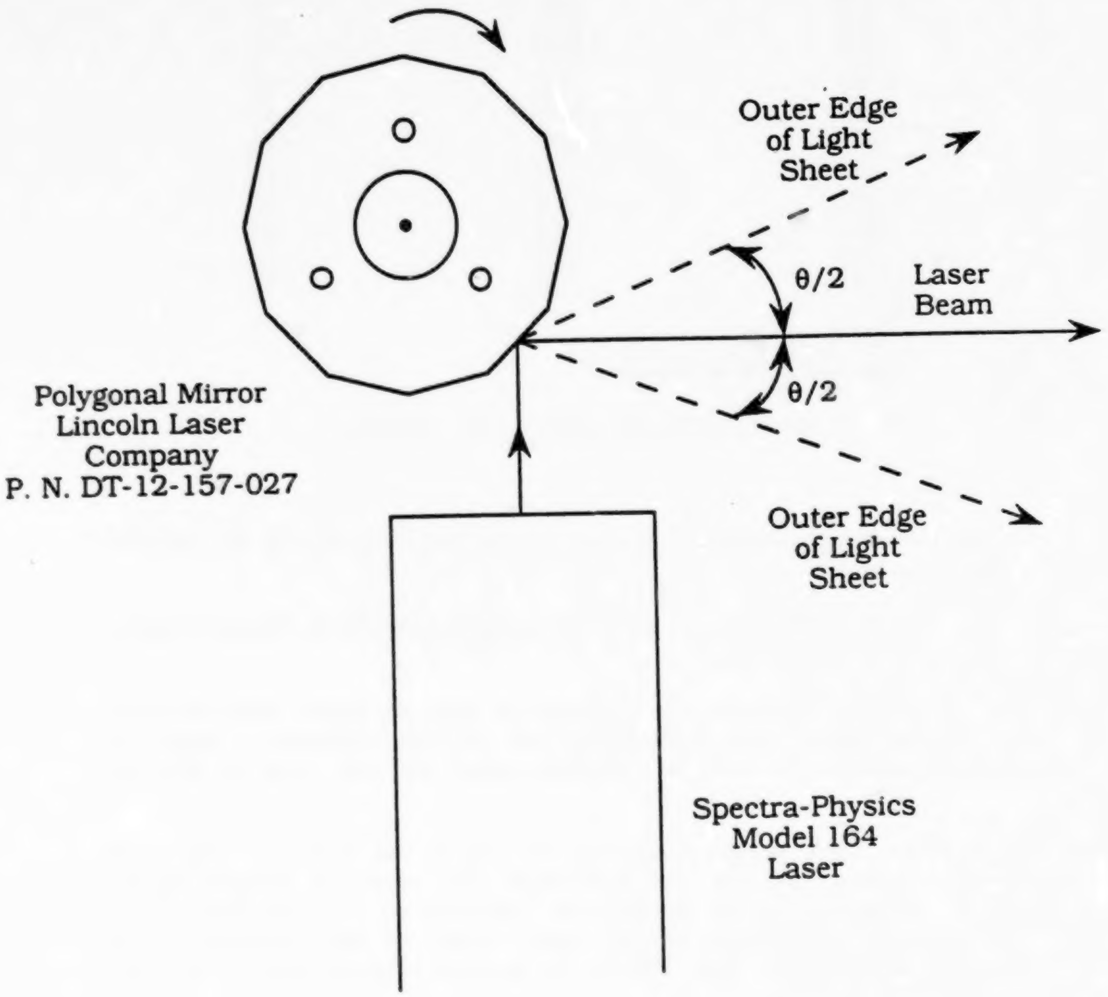
Outer Edge of Light Sheet
θ/2
Laser Beam
θ/2
Polygonal Mirror Lincoln Laser Company P. N. DT-12-157-027
Outer Edge of Light Sheet
Spectra-Physics Model 164 Laser

Figure 9. Laser light sheet produced using polygonal mirror

Power supply setting (volts)	Shaft speed (RPM)	framing rate (beam scans per field)
5.0	630	2.1
6.0	750	2.5
6.7	900	3.0 •
7.0	960	3.2
8.0	1100	3.7
8.7	1200	4.0 •
9.0	1240	4.1
10.0	1410	4.7
10.6	1500	5.0 •
11.0	1550	5.2
12.0	1710	5.7
12.6	1800	6.0 •
13.0	1860	6.2
14.0	2010	6.7

• Data calculated by interpolation

Table 1. Polygonal Mirror Speed Calibration

Use the following procedure to align the rotating polygon and its associated hardware:

1. With the laser off, mount the polygon apparatus as shown in Figures 10 and 11.

2. The apparatus was fabricated so that the fixture could effectively be rotated about a horizontal axis for one adjustment. Make this adjustment so that the polygonal mirror will spin along a horizontal plane.

3. Look straight down onto the top of the polygon. Adjust the apparatus so that the laser beam will strike the polygon halfway between its center and its outer circumference. (The beam should strike the polygon left of center facing the laser aperture.) This will cause the light sheet to be centered perpendicularly to the laser. See Figure 9.

4. Make sure that the laser is OFF. PLACE THE LINE SWITCH IN THE OFF POSITION, TURN THE CONTROL KEY-SWITCH OFF, REMOVE THE KEY, AND UNPLUG THE POWER PLUG FROM THE WALL OUTLET. Now, from the side of the laser where the light sheet will be present, look into the polygonal mirror. Using one eye, maintain your line of sight at the level of the polygon. Determine from the image present in the mirror if the polygon fixture needs to be raised or lowered. Raise or lower it accordingly. Make adjustments until the image of the laser aperture is centered vertically on the polygon surface. When it is perfectly aligned, you should be able to spin the

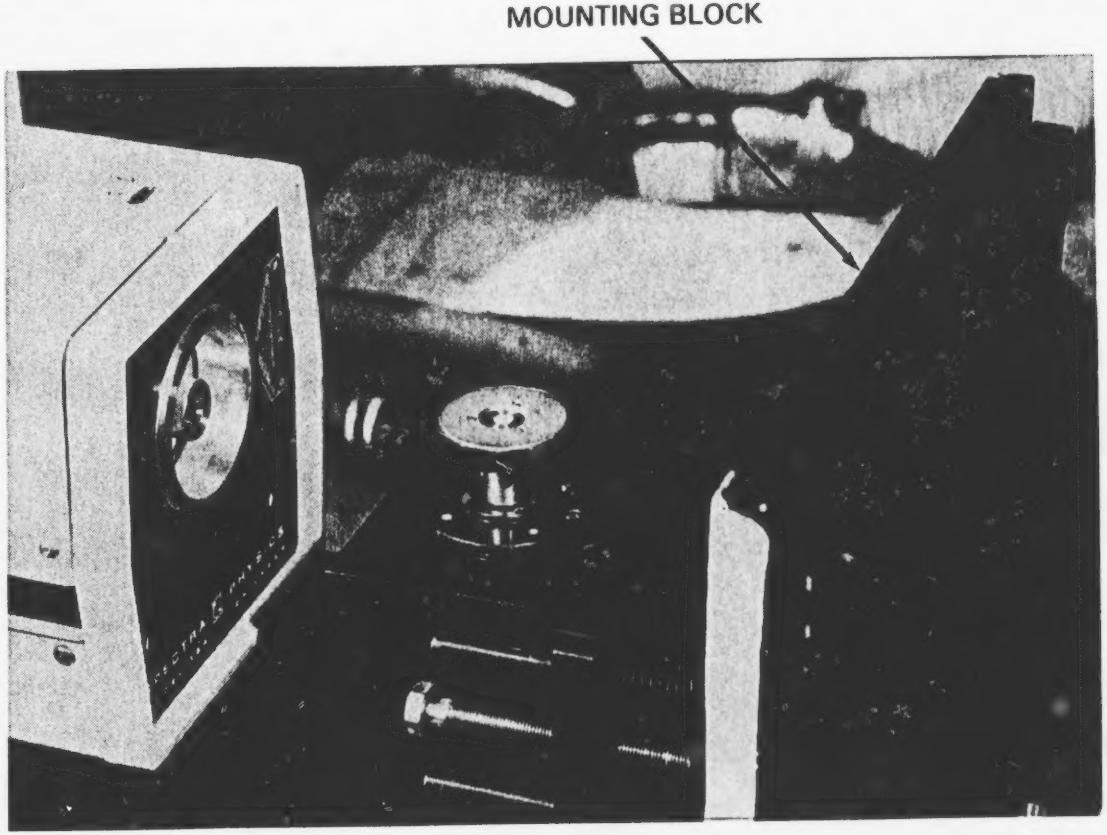
MOUNTING BLOCK

Figure 10. Mirrored polygon system.

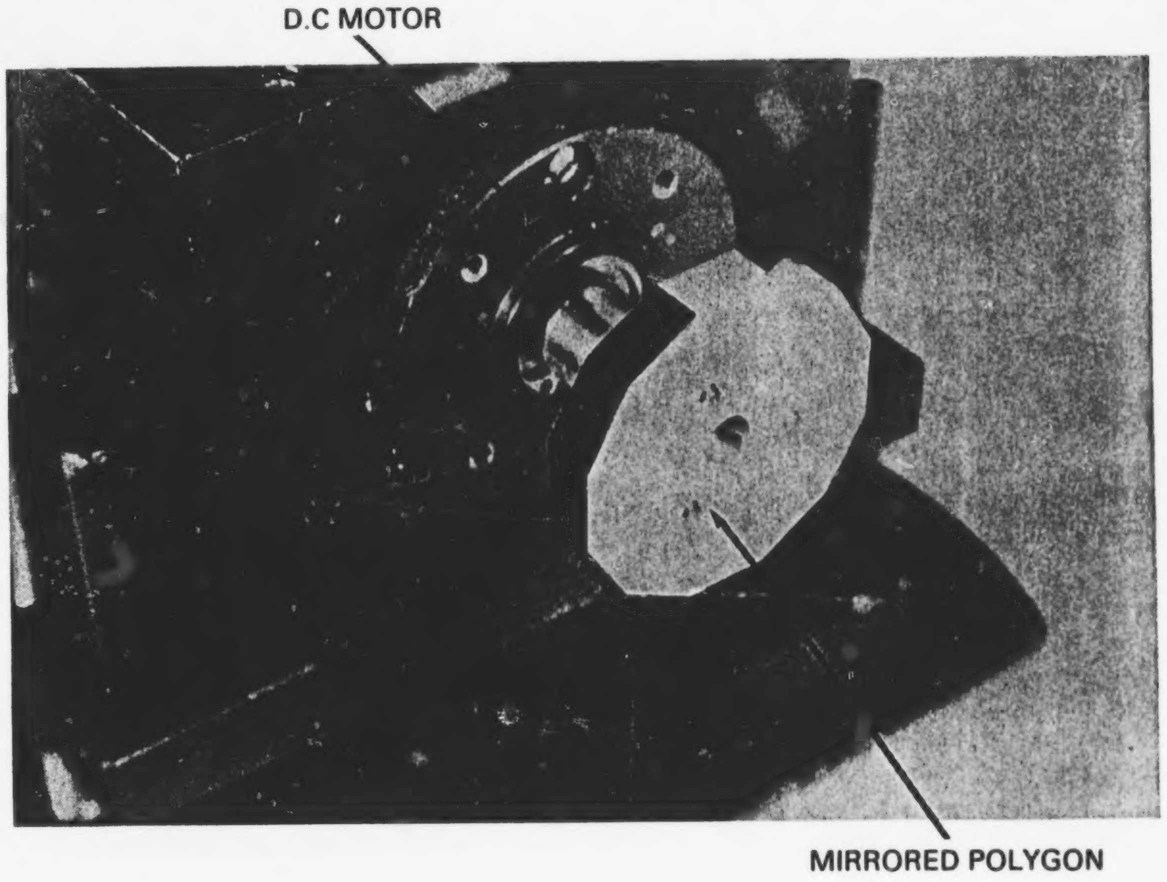
D.C MOTOR
MIRRORED POLYGON

Figure 11. Mirrored polygon hardware.

polygon very slowly and see your own eyeball in the polygonal mirror. This results from overhead light traveling off your eye, reflecting off the polygonal mirror, into the laser, reflecting off of the laser optics, and following the same return path.

5. Set up a tripod-mounted camera and monitor for viewing the light sheet. Set the monitor behind a wall or curtains for shielding the light.

6. Connect the cable and plugs from the d.c. motor to the VIZ WP-707 d.c. power supply. One banana plug should go in the "+" jack of the power supply and the other banana plug should go in the "-" jack. It is not important how the plugs and jacks are matched. Plug the power supply power plug into a 120 volt outlet. Using the appropriate allen wrench, make sure that the polygon coupling is securely tightened to the motor shaft. Set the power supply's current limit to maximum. Set the power supply's voltage output to 0. Turn on the power supply. Now, slowly increase the voltage to approximately 10 volts. Without getting your face too close to the polygon, make sure that it is rotating.

7. With your LaserGard goggles on, set the laser for minimum power. IMPORTANT: Always power the motor and have it rotating the polygon when the laser is turned on. This reduces the average power per unit area in the laser light and thus reduces the possible harm from laser exposure.

Now, turn the laser on and observe the results through the monitor. If the results are not satisfactory, repeat the above procedures.

The polygonal mirror will need cleaning from time to time. This must be done with much care since its surfaces scratch easily and its edges can crumble. To clean the polygon, leave it mounted on the motor shaft and remove the mounting assembly as a unit. Adhere strictly to the manufacturer's procedures which follow.

PROCEDURE FOR HAND CLEANING

DIAMOND MACHINED POLYGON MIRROR SURFACES

Diamond machined aluminum surfaces are considerably more fragile and difficult to clean without damaging than conventionally polished electroless nickel plated or glass surfaced mirrors. One particular hazard not normally encountered is the possibility of small metal particles breaking away from the machined sides of the facet, becoming embedded in the cleaning pad and causing scratches. A protective coat, silicon monoxide, for example, will improve durability of a diamond machined polygon.

The following procedures should be performed in a clean, dust-free environment.

Equipment and Materials Needed:

Acetone - Reagent grade
Freon TF - Reagent grade
(Solvents should be kept in glass bottles and dispensed with an eye dropper. Polyethylene bottles may be used, but glass is recommended.)
Lens Tissue (Type I), approximately 3-1/2 X 7 inches.
Nylon or cotton gloves. (Nylon is preferred due to troublesome cotton lint).
High-intensity lamp

Procedure:

CAUTION: FREON AND ACETONE ARE POTENTIALLY HAZARDOUS CHEMICALS. SECURE THE APPROPRIATE MATERIAL DATA SHEETS FROM THE CHEMICAL SUPPLIER AND FOLLOW THE APPLICABLE GUIDELINES.

Wearing nylon gloves or using a mirror holding fixture, hold polygon by the sides or the bore and flush off mirror surfaces thoroughly, first with acetone, then repeat flushing, using Freon TF solvent. For the final rinse, hold the mirror at an angle of approximately 50° from horizontal with one of the facet points down for the Freon to drip off. As the last Freon dries, slowly tilt the mirror to a horizontal position and gently blow the last clinging drop to the underside of the mirror. This eliminates spotting on the facets and corners of the mirror. Allow part to dry completely.

Fold a piece of lens tissue to form a wiping pad about 1/4" wide and 2" long, following steps a, b, and c below.

NOTE: USE GLOVES AND HANDLE TISSUE ONLY BY EDGES.

a) Carefully fold the tissue in half;
b) Pulling it taut, roll and fold it into a 1/4" wide strip.
c) While holding it taut, use the middle finger of one hand to push the folded strip toward you, touching only the backside. This will crease the middle and form a clean, untouched wiping pad. Try to avoid pinching or wrinkling the middle crease as this could cause contamination and/or scratches.

Saturate pad with Freon TF and shake off excess. While polygon is still cold from flushing, hold under high-intensity lamp and breathe on facet to be cleaned which will cause condensation to form on the facet surface. Using a VERY LIGHT TOUCH and VERY TIGHT CIRCULAR MOTION, wipe ACROSS THE WIDTH of the mirror facet. DO NOT USE STRAIGHT VERTICAL OR HORIZONTAL WIPING MOTIONS. AVOID WIPING INWARD ACROSS THE OUTSIDE EDGES OF THE FACETS.

NOTE: ACETONE MAY HARDEN TISSUE FIBERS CAUSING SCRATCHES. DO NOT USE ACETONE ON WIPING PAD.

Appendix A: Demonstration in the Fluid Modeling Facility Wind Tunnel

The laser system has been demonstrated in the Fluid Modeling Facility wind tunnel. The laser system was mounted on a base plate, which was secured to a wooden pallet. Using a fork-lift, the wooden pallet and laser apparatus were raised to the appropriate height for illuminating the wind tunnel from its side window. These steps are suggested for illuminating the tunnel with horizontal sheets of light:

1. Place the forks of the fork-lift under the wooden pallet, with the front of the laser pointing toward the fork-lift operator. Position the forks so that their entire lengths are under the pallet. Next, secure the pallet to the forks using C-clamps. In addition, strap chains from the pallet to the fork truck to help prevent the pallet from sliding off.

2. Put the cover over the laser and base-plate. Attach the hood which will extend between the opening in the main cover and the tunnel window. Position the fork-lift so that the length of the laser is parallel to the side window. The side of the pallet with the lenses should be closest to the tunnel window. The lenses should be located slightly downstream of the model. (40 cm downstream seems to work sufficiently well).

3. Now, lift the pallet while watching to be sure that it is in no danger of falling. After raising it to the appropriate height at the side of the window, make necessary adjustments so that the hood fits snugly between the laser and window.

4. Set up a tripod mounted camera near the side of the wind tunnel. Connect it to a monitor for viewing the laser light. Set up a partition or set of curtains and place the monitor behind it to establish a shielded viewing area.

5. Make two wooden blocks with heights at least as great as the height that you will raise the horizontal light sheet above the tunnel floor. Paint them flat black. Next, apply a strip of masking tape vertically along the center of each block. Mark the face of each block in one cm increments, using thick black lines on the masking tape.

6. Set the model to be studied in the appropriate location of the wind tunnel. Then, place one of the wooden blocks in the tunnel along the wall which is farthest from the laser. Place it on the floor of the tunnel about 1 meter upstream of the model. Place the other wooden block along the same wall about 1 meter downstream of the model. Orient them so that the markings can serve as vertical measuring instruments.

7. Exit the tunnel and put the LaserGard goggles on. Raise the laser with the fork-lift to where the light sheet is expected to be at half the model height. Start the laser at low power. By viewing the monitor, establish where the laser light sheet is located. It is more easily seen with the tunnel lights off. If the sheet is not striking

both wooden blocks, turn the laser off and adjust the fork-lift until it does. By carefully viewing the monitor, determine the height of the light sheet at each of the wooden blocks. (Use the 1 cm marks on the masking tape.) Adjust the tilt of the fork-lift until the light sheet strikes both blocks at the same height. Next, adjust the fork-lift vertically until the light sheet strikes the top of the model. Determine the height at which the light sheet is striking the wooden blocks now. It should be the same height as the height of the model. If it is not, turn the laser off, lower the fork-lift, remove the cover, and adjust the lens hardware for the appropriate tilt. Repeat the entire process until the laser light sheet strikes the model and both wooden blocks at the same height.

8. When the light sheet has been levelled, raise it to the height of the model. On the fork-lift, locate a section which moves vertically with the forks, but is adjacent to a stationary section. Place vertical strips of masking tape on both parts. Mark a reference point on the tape of the section which moves. On the stationary tape, measure and mark the heights at which to elevate the laser light sheet. This can now be utilized to quickly and accurately position the horizontal light sheet. Periodically, check the height of the light sheet on the wooden block scales by viewing the monitor.

9. When recording smoke flows in the tunnel using the laser sheets, it it necessary to turn off the lights in the tunnel and the middle two rows of overhead lights in the laboratory. By doing this, the smoke is illuminated exclusively by the laser.

The procedure for positioning and levelling the light sheet using the polygonal mirror is the same as for the lens apparatus. When using the polygon, remember these points:

1. As mentioned before, always have the polygon rotating when the laser is started.

2. Use Table 1 for setting the scanning speed of the beam. Generally, a large number of scans per field is desirable; therefore, a higher power supply setting should give better results than a lower one. A setting of 12.6 volts may be a good starting point. It produces a relatively high scanning rate which is roughly a whole multiple of a camera's framing rate. Calculations show that a supply voltage of less than 2.2 volts produces less than one beam sweep per recording field, resulting in aliasing. Consequently, you should keep the scanning speed well above this point.

APPENDIX D

Preliminary Evaluation of Laser Light Video Flow Data

Preliminary Evaluation of Laser Light Video Flow Data

by

A. H. Huber[1], D. S. Trotter[2], R. E. Lawson, Jr.[1],
S. A. Rajala[2], and R. E. Van Dyck[2]

1 U.S.EPA, Atmospheric Research and Exposure Assessment Laboratory,
RTP, NC 27711

2 North Carolina State University, Department of Electrical and Computer
Engineering, Raleigh, North Carolina, 27695

A series of figures showing some preliminary analyses is presented here to demonstrate the features of the video images from the laser sheet lighting experiments that are discussed in Chapter 6. The video images were digitized using the Imaging Tecnology Incorporated FG-101 frame grabber board which is part of the video image analysis system at the U.S. Environmental Protection Agency Fluid Modeling Facility (see Lee et. al. as referenced in Chapter 6). The data was them analysed using special software that was developed on the EPA IBM mainframe computer. We realize that the lack of explaination and discussion accompanying the figures may limit the usefulness of the presentation to some readers. We were not able to submit a complete discussion in time for this report. This appendix was included here because we believe the figures may be quite interesting and useful to some readers. A complete paper on these preliminary analyses is being prepared and will be published elsewhere as soon as possible.

The data presented in the figures are all from the same case study. The model building was 10-cm (along-stream, x-direction) by 10-cm (high, z-direction) by 20-cm (cross-stream, y-direction). Distances are normalized by the building height, H. The source of smoke or tracer gas was located centered at the downstream base of the building (x=y=z=0). Figures 1-3 show the camera data calibration correction for nonlinear camera response, correction for differences in light exposure time due to distance R along the radius of the rotating laser beam, and differences betweem image intensity resulting from a discrete integer calibration lookup table and that from a mathematical calibration function. Figures 4-6 compare normalized (by the value at x/H=3) image intensity with that of a similarly normalized tracer gas concentration. Figures 7-9 display examples of the image data at one cross-stream postion over time, an average image over the full frame, and a series of non-averaged full frames. The range of values and the detail within these video images were found to be significantly greater than was found in the earlier studies using flood lighting (see Appendix A).

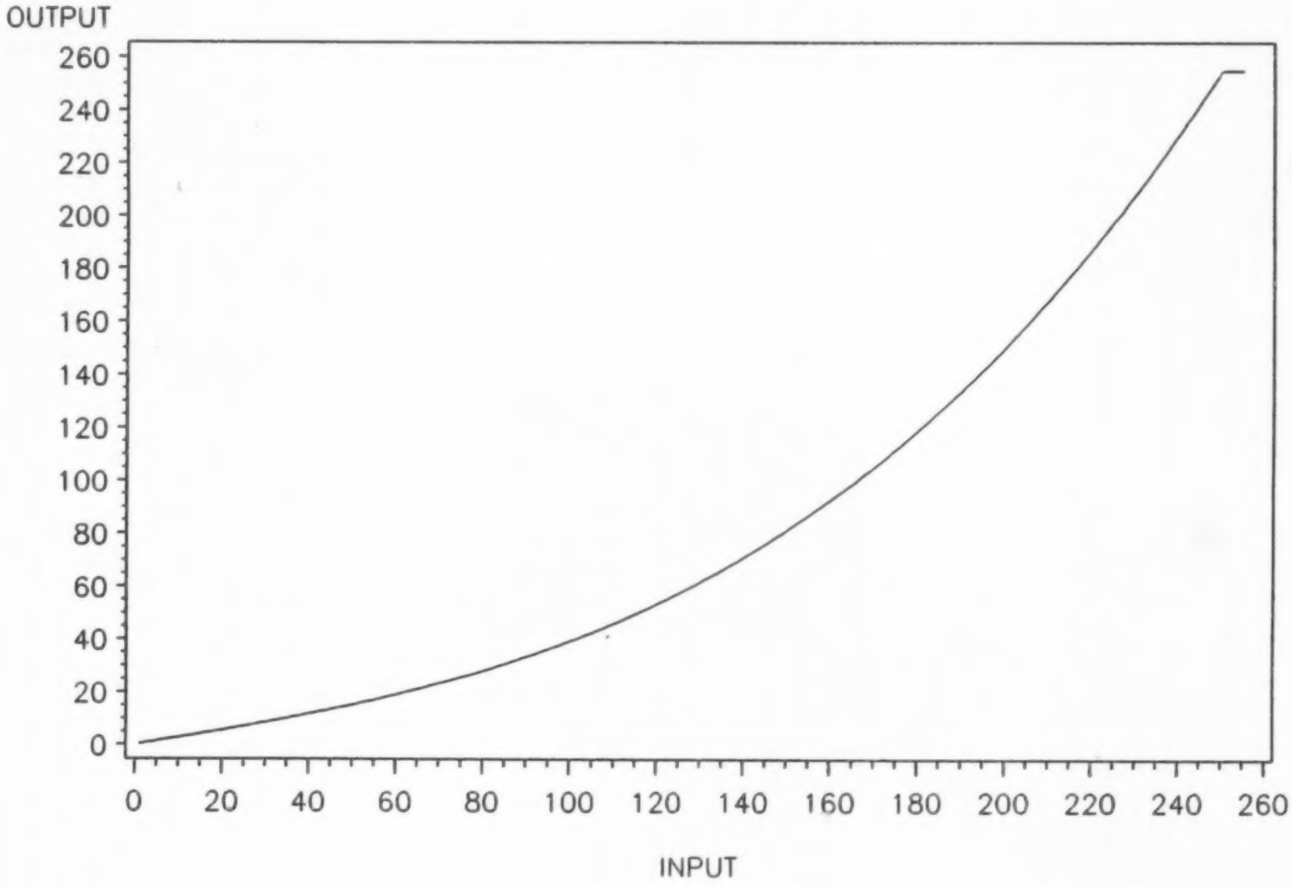

Fig. 1. Video camera calibration curve
(from experiments by Lee *et al.*, 1988).

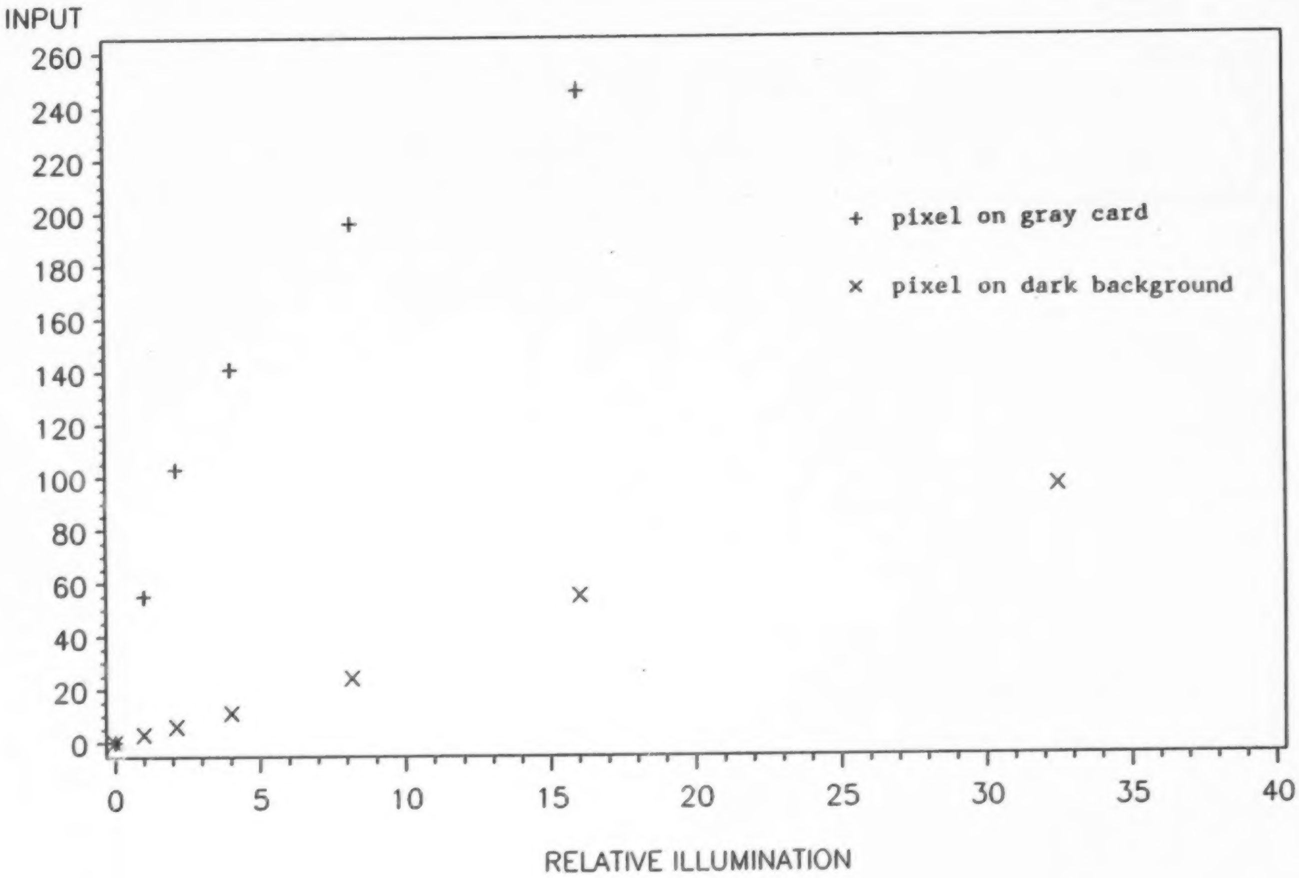

(a) calibration input

Fig. 2. Evaluation of camera calibration:
(a) calibration input, and (b) calibration output.

(b) calibration output

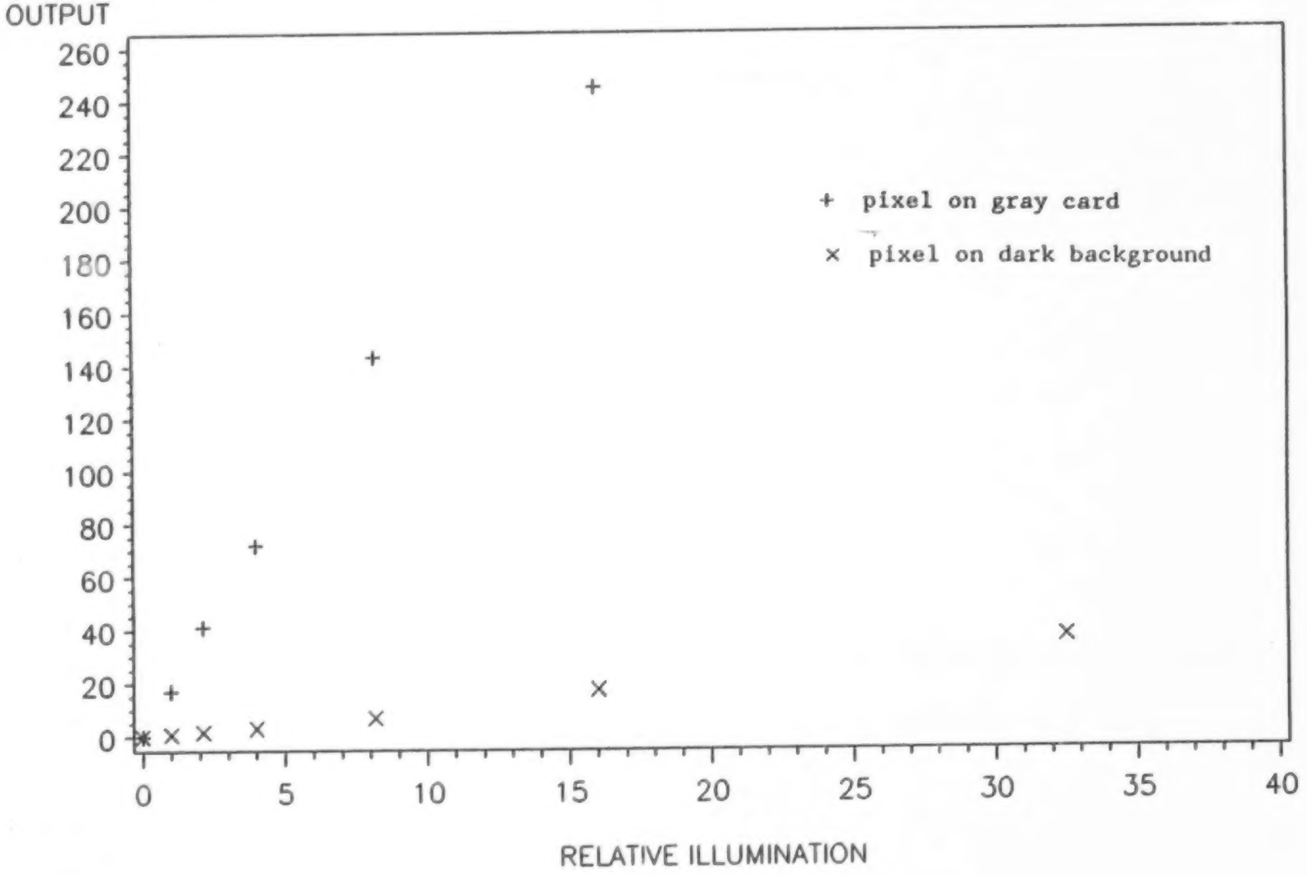

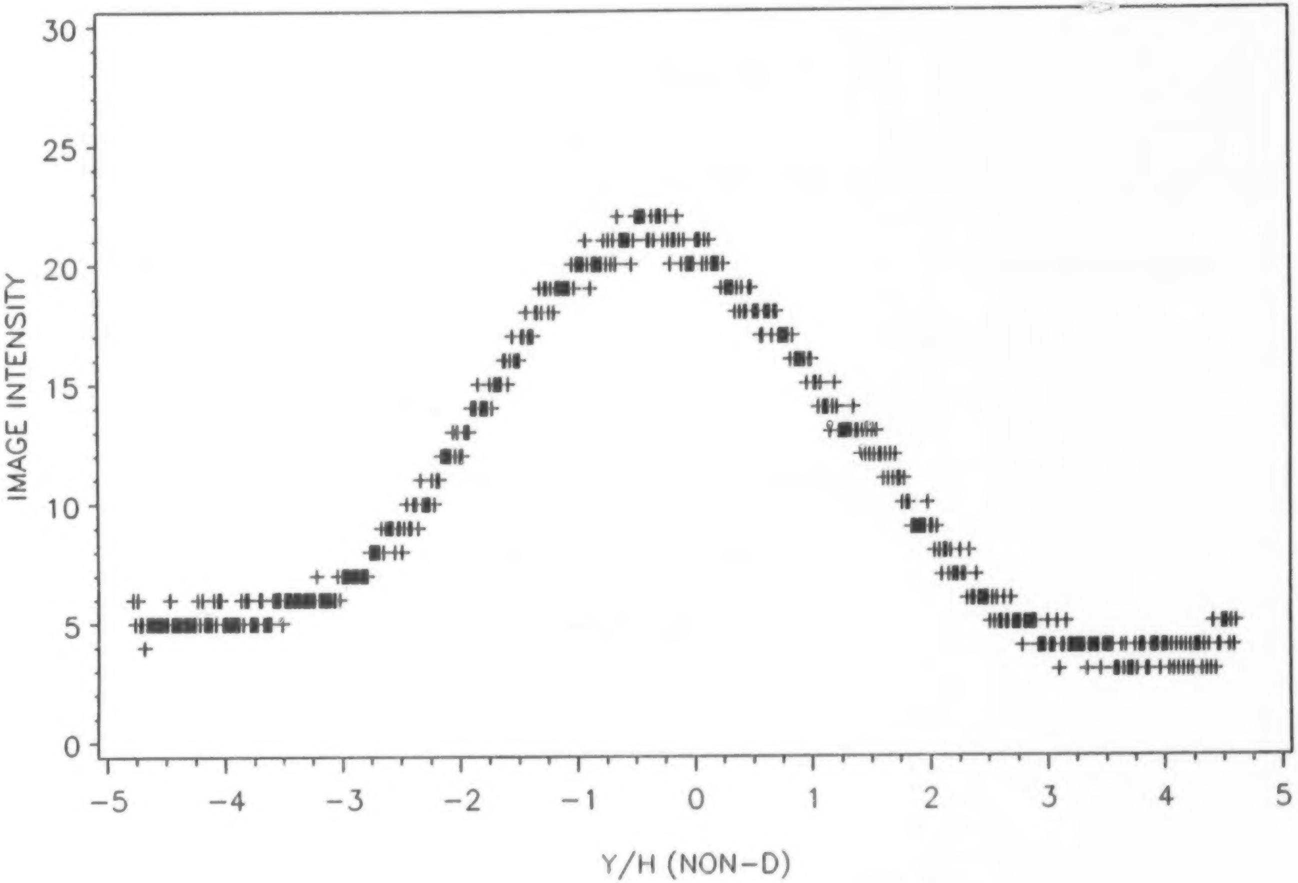
(a) integer output without calibration

Fig. 3. Example plots of an cross-stream profile (ground level at x/H=4.3) of average image intensity which demonstrate data processing issues:
(a) integer output without calibration,
(b) integer output using the integer calibration table,
(c) integer output using the integer calibration table
and 1/R correction, and
(d) integer output using the mathematical calibration function
and 1/R correction.

(b) integer output using the integer calibration table

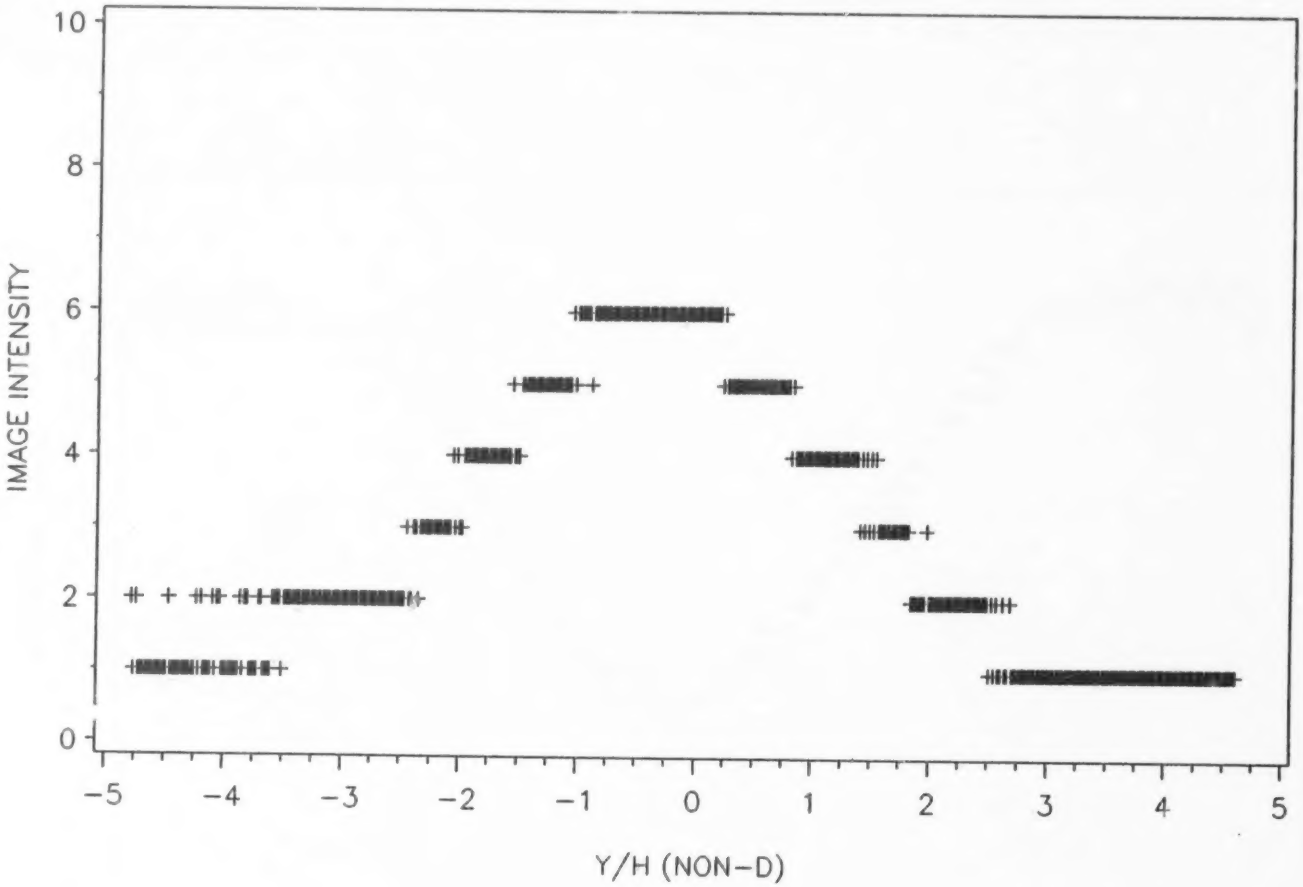

(c) integer output using the integer calibration table
and 1/R correction

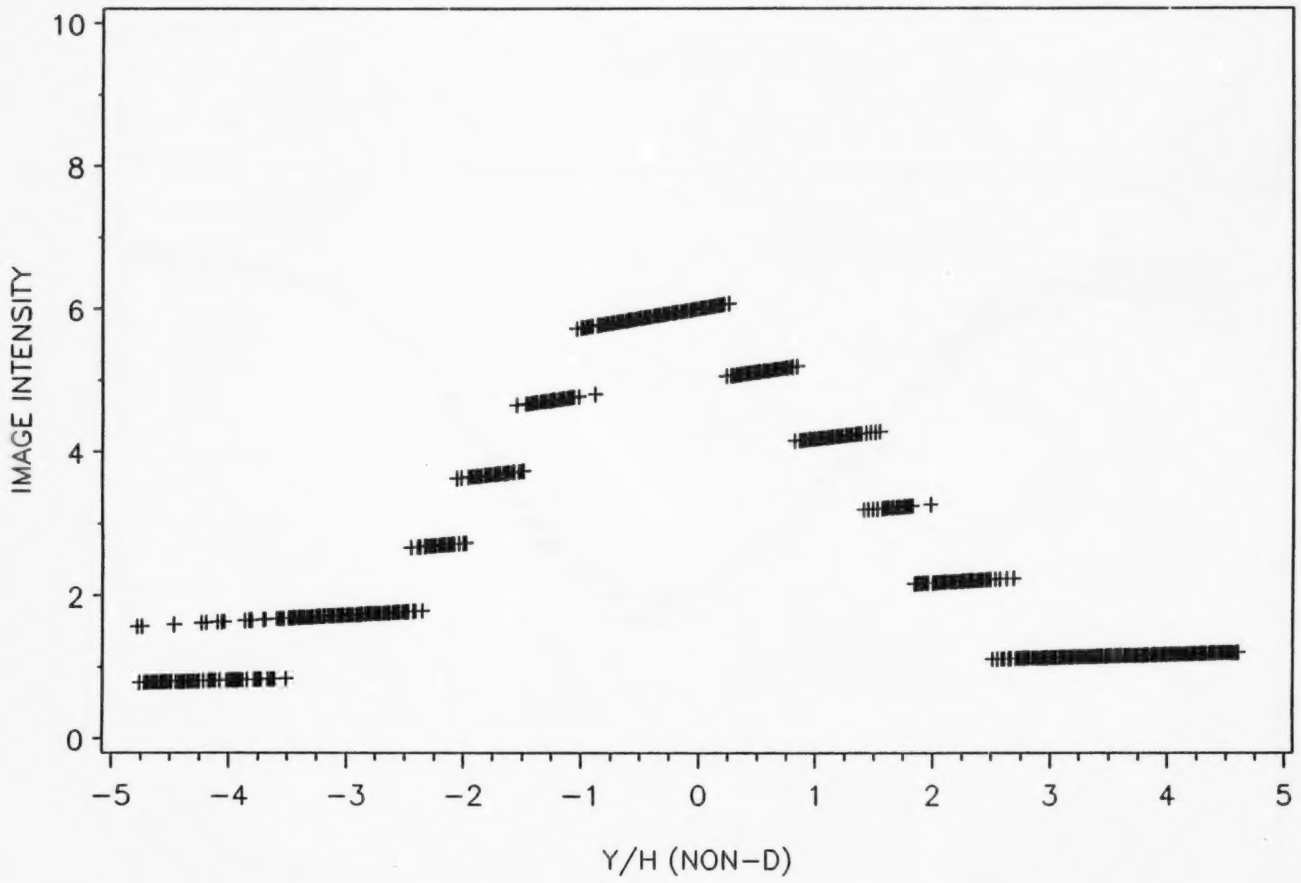

(d) integer output using the mathematical calibration function
and 1/R correction

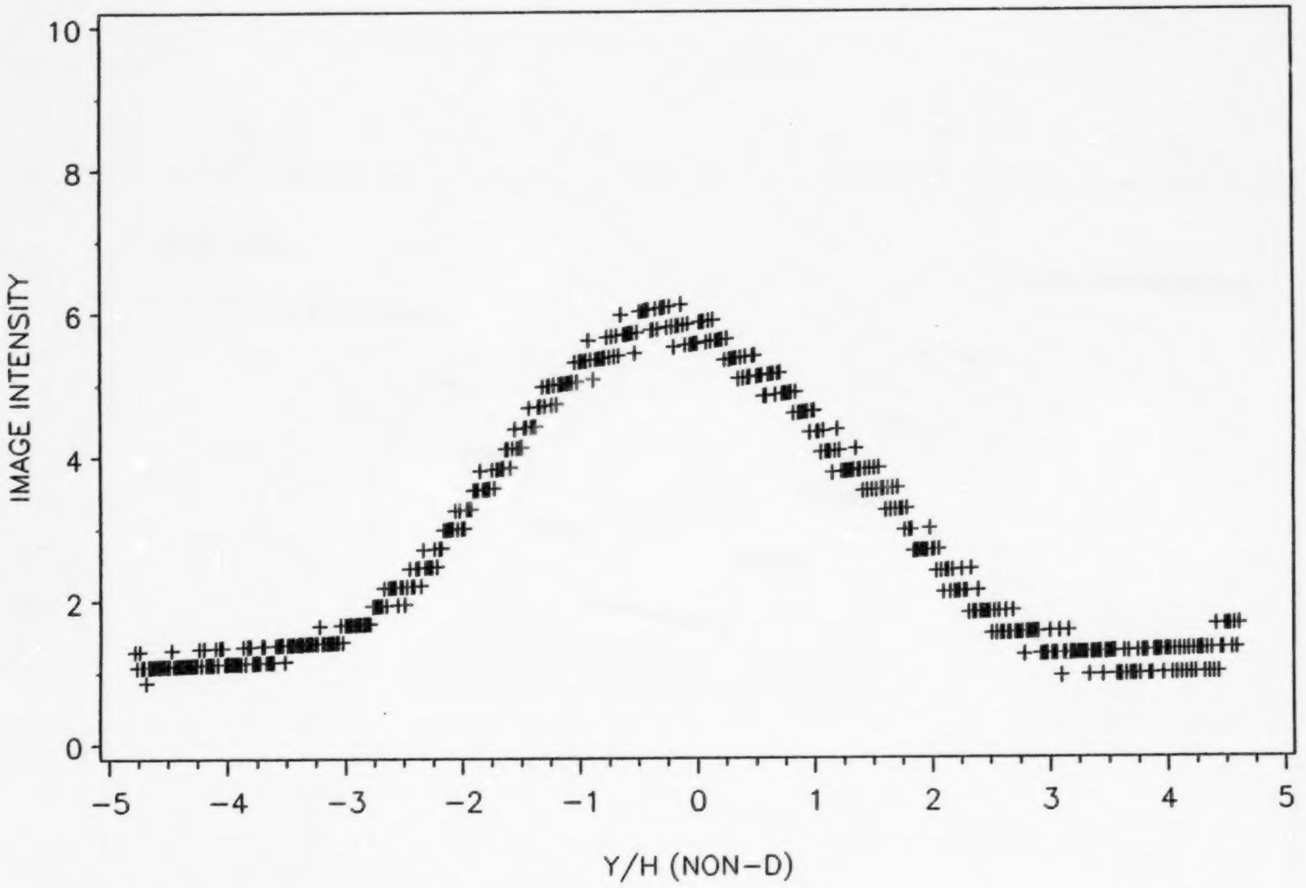

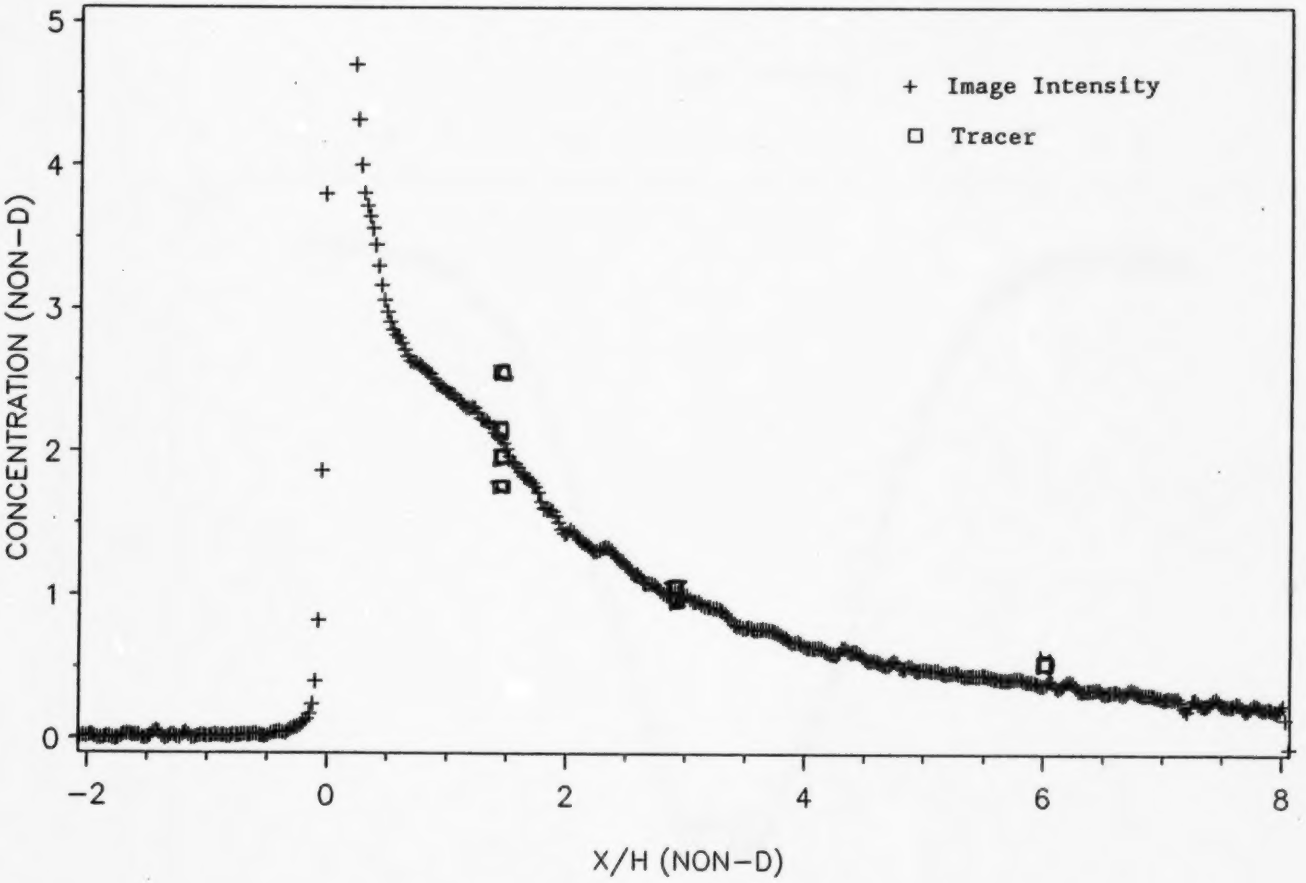

Fig. 4. The downstream profile (ground level at $y/H=0$) of average image intensity that has been normalized by the value at $x/H=3$; these values thus represent a relative concentration. These are compared with similarly normalized tracer concentrations.

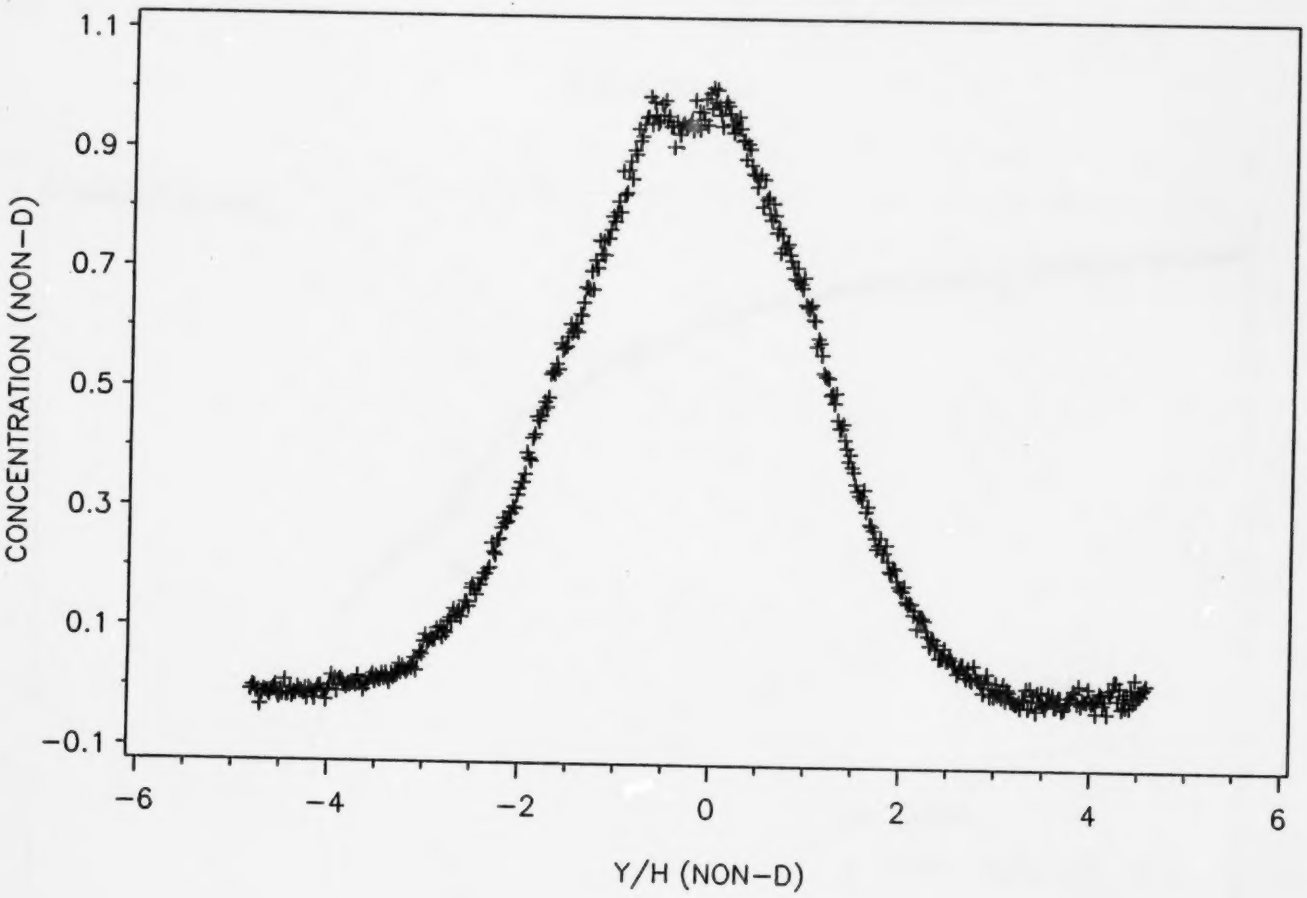
(a) z/H=0 to 0.2

Fig. 5. The cross-stream profile (at x/H=3) of average image intensity that has been normalized by the peak value:
(a) z/H=0 to 0.2, and (b) z/H=1.5 to 1.7

(b) z/H-1.5 to 1.7

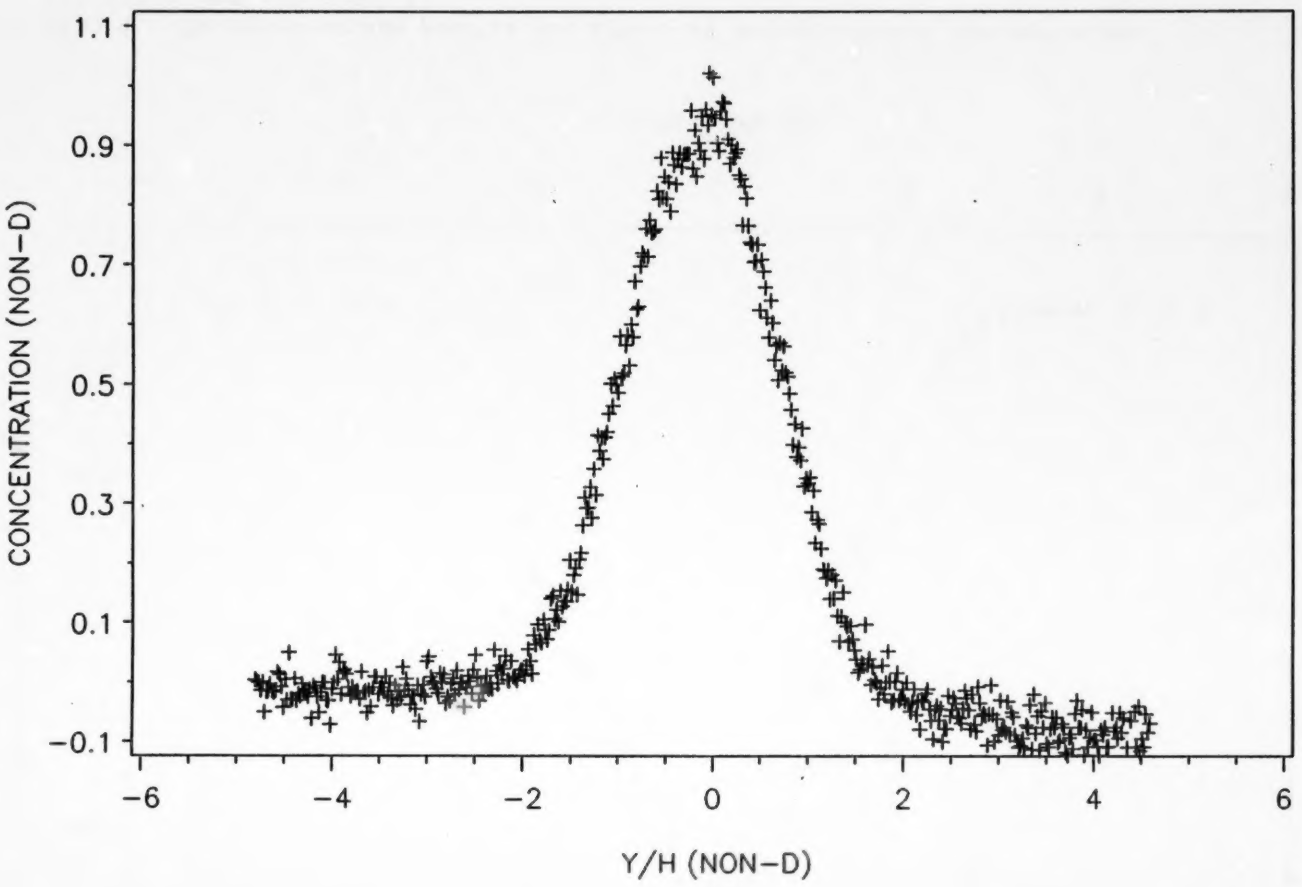

(a) z/H=0

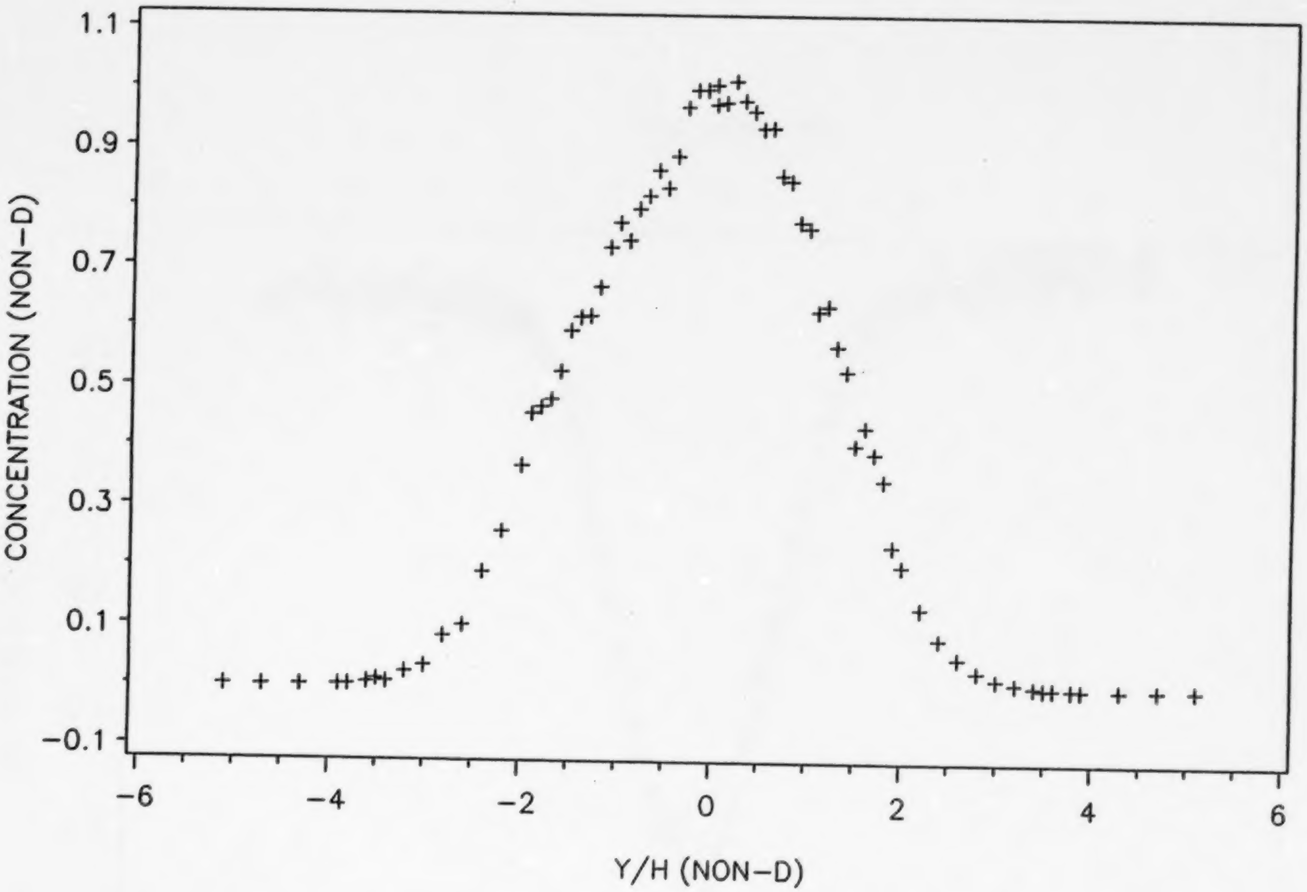

Fig. 6. The cross-stream profile (at x/H=3) of average tracer concentration: (a) z/H=0, and (b) z/H=1.5.

(b) z/H-1.5

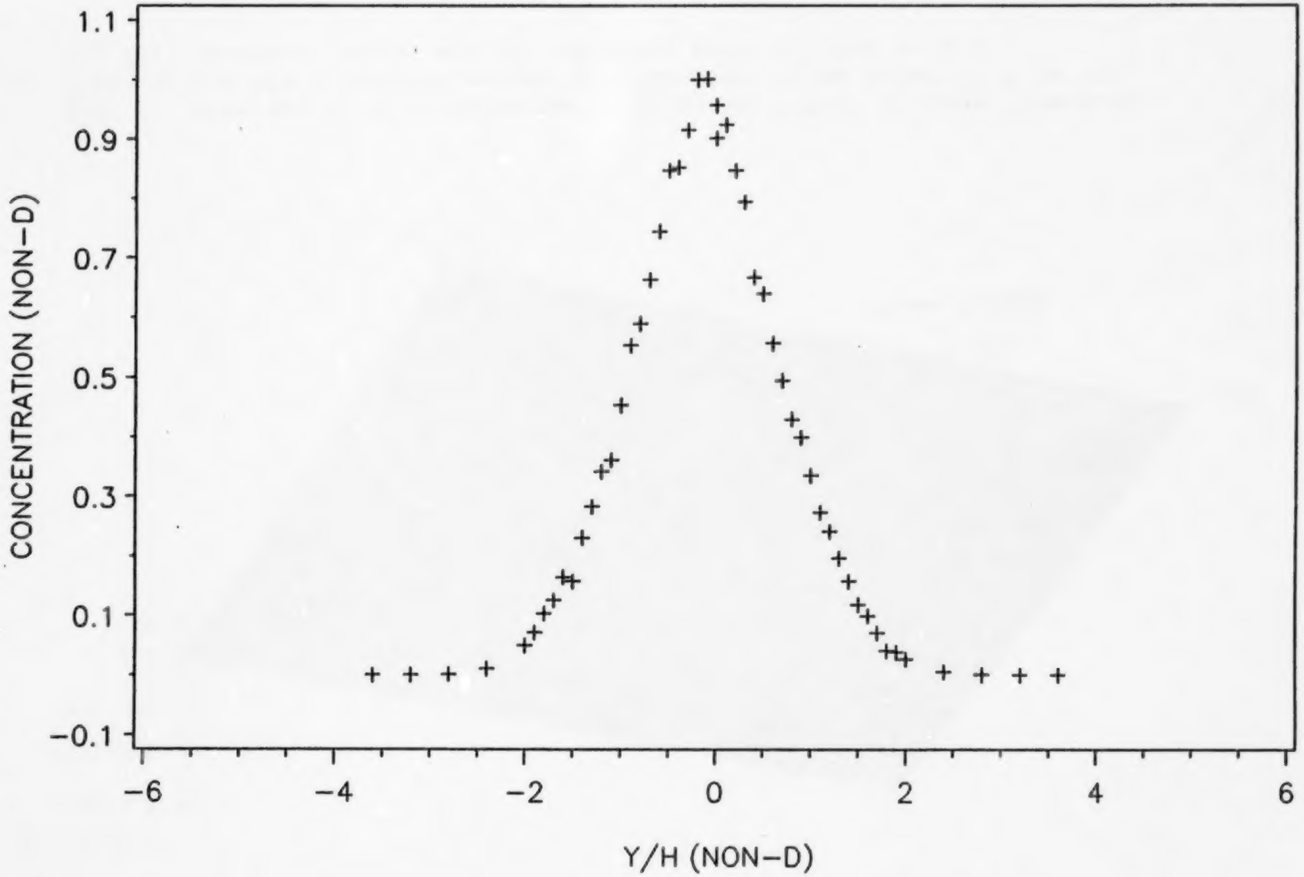

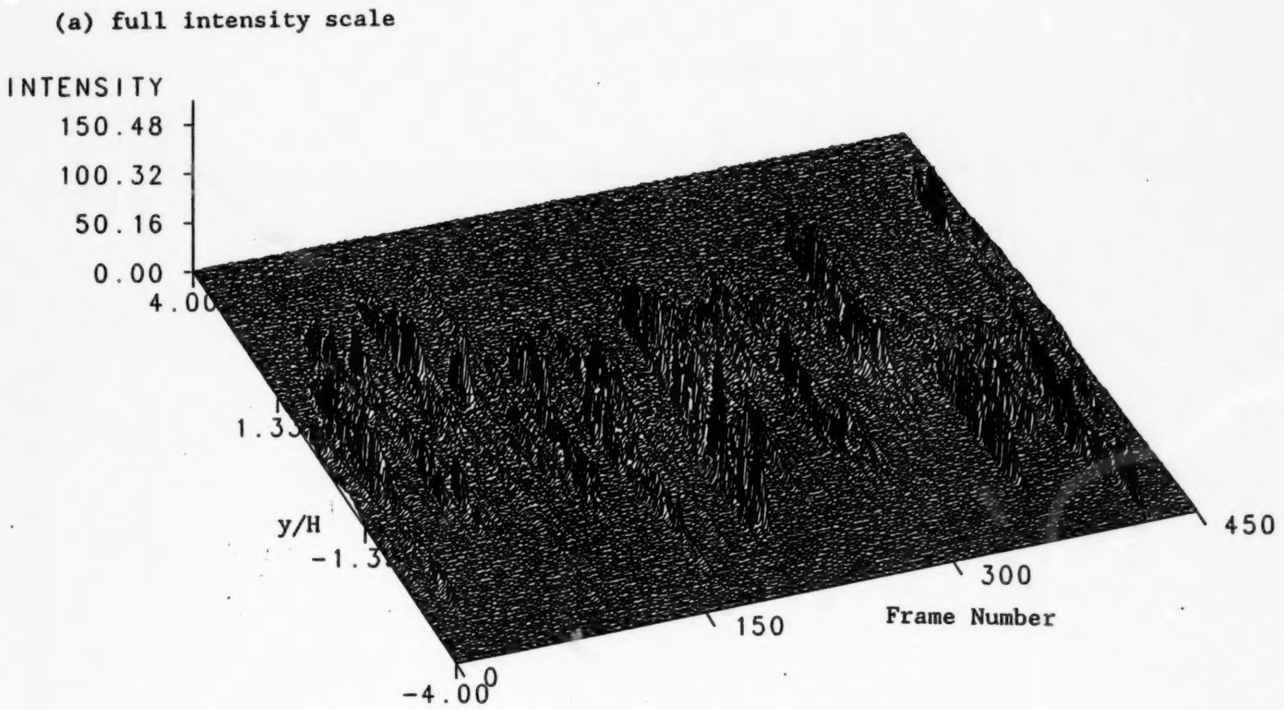
(a) full intensity scale

Fig. 7. Time series of cross-stream profiles (at $x/H=3$) of image intensity. There is a 0.033 s interval between profiles over frame number T= 0 to 450: (a) full intensity scale, and (b) intensity scale clipped at 50.0.

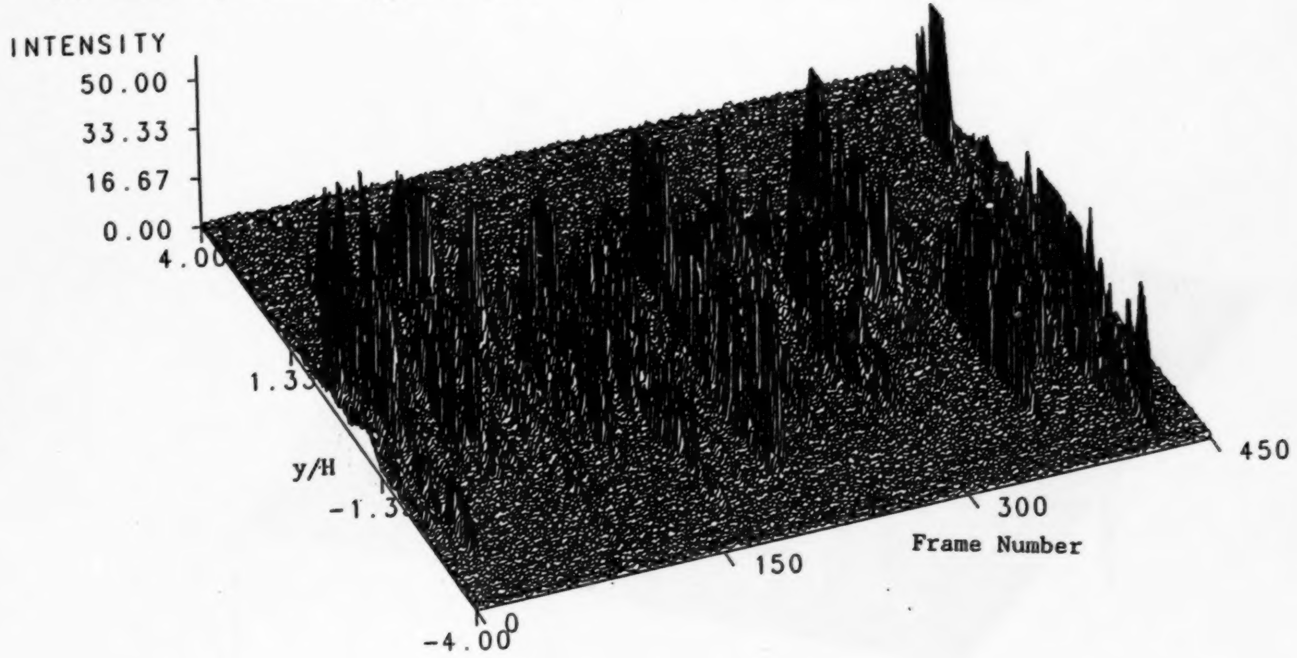

(b) intensity scale clipped at 50.0

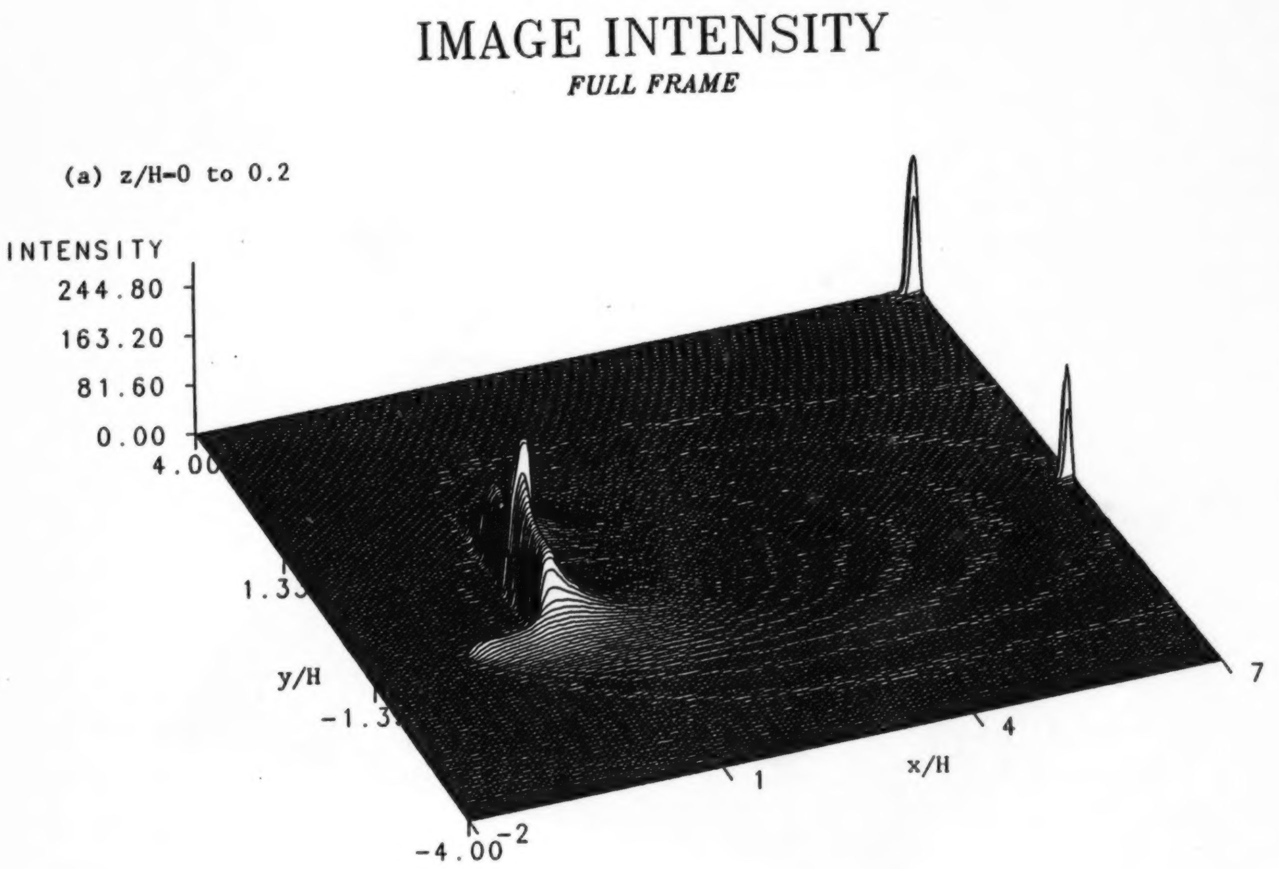

Fig. 8. Time average of image intensity over the full image frame: (a) z/H-0 to 0.2, and (b) z/H-1 to 1.2.

IMAGE INTENSITY

FULL FRAME

(b) z/H=1 to 1.2

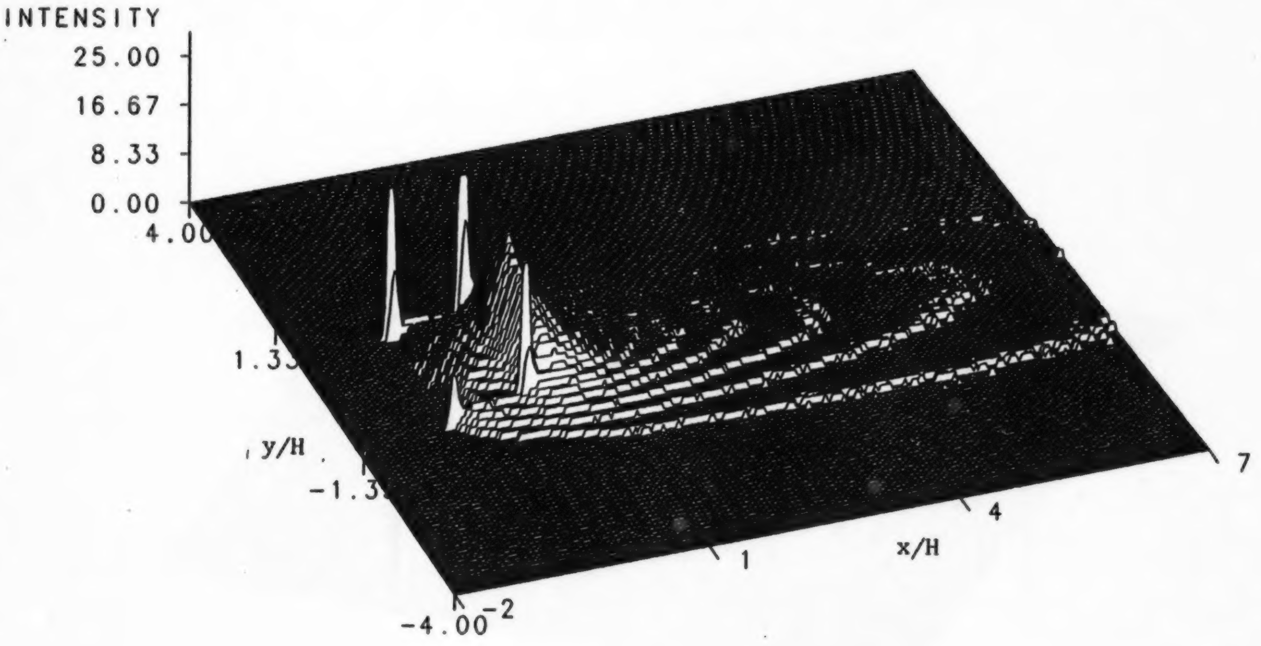

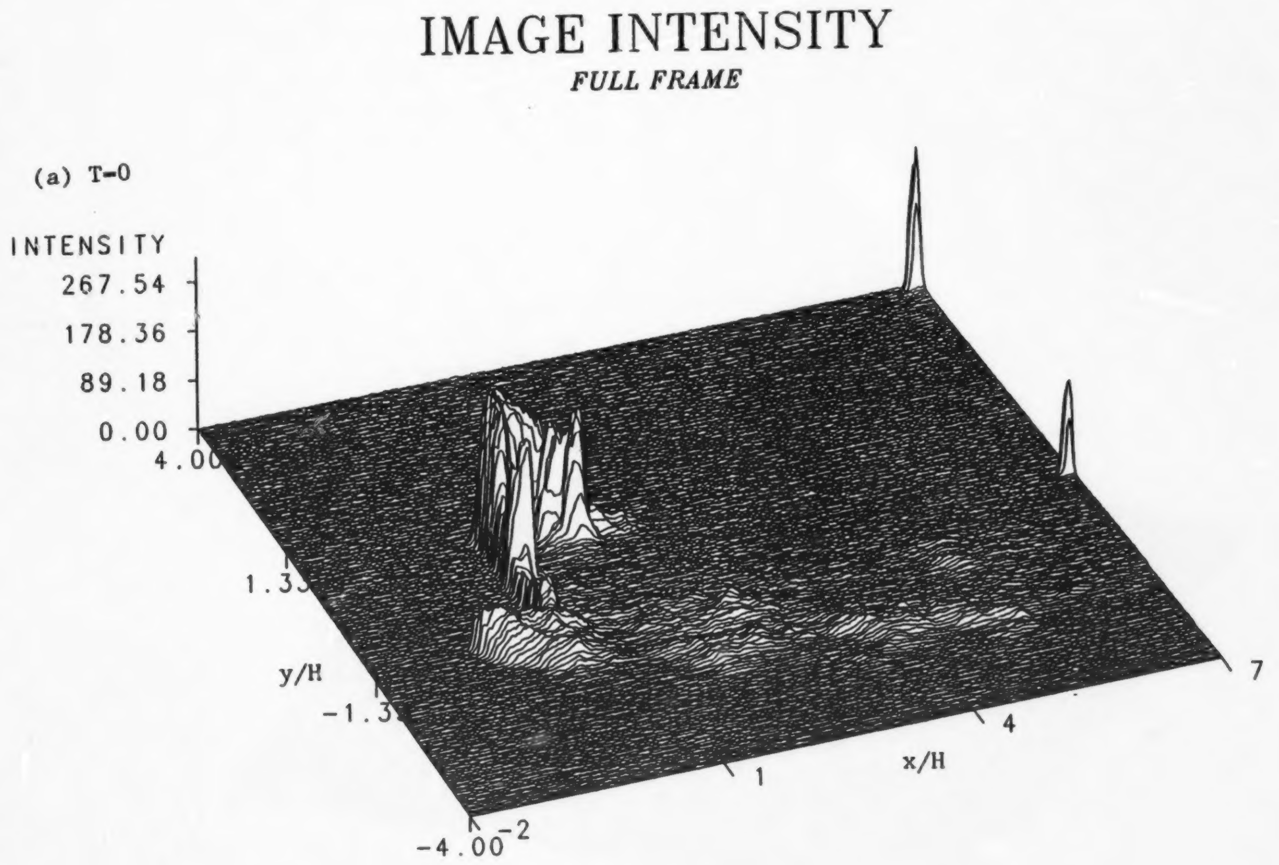

Fig. 9. Image intensity for a sequence of full image frames:
(a) T=0, (b) T=0.1 s, (c) T=0.133 s, (d) T=0.166 s, and (e) T=0.2 s.

IMAGE INTENSITY

FULL FRAME

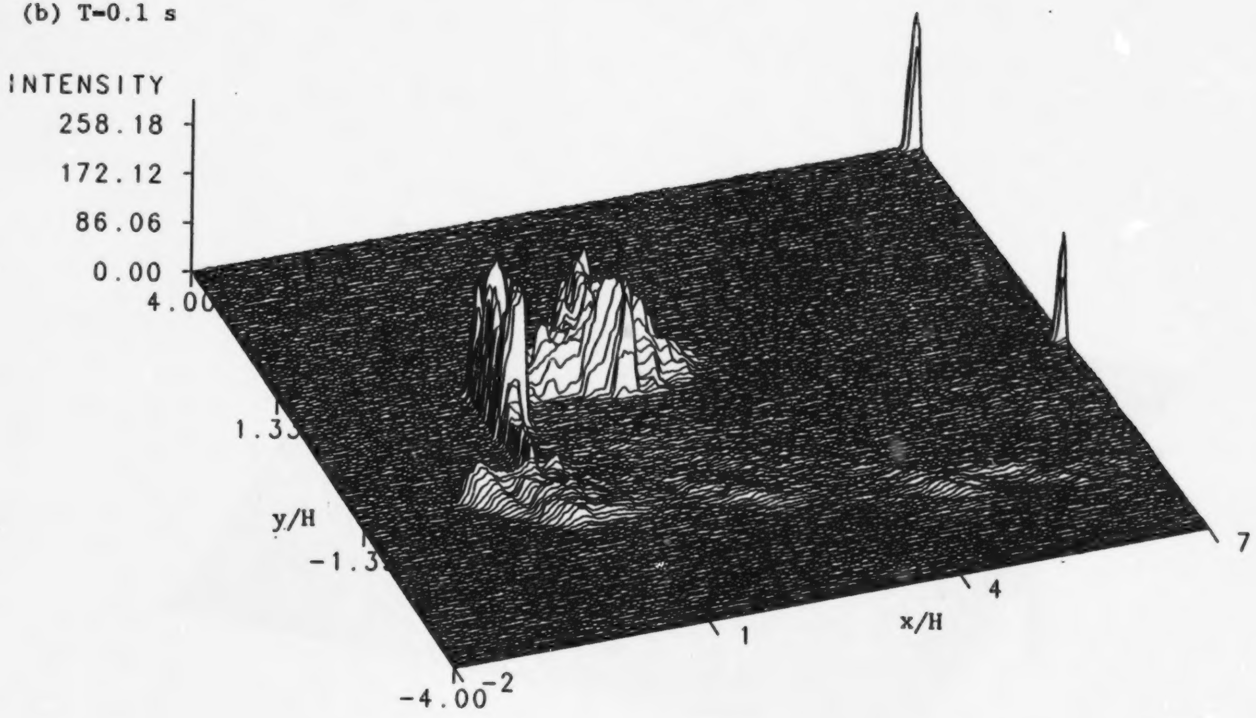

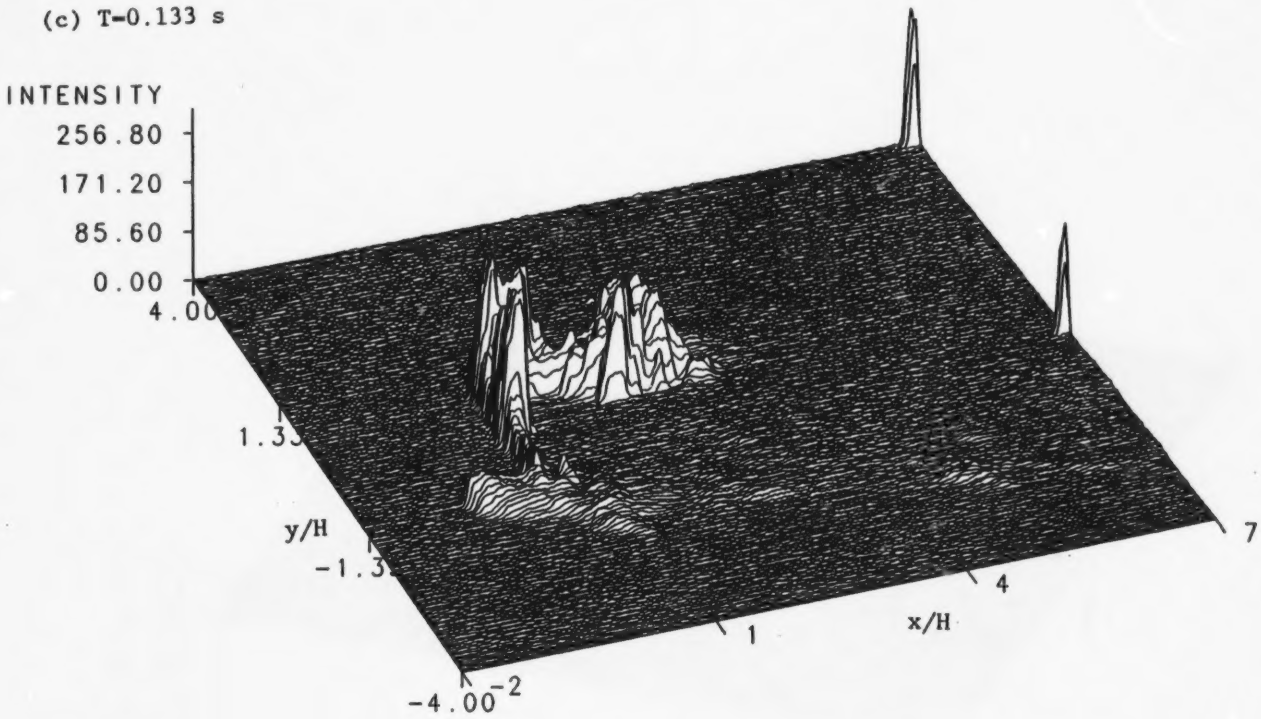

IMAGE INTENSITY

FULL FRAME

(c) T-0.133 s

IMAGE INTENSITY

FULL FRAME

(d) T-0.166 s

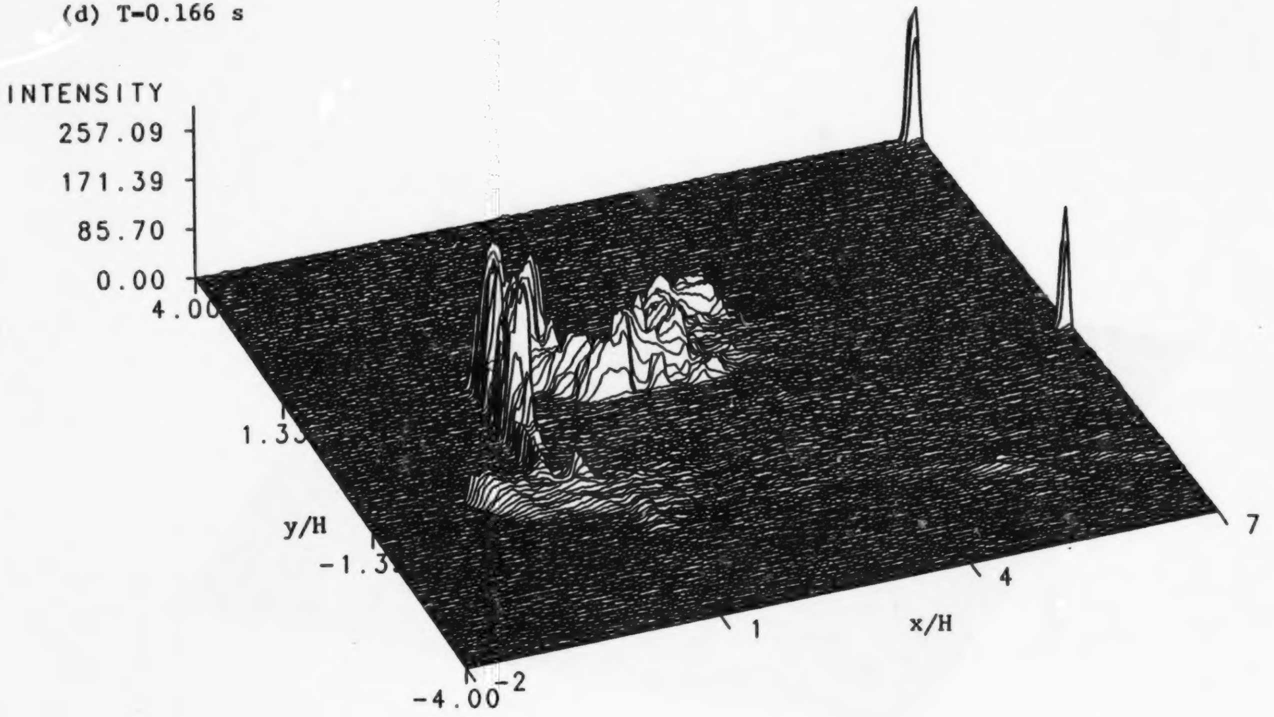

IMAGE INTENSITY

FULL FRAME